

Exploitation of distributed scatterers in synthetic aperture radar interferometry

Samiei Esfahany, Sami

DOI

[10.4233/uuid:22d46f1e-9061-46b0-9726-760c41404b6f](https://doi.org/10.4233/uuid:22d46f1e-9061-46b0-9726-760c41404b6f)

Publication date

2017

Document Version

Final published version

Citation (APA)

Samiei Esfahany, S. (2017). *Exploitation of distributed scatterers in synthetic aperture radar interferometry*. [Dissertation (TU Delft), Delft University of Technology]. <https://doi.org/10.4233/uuid:22d46f1e-9061-46b0-9726-760c41404b6f>

Important note

To cite this publication, please use the final published version (if applicable). Please check the document version above.

Copyright

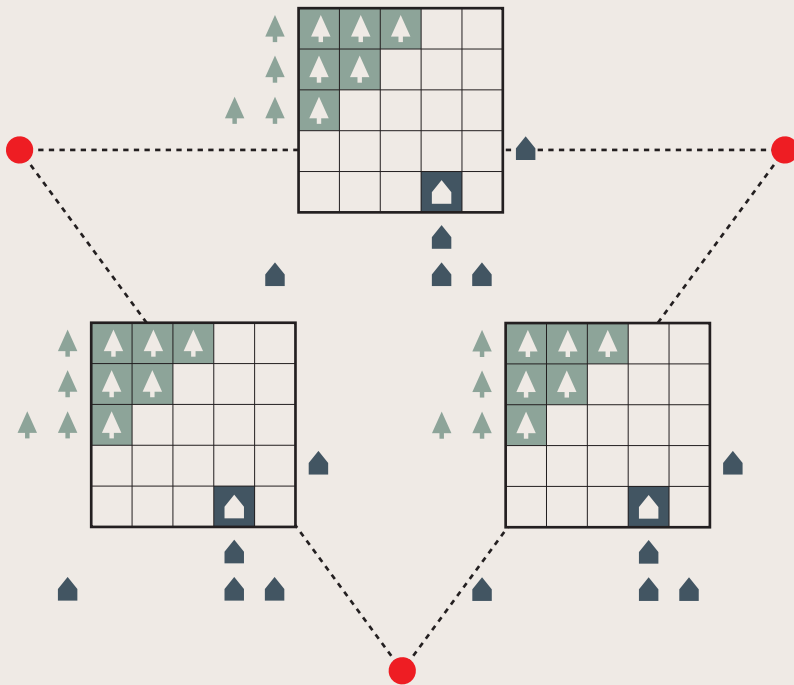
Other than for strictly personal use, it is not permitted to download, forward or distribute the text or part of it, without the consent of the author(s) and/or copyright holder(s), unless the work is under an open content license such as Creative Commons.

Takedown policy

Please contact us and provide details if you believe this document breaches copyrights. We will remove access to the work immediately and investigate your claim.

Exploitation of Distributed Scatterers in Synthetic Aperture Radar Interferometry

Sami Samiei Esfahany



Exploitation of
Distributed Scatterers in
Synthetic Aperture Radar Interferometry

Sami Samiei Esfahany

On the cover

Stylized depiction of the two key processing steps in exploitation of distributed scatterers: (i) adaptive multilooking, and (ii) ESM-phase estimation based on the phase consistency condition (see figs. 2.15 and 4.1 of this thesis).

Exploitation of Distributed Scatterers in Synthetic Aperture Radar Interferometry

Proefschrift

ter verkrijging van de graad van doctor
aan de Technische Universiteit Delft,
op gezag van de Rector Magnificus prof. ir. K.C.A.M Luyben,
voorzitter van het College voor Promoties,
in het openbaar te verdedigen op woensdag 31 mei 2017 om 12:30 uur

door

Sami SAMIEI ESFAHANY

Master of Science in Geomatics Engineering
Delft University of Technology, the Netherlands

geboren te Tehran, Iran.

This dissertation has been approved by the

Promotor: Prof. dr. ir. R.F. Hanssen

Composition of the doctoral committee:

Rector Magnificus	chairman
Prof. dr. ir. R.F. Hanssen	Delft University of Technology, promoter

Independent members:

Prof. dr. h.c. F. Rocca	Polytechnic University of Milan, Italy
Prof. dr. M. Eineder	Technical University of Munich, Germany & German Aerospace Center (DLR)
Prof. dr. J. Mallorqui	Polytechnic University of Catalonia, Spain
Prof. dr. -ing. habil. R. Klees	Delft University of Technology
Dr. P. López-Dekker	Delft University of Technology
Prof. ir. P. Hoogeboom	Delft University of Technology, reserve member

Other members:

Dr. ir. G. Ketelaar	Nederlandse Aardolie Maatschappij (NAM)
---------------------	---

Samiei-Esfahany, Sami

Exploitation of distributed scatterers in synthetic aperture radar interferometry

Department of Geoscience and Remote-Sensing (GRS), Delft University of Technology

Keywords: satellite radar interferometry, surface deformation, geodetic estimation, distributed scatterers

Citation: Samiei-Esfahany, S. (2017), Exploitation of distributed scatterers in synthetic aperture radar interferometry. PhD thesis, Delft University of Technology.

ISBN 978-94-6186-806-0

Copyright © 2017 by Sami Samiei-Esfahany

All rights reserved. No part of the material protected by this copyright notice may be reproduced or utilized in any form or by any means, electronic or mechanical, including photocopying, recording or by any information storage and retrieval system, without the prior permission of the author.

Cover design: Golsoo Samiee

Printed by Ridderprint, The Netherlands

Typeset by the author with the L^AT_EX documentation system

Contents

Contents	i
Acknowledgments	v
Summary	vii
Samenvatting (Summary in Dutch)	ix
Nomenclature	xi
1 Introduction	1
1.1 Motivation	1
1.2 Background	1
1.3 Problem formulation and research objectives	6
1.3.1 Methodology	7
1.4 Outline	8
2 Time-series InSAR and Distributed Scatterers: A Review	11
2.1 InSAR principle	11
2.1.1 SAR measurements	11
2.1.2 Interferometric SAR (InSAR)	12
2.1.3 InSAR processing: overview	22
2.1.4 Conventional InSAR: limitations	28
2.2 Time-series InSAR	28
2.2.1 Persistent scatterers vs distributed scatterers	29
2.2.2 TInSAR methodologies	31
2.3 TInSAR processing steps	36
2.3.1 Pixel selection	37
2.3.2 Spatio-temporal unwrapping	41
2.3.3 Atmospheric-signal mitigation	43
2.4 Filtering: adaptive multilooking for distributed scatterers	45
2.4.1 Non-parametric tests for brotherhood selection	46
2.4.2 Parametric tests for brotherhood selection	48
2.5 ESM-phase estimation for Distributed Scatterers	51
2.5.1 Post-unwrapping ESM-phase estimation	51
2.5.2 Pre-unwrapping ESM-phase estimation	52
2.6 Summary	53

3	Stochastic model for Distributed Scatterers	55
3.1	Noise components in SAR/InSAR stacks	55
3.2	Single-point complex statistics for DS in SAR stacks	56
3.2.1	Physical origin of noise	56
3.2.2	Circular Gaussian distribution	57
3.2.3	Single-point statistics for a single SLC image	61
3.2.4	Coherence matrix	63
3.3	Single-point phase statistics for single interferogram	69
3.4	Single-point phase statistics for interferogram stack	73
3.4.1	Causes of correlation between interferograms	74
3.4.2	Phase statistics for interferograms with a common image	75
3.4.3	First and second statistical moments	77
3.4.4	Evaluation of phase covariance matrix: Monte-Carlo method	78
3.4.5	Evaluation of phase covariance matrix: Analytical approximation	79
3.5	Summary and conclusions	83
4	Equivalent SM-phase Estimation: Complex optimization	85
4.1	Concept of phase consistency	86
4.2	Generic mathematical model	88
4.2.1	Functional model	88
4.2.2	Objective functions	89
4.3	A review of existing estimators	93
4.3.1	Maximum Likelihood method	93
4.3.2	MCSR mdethod	95
4.3.3	Eigendecomposition-based methods	96
4.3.4	Least circular variance estimator	97
4.3.5	Summary of the review of ESM-phase estimators	98
4.4	Practical considerations	98
4.4.1	Solution of different estimators	98
4.4.2	Conditions for multilooking	100
4.4.3	Posterior assessment	101
4.5	Cramér-Rao Bound for ESM-phase estimation	101
4.6	Conclusions	102
5	Equivalent SM-phase Estimation: Integer least squares method	103
5.1	Hybrid functional model for ESM-phase estimation	103
5.2	Integer Least Squares (ILS) for ESM-phase estimation	104
5.2.1	ILS Estimator	104
5.2.2	The choice of weight matrix	107
5.2.3	Practical Considerations	108
5.3	Synthetic Data Processing	109
5.3.1	Simulation setting	110
5.3.2	Simulation results	111
5.4	Case study	119
5.5	Conclusion	122
6	Feasibility study: Veendam subsidence field	125
6.1	Introduction	125

6.2	The Veendam test case	127
6.3	A priori analysis	128
6.3.1	Coherence behavior over urban areas	129
6.3.2	Coherence behavior over agricultural and pasture areas	130
6.3.3	Coherence behavior over roads	132
6.3.4	Cramér-Rao bound study of the whole area	133
6.4	A posteriori analysis	135
6.4.1	Processing setting	135
6.4.2	Results	136
6.5	Analytical model for seasonal temporal decorrelation	138
6.5.1	Model for periodic temporal decorrelation	138
6.5.2	Estimation of coherence model parameters	142
6.6	Feasibility study	145
7	Conclusions and Outlook	151
7.1	Conclusions	151
7.1.1	Mathematical model for ESM-phase estimation	151
7.1.2	ILS ESM-phase estimator	152
7.1.3	DS density over rural landscapes	154
7.1.4	Temporal decorrelation model	155
7.2	Contributions	156
7.3	Recommendations	157
	Appendices	161
	Appendix A Derivations	163
A.1	Derivations of Chapter 3	163
A.1.1	Derivation of the covariance matrix of eq. (3.83)	163
A.2	Derivation of Chapter 4	166
A.2.1	Proof of eq. (4.21)	166
A.2.2	Proof of eq. (4.27)	167
A.2.3	Explanation and proof of eq. (4.52)	168
	Appendix B Integer bootstrapping estimator, and the simulation setting	171
B.1	Integer Bootstrapping Estimator	171
B.2	Simulation setting	172
	Bibliography	175
	About the Author	195

Acknowledgments

This thesis could not be realized without the help, support, and contributions from many people that I had the pleasure to work with during the past several years.

Foremost, I would like to thank my promoter and daily supervisor, Ramon Hanssen, for making it all possible, for the freedom and flexibility he gave me in my research, for the open way in which we always communicated, and for the meticulous reading of this manuscript and the critical feedback he provided me. Ramon, I have learned a lot from you, and thank you very much for your constant and kind support, not only at work but also during a few difficult periods in my life.

This study has been sponsored by the Nederlandse Aardolie Maatschappij B.V. (NAM), Geomatics department. During this study, I got the chance to continuously collaborate and discuss with many people at NAM/Shell. I am very grateful to Gini Ketelaar for her active project management and her enthusiastic supervision during the first four years of this study. I also gratefully acknowledge Herman Bähr for his thorough comments and discussions during the last period of my research and during the collaborations we have had afterwards. Wim van der Veen is gratefully acknowledged for the management support and for providing me the chance to continue my post-doc research. I also would like to thank other people at the Geomechanics and Geomatics departments of NAM for the technical and critical discussions during our progress meetings. Special thanks go to Tony Mossop for his useful comments and for our technical and philosophical discussions regarding the uncertainties in geodetic observations for geo-modeling.

I would, furthermore, like to thank all my (former) colleagues within the InSAR research group at TU Delft for our fruitful discussions and the pleasant working atmosphere, for sharing software, knowledge, and experience, and for all the fun we have had together. The consultations, the brainstorming, and the friendship with Petar Marinkovic (now at PPO Labs) are greatly appreciated and valued. I would like to thank Freek van Leijen and Joana Martins for their valuable contributions to our paper on ILS phase estimation. The software I have developed during my research was built on the DePSI software developed by Freek. Special thanks to him for sharing his experience and thoughts. Many thanks go to my former colleague and officemate Pooja Mahapatra for proof-reading most of this thesis, and for all the collaborations we had during our PhD work. I am also grateful to Andy Hooper (now at the University of Leeds). The discussions with him and his viewpoints on different aspects of InSAR processing and modeling were always

enlightening and helpful. At the later stages of my research, the chats and brainstorming with Paco López-Dekker were always informative, deepening my knowledge about radar. I would also thank Tomokazu Kobayashi (guest researcher from Geospatial Information Authority of Japan) for his contribution in the implementation of different ESM-phase estimation algorithms. I would also like to mention the names of other members of InSAR group who have helped me at some point in time to complete this work: Zbigniew Perski, Miguel Caro Cuenca, Shizhuo Liu, Anneleen Oyen, Manu Delgado Blasco, Ling Chang, Prabu Dheenathayalan, Gertjan van Zwieten, Lorenzo Iannini, Ramses Molijn, Ali Mousivand, Bram te Brake, Gert Mulder, Floris Heuff, and Mengshi Yang. Furthermore, I would like to thank the MSc students—Piers van der Torren, Naresh Soni, and Amirpasha Vazifehdoust—whom I have a chance to advise during their MSc research. I learned a lot from them, and their work, directly or indirectly, has contributed to my research.

I am also grateful to my other colleagues and fellow PhD students within the group of mathematical geodesy and positioning (MGP) and the department of Geoscience and Remote Sensing (GRS) for their support and providing a friendly work environment. I am grateful to Peter Teunissen for sharing his knowledge in a few enlightening discussions about the concept of ILS estimation. I am indebted to Sandra Verhagen who kindly took over some of my responsibilities during our online course development, giving me the opportunity to finalize my PhD thesis. Discussions with her, Hans van der Marel, Christian Tiberius, and Roderik Lindenbergh were always instructive. Special thanks go to Danko Roozmond, Lidwien de Jong, Rebeca Domingo, Marjolein de Niet-de Jager, File Koot-Stomp, Debbie Rietdijk, and Irma Zomerdijk for their administrative and project support.

I would also like to express my appreciation to my defense committee: Fabio Rocca, Michael Eineder, Jordi Mallorqui, Roland Klees, Peter Hogeboom, Gini Ketelaar, and Paco López-Dekker, for the time they invested in the thorough reading of this work and their constructive comments.

I am greatly thankful to all my friends outside of work, for providing enough fun, laughter, drinks, food, support, and parties during the past several years in Delft. To avoid the unavoidable of missing a name, I will not mention any! I am sure that each of you will feel my appreciation when you read these lines.

I am much indebted to my family. The memory of my father was always with me during the PhD years. With his powerful and kind gaze from his photo on my desk, he was pushing me forward everyday. I am greatly thankful to my mother for her constant and never-ending love and support during these years. My sisters, Sogol and Golsoo, and my brothers, Kiawasch and Amirmohammad, thank you for all your kindness and support. I would like to specially thank Golsoo for designing the cover of the thesis.

Finally, I would like to thank Delaram who continuously and eagerly pushed and forced me to finish my thesis. Deli, I will never forget, and I always value your patience in life and your understanding during all the days, months, and years that I stole from you.

*Sami Samiei Esfahany,
Delft, April 2017*

Summary

During the last decades, time-series interferometric synthetic aperture radar (InSAR) has emerged as a powerful technique to measure various surface deformation phenomena of the earth. Early generations of time-series InSAR methodologies, i.e. Persistent Scatterer Interferometry (PSI), focused on point targets, which are mainly man-made features with a high density in urban areas and associated infrastructure. Later, methodologies were introduced aiming to extract information from other targets known as *distributed scatterers* (DS), which are associated with ground resolution cells occurring mainly in rural areas. Unfortunately, the underlying properties and assumptions behind various DS-phase estimation methodologies are sometimes subjective and incomparable, which hampers the objective application of the different methods. Moreover, for some terrain types, such as agricultural terrain or pastures, the feasibility of DS-methodologies is not straightforward.

In view of these challenges, the two main objectives of this study are (i) to formulate and implement the estimation methodology of DS-pixels in a standard geodetic framework and to compare it with other existing methods, and (ii) to assess the feasibility of exploiting distributed scatterers for deformation monitoring over agricultural and pasture areas.

We review state-of-the-art time-series InSAR methodologies with special attention to processing aspects related to distributed scatterers. From an estimation theory perspective, the key processing step to extract information from DS-pixels is the equivalent single-master (ESM) phase estimation. To situate this estimation in a geodetic framework, a mathematical model is proposed in the form of a Gauss-Markov model. To evaluate the stochastic part of the model, a numerical Monte-Carlo methodology as well as an analytical approach are introduced. Regarding the functional part, the ESM-phase estimation is formulated in the form of a hybrid linear system of observation-equations with both real-value and integer unknowns. The solution of the proposed model is given by the integer least-squares (ILS) estimator. The properties of such an estimator for ESM-phase estimation are described and demonstrated using synthetic and real datasets. Furthermore, to provide a theoretical comparison between the proposed ILS estimator and other existing ESM-phase estimators, a unified mathematical model in the form of a system of observation equations is proposed. Evaluating all the existing DS-methods shows that, although they all provide specific solutions, their fundamental difference is in how they assign weights to the interferometric observations.

The feasibility of exploiting PS, DS, and their combination over agricultural and rural landscapes is assessed via a case study on a subsidence area near city of Veendam, the Netherlands, based on the coherence behavior of different types of land use. It is shown that, under the condition of using the entire time-series, agricultural and pasture areas show only limited improvement in point density compared to the results of PS-only processing. This is due to the seasonal behavior of the temporal coherence, which causes an almost complete drop in coherence during summer periods, mainly as a result of tillage, crop growth and harvesting.

To model this periodicity, a new analytical model is introduced. In this model, the hypothetical movements of elementary scatterers within DS resolution cells are modeled as a stochastic process with non-stationary but periodic increments. The parameters of this model are estimated for pasture areas, and are subsequently used to assess the feasibility of exploiting DS-pixels in agricultural areas by different satellite missions. The results confirm that, assuming a three-year stack of data, the information content in DS-pixels from current C-band and X-band missions is not enough for the successful utilization of their entire time-series. However by using intermittent series, e.g., by processing individual coherent periods, the results indicate that DS-pixels can be exploited: based on the proposed decorrelation model, the short repeat times of Sentinel-1 (6 or 12 days) results in a sufficient number of coherent interferograms over each winter period, enabling DS exploitation even over agricultural and pasture areas.

Samenvatting (Summary in Dutch)

SAR interferometrie, in het bijzonder toegepast op reeksen van satellietbeelden, is gedurende de laatste decennia opgekomen als krachtige techniek om beweging van (objecten op) het aardoppervlak in kaart te brengen. De eerste methoden, zoals *persistent scatterer* interferometrie (PSI) gebruiken daarbij voornamelijk reflectoren die als puntbron kunnen worden beschouwd. Deze zijn vaak afkomstig van door de mens gemaakte objecten, en komen derhalve vaak voor in stedelijk gebied of op infrastructuur. In een later stadium werden methoden ontwikkeld die gebruik maken van gedistribueerde reflecties (*distributed scatterers*, of DS). Deze komen vooral voor in natuurlijke gebieden, waarbij binnen een resolutie-element een veelheid van reflecties voorkomt.

Er zijn verschillende verwerkingswijzen voor het verkrijgen van informatie uit distributed scatterers. De onderliggende aannames en eigenschappen van deze verwerkingswijzen zijn vaak subjectief, en moeilijk met elkaar te vergelijken. Hierdoor wordt een objectieve en herhaalbare toepassing van de methoden bemoeilijkt. Tevens is voor specifieke types landgebruik, zoals weilanden of akkers, de toepasbaarheid van de DS-methodes niet vanzelfsprekend.

Deze uitdagingen leiden tot de twee hoofddoelstellingen van dit onderzoek. De eerste doelstelling is om een uniforme geodetische schattingsmethodiek voor distributed scatterers te formuleren en te implementeren, en deze te vergelijken met de bestaande methoden. De tweede doelstelling is de haalbaarheid te bepalen van het gebruik van distributed scatterers voor deformatie monitoring over weilanden en akkers.

In dit onderzoek worden de huidige InSAR-tijdreeks methodes nader onderzocht, in het bijzonder de dataverwerkingsaspecten voor distributed scatterers. In de context van schattingstheorie is de belangrijkste verwerkingsstap de zogenaamde *equivalent single-master* (ESM) schatting en de daaruitvolgende schatting van de interferometrische fase. Hiervoor wordt een Gauss-Markov wiskundig model geïntroduceerd. Voor het stochastische deel van dit model kan zowel een numerieke Monte Carlo methode als ook een analytische methode worden gebruikt. Voor het functionele deel van het model wordt de ESM-faseschatting geformuleerd in de vorm van een gemengd lineair systeem van waarnemingsvergelijkingen met zowel geheeltallige als reële onbekenden. De oplossing voor dit model wordt gegeven door een geheeltallige kleinste-kwadratenschatter. Een beschrijving wordt gegeven van de eigenschappen van dit type schatter voor ESM faseschatting, middels kunstmatige en werkelijke metingen. Tevens wordt een uniform wiskundig model

gepresenteerd, in de vorm van een stelsel van waarnemingsvergelijkingen, om een theoretische vergelijking tussen de voorgestelde geheeltallige kleinste-kwadratenschatter en conventionele ESM faseschatters mogelijk te maken. Geconcludeerd wordt dat het fundamentele verschil tussen alle DS-methoden ligt in de wijze waarop de interferometrische waarnemingen worden gewogen.

De tweede doelstelling—de bepaling van de haalbaarheid van het gebruik van PS, DS en hun combinatie over weilanden en akkers—wordt onderzocht via een case study op gegevens van een bodemdalingsgebied bij Veendam. Dit is gebaseerd op het coherentiegedrag van verschillende types landgebruik. Onder de beperking dat de volledige reeks satellietbeelden moet worden gebruikt blijkt dat er bij weilanden en akkers slechts een beperkte toename in punt dichtheid kan worden bereikt, in vergelijking met de standaard PS dataverwerking. Dit wordt veroorzaakt door het nagenoeg complete verlies van coherentie als gevolg van seizoensvariatie, in het bijzonder als gevolg van landbouwactiviteiten zoals ploegen, oogsten en gewasgroei.

Om deze seizoensperiodiciteit te kunnen ondervangen wordt een nieuw analytisch model geïntroduceerd. Hierin worden de (hypothetische) bewegingen van elementaire reflectoren binnen een DS resolutie-element gemodelleerd als een stochastisch proces met niet-stationaire, periodieke incrementen. De parameters van dit model worden geschat voor weilanden, en worden vervolgens gebruikt om de haalbaarheid van het gebruik van distributed scatterers over landbouwgebieden te bepalen voor verschillende satellietmissies. Onder de aanname van een volledige reeks van drie jaar aan data tonen de resultaten aan dat dit bij de huidige C- en X-band missies niet haalbaar is. Echter, door gebruik te maken van onderbroken deelreeksen, bijvoorbeeld van beperkte coherente periodes in landgebruik, tonen de resultaten aan dat distributed scatterers kunnen worden gebruikt in de analyse. Gebaseerd op het geïntroduceerde decorrelatiemodel resulteert de korte (6-daagse) herhalingsperiode van Sentinel-1 in een voldoende aantal coherente interferogrammen gedurende de winterperiodes, waardoor distributed scatterers mogelijk ook kunnen worden gebruikt om deformaties te schatten over weilanden en akkers.

Nomenclature

List of acronyms

1D	one-dimensional
2D	two-dimensional
3D	three-dimensional
AD	Anderson-Darling
ALOS	Advanced Land Observing Satellite
AOI	Area Of Interest
APS	Atmospheric Phase Screen
CAESAR	Component extrAction and sElection SAR
CDF	Cumulative Distribution Function
CRB	Cramér-Rao bound
CV	coefficient of variation
dB	decibel
DEM	Digital Elevation Model
DePSI	Delft implementation of Persistent Scatterer Interferometry
DInSAR	Differential Interferometric Synthetic Aperture Radar
DS	Distributed scatterer
ECDF	Empirical Cumulative Distribution Function
EMCF	Extended Minimum Cost Flow
Envisat	Environmental satellite
ERS	European Remote Sensing satellite
ESA	European Space Agency
ESM	Equivalent Single Master
EVD	EigenValue Decomposition
EVC	EigenValue-decomposition of Coherence matrix
EVQ	EigenValue-decomposition of Covariance matrix
FFT	Fast Fourier Transform
FIM	Fisher Information Matrix
GNSS	Global Navigation Satellite System(s)
GPS	Global Positioning System
HCRB	Hybrid Cramér-Rao bound
IB	Integer bootstrapping

ILS	Integer least-squares
InSAR	Interferometric Synthetic Aperture Radar
KS	Kolmogorov-Smirnov
LCV	Least Circular Variance
LOS	Line of Sight
LS	Least Squares
MC	Monte-Carlo
MCF	Minimum Cost Flow
MCSR	Maximum Coherence-based-weighted Sum of Residual phasors
ML	Maximum Likelihood
NWM	Numerical Weather Model
PDF	Probability Density Function
PS	Persistent Scatterer
PS1	First-order Persistent Scatterer
PS2	Second-order Persistent Scatterer
PSC1	First-order Persistent Scatterer Candidate
PSC2	Second-order Persistent Scatterer Candidate
PSC	Persistent Scatterer Candidate
PSI	Persistent Scatterer Interferometry
PSInSAR	Persistent Scatterer Interferometric Synthetic Aperture Radar
PTA	Phase Triangulation Algorithm
RAR	Real Aperture Radar
RCS	Radar Cross Section
RR	Real-value of Resultant vector
RSR	Range Sampling Rate
SAR	Synthetic Aperture Radar
SBAS	Small BAseline Subset
SB	Small Baseline
SCR	Signal-to-Clutter Ratio
SHP	Statistically homogeneous pixels
SLC	Single-Look Complex
SM	Single Master
SNR	Signal to Noise Ratio
SRTM	Shuttle Radar Topography Mission
StaMPS	Stanford Method for PS
STB	Small Temporal Baselines
STC	Spatio-Temporal Consistency
SVD	Singular Value Decomposition
TEC	Total Electron Content
TInSAR	Time-series Interferometric Synthetic Aperture Radar
TOPS	Terrain Observation with Progressive Scan
TU Delft	Technical University of Delft
VCE	Variance Component Estimation
VLBI	Very long baseline interferometry
WGS84	World Geodetic System 1984

List of symbols

A	Amplitude; Design matrix
a_i	Amplitude of an elementary scatterer within a cell
b	Real-valued unknowns (unknown ESM-phase vector in ESM-phase estimation)
\hat{b}	Estimated ESM-phase vector
B	Baseline [m]; Design matrix of real unknowns in ILS
B_{\parallel}	Parallel baseline [m]
B_{\perp}	Perpendicular baseline [m]
B_{dop}	Doppler baseline [Hz]
B_{rg}	Range bandwidth
B_{az}	Azimuth bandwidth
B_{T}	Temporal baseline [year]
C	Coherence matrix
c	Speed of light, or a constant value
C_y	Coherence matrix of the vector y
D_{LOS}	Deformation in radar Line of Sight
D_A	Normalized amplitude dispersion
$D_{\Delta A}$	Normalized amplitude difference dispersion
D_u	Up component of Deformation
D_n	North component Deformation
D_e	East component Deformation
e_i	Residuals phase of the i th observation
F	Projection matrix in integer least squares
f	Carrier frequency
f_{ϕ}	Frequency shift
H	Height [m]
H_0	Null hypothesis
H_a	Alternative hypothesis
I	Complex Interferogram ; Identity matrix
\bar{I}	Average intensity matrix with elements ζ_{ij}
j	Imaginary unit
k_{α}	Critical value corresponding to the level of significance α
L	Number of looks
M	Master image antenna position; Number of simulations
n	Noise
N	Number of interferograms; Number of images
P	Phasor
p	Power
P_0	Point on reference surface
P_H	Point at height H
Q	Covariance matrix
Q_{atm}	Covariance matrix of atmospheric signal
Q_n	Covariance matrix of noise
$Q_{\hat{b}}$	Covariance matrix of estimated real unknowns
Q_y	Covariance matrix of observations

\mathbb{R}	Domain of real values
R_m	Range to master antenna position [m]
r	Vector of residual phasors with elements r_i
r_i	Phasor of the i th phase residual ($r_i = \exp(je_i)$)
S	Slave image antenna position
S_i	Phasor of the i th elementary scatterers within a cell
s	Signal
s_e^2	Ensemble circular variance
T	Period of a periodic function
T_{KS}	Test statistic for KS-test
T_{AD}	Test statistic for AD-test
T_{mean}	Test statistic for testing the mean
T_{var}	Test statistic for testing the variance
t_M	Time of the master acquisition
t_S	Time of the master acquisition
W	Weight matrix
w_i	the i th element of a weight matrix
ω	Angular frequency ($\omega = \frac{2\pi}{T}$)
x	Unknown variables
\hat{x}	Estimated unknowns
\underline{y}	Vector of observations/variables (stochastic)
$\underline{y}_{\text{slc}}$	Vector of SLC values
α	Baseline orientation; Level of significance of test
ΔH	Residual Height [m]
$\delta\phi^{\text{topo}}$	Residual topographic phase
Γ	Coherence matrix (complex)
$\hat{\Gamma}$	Estimated coherence matrix (complex)
γ	Coherence (complex)
$\hat{\gamma}$	Estimate of coherence / ensemble coherence
$\hat{\gamma}$	Coherence estimator
$ \hat{\gamma}_{ij}^{\text{PC}} $	Phase corrected absolute coherence
$ \hat{\gamma}_{ij}^{\text{M}} $	Amplitude-based coherence estimate
γ_{dc}	Coherence (reduction) due to Doppler centroid decorrelation
γ_{geom}	Coherence (reduction) due to geometric decorrelation
γ_{procc}	Coherence (reduction) due to processing induced decorrelation
γ_{coreg}	Coherence (reduction) due to coregistration
γ_{T}	Coherence (reduction) due to temporal decorrelation
γ_{thermal}	Coherence (reduction) due to thermal or system noise
γ_{tot}	Total coherence
γ_{ens}	Ensemble coherence
γ_{st}	Spatio-temporal coherence
γ_{vol}	Coherence (reduction) due to volume decorrelation
$\hat{\gamma}_{\text{PTA}}$	Extended temporal coherence (goodness-of-fit measure for SM-phase estimation or for phase triangulation)
Δf_{DC}	Doppler baseline
λ	Radar wavelength [m]

$\lambda_{i,j}$	Elements of the inverse of the absolute coherence matrix
μ_A	Mean of amplitude
Υ	Absolute coherence matrix
Ψ	Diagonal complex matrix with elements $\exp\{j\varphi\}$
ψ	SLC phase
ψ_0	Expected SLC phase
ψ^{atmo}	Atmospheric SLC phase
ψ^{range}	Range dependent SLC phase
ψ^{scat}	Scattering SLC phase
ψ^{noise}	Noise SLC phase
ϕ	Interferometric phase
ϕ_0	Argument of expectation of complex interferometric value
$\hat{\phi}$	Multilooked interferometric phase
ϕ^{flat}	Flat Earth interferometric phase
ϕ^{topo}	Topographic interferometric phase
ϕ^{defo}	Deformation interferometric phase
ϕ^{atmo}	Atmospheric interferometric phase
ϕ^{orb}	Orbital interferometric phase
ϕ^{geom}	Geometric interferometric phase
ϕ^{noise}	Noise interferometric phase
ϕ^{range}	Range dependent interferometric phase
ϕ^{scat}	Scattering interferometric phase
ϕ^{turb}	Turbulent mixing component of atmospheric interferometric phase
ϕ^{strat}	Vertical stratification component of atmospheric interferometric phase
$\phi^{\text{G-dec}}$	Interferometric phase induced by geometrical decorrelation
$\phi^{\text{D-dec}}$	Interferometric phase induced by Doppler centroid decorrelation
$\phi^{\text{T-dec}}$	Interferometric phase induced by temporal decorrelation
$\phi^{\text{V-dec}}$	Interferometric phase induced by volume decorrelation
ϕ_{s_n}	Systematic interferometric phase component
φ_m	True phase value of the SLC image m
φ_{mn}	True phase value of the interferogram constructed from images m and n
$\hat{\phi}_i^{\text{sc}}$	Estimated spatially correlated phase in i th interferogram
$\hat{\phi}_k$	Estimated phase; Multilooked phase
σ_A	Standard deviation of amplitude
$\sigma_{\Delta A}$	Standard deviation of amplitude differences
σ_n	Standard deviation of noise component
σ_ψ	Standard deviation of SLC phase
$\sigma_{x,y}$	Covariance between x and y
σ_n^2	Variance motion of elementary scatterers within a cell in unit time
σ_r^2	Variance of motion of elementary scatterers within a cell
σ_n^2	Variance motion of elementary scatterers within a cell in unit time
σ_h^2	Variance of horizontal motion of elementary scatterers
σ_v^2	Variance of vertical motion of elementary scatterers

$\sigma_{r,\text{short}}^2$	Variance of sudden motion of elementary scatterers
$\sigma_{r,\text{long}}^2$	Variance of long term motion of elementary scatterers
σ_x^2 ^{CRB}	Lower Cramér-Rao bound for variance of \underline{x}
σ_{ϕ}^2	Variance interferometric phase
$\sigma_{\phi_{PS}}^2$	Variance of interferometric phase for point scatterers
τ	Temporal decorrelation range
Θ	Jacobian matrix (first derivatives) of SLC phases with respect to ESM-phases
θ_{inc}	Incidence angle
ϑ^m	Squint angle of master acquisition
ϑ^s	Squint angle of slave acquisition
ζ_i	Phase of the i th elementary scatterer within a cell
Ω	Set of homogeneous pixel (brotherhood area)
X	Fisher Information Matrix (FIM) associated to the ESM-phases
\mathbb{Z}	Domain of integer values
ζ	Topographic slope
ζ_{ij}	Average intensity between two images i and j ($\zeta_{ij} = \sqrt{E\{ \underline{P}_i ^2\}E\{ \underline{P}_j ^2\}}$)

List of operators, annotations, and functions

$\{\cdot\}$	Stochasticity
$\ \cdot\ _W^2$	Weighted norm, $\ \cdot\ _W^2 = (\cdot)^T W (\cdot)$
$ \cdot $	Determinant of a matrix or absolute value a scalar
$\{\cdot\}^{-1}$	Inverse
$\{\cdot\}^T$	Transpose
$\{\cdot\}^*$	Conjugate/Hermitian transpose
$d(\cdot, \cdot)$	Distance operator
$\det(\cdot)$	Determinant
$D\{\cdot\}$	Dispersion operator
$\bar{D}\{\cdot\}$	complementary dispersion operator
$\text{Cov}\{\cdot, \cdot\}$	Covariance operator
$\exp(\cdot)$	Exponential function
$\exp^\circ(\cdot)$	Hadamard (entry-wise) Exponential function
$E\{\cdot\}$	Expectation operator
$\text{Im}\{\cdot\}$	Imaginary part
$\ln(\cdot)$	Natural logarithm
$\text{nint}(\cdot)$	Rounding to the nearest integer
$\max(\cdot, \cdot)$	Maximum operator
$\text{Pr}(\cdot)$	Probability
$f_{\cdot}(\cdot)$	Probability density function
$f_{\underline{x}, \underline{y}}(\underline{x}, \underline{y})$	Joint probability distribution function of \underline{x} and \underline{y}
$F_{\cdot}(\cdot)$	Cumulative distribution function
$\hat{F}_{\cdot}(\cdot)$	Empirical cumulative distribution function

$\text{Re}\{\cdot\}$	Real part
$\text{W}\{\cdot\}$	Wrapping operator
$\angle(\cdot)$	Argument of a complex number
$\langle \cdot \rangle$	Complex Spatial averaging or multilooking operator
$N(\mu, \sigma^2)$	Normal distribution with mean μ and variance σ^2
sup	Supremum (least upper bound)
sum(\cdot)	Sum of vector/matrix elements
$S\{\cdot\}$	Mapping operator in integer least squares
tr(\cdot)	Trace of matrix, i.e., the sum of diagonal elements
$\mathcal{I}_y(x)$	Fisher information of y about x
$M_k(\cdot)$	k th statistical moment
$J_F(\underline{x})$	Jacobian of the function $F(\underline{x})$ wrt \underline{x}
$J_F(\underline{x} x_0)$	Jacobian of the multivariate function $F(\underline{x})$ wrt \underline{x} evaluated at x_0
${}_2F_1(\cdot)$	Classical standard hypergeometric function
$\Gamma(\cdot)$	Gamma function
${}_3F_2(\cdot)$	Generalized hypergeometric function
$K_{L-1}(\cdot)$	Modified Bessel function of the third kind
$\text{Li}_2(\cdot)$	Euler's dilogarithm

Introduction

1.1 Motivation

Persistent Scatterer Interferometry (PSI) is a useful technique for measuring deformation of the earth's surface, but it does not extract the full potential of information from a given set of data. In this study, information extraction is improved by adding distributed scatterers (DS) in the estimation process in a more complete geodetic framework.

1.2 Background

Geodesy and surface deformation

Geodesy is defined classically as the science of measuring and mapping the earth's surface (Helmert, 1980). The objective of geodesy is described more precisely by Torge and Müller (2012):

"... to determine **the figure of the earth** and its external gravity field, as well as its orientation in space, as a function of time, from measurements on, and exterior to, the earth's surface."

The term "the figure of the earth" here means the physical surface of the solid earth (i.e., continental and ocean floor topography), and the border between fluid masses and the atmosphere (i.e. water surfaces and sea level). One of the main aspects of geodesy, mainly focused upon during the last couple of decades, is studying the temporal variations of the solid part of this physical surface.

The availability of modern, and mainly space-based, geodetic measurements was a stimulating factor in studying where, when, how much, and why the earth's surface deforms. By providing continuous, fine resolution, and precise measurements of surface deforma-

tion, from global via continental to regional and local scales, geodesy contributes to different disciplines such as geophysics, geodynamics, glaciology, volcanology, tectonics, environmental studies, hydrology, and civil engineering¹.

At a global scale, continuous monitoring of the relative motion of tectonic plates has improved our understanding of the earth's dynamics and the evolution of earthquakes and other tectonic phenomena (e.g., Kreemer et al., 2003; Wright et al., 2012; Calais et al., 2008). At a continental scale, it became possible to study and monitor crustal deformation induced by volcanoes and earthquakes (e.g., Rogers and Dragert, 2003; Poland et al., 2006; Sigmundsson et al., 2015; Elliott et al., 2016). Monitoring changes in ice cap elevation and movements of ice bodies has increased our knowledge about glacier flow dynamics, post-glacial rebound, global mass transport processes, and the rate of sea level rise (e.g. Goldstein et al., 1993; Velicogna and Wahr, 2006; Nerem et al., 2006; Sella et al., 2007; Lidberg et al., 2010; Khan et al., 2010). At more local scales, there has been considerable progress in the geodetic monitoring of anthropogenic deformation induced by water and mineral extraction/injection, in studying surface deformation processes such as landslides, and even in detecting very localized deformation on buildings and infrastructure such as dikes and bridges (e.g. Dixon et al., 2006; Amelung et al., 1999; Roering et al., 2009; Famiglietti et al., 2011). Furthermore, new challenges and concerns about public safety, natural hazards, global warming, environmental issues, and optimal use of energy and water resources have created a more application-driven demand for geodetic observations as an essential source of information to support policy- and decision-making (e.g. Dixon and Dokka, 2008; England and Jackson, 2011).

In all the aforementioned developments, there is a significant, and often a leading, contribution from space-based geodetic techniques such as very long baseline interferometry (VLBI), global navigation satellite systems (GNSS), satellite radar and laser altimetry, and interferometric synthetic aperture radar (InSAR). Along with the opportunities and benefits, these new technologies also bring new methodological challenges. Correct mathematical treatment of—and optimal information extraction from—these new types of geodetic observations is not always straightforward and sometimes it is much more complicated than classical geodetic routines. Geometrically and physically sophisticated measurement techniques can create a complicated relationship between raw observations and the parameters of interest, and consequently result in complex and highly nonlinear functional models. The remoteness of space-based observations introduces interaction of electromagnetic waves with different media and generates observations that sometimes have multivariate, non-Gaussian, non-stationary, and spatio-temporally correlated statistics which require special care in the stochastic modeling and the uncertainty description of the observations. Numerical and algorithmic problems related to the very large data volumes is another challenging aspect.

This study is an attempt to address some of these challenges with respect to one of the most novel geodetic techniques: InSAR.

¹As a review of new developments and advances in geodesy and geodetic deformation monitoring, see e.g. Wdowinski and Eriksson (2009); Plag and Pearlman (2009).

InSAR: a geodetic tool for deformation monitoring

Since the late 1980's (Gabriel et al., 1989), InSAR has been gradually identified as a promising and effective technique to measure the earth's surface deformation due to different phenomena such as earthquakes, volcanism, fluid-extraction-induced subsidence, ice and glacier motion, and landslides (see e.g. Massonnet et al., 1993; Zebker et al., 1994a; Massonnet et al., 1995; Rosen et al., 1996; Sigmundsson et al., 1997; Massonnet et al., 1997; Amelung et al., 1999; Goldstein et al., 1993; Hartl et al., 1994; Rott et al., 1998; Fruneau et al., 1996). The beneficial properties such as high spatial resolution, relatively high temporal sampling, wide scale coverage, availability of archived data, and relatively low cost have stimulated the use of InSAR as a geodetic tool for deformation monitoring in various applications.

The concept of InSAR is based on the principle of distance estimation using the phase of electromagnetic waves. In a SAR image, the observed phase at every pixel is sensitive to the distance of the terrain to the radar sensor. Consequently, the phase difference between two images (i.e. the interferometric phase) is related to the geometrical and physical changes in this terrain-sensor distance. The interferometric phase then has different contributions related to topography, atmospheric delay, and deformation in the direction of the satellite line of sight (LOS). Under the condition that the deformation component is dominant or other contributions can be estimated independently, it is feasible to estimate the relative LOS deformation for each pixel. However, if the aforesaid conditions do not hold, the limitations of the technique are revealed. Under unfavorable conditions, i.e. small displacements under strong atmospheric conditions or over a long time period, the deformation signal is obscured by atmospheric interference, temporal decorrelation (i.e. a decrease of the signal-to-noise ratio due to changes in the scattering characteristics of the earth's surface and incoherent movement of individual scattering elements) and geometrical decorrelation (i.e. a decrease of the signal-to-noise ratio due to different viewing angles). In order to overcome these limiting factors and to improve the capability in extracting a useful deformation signal from noisy InSAR data, different kinds of *time-series InSAR* approaches have been developed.

Time-series InSAR data processing: history and recent advances

Some initial efforts to overcome the limitations of InSAR were targeted towards atmospheric disturbances. Based on the fact that atmospheric effects are mostly uncorrelated temporally, these methods filter out the atmospheric effects by temporal averaging over a stack of interferograms. The family of these methods is called *stacking methods*, and examples can be found in Sandwell and Price (1998); Wright et al. (2001); Lyons and Sandwell (2002).

Some other developments focused on target decorrelation. In the 1990s, it was recognized that some targets, especially man-made structures, have stable backscattering characteristics over long time intervals (van der Kooij et al., 1995; Usai, 1997; Usai and Hanssen, 1997; Usai and Klees, 1999). This led to the development of an innovative methodology called Permanent Scatterer InSAR, or PSInSAR (Ferretti et al., 2000, 2001) which uses these targets to estimate the deformation over long time periods and overcome the main limitations of conventional InSAR. The principle of PSInSAR can

be described as follows. In SAR images, the phase measurement of each pixel is the sum of contributions from all scatterer elements within the associated resolution cell. "PS-pixels" are those ground resolution cells which contain a persistently dominant scatterer, effectively referred to as the PS^2 , so their decorrelation phase variation is small. Consequently, most of the PS are man-made features, which have a high density in urban areas, and on infrastructure such as bridges, buildings, dams and dikes. The main characteristics of the PSInSAR processing method are that only "PS-pixels" are considered, and that it utilizes a *single-master* (SM) stack of differential interferograms. The latter means that given an N number of radar images, it uses $N-1$ interferograms (phase differences) with respect to one acquisition called the *master* image. Since the development of the first PS technique by Ferretti et al. (2000), other methods have been introduced using comparable concepts (Van der Kooij, 2003; Adam et al., 2003; Werner et al., 2003; Hooper et al., 2004; Kampes, 2005; Costantini et al., 2009; van Leijen, 2014). Nowadays, the term *Persistent Scatterer Interferometry* (PSI) is used to address all these methodologies which use a single-master time-series of differential interferograms and only consider the PS-pixels for measuring deformation of the earth's surface.

Parallel to the developments in PSI methodologies, some other techniques emerged with the objective of extracting information also from pixels that are affected by decorrelation phenomena, but which may still contain some coherent information. These pixels are called *distributed scatterers* (DS) and they are associated with ground resolution cells containing no dominant scatterer, occurring mainly in rural areas. As DS pixels are affected by temporal and geometrical decorrelation, they may contain coherent information only in specific interferometric pairs, mainly separated by a short time interval and having a very similar viewing geometry. Therefore, unlike for PS, the information content in a single-master interferogram stack is neither optimal nor complete for DS. A leading approach to extract information also from DS was developed using the concept of small baseline subsets (SBAS) (Berardino et al., 2002; Schmidt and Bürgmann, 2003). Baseline here means either the spatial distance between satellite positions, or the temporal separation between acquisition times. In SBAS algorithms, only small-baseline interferograms are exploited with extra spectral or spatial filtering in order to further reduce the decorrelation noise.

As these two different groups of methodologies, i.e. PSI and SBAS, have been developed for two different types of targets, they are complementary to each other. This is the idea behind the third group of methodologies, called *hybrid methods*, which intends to extract information from both PS and DS targets. Two examples of these methods are the extended SBAS method that integrates multilooked and single-look interferograms (Lanari et al., 2004), and the multi-temporal InSAR method incorporating both persistent scatterers and the small baseline approach (Hooper, 2008). The latest development in time-series InSAR methodologies is the advent of more advanced hybrid approaches that have been designed to extract all the information in SAR stacks by exploiting not only SBAS interferograms, but all the possible interferograms (Monti-Guarnieri and Tebaldini,

²Note that the concept of a persistent scatterer allows us to leave the common perception of an image with pixels, as the observation space is now filled with randomly dispersed persistent scatterers, irrespective of the sampling via resolution cells or on image. In this study, the term "PS" is associated with persistent scatterers, and the term "PS-pixel" addresses a resolution cell containing a PS.

2008; Ferretti et al., 2011b).

InSAR data processing: a geodetic perspective

Alongside InSAR methodological advances—which have a multi-disciplinary nature but have been predominantly developed in the signal processing domain—there is a persistent attempt by Delft University of Technology (TUDelft) to formulate all these developments into a standard geodetic framework³. A key property of the geodetic framework is the clear formulation of a twofold mathematical model composed of a functional and a stochastic model, with a strong consideration of quality aspects such as full error propagation, and the precision and reliability of the estimated parameters (Rummel and Teunissen, 1988; Rummel, 2014). In the last 15 years, this geodetic methodology has been applied to various aspects of radar interferometry. The functional and stochastic model for conventional InSAR and stacking methods together with error description and interpretation was given by Hanssen (2001). With respect to time-series InSAR, the geodetic methodology has been proposed for a stacking approach by Usai (2003), and later for persistent scatterer interferometry (Kampes, 2005; van Leijen, 2014). Regarding InSAR error sources, detailed geodetic analysis and estimation methodology of atmospheric and orbital errors was given by Liu (2012) and Bähr (2013) respectively. Some other important InSAR aspects have also been investigated from this geodetic perspective: including temporal phase unwrapping (Kampes and Hanssen, 2004; Teunissen, 2006), precision estimation of PS phase measurements (Marinkovic et al., 2008; Mahapatra et al., 2014), recursive PSI processing (Marinkovic and Hanssen, 2007), geodetic network design for artificial PS (Mahapatra et al., 2015; Mahapatra, 2015), PS targets classification using geodetic testing theory (Chang and Hanssen, 2016; Chang, 2015), and precise positioning of radar scatterers (Dheenathayalan et al., 2016). Last but not least, applications of InSAR for subsidence monitoring have also been considered through this geodetic framework by Ketelaar (2008), Caro-Cuenca (2012), and Fuhrmann et al. (2015).

InSAR for subsidence monitoring in the Netherlands

Land subsidence is a deformation mechanism which can sometimes cause serious socio-economic problems. Damage to infrastructure and buildings can be mentioned as examples. In coastal and low-lying areas such as the Netherlands, land subsidence is a highly challenging phenomenon due to its impact on water management and ecological systems, and most importantly on flood risk (Dixon and Dokka, 2008; Tosi et al., 2013; Erkens et al., 2016). During the last decade, InSAR, particularly PSI, has been applied to study different subsiding areas in the Netherlands, e.g., the subsidence induced by hydrocarbon production in Groningen (Ketelaar, 2008), and fault-related surface deformation in the Roer Valley Graben (Caro-Cuenca, 2012). Despite the challenging factors such as slow deformation rates (smaller than 1 cm/year) and rural/agricultural landscapes, the results of these studies have proven the feasibility of the technique for subsidence monitoring in the Netherlands. The majority of buildings and structures appears to serve

³Special attention has been given to the so-called *Delft school* framework comprising geodetic estimation theory (Tienstra, 1956), testing theory (Baarda, 1968), quality control (Teunissen, 1990), variance component estimation (Teunissen and Amiri-Simkooei, 2008; Amiri-Simkooei, 2010), geodetic integer inference (Teunissen, 1995, 1999), and best prediction (Teunissen, 2008, 2007).

as reliable measurement points (i.e. PS), and the accuracy of PSI has been quantified by combining multiple satellite tracks. A correlation of 94% with ground optical leveling measurements was achieved for the Groningen subsidence area (1993-2003). Nowadays InSAR is operationally used for various subsidence monitoring projects in the Netherlands.

1.3 Problem formulation and research objectives

The main motivation to initiate this study arose from the following problems.

The first problem regards the phase retrieval from distributed scatterers. Unlike PS-pixels, the information content in a single-master (SM) interferogram stack is neither optimal nor complete for DS-pixels, as these may contain coherent information only in specific interferometric pairs. Therefore, in all the methodologies that exploit DS-pixels, the key question is how to optimally combine a multitude of interferometric combinations to estimate the parameters of interest. Also, from the perspective of estimation theory, the main difference between the PSI methods and DS-methods is the application of an extra processing step of equivalent single-master (ESM) phase estimation (which is called in other literature *phase linking* (Monti-Guarnieri and Tebaldini, 2008), *phase triangulation* (Ferretti et al., 2011b), or *phase inversion* (Berardino et al., 2002)). At the beginning of this study, there had been relatively few investigations on the detailed mathematical aspects of this estimation problem. This includes challenges for clear algorithm implementation, applicability requirement specification, and comparative performance-assessment of different existing methods. Therefore, **there is a need for a unified formulation of this particular estimation problem**. Besides, **it is beneficial to formulate this problem in a standard geodetic framework**, allowing one to directly apply the existing body of knowledge of geodetic theory, e.g. quality description and testing theory, on the ESM-phase estimation.

The second problem is related to the application of PSI for subsidence monitoring over rural areas. Although PSI has been successfully applied for subsidence monitoring in the Netherlands, there are still areas, mainly in rural regions, with a limited number of PS targets. Especially smaller subsidence fields in rural areas may be sparsely covered with PS measurements compared to the extent of the subsiding area. Moreover, the subsidence observed via non-PS targets is often related to also other driving mechanisms, such as shallow soil compaction. Therefore there is a potential value in methods exploiting DS. However **the feasibility of DS methods for subsidence monitoring over rural areas in the Netherlands with a pasture or agricultural landscape is still a pending question**.

In view of the problems above, two main objectives of this study are (i) to formulate and implement the equivalent SM-phase estimation methodology for DS-pixels in a standard geodetic framework, and (ii) to assess the feasibility of exploiting distributed scatterers for deformation monitoring over a typical rural landscape in the Netherlands.

Regarding these objectives, four specific research questions are addressed in this study.

1. How to formulate the functional and the stochastic part of the mathematical model for ESM-phase estimation in the form of a Gauss-Markov model of observation-equations?
2. How to estimate ESM-phases using the weighted least squares estimator and how does it compare to other existing methods?
3. How much can the DS-exploitation methods improve the spatial density of time-series InSAR measurements over a typical rural landscape in the Netherlands?
4. How to model the coherence behavior and its temporal variations over agricultural and pasture areas in the Netherlands? With such a model, what is the performance of different existing satellite missions regarding the exploitation of distributed scatterers?

1.3.1 Methodology

The first two questions address how to situate the ESM-phase estimation in a standard geodetic framework. To do so, a mathematical model will be designed in the form of a Gauss-Markov model (Gauss, 1809; Markoff, 1912), as commonly used in geodesy. This model comprises the functional and the stochastic model. The functional model is formulated in a linear (or linearized) system of observation-equations. For ESM-phase estimation, the main challenge is how to deal with the non-linearity induced by the wrapping operator in the InSAR phase observations. The stochastic model is characterized by the second statistical moment of observations which, in the case of ESM-phase estimation, will be described by the full covariance matrix of multi-looked interferometric phases associated with a DS-pixel. Methodology will be developed to evaluate the full covariance matrix of observations. The solution of the proposed Gauss-Markov model will be given by the least-squares (LS) estimator. The properties of such an estimator for ESM-phase estimation will be described, and a comparison with other existing methodologies will be given.

The third and the fourth research question regard the application of exploiting DS-pixels in typical rural landscapes in the Netherlands. The main complication is how to parametrize the coherence behavior and its temporal variation over rural landscapes. Using this parametrization, it will be assessed whether the DS exploitation method is capable to extract the desired information in these areas. Both real-case experiments and theoretical feasibility studies will be considered.

Research limitations

The estimation of phase timeseries from DS-pixels comprises two main steps: (i) adaptive multilooking and coherence estimation, (ii) ESM-phase estimation. The latter is the main focus of this study. We assume that the phase inconsistencies in interferogram stacks are purely induced by random noise. So the situations where systematic phase inconsistencies may occur (e.g., due to soil moisture variation or volume scattering, see De Zan et al., 2015) are not investigated. Moreover, in the feasibility study over rural areas in the Netherlands, we will only study the DS exploitation in the entire timeseries,

and therefore, the option of using subset of interferograms to exploit temporally coherent targets is not considered.

1.4 Outline

We first give a review of the state-of-the-art of time-series InSAR methodologies in **chapter 2**. Special attention is given to processing aspects related to DS targets. Then in **chapter 3**, we describe a stochastic model for ESM-phase estimation. Multivariate statistics of both complex SAR and InSAR phase observations are discussed in detail. Different issues regarding the estimation of these statistics from real data are also discussed. Both a numerical Monte-Carlo methodology and an analytical approach are presented to evaluate the full covariance matrix for InSAR phase stacks.

In **chapter 4**, we present a generic functional model for ESM-phase estimation. A theoretical comparison of different existing methods, which are all formulated as an optimization in the complex domain, is given. In order to formulate the ESM-phase estimation in a standard geodetic framework, in **chapter 5**, we propose a new method for this estimation based on the integer least squares (ILS) principle. We model the ESM-phase estimation problem in the form of a linear system of observation-equations by introducing additional integer ambiguities, and use a bootstrap estimator for the joint estimation of ESM-phases and the integer unknowns. In addition, a full error propagation scheme is introduced in order to evaluate the precision of final ESM-phase estimates. Results from both synthetic experiments and a case study over the Torfajökull volcano in Iceland demonstrate the properties of the proposed method (this chapter has been published by Samiei-Esfahany et al., 2016).

To assess the feasibility of exploitation of DS-pixels over typical landscapes in the Netherlands, in **chapter 6**, we present the results obtained by a case study on a subsidence area near Veendam, the Netherlands. A feasibility analysis of exploiting DS in this area is given based on the coherence behavior of different kinds of landscape. The results of applying combined PS and DS processing are given, including the comparison with PS-only processing. A new model is introduced for temporal decorrelation of agricultural and pasture areas. Using the estimated decorrelation model parameters, the feasibility of the exploitation of DS-pixels is assessed for different satellite missions.

Conclusions, contributions of this study, and the recommendations for further research are reported in **chapter 7**.

A schematic outline of this study is depicted in fig. 1.1.

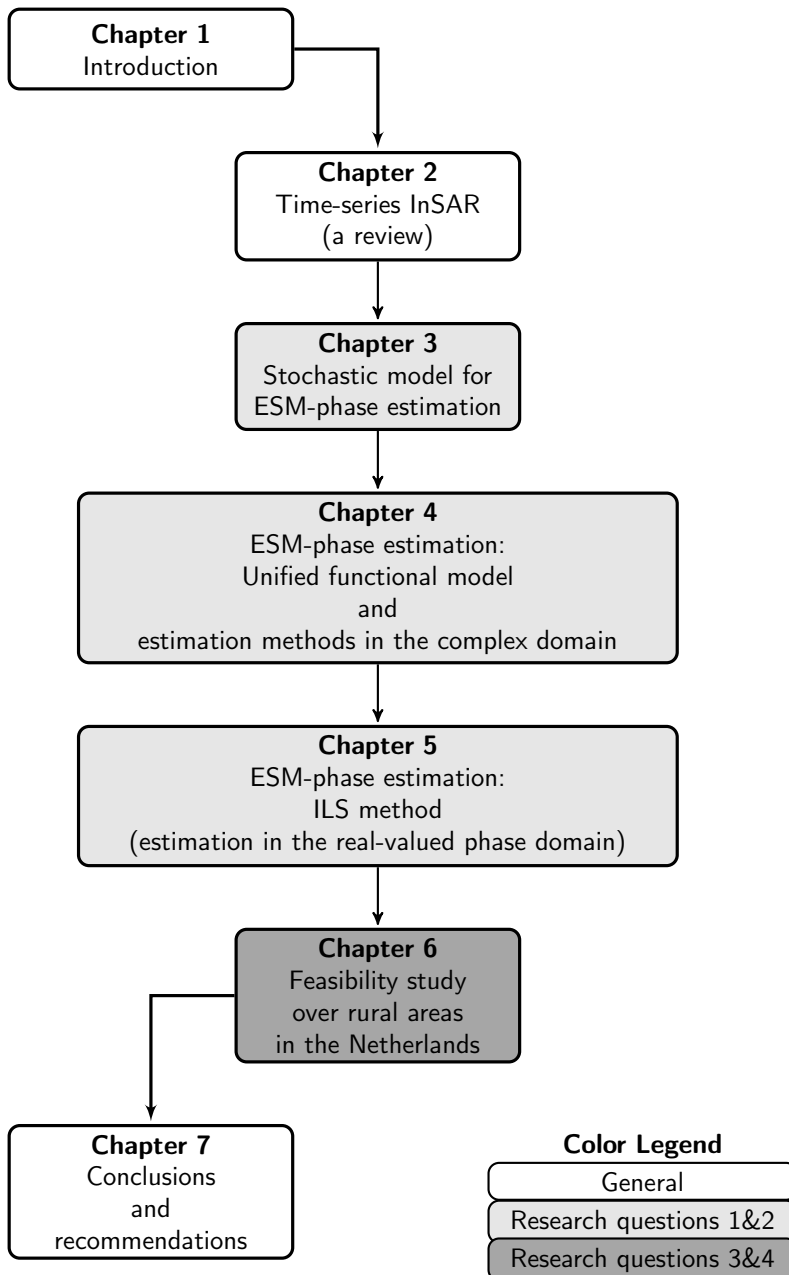


Figure 1.1: Thesis at a glance

,

Time-series InSAR and Distributed Scatterers: A Review

2

This chapter reviews the basic concepts of interferometric synthetic aperture radar or InSAR (sec. 2.1), followed by a review of different time-series InSAR methodologies (sec. 2.2). Detailed explanation of the main processing blocks of different time-series InSAR algorithms is given in sec. 2.3. Specific aspects related to distributed scatterers (DS), i.e. adaptive multilooking (sec. 2.4) and equivalent single-master phase estimation (sec. 2.5) are emphasized and described in detail.

2.1 InSAR principle

The principle of InSAR is based on the interference of two synthetic aperture radar (SAR) images. First we briefly review the concept of SAR, followed by the InSAR measurement principle and processing steps.

2.1.1 SAR measurements

To acquire a radar image, a side-looking moving radar sensor (mounted on a ground-based, airborne, or spaceborne platform) transmits a radar signal/pulse to the earth and measures the complex return of the back-scattered pulses. The received signals are digitized and stored together with annotated transmission/reception times, and create raw data or a real aperture radar (RAR) image, with a very coarse resolution in the flight direction due to physical length restrictions of the radar antenna. Exploiting the fact that every target on earth is illuminated by many pulses during the sensor trajectory, the raw data are subsequently combined (or *focused*) by signal processing techniques in order to artificially build a long antenna and create a SAR image with much higher resolution. For details on SAR and focusing principles, see Bamler and Schättler, 1993; Cumming and Wong, 2005; Massonnet and Souyris, 2008

In a SAR image, every pixel is associated with a rectangular resolution cell on the ground.

The data are sampled in an azimuth (i.e. flight direction) and slant-range coordinate system, so every pixel has a unique range and azimuth coordinate. Focused SAR images are stored in a standard format known as *single-look complex* (SLC) data. In this format, every pixel has a complex phasor P as

$$P = \text{Re}(P) + j \text{Im}(P) = A \exp(j\psi), \quad (2.1)$$

where j is the imaginary unit, A represents the pixel amplitude which is the square root of the intensity of the radar reflection from the ground resolution cell associated with the pixel, and ψ is the fractional phase of the received radar signal. $\text{Re}(P)$ and $\text{Im}(P)$ are the real and imaginary parts of the complex value P , and they are related to A and ψ as

$$\text{Re}(P) = A \cos(\psi), \quad \text{Im}(P) = A \sin(\psi), \quad (2.2)$$

with

$$A = \sqrt{\text{Re}(P)^2 + \text{Im}(P)^2}. \quad (2.3)$$

The SLC phase ψ can be written as a summation of four components as

$$\psi = W\{\psi^{\text{range}} + \psi^{\text{atmo}} + \psi^{\text{scat}} + \psi^{\text{noise}}\}, \quad (2.4)$$

where $W\{\cdot\}$ is the modulo- 2π wrapping operator, ψ^{range} the range-dependent phase related to the distance between the radar sensor and the effective phase center of the resolution cell on the ground, ψ^{atmo} the phase delay induced by the atmosphere, ψ^{scat} the scattering phase that is related to the distribution of all scatterers within a resolution cell, and ψ^{noise} the additional system or thermal noise which is dependent on sensor specifications.

2.1.2 Interferometric SAR (InSAR)

The idea of InSAR is based on interference of two SAR images, acquired from different positions or at different times, exploiting mainly the phase difference between the two acquisitions. As the phase information of SLC images is proportional to the sensor-target distance (via ψ^{range}), the phase difference between two images can be exploited to get information about the position of the target, or about the displacement during the time between two acquisitions.

The result of interfering two SAR images is another complex image called an *interferogram*. As SAR images are acquired from slightly different positions, and therefore the sampling grid of the two images is generally not identical, it is required, preceding interferogram formation, to align or coregister one image to the geometry of the other. Then an interferogram is produced by complex conjugate multiplication of the two aligned SLC images. If P_M and P_S are two coregistered SLC images, the interferogram I_{MS} constructed from these images can be written for every pixel as

$$I_{MS} = P_M P_S^* = A^M A^S \exp\left(j(W\{\psi_M - \psi_S\})\right), \quad (2.5)$$

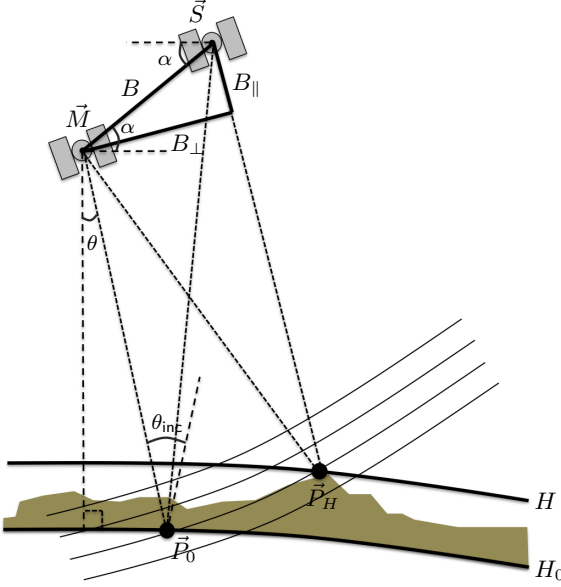


Figure 2.1: InSAR acquisition geometry for point P_H at height H viewed in the plane perpendicular to the flight direction (i.e. the orbit trajectories are into the paper). Master and slave antenna positions are denoted by \vec{M} and \vec{S} , respectively. The difference in positions of the master and slave antennas is denoted by baseline B which is decomposed into the two orthogonal components B_{\parallel} in range direction and B_{\perp} in direction normal to the line of sight (LOS). Point \vec{P}_0 is the counterpart of \vec{P}_H on the reference surface (at height H_0) with the same distance as \vec{P}_H to the master antenna \vec{M} . After van Leijen (2014) and Hanssen (2001).

where $*$ denotes the complex conjugate, and the M and S indices stand for *master* and *slave* image, respectively. In relation to eq. (2.4), the *interferometric phase* ϕ_{MS} for a single pixel can be written as the summation of four components:

$$\phi_{MS} = W\{\psi_M - \psi_S\} = W\{\phi^{\text{range}} + \phi^{\text{atmo}} + \phi^{\text{scat}} + \phi^{\text{noise}}\}. \quad (2.6)$$

In the following, these four interferometric phase components and their further decomposition are discussed. The diagram in fig. 2.2 shows the detailed decomposition of interferometric phase.

2.1.2.1 Range-dependent interferometric phase (ϕ^{range})

The range-dependent interferometric phase is related to the difference between the range phases in the two SLC images. The range component of the master and slave SLC phases, acquired by the radar antenna at position \vec{M} and \vec{S} from a resolution cell with phase-center \vec{P}_H , can be written as (see fig. 2.1) (Hanssen, 2001)

$$\psi_M^{\text{range}} = \frac{-4\pi}{\lambda} d(\vec{M}, \vec{P}_H) \quad \text{and} \quad \psi_S^{\text{range}} = \frac{-4\pi}{\lambda} d(\vec{S}, \vec{P}_H), \quad (2.7)$$

where $d(\cdot, \cdot)$ is the Euclidean distance operator, and λ the radar wavelength. The range-dependent interferometric phase is then the subtraction of the two SLC range phases, i.e.

$$\phi^{\text{range}} = \psi_M^{\text{range}} - \psi_S^{\text{range}} = \frac{-4\pi}{\lambda} \left(d(\vec{M}, \vec{P}_H) - d(\vec{S}, \vec{P}_H) \right). \quad (2.8)$$

The phase component ϕ^{range} can be further decomposed into three contributions as follows.

1. **Flat earth phase:** This phase component is the effect of a (curved) reference surface (e.g., an earth ellipsoid) on the interferometric phase, and exclusively depends on the viewing geometry. Based on fig. 2.1, for point \vec{P}_H , the flat earth phase is computed at the counterpart of \vec{P}_H on the reference surface, i.e. \vec{P}_0 , as

$$\phi^{\text{flat}} = \frac{-4\pi}{\lambda} \left(d(\vec{M}, \vec{P}_0) - d(\vec{S}, \vec{P}_0) \right). \quad (2.9)$$

The viewing geometry can be characterized by the interferometric baseline (B) which is decomposed into two orthogonal components which are the parallel baseline (B_{\parallel}) in range direction and the perpendicular baseline (B_{\perp}) in the direction normal to the line of sight (LOS). The phase component ϕ^{flat} can be approximated, based on the so-called *far-field* approximation (Zebker and Goldstein, 1986; Hanssen, 2001), by

$$\phi^{\text{flat}} = \frac{4\pi}{\lambda} \underbrace{B \sin(\theta - \alpha)}_{B_{\parallel}}, \quad (2.10)$$

where α and θ_{inc} are the baseline orientation angle and look angle, respectively.

2. **Topographic phase:** This component is the effect of the surface height above the reference surface. Similar to the flat earth component, it solely depends on the viewing geometry. Based on the configuration of fig. 2.1, for point \vec{P}_H at height H , the topographic phase ϕ^{topo} is defined as

$$\phi^{\text{topo}} = \frac{-4\pi}{\lambda} \left(\left(d(\vec{M}, \vec{P}_H) - d(\vec{S}, \vec{P}_H) \right) - \left(d(\vec{M}, \vec{P}_0) - d(\vec{S}, \vec{P}_0) \right) \right). \quad (2.11)$$

Note that the point \vec{P}_0 is the counterpart of \vec{P}_H on the reference surface with the same distance as \vec{P}_H to the master antenna \vec{M} . So in eq. (2.11) the distances to the master antenna cancel each other, and hence

$$\phi^{\text{topo}} = \frac{-4\pi}{\lambda} \left(d(\vec{S}, \vec{P}_0) - d(\vec{S}, \vec{P}_H) \right). \quad (2.12)$$

Using the far-field approximation, the topographic phase can be written as a function of height H , perpendicular baseline B_{\perp} , and the range to the master antenna R as (Zebker and Goldstein, 1986; Hanssen, 2001)

$$\phi^{\text{topo}} = \frac{-4\pi}{\lambda} \frac{B_{\perp}}{R \sin(\theta_{\text{inc}})} H. \quad (2.13)$$

3. **Deformation phase:** This component is induced by surface deformation during the time between the master and slave acquisitions. Note that in fig. 2.1, to avoid complexity, it is assumed that point \vec{P}_H has zero displacement and it represents the very same physical point in both acquisitions. However, in practice, a displacement of point \vec{P}_H changes the target-sensor distance and results in deformation phase ϕ^{defo} as

$$\phi^{\text{defo}} = \frac{-4\pi}{\lambda} D_{\text{LOS}}, \quad (2.14)$$

where D_{LOS} is the projection of the 3D displacement of \vec{P}_H onto the radar LOS as¹ (Hanssen, 2001)

$$D_{\text{LOS}} = D_u \cos(\theta_{\text{inc}}) + D_n (\sin(\theta_{\text{inc}}) \sin(\alpha_h)) + D_e (-\sin(\theta_{\text{inc}}) \cos(\alpha_h)), \quad (2.15)$$

where α_h is the satellite heading angle, and D_e , D_n , and D_u are the real deformation components in East, North, and Up directions, respectively.

From the above components of ϕ^{range} , the first two terms (i.e. ϕ^{flat} and ϕ^{topo}) are purely dependent on sensor-target geometry at the time of master and slave acquisitions, and so they are together sometimes called *geometric phase* (ϕ^{geom}). In summary, the range-dependent interferometric phase can be written as combination of the two geometric phase components (ϕ^{flat} and ϕ^{topo}), and the deformation phase as

$$\phi^{\text{range}} = \underbrace{\phi^{\text{flat}} + \phi^{\text{topo}}}_{\phi^{\text{geom}}} + \phi^{\text{defo}}. \quad (2.16)$$

For deformation studies, it is a common practice to calculate (using eqs. 2.10 and 2.13) and remove the ϕ^{geom} contribution from interferograms using precise orbit information, parameters of the reference surface, and an auxiliary digital elevation model (DEM). When removing the geometric phase, two kinds of residual errors may remain in the range-dependent phase, as follows.

- Errors and uncertainties in the precise orbit information induce errors in the computation of baseline parameters. These errors are propagated to the estimated flat-earth phase (and the estimated topographic phase) via eq. (2.10). These residual phase components induced by orbital errors are called *orbital phase*, denoted by ϕ^{orb} . A detailed expression and explanation of the orbital phase can be found in Bähr (2013).
- Imperfections in the external DEM used to calculate topographic phase via eq. (2.13) cause part of the topographic signal to remain in the interferogram. This remaining phase component is called *residual topographic phase* and is expressed as $\phi^{\text{dtopo}} = \frac{4\pi}{\lambda} \frac{B_{\perp}}{R \sin(\theta_{\text{inc}})} \Delta H$, where ΔH is the residual height, or DEM error.

If the geometric phase is removed from the interferogram, eq. (2.16) can be rewritten as

$$\phi^{\text{range}} = \underbrace{\phi^{\text{orb}} + \phi^{\text{dtopo}}}_{\phi^{\text{geom}}} + \phi^{\text{defo}}. \quad (2.17)$$

The decomposition of the range phase and its components are visualized in the first column of the diagram of fig. 2.2.

¹This equation is only valid for SAR sensors in the right-looking mode, which is the most common mode in current space platforms.

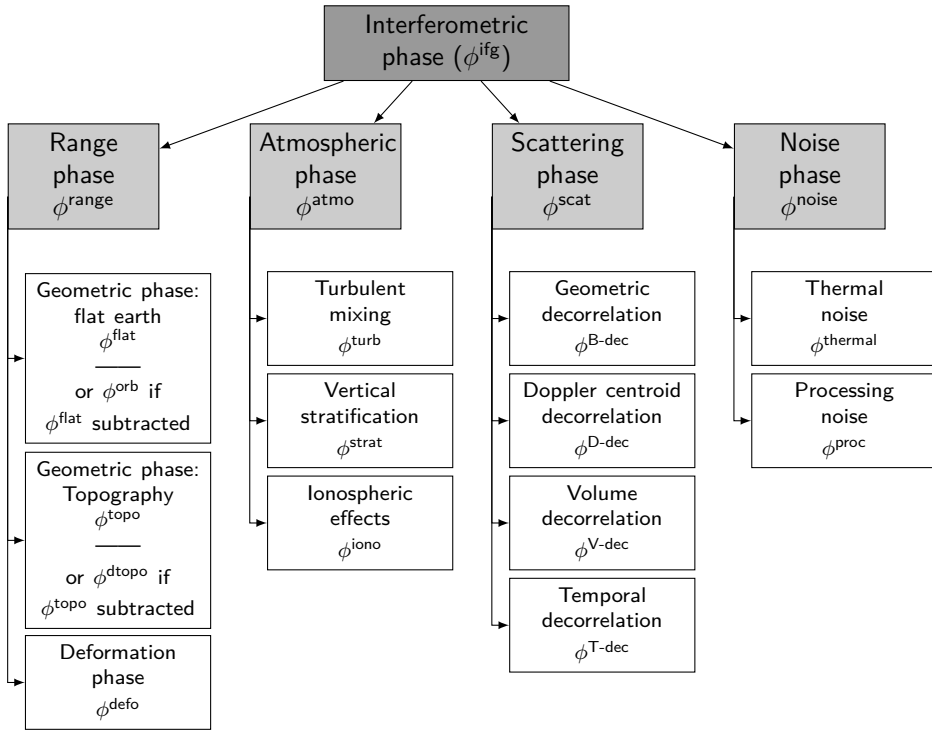


Figure 2.2: Decomposition of interferometric phase.

2.1.2.2 Interferometric atmospheric phase (ϕ^{atmo})

The interferometric atmospheric phase is the result of the difference between the atmospheric phase components in master and slave acquisitions. Based on eq. (2.4), ϕ^{atmo} can be written as

$$\phi^{atmo} = \psi_M^{atmo} - \psi_S^{atmo}. \quad (2.18)$$

This differential phase delay can be due to contributions from different layers of the atmosphere. The most significant contributions are induced by the troposphere (i.e. lower atmospheric layers from sea level to ~ 12 km altitude). Hanssen (2001) subdivided the tropospheric effect into two contributions as follows.

1. **Turbulent mixing (ϕ^{turb}):** This signal is caused by different turbulent processes in the troposphere such as solar heating of the earth's surface, or difference in wind direction/velocity. These processes are strongly nonlinear and behave on a wide range of scales. Based on Kolmogorov turbulence theory, Hanssen (2001) describes the behavior of interferometric turbulence signal as a spatially correlated stochastic process with a power-law behavior in space. This means that for pixels with a short distance between them, the interferometric phases induced by turbulent mixing are more similar. Regarding the temporal behavior, the turbulent mixing effect is generally only correlated in time on the scale of hours. As the time between two

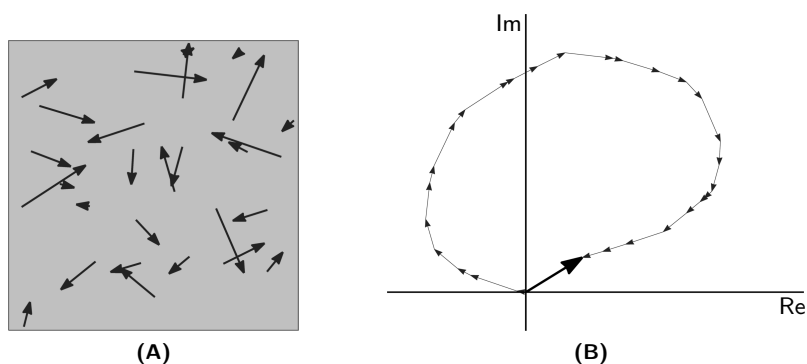


Figure 2.3: Superposition/summation of elementary scatterers within a resolution cell (gray box). **(A)** An arbitrary distribution of elementary scatterers' phasors within the resolution cell. **(B)** The summation of all the phasors (scaled) in complex domain. The bigger arrow indicates the sum. After Hanssen (2001).

acquisitions in common SAR acquisitions is of the order of a couple of days to a month or more, the turbulent atmospheric signal can be considered effectively uncorrelated in time.

2. **Vertical stratification (ϕ^{strat}):** This signal is the result of different vertical refractivity profiles during the two SAR acquisitions and is only relevant if there are elevation differences in the image. For two different resolution cells with a different elevation, the difference in the vertical refractivity profiles between the two acquisitions introduces a new phase component in the interferometric phase. This effect will only affect pixels which have different topographic height, and it is highly correlated with topography. Over flat terrain, the effect is insignificant.

In addition to tropospheric signals, the interferometric phase is also affected by differential delay in the ionosphere (i.e. upper atmospheric layers from ~ 80 km to ~ 600 km altitude). This phase delay is induced by variations in the free electron density in the ionosphere, and is quantified by the *Total Electron Content* (TEC). According to Meyer et al. (2006), TEC variation shows significant spatial correlation. Consequently, its effect on interferometric phases (usually over spatial distances less than a few hundreds of kilometers) is far less significant than tropospheric effects. A detailed and in-depth explanation of different atmospheric effects in InSAR can be found in Goldstein (1995); Zebker et al. (1997); Massonnet and Feigl (1998); Hanssen (2001); Meyer et al. (2006); Ding et al. (2008); and Liu (2012).

2.1.2.3 Interferometric scattering phase (ϕ^{scat})

This phase component is induced by the difference in scattering phase between the master and slave acquisitions:

$$\phi^{\text{scat}} = \psi_M^{\text{scat}} - \psi_S^{\text{scat}}. \quad (2.19)$$

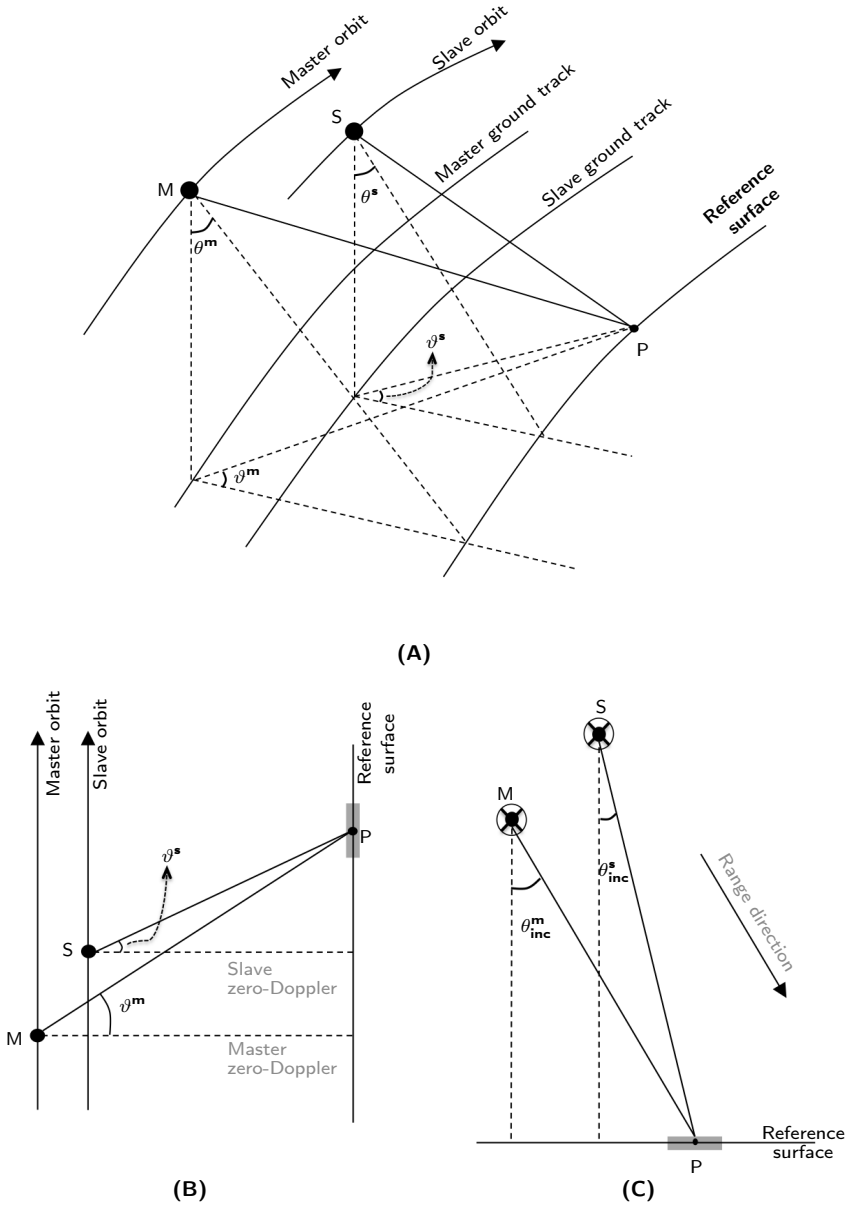


Figure 2.4: InSAR acquisition geometry: demonstration of variation in incidence and squint angles. **(A)** 3D viewing geometry for point P on the reference surface observed by radar antennas at point M on the master orbit and point S on the slave orbit, where θ_{inc}^m and θ_{inc}^s are the incidence angles, and ϑ^m and ϑ^s are the squint angles for the master and slave acquisition respectively. **(B)** 2D top view of the configuration, showing the zero-Doppler directions and variation in squint angles. **(C)** 2D perspective viewed in the plane perpendicular to the flight direction (i.e. the orbit trajectories are into the paper), showing the variation in incidence angles. Note that in these visualizations, we have assumed an idealized/simplified geometry with exactly parallel orbits. In practice, we can have convergent/divergent orbits, which is another cause for different squint angles between master and slave acquisitions.

Note that the reflected signal received from a resolution cell on the ground is the superposition of the reflection from a multitude of elementary scatterers within the cell, see fig. 2.3. The scattering phase (ψ^{scat}) in each SLC image is a function of the relative positions of all the elementary scatterers within a cell with respect to the radar sensor, and the electrical characteristics of the scatterers. Although the scattering phase is intrinsically a deterministic quantity, i.e. it is invariant if the measurements are repeated under the same conditions, it is unpredictable and hence cannot be described mathematically in a deterministic manner. Therefore in radar interferometry, it is standard practice to explain this phase component stochastically by the degree of correlation between master and slave scattering phases. A common measure of correlation between two phase values is the magnitude (or absolute value) of the complex correlation coefficient, called *coherence*² and denoted by $|\gamma| \in [0, 1]$. In the extreme scenario of $|\gamma|=1$, the master and slave scattering phases have exactly the same values (i.e. $\psi_M^{\text{scat}} = \psi_S^{\text{scat}}$) and cancel each other in the interferogram, resulting in $\phi^{\text{scat}} = 0$. For other coherence values between zero and one, the difference in SLC scattering phases results in loss of interferometric coherence, known as *decorrelation*.

The total decorrelation induced by the scattering phase variation can be subdivided into different effects based on the exact source of the decorrelation. In general, four main decorrelation mechanisms can be distinguished (Zebker and Villasenor, 1992; Hanssen, 2001):

1. **Baseline decorrelation:** This effect is the result of different incidence angles between master and slave acquisitions. When a resolution cell on the ground is seen by two radar antennas from different positions and therefore different incidence angles, the range distances of individual elementary scatterers within the cell to the two antennas will be different, and hence their phase contribution will change, resulting in a different scattering phase between master and slave acquisitions. We call this phase difference *baseline decorrelation phase* and denote it by $\phi^{\text{B-dec}}$. The degree of baseline decorrelation is expressed by the baseline coherence (γ_B). This coherence decreases linearly with increasing perpendicular baseline (B_{\perp}). Assuming surface (2D) scattering, where all the elementary scatters are distributed over a 2D plane spanned by azimuth and range directions, the baseline decorrelation can be explained and predicted by a frequency shift in the ground reflectivity spectrum (Gatelli et al., 1994). This frequency shift can be effectively compensated for in radar interferometry by different kinds of spectral filtering methods at the expense of reduced resolution, see sec. 2.1.3.
2. **Doppler centroid (azimuthal) decorrelation:** Similar to baseline decorrelation which is caused by the difference in incidence angles, the Doppler centroid decorrelation is caused by a change in acquisition squint angle, which is defined as the angle between the pointing direction of the antenna and the perpendicular line to the flight direction. The latter is called *zero Doppler direction*, see fig. 2.4. In other words, baseline decorrelation is caused by varying the viewing direction in range, whereas the Doppler centroid decorrelation is the result of varying the viewing direction in azimuth. Again, the phase contribution of elementary scatterers

²A detailed mathematical description of coherence γ is given in chapter 3

within a resolution cell will be different between master and slave acquisitions due to different squint angles, resulting in a scattering phase difference called *Doppler centroid decorrelation phase* and denoted by $\phi^{\text{D-dec}}$. The degree of Doppler centroid decorrelation is expressed by the Doppler centroid coherence (γ_{dc}). This coherence decreases linearly with increasing Doppler baseline B_{dop} (i.e. the difference in Doppler centroid frequencies between master and slave images). Similar to baseline decorrelation, the Doppler centroid decorrelation can be compensated for by spectral filtering in azimuth direction at the expense of reduced resolution.

3. **Volume decorrelation:** Although, assuming surface (2D) scattering, both baseline decorrelation and Doppler centroid decorrelation can be compensated for by spectral filtering in range and azimuth direction, respectively, the scattering mechanism can be more complex than just 2D scattering in practice. If the elementary scatterers are distributed in a 3D volume (e.g., branches of canopies or trees in forest areas), the decorrelation mechanism induced by different imaging geometries is more complicated. This decorrelation is often called *volume decorrelation* (denoted by γ_{vol}) and is in principle unpredictable. The volume decorrelation effect is stronger in vegetated areas where radar waves can penetrate into a volume of scatterers. Consequently, for larger radar wavelengths (e.g. P-/L-bands) which have a stronger penetration capability, volume decorrelation is relatively larger than for shorter wavelengths such as C-/X-bands.
4. **Temporal decorrelation:** This decorrelation is the result of variation in scattering phases between the two acquisitions, due to the actual changes in the scattering characteristics of the elementary scatterers within a resolution cell. This could be either due to a change in the physical distribution of elementary scatterers (e.g. caused by soil weathering, anthropogenic activities, vegetation growth, and plant movements in the wind), or due to the variation in electrical properties of the scatterers (e.g. change in the dielectric constant of targets influenced by a variation in moisture content). The phase variation due to temporal decorrelation ($\phi^{\text{T-dec}}$) results in loss of coherence which is expressed by the temporal decorrelation factor γ_{T} . High temporal coherence is common on surfaces without vegetation (e.g., arid areas, deserts, road and building surfaces). The lower extreme of temporal decorrelation is associated with water bodies where the scattering characteristics are changing rapidly within seconds. Due to the wide range of mechanisms inducing temporal decorrelation, it is very difficult to model the coherence behavior as a function of time (or as a function of the temporal difference between two acquisitions, called temporal baseline B_{T}). For some simplified situations and natural processes, models have been introduced in literature, for example in Zebker and Villasenor (1992); Hoen and Zebker (2000); Rocca (2007); Morishita and Hanssen (2015b). A brief review of some of these models is given in chapter 3.

Note that the interferometric scattering phase ϕ_{scat} is mainly induced by a change in superposition of all scatterers' contributions in a resolution cell. So if the resolution cell contains only one dominant scatterer, the scattering phase will be zero or practically very small. This is an important characteristic which is exploited in time-series InSAR methodologies, which detect and extract information from scatterers that are minimally affected by scattering-induced decorrelation, see sec. 2.2.

2.1.2.4 Interferometric Noise phase (ϕ^{noise})

The other interferometric phase term in eq. (2.6), is ϕ^{noise} , see also fig. 2.2. This component is related to different noise contributions which are neither related to the imaging geometry nor to the scattering mechanisms. This term can be subdivided into two components based on the source of the noise: system related noise, and processing noise.

1. **System noise:** This noise component mainly includes the system thermal noise, which depends on the system bandwidth and receiver temperature. Similar to decorrelation phase, the phase introduced by thermal noise (ϕ^{thermal}) results in loss of coherence, which is described by thermal coherence γ_{thermal} . It has been shown that the thermal coherence is theoretically dependent on the signal-to-noise (SNR) ratio of a particular radar system (Zebker and Villasenor, 1992; Zebker et al., 1994b). Note that the SNR not only depends on system characteristics but also on the power of the reflected signal from the surface, the radar cross section, which is determined by surface characteristics such as roughness, slope, and moisture content. In this sense the name system/thermal coherence may be slightly misleading as it is not purely a function of system parameters.
2. **Processing-induced noise:** This noise term is the result of a chosen algorithm used for interferogram formation, mainly the procedure of aligning the master and slave images (i.e. coregistration and interpolation of the slave image on the master grid). The processing noise also causes a decorrelation effect which can be denoted as γ_{proc} . The processing phase noise component introduced in interferogram can be expressed as ϕ^{proc} .

To summarize, from the four main components of the interferometric phase (i.e. ϕ^{range} , ϕ^{atmo} , ϕ^{scat} , and ϕ^{noise} , see eq. (2.6) and fig. 2.2), the scattering phase and noise phase, which are modeled stochastically by coherence factors, cause a decorrelation effect in the interferometric phase. The different coherence terms are multiplicative (Zebker and Villasenor, 1992), and the total coherence can be expressed by γ_{total} as

$$\gamma_{\text{total}} = \gamma_B \cdot \gamma_{\text{dc}} \cdot \gamma_{\text{vol}} \cdot \gamma_T \cdot \gamma_{\text{thermal}} \cdot \gamma_{\text{proc}} \quad (2.20)$$

Under the condition that the scattering and noise terms are zero, or in other words $\gamma_{\text{total}}=1$, we say that the image is *coherent*, and the interferometric phase of a pixel solely depends on the two-way physical travel time of the radar signal between the sensor and the pixel phase center. This is the ideal situation for using InSAR to observe deformation, topographic, or atmospheric signals. However this situation never happens in reality, and there are always some noise terms. In fact, the main challenge in InSAR analysis is to extract coherent information from noisy interferometric phases with variable coherence values. The coherence factor is a key parameter for stochastic modeling of InSAR observations and can be directly related to interferometric phase statistics such as probability density functions and phase variance. This is discussed in depth in chapter 3.

2.1.3 InSAR processing: overview

In order to produce an interferogram from two SLC images, different processing steps are applied. A detailed explanation and mathematical presentation of these steps are beyond the scope of this study. Although there are various algorithms and processors available for interferometric processing and they differ in some details and implementations, all InSAR processors include some key steps which are reviewed briefly in this section.

Coregistration and resampling

In order to make an interferogram by complex conjugate multiplication of master and slave SLC images (see eq. (2.5)), identical scatterers need to be combined. Often this means that the sampling grid of the two images should be aligned to each other, making it possible to associate the pixels in the both images to the same area on the ground. This procedure can be applied in two main steps: first, for each pixel the amount of shift between the two images is computed (called the *coregistration* step), and then one of the images is interpolated/resampled onto the grid of the other (called the *resampling* step). The common convention is to resample the slave image onto the master image grid. In principle, the coregistration step should account for geometrical misalignment and distortions induced by differing incidence angles, orbit crossings, varying sensor attitudes, different sampling rates due to different sensor velocities, and along-track and across-track shifts due to the start/stop times of the SAR sensor.

Coregistration itself is usually applied in two steps. First, *orbit/coarse coregistration* can be applied to compute/approximate a single offset between two images based on satellite precise orbits (i.e. the precise positions of the satellites during the acquisitions) and timing information. In the second step, fine (or sub-pixel) coregistration is performed by direct cross-correlation techniques to define the two offsets per pixel in azimuth and range direction. Cross-correlation is usually applied over the amplitudes or squared amplitudes (power) of SLC images. By cross-correlating a pair of patches/windows from two amplitude (or power) images, the correlation peak is associated to the offset vector in azimuth and range directions. Ideally the cross-correlation is applied over all pixels, making it a very slow process. Therefore, in practice, it is performed over a large number of windows (e.g 3000+) distributed over the scene. Then the offsets for other pixels can be computed by fitting an analytic function to the estimated offsets. Assuming all targets lying on an Earth ellipsoid, a 2D polynomial of a certain degree (e.g, between degree 2 and 5) is usually used as the analytical function to efficiently approximate the offsets. For a detailed overview of InSAR coregistration methods based on cross-correlation offset estimation, see Brown (1992); Samson (1996); Michel et al. (1999), and Strozzi et al. (2002).

As offsets are theoretically dependent on target elevation on the ground, for areas with high topographic variations, polynomial functions cannot describe the offset variations within a scene with high accuracy. For these areas the topography should also be accounted for in the coregistration. This is done by Digital Elevation Model (DEM)-based coregistration. In this approach, the coregistration offsets are computed for each pixel based on orbit information and an existing DEM of the area. Details of DEM-based coregistration can be found in Adam et al. (2003); Sansosti et al. (2006); Arikan et al.

(2008), and Nitti et al. (2008, 2011). For InSAR applications, a high accuracy of coregistration is generally required. Just and Bamler (1994) and Hanssen (2001) have shown that the accuracy of around 0.1 pixels in both azimuth and range directions is adequate for negligible loss of coherence. This accuracy is achievable by the coregistration procedure described above. Note that the accuracy requirement of 0.1 pixels is based on the assumption of relatively small squint angles, which is the case for strip-map radar modes and most of the common medium-resolution SLC products. However, for imaging modes in which the small squint angle assumption is not valid (e.g. ScanSAR, or the recently developed *terrain observation with progressive scan* (TOPS) mode applied on Sentinel-1 satellite), a much higher coregistration accuracy (in the order of 0.001 pixels) is needed (Monti-Guarnieri and Prati, 1996; Bara et al., 2000; Holzner and Bamler, 2002; Prats-Iraola et al., 2012). Achieving such a high accuracy requires more advanced coregistration algorithms. A detailed overview of such methods can be found in Scheiber and Moreira (2000); Prats-Iraola et al. (2012), and Scheiber et al. (2015).

After the coregistration, the resampling step is performed. In this step, the complex values of slave image are evaluated at the pixel positions of the master image based on the offsets computed in the coregistration step. In a generic sense, resampling is done in two steps. First, a continuous signal is constructed from discrete/sampled values in the slave image by convolution with a small resampling kernel. The design of an optimal kernel was discussed in Laakso et al. (1996) and Hanssen and Bamler (1999). In the second step, the reconstructed continuous signal is sampled at the new locations using the offsets computed in the coregistration step.

Oversampling

From a signal processing point of view, the complex conjugate multiplication of two SLC images to form an interferogram is equivalent to the convolution of the images in the frequency domain. As a consequence of convolution, the frequency range or spectrum of the interferogram is the cross-correlation of the master and slave spectra, and hence it is twice as wide as the individual spectra of the two images. As the sampling frequency of the interferogram is the same for the two images, the spectrum widening results in an aliasing effect which appears as phase noise in the interferogram (Hanssen, 2001). In order to prevent this aliasing effect, it is required to oversample both master and slave images by a factor of two before interferogram formation. This is done by first computing the frequency spectrum of every image via Fourier transformation, and then zero-padding of the two spectra with the same number of original samples in the images. After zero-padding, the inverse Fourier transformation is applied to obtain a copy of the master and slave images with twice the number of samples. Note that the pixel area of the oversampled images — and thus of the obtained interferogram — is a quarter of the original pixel area.

Flat earth and topographic phase subtraction

After the formation of an interferogram, it is a common practice to subtract and compensate for phase contributions that can be predicted, the so-called *phase reduction*. This is a deterministic approach, which reduces the phase variability in the interferogram, and it can encompass both range phase and atmospheric phase components. Most well-known is the phase contribution of the ellipsoidal shape of the earth (i.e. flat earth phase, see sec. 2.8). This phase contribution is computed for every pixel using

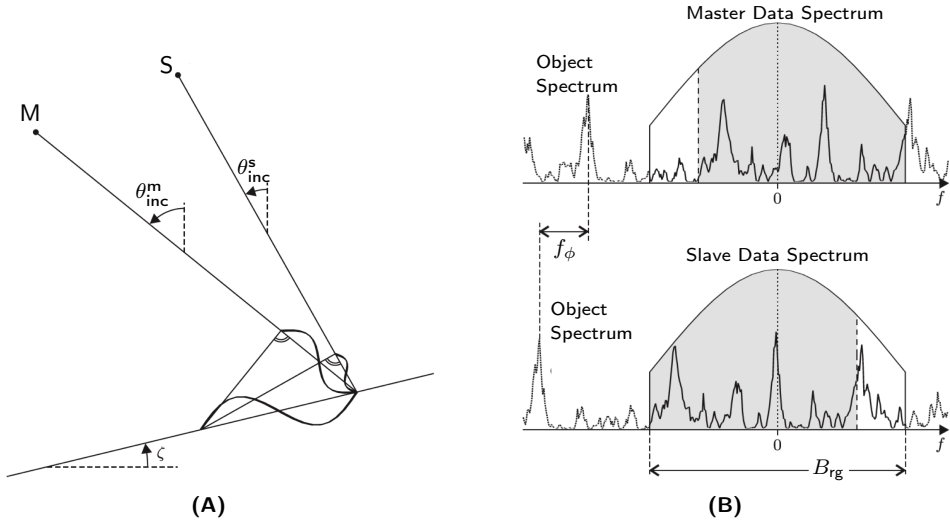


Figure 2.5: Demonstration of range frequency/wavenumber shift induced by different incidence angles: **(A)** a particular spatial wavelength (i.e. the sinusoidal structure) is mapped differently to the lines of sight of master (M) and slave (S), resulting in different wavelengths associated with different spatial frequencies (or wavenumber). The amount of shift is not only related to the incidence angles but to the terrain slope ζ . **(B)** Extending the concept of frequency shift to other frequencies will result in a wavenumber/frequency shift in the whole data spectrum of the two images. The object spectrum is mapped to a different portion of the data spectrum, with a frequency shift of f_ϕ . The overlapping part of master and slave spectra (i.e the gray area) is defined by the range bandwidth B_{rg} and f_ϕ . The non-overlapping parts in each spectrum can be considered as noise which should be removed by range spectral filtering. (Figures courtesy of Bähr (2013)).

eq. (2.9) or (2.10). In order to evaluate these equations, the reference location of each pixel (i.e., the vector \vec{P}_0 in eq. (2.9)) is computed. This process is called *geocoding*. The Doppler frequency used in SAR processing, range time information, and the definition of the reference surface body are used in order to define the pixel coordinates on the ground. A detailed mathematical explanation of geocoding computation is given in Schwäbisch (1995); Madsen et al. (1993), and DUT (1998). For deformation monitoring applications, if topographic information or a DEM of the radar scene is available, it is recommended to also subtract the interferometric contribution of topography. The topographic phase is computed based on eq. (2.13) for every pixel, and it is subtracted from the interferogram which has been already corrected for the flat earth phase. Phase reduction can also include an a-priori deformation model or an atmospheric model.

Spectral filtering

The objective of this step is to reduce some phase noise contributions in an interferogram. Reducing noise can facilitate the unwrapping step and the interpretation of interferograms. Conceptually, the noise phase comprises all the phase contributions which cause decorrelation in an interferogram. Although the physical mechanism behind different kinds of decorrelation are different, some of them, such as baseline and Doppler-centroid decorrelation, are strongly related to acquisition geometry and so can be predicted and compensated for based on some information on the viewing geometry. As mentioned before, baseline and Doppler-centroid decorrelation are the results of frequency shifts in

the data spectrum of the master and slave images. The idea of spectral filtering is to reduce these effects by filtering the azimuth and range spectra of the images before interferogram generation, and in this way, to reduce decorrelation effects. In the following, we briefly explain the filtering procedure in range and azimuth directions, respectively.

1. Spectral filtering in range: As discussed in sec. 2.1.2.3, baseline decorrelation is the result of varying incidence angles between the two images. The induced frequency shift by different incidence angles is demonstrated in fig. 2.5. In fig. 2.5A, a particular spatial wavelength (i.e. the sinusoidal structure) is mapped differently to the lines of sight of the master and the slave, resulting in different wavelengths associated with different spatial frequencies (or wavenumbers). Note that the amount of shift is not only related to the incidence angles but also to the terrain slope ζ . Extending the same concept to all the frequencies results in a wavenumber/frequency shift in the data spectra of the two images, see fig. 2.5B. As a result, there will be non-overlapping parts in the master and slave data spectra. During interferogram formation by complex multiplication of two images (or convolution of image spectra in the frequency domain), the non-overlapping parts of the two spectra will spread over all the frequencies of the resulting interferogram, introducing phase noise or decorrelation. The idea of range spectral filtering is to estimate the amount of the frequency shift based on information about satellite orbits and ground topography, and subsequently to remove the resulting non-overlapping part of the master and slave spectra. Theoretically, the amount of the frequency shift is computed as (Gatelli et al., 1994; Bamler and Hartl, 1998; Hanssen, 2001)

$$f_\phi = \frac{2B_\perp}{\lambda R_m \tan(\theta_{\text{inc}}^m - \zeta)}, \quad (2.21)$$

where B_\perp is the perpendicular baseline B_\perp , λ the radar wavelength, R_m the slant-range between the target and the master satellite, and θ_{inc}^m the master incidence angle. After computation of f_ϕ , the master and slave images are transformed to frequency domain, and the non-overlapping parts of their spectra are removed, followed by inverse Fourier transformation to spatial domain. Constructing interferograms with the filtered images results in reduced decorrelation. Note that due to filtering, the range bandwidth of images reduces from B_{rg} to $B_{\text{rg}} - f_\phi$. Reduction in bandwidth in the frequency domain is equivalent to reduction in resolution in the spatial domain. So the price to pay for filtering and reducing decorrelation is losing spatial resolution. As we see in eq. (2.21), the phase shift is related strongly to the terrain slope, whose computation for every pixel is not trivial. The common practice is to assume a flat surface (i.e. $\zeta=0$) and compute one frequency shift for the whole image. Although this works effectively for some areas with low topographic variation, it may worsen the quality of the interferogram in other areas (Rocca, 2000). For areas with high topographic variation, an alternative is to estimate the frequency shift per line or patch from the data (Davidson and Bamler, 1999; Rocca, 2000).

2. Spectral filtering in azimuth: This step is equivalent to range spectral filtering but in the azimuth direction. The main objective is to reduce Doppler-centroid decorrelation induced by a varying squint angle between master and slave. As

discussed before, the angular variation in azimuth is directly related to the Doppler baseline B_{dop} . Here again, the variation in squint angle causes a frequency shift in the azimuth data spectra of the master and slave images. Similar to range filtering, the idea of azimuth spectral filtering is to remove the non-overlapping part of the azimuth data spectra of the master and slave. Contrary to spectral shift in range direction, Monti-Guarnieri and Rocca (1999) have shown that the effect of slope on frequency shift in azimuth direction is insignificant and can be ignored. Hence the azimuth frequency shift is directly equivalent to the Doppler-centroid change or the Doppler baseline B_{dop} . Furthermore, converging/diverging orbits can induce additional frequency shift in azimuth data spectra. This shift is mainly related to the convergence/divergence angle between master and slave orbits (The full calculation of such a shift is given by Bähr (2013)), however its effect is usually insignificant for common satellite sensors and standard acquisition scenarios.

Note that both azimuth and range spectral filtering are effective only when resolution cells are mainly affected by surface scattering. For resolution cells with dominant point scatterers already minimally affected by baseline or Doppler-centroid decorrelation, spectral filtering would result in worsening the coherence and introduction of additional noise.

Complex multilooking

This step is another optional step with the objective of reducing phase noise in interferograms. The main idea is that if adjacent pixels contain a constant signal component, the spatial (complex) averaging of them will result in noise reduction. This process is called *complex multilooking* (Goldstein et al., 1988; Rodriguez and Martin, 1992; Lee et al., 1998). Assuming M and S are master and slave SLC image, the multilooked interferogram for a pixel k is computed as

$$\langle I_k \rangle = \frac{1}{L} \sum_{i=1}^L M_i S_i^* \quad (2.22)$$

where $\langle \cdot \rangle$ denotes the spatial averaging or multilooking operation, L is the number of looks or the multilooking factor, and i is the index of all the adjacent pixels used in the averaging. The phase of the multilooked interferogram can also be written as

$$\angle(\langle I_k \rangle) = \hat{\phi}_k = \arctan \left(\frac{\sum_{i=1}^L \text{Im}(M_i S_i^*)}{\sum_{i=1}^L \text{Re}(M_i S_i^*)} \right). \quad (2.23)$$

We will show in chapter 3 that the noise variance of the interferometric phase can be significantly reduced by multilooking under the assumption of spatial (smoothness) of the signal, and ergodicity (Lee et al., 1994; Hanssen, 2001). Assuming ergodicity, the averaging area around each pixel can have any geometrical shape. The most convenient approach is to use rectangular (boxcar) windows with size L_{az} and L_{ra} in azimuth and range directions, resulting in multilooking factor of $L=L_{\text{az}}L_{\text{ra}}$. In this case, multilooking

can be done by spatial 2D boxcar convolution, which is equivalent to 2D sinc multiplication in the frequency domain. Note that the multilooking operation is based on the two following implicit assumptions:

1. **Signal consistency (stationarity):** In multilooking, it is assumed that the signal of *interests* is constant over the averaging area. This is why multilooking is usually applied after the removal of flat-earth and topographic phase. If high spatial variation of signal components is expected, this phase variation should be compensated for before multilooking. Examples of variable signals are high topography gradients or orbital errors. These kinds of spatially-variable signals can be removed by different kind of phase flattening or low-pass filters such as the adaptive multi-resolution defringe algorithm (Prati and Rocca, 1992; Davidson and Bamler, 1999; Wang et al., 2012), patch detrending (Zebker and Chen, 2005; Bamler and Hartl, 1998), and the low-pass filtering method presented by Hooper et al. (2004).
2. **Statistical homogeneity:** The multilooked phases are computed by spatial averaging over pixels that are assumed to be statistically homogeneous, or in other words the scattering and noise phases of all the averaging pixels show statistically a similar behavior. In order to satisfy the homogeneity condition, it is recommended to use spatially adaptive windows for multilooking. An example is the spatial adaptive approach introduced by Ferretti (1997), which identify homogeneous pixels in a single interferogram based on speckle-Lee filter methodology (Lee et al., 1998). For a stack of SAR images, some space-adaptive methods have been introduced by Ferretti et al. (2011b); Parizzi and Brcic (2011); Wang et al. (2012); Goel and Adam (2014); Jiang et al. (2014b), and Jiang et al. (2014a). We review some of these methods in sec. 2.4.

Phase unwrapping

One of the main (and also challenging) steps in InSAR processing is the phase unwrapping. InSAR observations are wrapped (modulo- 2π), see eq. (2.6). For InSAR applications, the estimation of the unknown absolute phase from the wrapped observations is required. From an estimation point of view, the unwrapping problem is inherently undetermined, and hence non-unique. As a consequence, it is impossible to solve the unwrapping problem without any a-priori knowledge or assumption about the signal of interest. The most common assumption, traditionally used in InSAR, is that the difference between the phase of two adjacent pixels is not more than half a wave cycle. In areas with a high spatial gradient of signal components (e.g high topographic variations in mountainous areas or high gradient of deformation induce by an earthquake close to a fault), this assumption may be violated and more information and assumptions are required for correct unwrapping. Resolving 2π cycle ambiguities in a single interferogram, i.e. in two-dimensional space domain, is called 2D unwrapping. A detailed overview and explanation about 2D unwrapping can found in Goldstein et al. (1988); Ghiglia and Pritt (1998); Bamler and Hartl (1998); Bamler et al. (1998); Costantini (1998); Eineder and Holzner (1999); Chen (2001), and Ferretti et al. (2007). In stack processing and time-series InSAR methodologies, different approaches have been developed to also resolve ambiguities based on models/assumptions in the time domain (i.e. 1D unwrapping),

or in both spatial and temporal domains (i.e. 3D unwrapping). We will review these methodologies in sec. 2.2.

2.1.4 Conventional InSAR: limitations

Using InSAR to study a certain phenomenon (e.g. deformation or topography) requires to isolate the signal of interest from other components. Therefore, estimating the signal of interest from a single interferogram is challenging when the other signal/noise components significantly interfere with the signal of interest. In principle, the interference of ϕ^{scat} and ϕ^{atmo} with the signal of interest forms the main shortcomings of conventional InSAR, summarized as follows.

1. Temporal and baseline decorrelation: The change ψ^{scat} due to temporal and baseline decorrelation results in large scattering noise components in interferograms. Temporal decorrelation makes InSAR measurements useless in vegetated areas and in other areas where the scattering characteristics or the positions of the scatterers change rapidly compared to the SAR acquisition interval. Furthermore, baseline decorrelation prevents information extraction from interferograms with large perpendicular baseline, more precisely with B_{\perp} larger than a *critical baseline* which is defined as the minimum value of B_{\perp} for which the backscatter signal from pixels with surface scattering mechanism is completely decorrelated (Hanssen, 2001).
2. Atmospheric heterogeneity: The spatially and temporally variable state of the atmosphere superimposes another signal (ϕ^{atmo}) that interferes with the signal of interest especially in case of small signal magnitude (e.g., millimeter-level surface deformation), making it impossible to distinguish deformation signal from atmospheric effects.

Coping with these limitations is the main driving factor to develop *time-series InSAR methodologies* and to systematically exploit multiple interferograms from the same area.

2.2 Time-series InSAR

The first efforts to overcome the above limitations of InSAR were mainly targeted towards atmospheric disturbances. Based on the fact that atmospheric effects are mostly uncorrelated temporally, these methods filter them out by temporal averaging over a stack of interferograms. They are called *stacking methods*, and examples can be found in Sandwell and Price (1998); Wright et al. (2001); Lyons and Sandwell (2002). In general, when a stack of interferograms is available, atmospheric phase can be separated from other signals based on its different spatio-temporal behavior than the signal of interests. The atmospheric effect is generally only correlated in time on the scale of hours to a day (Hanssen, 2001). As the time between two acquisitions is of the order of a couple of days to a month or more, the turbulent part of atmospheric signal can

be assumed uncorrelated in time. At the same time, atmospheric signal has a strong correlation in space over length of a few kilometers. So based on these spatio-temporal characteristics, atmospheric effects can be separated from other signals with different behaviors, for example from deformation signals which are spatially and also temporally correlated. This is the main concept behind different atmospheric-signal mitigation algorithms in time-series InSAR (TInSAR) methods.

The other developments in TInSAR focused on circumventing target decorrelation. In general there are two ways of thinking for this: one is to discern and isolate pixels which are not (or minimally) affected by decorrelation, and therefore have high SNR in all interferograms, and then exclusively exploit these pixels to extract useful information, and another way is to process pixels affected by decorrelation but reduce/filter the decorrelation effect by a smart processing scheme.

These two lines of thought have led to development of two different kinds of TInSAR methodologies, optimized towards two categories of pixels with different models of ground scattering: one is the so called *persistent scatterers* (PS) pixel, which is the resolution cell with a dominant scatterer, minimally affected by decorrelation. The other category is the *distributed scatterers* (DS) pixel associated with ground resolution cells which contain no dominant scatterer and are affected by decorrelation. In the rest of this section, we first give a more in-depth description of the characteristics of PS versus DS pixels. Then we review the main TInSAR developments and methodologies, followed by brief description of the key steps in TInSAR processing algorithms.

2.2.1 Persistent scatterers vs distributed scatterers

As discussed before, in SAR images, the phase measurement of each pixel follows from the coherent sum of contributions from all scattering elements within the associated resolution cell. The degree of decorrelation of radar signals depends on the distribution of scattering centers within a resolution cell. If the phase of a pixel were determined by just one stable point scatterer, the decorrelation would be zero. Although this is never the case for real scatterers, there are pixels which behave somewhat like point scatterers, and for which decorrelation is greatly reduced. In these pixels, a strong reflecting object dominates the radar measurement, and other scatterers just introduce additional noise, called *clutter*. Fig. 2.6 shows the difference between a distributed scattering pixel and a pixel with a dominant scatterer, and shows the different phase behavior for different resolution cells. "PS-pixels" are those ground resolution cells which contain a persistently dominant scatterer, effectively referred to as the PS³, so their decorrelation phase variation is small. In other words, for PS-pixels, ϕ^{scat} is minimal in all interferograms, even in those with very large temporal or perpendicular baselines. Hence, information can be extracted from PS from a stack of interferometric pairs, all referenced to the same master image. Such a configuration of interferograms is called *single master stack*, see fig. 2.7A. Most PS are man-made features, and so there is a high density of them in urban areas and on infrastructure such as bridges, roads, dams and dikes. Also in mountainous areas, some rocks and boulders can be natural PS.

³see footnote 2, page 4

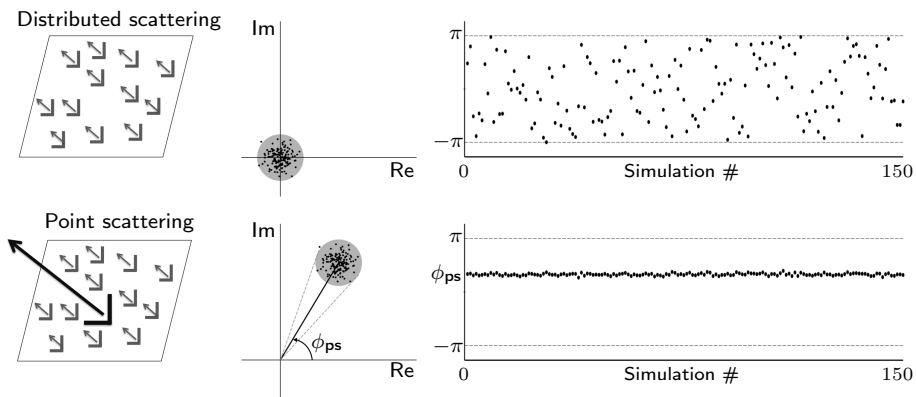


Figure 2.6: Distributed vs point scattering - Top row: a distributed scatterer resolution cell, bottom row: dominant point scatterer resolution cell. The plots on the left show stylized arrangements of elementary scatterers within a resolution cell. The bigger object corresponds to a dominant point scatterer. The plots on the middle show the phasors corresponding to 150 simulations. In each simulation, the location of the scatterers (except the dominant scatterer) changed randomly. The plots on the right show the phase behavior of different scattering resolution cells for 150 simulations. It is clear how the large amplitude of the dominant scatterer influences the phase dispersion. While for distributed scattering, phase values are randomly distributed between $-\pi$ and π , for the point scattering case, they are distributed with much smaller dispersion around the phase of the dominant scatterer (ϕ_{ps}). After Hooper (2006).

Contrary to PS-pixels, resolution cells with no dominant scatterer may be affected strongly by decorrelation, but they may still contain some coherent information in some interferograms, mainly with small temporal and perpendicular baselines. Therefore, unlike for PS, the information content in a single-master interferogram stack is neither optimal nor complete for DS, and so multi-baseline configurations should be exploited. Another difference compared to PS is that filtering steps such as complex multilooking and spectral filtering are effective to reduce DS-pixel noise. However, for PS-pixels, as discussed in sec. 2.1.3, spectral filtering deteriorates the phase quality or coherence. Also, multilooking is not recommended for PS-pixels as they have usually different statistical characteristics with respect to their surrounding pixels.

In addition to PS and DS, some other scattering models can also be recognized. For example *temporary-PS* are associated with resolution cells which contain a dominant scatterer only in a certain period of time, and so only on a subset of images. Basilico et al. (2004) proposed a methodology to exploit temporary-PS. Another scattering model is multiple-scattering due to the existence of multiple dominant scatterers in one resolution cell. Detection and decomposition of multiple point scatterers within a single resolution cell is the subject of *tomographic SAR* analysis (Reigber and Moreira, 2000; Lombardini, 2005; Fornaro et al., 2009; Zhu and Bamler, 2010), and is not discussed further in this thesis.

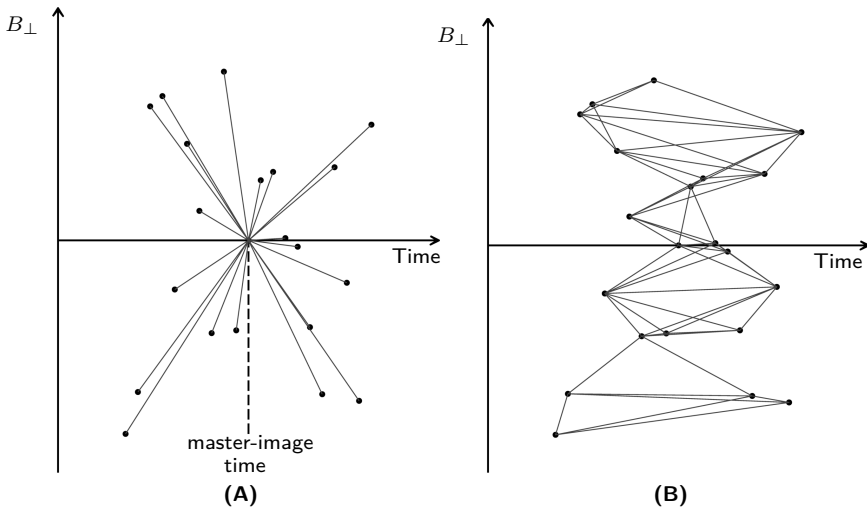


Figure 2.7: Example of baseline configurations for **(A)** a single-master stack, and **(B)** a small (perpendicular) baseline subset. The horizontal axis is the time of acquisitions, and vertical axis show the relative spatial separation perpendicular to sensor look direction (i.e. perpendicular baseline B_{\perp}). Arcs correspond to interferograms, and nodes correspond to SLC images.

2.2.2 TInSAR methodologies

2.2.2.1 Persistent scatterer interferometry (PSI)

In the late 1990s, it was recognized that some features, especially man-made structures, have stable backscattering characteristics over long time intervals (Usai, 1997; Usai and Hanssen, 1997; Usai and Klees, 1999). This led to the development of an innovative methodology called Permanent Scatterer InSAR, or PSInSAR (Ferretti et al., 2000, 2001) which exploits PS-pixels to obtain deformation time-series over long time periods and overcome the main limitations of conventional InSAR. The main characteristics of the PSInSAR processing method are that only PS-pixels are considered and it utilizes a single-master stack of differential interferograms. Since the development of the first PS technique by Ferretti et al. (2000), other algorithms have been introduced using comparable concepts (Van der Kooij, 2003; Adam et al., 2003; Werner et al., 2003; Hooper et al., 2004; Kampes, 2005; Costantini et al., 2009; van Leijen, 2014). The term *Persistent Scatterer Interferometry* (PSI) is used to collectively address all these algorithms.

Although the details of these algorithms vary depending on the implementation, all of them contain three main processing blocks: *coherent pixel selection*, *spatio-temporal (3D) unwrapping*, and *atmospheric-signal mitigation*. These steps may be applied in combination, independently, or iteratively in different PSI implementations. More details about each block are given in sec. 2.3. Here, we review generic work-flows of two kinds of PSI methods: those that identify PS-pixels based on the phase variation in time, and those that use phase correlation in space as the selection criterion.

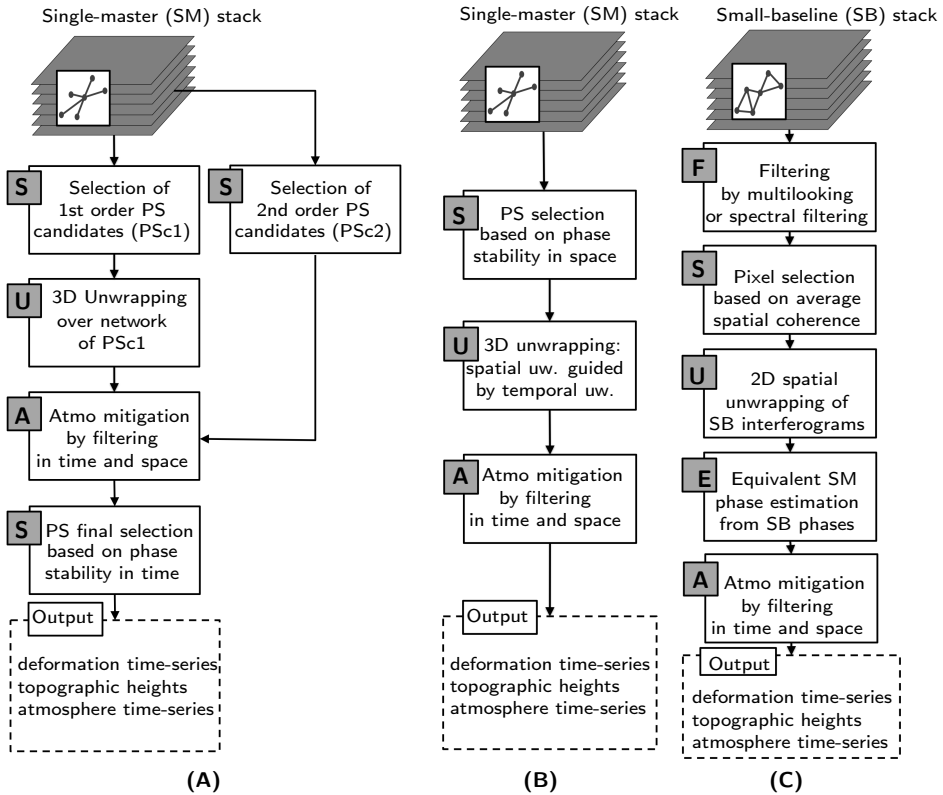


Figure 2.8: Generic flowchart of (A) PSI processing (1st category) (B) PSI processing (2nd category), and (C) SBAS method. The steps are classified into five basic TInSAR processing blocks (expressed in the gray boxes) as **S**: pixel selection, **U**: unwrapping, **A**: atmospheric-signal mitigation, **F**: filtering, and **E**: ESM-phase estimation from multi-master phases. Processing-blocks **F** and **E** is specific to distributed scatterers and are hence applied only in SBAS processing. Note that the abbreviation *uw.* refers to unwrapping.

The main idea of the first category (e.g. Ferretti et al. (2000), and Kampes (2005)) is to detect highly coherent point-like PS by using amplitude stability in time as an indicator for scattering phase variability. Pixels whose amplitudes variation is small in the stack of SLC images are selected as candidates for coherent PS (PSc1). Then, for every PSc1 candidate, the single-master wrapped phase time-series is exploited. They are first unwrapped in the time domain, followed by integration/unwrapping in space per epoch. In combination with this 3D unwrapping, different signal components, i.e. deformation, topography, and atmospheric effects, are effectively estimated/separated. Although in principle the 3D unwrapping and signal separation can be performed for all pixels in one step, in order to reduce computational burden, this is usually done in an iterative manner as follows. First a network/grid of higher coherence PS-candidates distributed over the scene is selected. They are then unwrapped with respect to each other in time and space. For these pixels, the atmosphere signal is estimated relative to the other phase components based on spatial correlation and temporal decorrelation properties. The estimated atmospheric signal is then spatially interpolated and subtracted from

the wrapped phase time-series of the rest of the PS-candidates (PSc2). Finally, all the PSc1 and PSc2 pixels are unwrapped in space and time. The final selection of PS is performed based on the deviation of the unwrapped deformation time-series of each pixel from a pre-defined/assumed deformation model. The final results of the PSI technique for deformation monitoring, after removing the atmospheric effects, are time-series of deformation, and the derived products such as deformation rate (velocity) and height of each PS. Fig. 2.8A shows the generic flowchart of the explained category, highlighting the three main basic PSI processing blocks. More details about this category of algorithms can be found in Ferretti et al. (2000, 2001); Adam et al. (2003); Kampes (2005); Costantini et al. (2009) and van Leijen (2014).

The second category of PSI methods (e.g. Hooper et al. (2004)) uses the phase stability with respect to predefined model in space to select PS-pixels. Here, pixel candidates are selected if their interferometric phases have a small deviation from their neighboring PS. After selection of PS, 3D unwrapping is performed, followed by mitigation of atmospheric signal using high-pass filtering in time and low-pass filtering in space. The generic flowchart of this algorithm is sketched in fig. 2.8B. A comprehensive review of different PSI methodologies has been given by Crosetto et al. (2016).

2.2.2.2 Small Baseline Subset (SBAS) Technique

Parallel to the developments in PSI methodologies, other techniques emerged with the objective of extracting information from distributed scatterers. As DS-pixels are affected by temporal and baseline decorrelation, they may contain coherent information only in interferograms with small perpendicular and temporal baselines. Therefore, unlike for PS, a single master stack cannot be utilized for DS. A leading approach to extract information from DS was developed using the concept of small baseline subsets (SBAS). The original SBAS approach (presented by Berardino et al. (2002)) mainly accounted for minimizing the baseline decorrelation by disregarding interferograms with large perpendicular baselines and using subsets of interferometric pairs with only small baselines, see fig. 2.7B. However, in principle, other baseline configurations with small temporal-/Doppler baselines can be also utilized, reducing the effect of temporal or Doppler-centroid decorrelation. Note that the constraint on baseline length may yield a clustered baseline configuration with disconnected interferogram subsets.

In this method, all selected interferograms are first filtered (spectral filtering or/and multilooking) in order to further reduce the decorrelation noise. Applying the filtering step is one of the main differences of SBAS compared to PSI. As mentioned before, spectral filtering or multilooking is not recommended over PS-pixels. After filtering, coherent pixels are identified based on their average spatial coherence over the interferogram subset. Then the phases of the selected pixels in all the small baseline (SB) interferograms are unwrapped in spatial domain (using conventional 2D unwrapping methodologies, see sec. 2.1.3). In order to estimate the final time-series for each pixel, the unwrapped interferograms are inverted to a single-master time-series. We call this step *equivalent single master or ESM-phase estimation*. Different estimation strategies can be used here even to account for disconnected baseline configurations, see sec. 2.5.1. After ESM-phase

estimation, different signals can be separated and atmospheric effects are filtered out similar to PSI methods. Fig. 2.8C shows the generic flowchart of the SBAS methodology. Note that in addition to the three basic processing blocks of PSI, SBAS method includes two additional blocks: *phase filtering* and *ESM-phase estimation*. More information on the SBAS methodology and different SBAS implementations can be found in Berardino et al. (2002); Mora et al. (2003); Schmidt and Bürgmann (2003); Berardino et al. (2004); Pepe and Lanari (2006); Pepe et al. (2011), and Pepe et al. (2015).

It should be noted that although we have presented PS- and DS-pixels with two distinct definitions, in practice the scattering characteristics of real targets are somewhere between them. As a consequence, the set of pixels detected by PSI may overlap with the pixels detected by SBAS. For example, very bright and coherent PS-pixels which show high spatial coherence may be detected by SBAS approach. Or, highly coherent DS-pixels in rocky or desert areas may be detected also by PSI methods, especially in SAR stacks with relatively small perpendicular baselines. This is in fact the case for most of the new satellite SAR missions, e.g. Sentinel-1 or TerraSAR-X, with narrower orbital tubes compared to the earlier satellites. However, the final phase values of the common pixels, extracted by SBAS and PSI methods, are different mainly because of the effect of different kind of phase filtering applied by these methods.

In general, because the two different groups of methodologies, i.e. PSI and SBAS, have been developed for two different types of targets, they are largely complementary to each other. This is the idea behind the third group of methodologies, which we call *hybrid methods*,

2.2.2.3 Hybrid methods

Hybrid methods intend to extract information by joint processing of both PS and DS targets. The concept behind hybrid methods can be seen from two different perspectives: either extending SBAS methodology by integrating phase information of single-look (un-filtered) PS-pixels into multi-baseline filtered interferograms, or extending PSI methodology by embedding filtered multi-baseline DS into single-master stacks. Here we briefly discuss the generic concept of three examples of hybrid methodologies.

1. Extended SBAS method combining multilooked and single-look interferograms (Lanari et al., 2004)

This algorithm extends the functionality of the conventional SBAS approach by stepwise processing of two distinct SB subsets of interferograms: a filtered (multilooked) subset, and a single-look full-resolution subset. First, the multilooked SB interferograms are processed using the conventional SBAS method in order to estimate wide scale deformation, topographic, and atmospheric signal. Then, in a second step, the phases of multilooked interferograms are subtracted from single-look pixels, resulting in residual phases for all pixels, see fig. 2.9. Highly coherent pixels are selected based on their temporal residual-phase stability (similar to final detection in PSI processing), followed by estimation of the temporal evolution of local deformation and topographic signals for the selected full-resolution pixels. The overall algorithm of this method is shown in

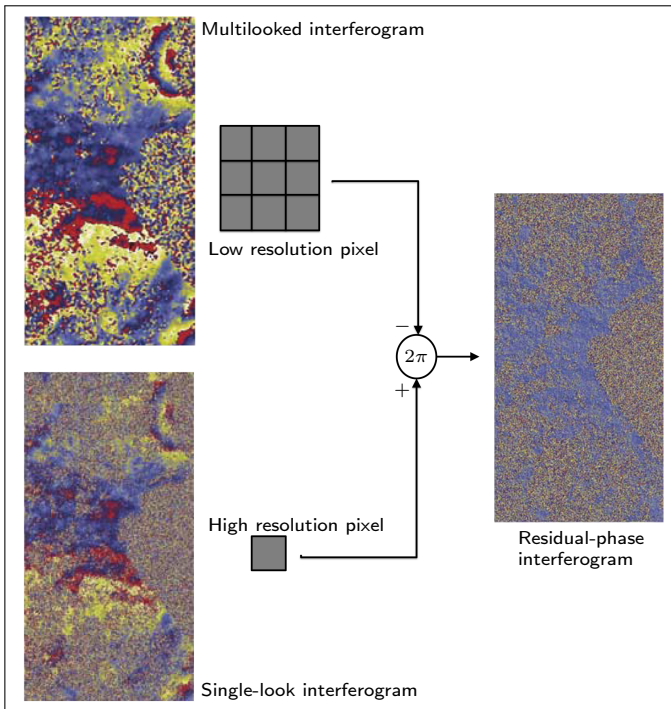


Figure 2.9: Example of coupling multilooked and single-look interferograms by (modulo 2π) subtraction. This coupling is performed in the extended SBAS methodology presented by Lanari et al. (2004). Figure adopted from the same paper.

fig. 2.10. It should be noted that although in the explanation of this method, the term "PS" is not explicitly mentioned, the detected full-resolution (single-look) pixels are implicitly equivalent to PS-pixels (i.e. pixels that preserve coherence in all interferograms without filtering and multilooking), and are mainly associated with buildings, structures, and rocks (Lanari et al., 2004).

2. Multi-temporal InSAR method incorporating both PSI and SBAS approach (Hooper, 2008)

Similar to the extended SBAS approach, this method also exploits two different sets of interferograms. One is the set of single-master and single-look interferograms, and the other the SB subset of spectral-filtered interferograms. At the first step, coherent DS- and PS-pixels are selected using the phase stability criterion in space (similar to the PSI method of Hooper et al. (2004)) over filtered SB and single-look interferograms, respectively. Then for PS-pixels, the equivalent SB phases are computed from single-master (un-filtered) interferogram phases. The SB phase of both PS and DS pixels are then combined in the same (SB) dataset. In the final step, the reconstructed dataset (including both PS and DS phases) is processed using a conventional SBAS algorithm. The flowchart of this algorithm is depicted in fig. 2.11.

3. Two-step hybrid methodology (Monti-Guarnieri and Tebaldini (2008) and SqueeSAR (Ferretti et al., 2011b))

The other development in time-series InSAR methodologies is the advent of more advanced hybrid methods that have been designed to extract all the information in SAR stacks by not only exploiting the limited set of SBAS interferograms, but processing all the possible interferograms (Monti-Guarnieri and Tebaldini, 2008; Ferretti et al., 2011b).

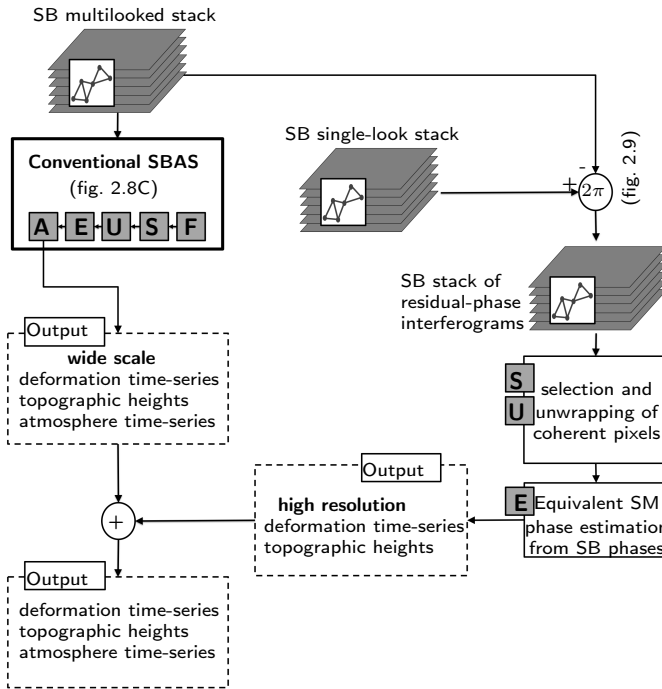


Figure 2.10: Generic flowchart of the extended SBAS methodology combining multilooked and single-look interferograms (Lanari et al., 2004). The processing steps are classified into the five basic TInSAR processing blocks (expressed in the gray boxes) as **S**: pixel selection, **U**: unwrapping, **A**: atmospheric-signal mitigation, **F**: filtering, and **E**: ESM-phase estimation.

In the first step, all possible combinations of interferograms (i.e., $N(N-1)/2$ interferograms derived from N acquisitions) are multilooked in an adaptive manner in order not to filter PS pixels (for more information on adaptive multilooking, see sec. 2.4). Then, all the multilooked interferograms are used to estimate the ESM *wrapped* phase time-series for each pixel. This step is similar ESM-phase estimation in SBAS methodology, however it is applied now before phase unwrapping. This pre-unwrapping ESM-phase estimation is called *phase linking* by Monti-Guarnieri and Tebaldini (2008) or *phase triangulation* by Ferretti et al. (2011b). In the view of these methods, the entire information content of a SAR stack is *squeezed* into a set of SM interferograms, hence the name *SqueeSAR*. After ESM-phase estimation, all the estimated SM interferograms may be processed using other standard PSI methodologies for unwrapping and estimation of the parameters of interest. The flowchart of this algorithm is depicted in fig. 2.12.

2.3 TInSAR processing steps

As discussed in the previous section, all TInSAR methodologies include steps which can be broadly classified into five basic processing blocks: pixel selection, 2D/3D unwrapping, atmospheric-signal mitigation, filtering, and ESM-phase estimation. From these

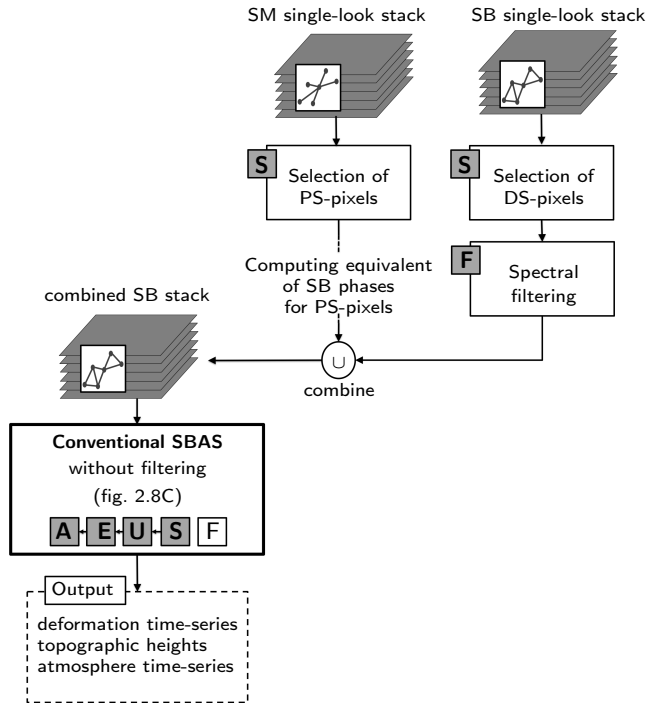


Figure 2.11: Generic flowchart of multi-temporal InSAR method incorporating both persistent scatterers and the small baseline approach (Hooper, 2008). The processing steps are classified into the five basic TInSAR processing blocks (expressed in the gray boxes) as **S**: pixel selection, **U**: unwrapping, **A**: atmospheric-signal mitigation, **F**: filtering, and **I**: ESM-phase estimation.

five processing blocks, ESM-phase estimation and filtering (or adaptive multilooking) are applied only in multi-master methodologies and they are specific processing steps for information extraction from DS-pixels. Therefore, they deserve special attention in this study and will be discussed separately in sections 2.4 and 2.5. In this section, we review the first three processing blocks, i.e. pixel selection, 2D/3D unwrapping, and atmospheric-signal mitigation, in more details.

2.3.1 Pixel selection

PS-pixel selection

For PS-pixels, the common selection criterion is the degree of fit between the phase variation of pixels in time and a pre-defined temporal model (Ferretti et al., 2001). However, the observed wrapped interferometric phases cannot be used directly to identify these stable points due to the juxtaposition of different phase contributions. As a consequence most of the PSI methodologies detect the coherent pixels in two steps. First the temporal amplitude stability is used as a proxy of phase stability. And then, in the following steps, after phase-unwrapping and atmospheric mitigation, the final selection is applied based on the phase stability criterion. In the initial selection, the

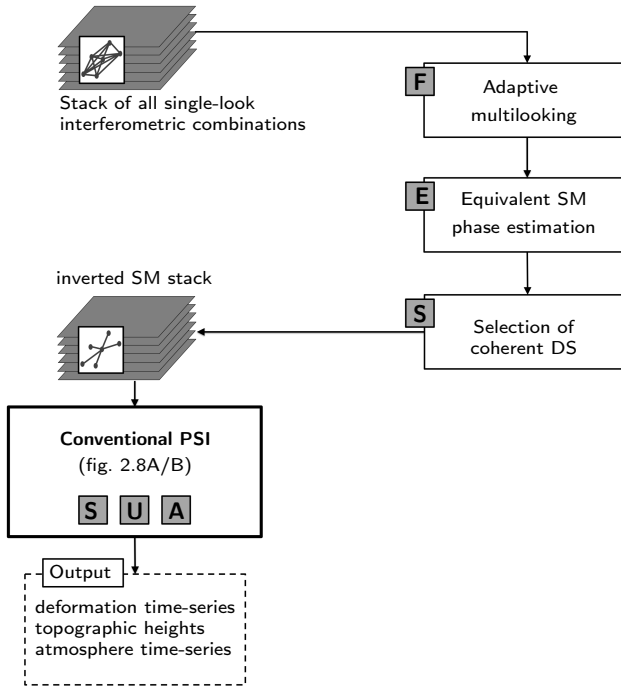


Figure 2.12: Generic flowchart of the *SqueeSAR* hybrid methodology (Ferretti et al., 2011b). The processing steps are classified into the five basic TInSAR processing blocks (expressed in the gray boxes) as **S**: pixel selection, **U**: unwrapping, **A**: atmospheric-signal mitigation, **F**: filtering, and **E**: ESM-phase estimation.

logic behind the approximation of phase stability by amplitude stability can be explained by considering the phasor of PS-pixels (see fig. 2.13). Assume that the complex SAR observation for PS-pixels can be decomposed into two components as

- s (*signal*): the constant (and hence deterministic) contribution of a point scatterer within a resolution cell, and
- n (*noise*): the noise component which is the superposition of contributions from all other elementary scatterers that influence that particular pixel.

Assuming n has circular complex Gaussian distribution⁴, Ferretti et al. (2001) introduced the normalized amplitude dispersion index (D_A) as an approximation of phase standard deviation (σ_ψ):

$$D_A = \frac{\sigma_A}{\mu_A} = \frac{\sigma_n}{\mu_A} = \tan(\sigma_\psi) \approx \sigma_\psi, \quad (2.24)$$

where μ_A is the mean amplitude for the considered pixel over time, and σ_A and σ_n the standard deviations of amplitude and noise, respectively ($\sigma_A = \sigma_n$ due to the assumption

⁴See sec. 3.2 for detailed explanation of circular complex Gaussian distribution, and its validity for the clutter noise.

of circular Gaussian distribution). Note that the approximation $\tan(\sigma_\psi) \approx \sigma_\psi$ is valid only for pixels with high signal to noise ratio, i.e. the pixels either with high amplitude or with very low noise. Fig. 2.14 shows the relation between σ_ϕ and D_A based on simulation of 3000 points in the stack of 50 SAR images. The signal was fixed to $s=1$, while the noise component n was simulated 3000 times with standard deviation (of the real and imaginary parts) randomly chosen between 0 and 0.8. We see that points with smaller amplitude dispersion index have smaller phase standard deviation. Thus, a threshold on D_A can be used as a practical way to select PS with stable phase behavior.

Other amplitude-based approaches are also introduced in literature, for example thresholding on amplitude directly (Kampes and Adam, 2004), or the *signal-to-clutter ratio* (Adam et al., 2004). Note that, the normalized amplitude dispersion is, in principle, equivalent to the signal-to-clutter ratio, but in the latter, the clutter is estimated elsewhere in space instead of time. All these amplitude-based selection methods work properly for very bright pixels, and are therefore effective in urban areas with many bright reflections from buildings and infrastructure. Furthermore, in order to use amplitude-based methods, SAR amplitude calibration should be performed prior to PS selection, to avoid amplitude variations due to sensor characteristics and viewing geometry. Different calibration methods can be used as described in Laur et al. (2002), and Ketelaar et al. (2005).

It should be noted that amplitude-based selection is applied usually for initial (a-priori) selection of PS-pixels. In some PSI methodologies (i.e. in the first category of PSI methodologies, see sec. 2.2.2.1 and fig. 2.8A), a-posteriori selection is also performed, to detect reliable pixels among all initially selected PS-candidates. Various selection criteria exist, some of which analyze the spatio-temporal consistency of the final unwrapped time-series with respect to the surrounding PS (Hooper et al., 2004), while others use the deviation of the time-series from a predefined deformation model as criterion for final selection (Ferretti et al., 2001). The most common indicator is the *ensemble coherence*⁵ which is defined as:

$$\hat{\gamma}_{\text{ens}} = \frac{1}{N} \left| \sum_{i=1}^N \exp \left(j \left(\hat{\phi}_i - \phi_i^{\text{model}} \right) \right) \right| \quad (2.25)$$

where N is the number of interferograms, $\hat{\phi}_i$ the unwrapped interferometric phase in the i th interferogram after unwrapping and atmospheric-signal mitigation, and ϕ_i^{model} is the estimated phase time-series based on a pre-assumed model. PS-pixels are identified by thresholding on γ_{ens} . There are other indicators also for final selection, such as spatio-temporal consistency (Hanssen et al., 2008), and variance factor (Kampes and Hanssen, 2004; Kampes and Adam, 2006). A comprehensive review on a-posteriori PS selection methods can be found in van Leijen (2014) and Crosetto et al. (2016).

An alternative approach for PS-selection is presented by Hooper et al. (2004, 2007) and is used in the second category of PSI methodologies (see sec. 2.2.2.1 and fig. 2.8B). This method directly analyses phase values. For each pixel, the phase contribution of spatially correlated signals (i.e., atmosphere, deformation, and orbital errors) are estimated by band-pass filtering the surrounding PS-pixel. The spatially uncorrelated signals, e.g

⁵For analytical definition of coherence parameter, see sec. 3.2.2

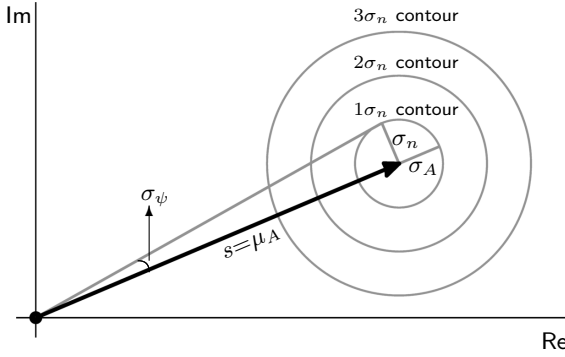


Figure 2.13: Phasor for a PS-pixel in an SLC image: s (*signal*) is the deterministic contribution of a point scatterer within a resolution cell, and σ_n the standard deviation of the noise component induced by the contribution of all other elementary scatterers. Assuming noise with circular complex Gaussian distribution (whose 1-3 σ contours has been plotted) and for small σ_ψ , we have: $\tan(\sigma_\psi) = \sigma_n / \mu_A = \sigma_A / \mu_A$. This ratio is defined as amplitude dispersion. For large amplitudes (i.e. bright point scatterers) or low noise, we have $\tan(\sigma_\psi) \approx \sigma_\psi$, and so the normalized amplitude dispersion can be used as an indicator for the phase standard deviation.

due to topographic variations, are estimated based the correlation with perpendicular baselines. Subtraction of both the estimated spatially correlated and uncorrelated signals yields a time-series of residuals for a pixel. These residuals can be interpreted as estimates of decorrelation noise for a pixel in every interferogram. In order to combine the residuals in one scalar measure, an equivalent spatio-temporal coherence (γ_{st}) is introduced as (similar to ensemble coherence)

$$\hat{\gamma}_{st} = \frac{1}{N} \left| \sum_{i=1}^N \exp \left(j \left(\phi_i - \hat{\phi}_i^{sc} - \hat{\phi}_i^{topo} \right) \right) \right| \quad (2.26)$$

where N is the number of interferograms, ϕ_i the interferometric phase in the i th interferogram, and $\hat{\phi}_i^{sc}$ and $\hat{\phi}_i^{topo}$ the estimates of spatially correlated and uncorrelated (mainly topographic) phase, respectively. PS-pixels are identified by thresholding on γ_{st} . Note that in order to estimate spatially correlated signal based on surrounding PS-pixels, the location of adjacent PS-pixels should be known beforehand. To solve this problem, Hooper et al. (2004) proposed an iterative algorithm initialized by selection of adjacent PS-pixels based on amplitude dispersion index.

DS-pixel selection

For methodologies which focus on distributed scatterers, often the estimate of spatial coherence is used to select coherent DS-pixels (Touzi et al., 1999). Assuming an interferogram constructed from master P_M and slave images P_S , the spatial coherence for a pixel k is estimated as

$$\hat{\gamma}_k = \frac{\sum_{i \in \Omega} P_{M,i} P_{S,i}^*}{\sqrt{\left(\sum_{i \in \Omega} |P_{M,i}|^2 \right) \left(\sum_{i \in \Omega} |P_{S,i}|^2 \right)}}, \quad (2.27)$$

where Ω is the set of surrounding/adjacent pixels. Ω can be selected as a square window around the pixel, or as adjacent pixels with similar scattering mechanism as pixel k (see

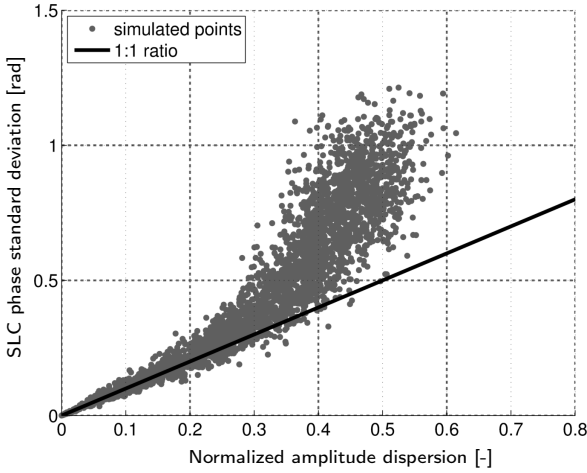


Figure 2.14: Simulated scatter plot of the relation between amplitude dispersion and phase standard deviation (Ferretti et al., 2001). A complex variable $z = s + n$ is simulated for 3000 points in the stack of 50 SAR images. The signal was fixed to $s=1$, while the noise component n was simulated 3000 times with a standard deviation of the real and imaginary parts randomly chosen between 0 and 0.8. The plot shows that small values of the normalized amplitude dispersion are good estimates of the phase standard deviation.

sec. 2.4 for more information on selection of similar adjacent pixels). In a stack of interferograms, the stability of spatial coherence in time (or in stack of interferograms) is used for the selection of coherent DS-pixels.

An alternative approach has been proposed by Hooper (2008) to select DS pixels. This approach is the same as the PS-selection method of Hooper et al. (2004) based on spatial phase consistency, however it uses SB filtered interferograms instead of a single-master and single-look stack. Furthermore, for the initial selection of DS-pixels (in order to initiate the selection or to reduce computational burden), Hooper (2008) introduced a new amplitude-based indicator, called *amplitude difference dispersion* which is defined as

$$D_{\Delta A} = \frac{\sigma_{\Delta A}}{\mu_A}, \quad (2.28)$$

where μ_A is the mean amplitude, and $\sigma_{\Delta A}$ the standard deviation of amplitude *differences* between master images and slave images. Compared to the normalized amplitude dispersion (see eq. (2.24)), $D_{\Delta A}$ is better approximation of phase stability if spectral filtering has been applied on interferograms (for more information see auxiliary materials of Hooper (2008)).

In multi-baseline methodologies which include the ESM-phase estimation, a-posteriori selection of DS-pixels is also performed based on the evaluation of residuals of the estimation. For example, in the SqueeSAR (Ferretti et al., 2011b), the an ensemble coherence estimator is introduced for assessing the quality of ESM-phase estimation and selecting reliable DS-pixels. See sec. 2.5 for more information on ESM-phase estimation methodologies.

2.3.2 Spatio-temporal unwrapping

One of the most crucial processing blocks in TInSAR methodologies is the phase unwrapping. It is crucial because the problem is inherently ill-posed and non-unique, see sec. 2.1.3 . As a consequence, a-priori information or assumptions about the signals of

interest should be introduced in order to solve the unwrapping problem. Some methods assume a pre-defined kinematic behavior in time, and so they solve the problem primarily in the time domain (i.e., 1D unwrapping), while other methods assume a predefined spatial deformation behavior and solve the problem mainly in the spatial domain.⁶

The most common unwrapping approach in PSI methodologies (Ferretti et al., 2000, 2001; Adam et al., 2003; Kampes, 2005; van Leijen, 2014) uses assumptions on the relative deformation behavior of nearby PS-pixels (or arcs) in time, and so defines the problem mainly in time domain. The advantage of using relative phases between two nearby pixels (i.e. arc phases) is that the contribution of atmospheric and orbital errors will be then minimal due to their high spatial correlation. In this method, phase time-series per arc are unwrapped relative to the assumed pre-defined temporal kinematic model (usually a constant velocity model is used, but in principle other models such as periodic models or higher order polynomials can be also assumed) by simultaneously estimating model parameters and relative topographic phase. After the temporal unwrapping of all the arcs, temporally unwrapped phases are integrated spatially per interferogram in order to obtain final unwrapped time-series with respect to a common reference point. Various algorithms exist for arc-based temporal unwrapping. A comprehensive overview is given by van Leijen (2014), and different approaches can be found in Ferretti et al. (2001); Hooper et al. (2004); Kampes and Hanssen (2004), and Cuenca et al. (2011).

Another unwrapping method, mainly used in the second category of PSI methodologies (see sec. 2.2.2.1 and fig. 2.8B), applies unwrapping in both time and space. The main strategy is to unwrap every interferogram spatially by the *minimum cost flow* (MCF) approach (Chen, 2001). However, before spatial unwrapping by MCF, all the arc phases are first unwrapped in time (assuming no phase jump larger than π between two adjacent acquisitions), and then the unwrapped phases are used to assign, per arc, the parameters of the cost function required by MCF method. In other words, the output of the 1D temporal unwrapping is used to guide the 2D unwrapping in space, and so this method sometimes is called 1D+2D unwrapping. More information can be found in Hooper (2006), and Hooper (2010).

For SBAS methodologies, unwrapping is mainly applied in the spatial domain per SB interferogram, followed by ESM-phase estimation from unwrapped interferometric phases for each detected pixel. For an overall discussion on different 2D unwrapping methods, see sec. 2.1.3. In addition to all the aforementioned unwrapping methods, full 3D methodologies (Hooper and Zebker, 2007; Pepe and Lanari, 2006) have been also introduced. More advanced formulations of phase unwrapping have been presented by Shanker (2006); Shanker and Zebker (2010) and Costantini et al. (2012), providing a possibility to easily insert a-priori knowledge (e.g., information about the locations of phase discontinuities) into the unwrapping mathematical model in order to improve unwrapping over challenging data sets, for example in areas with a sparse grid of coherent

⁶It should be noted that whatever method is used (1D or 2D), the ambiguities (i.e. the unknown integer number of phase cycles) always, and in all unwrapping methods, are estimated for phase differences in time and space or, in other words, double difference phases. Hence unwrapping is essentially always performed in 3D, in both space and time. From this perspective the popular terminologies such as "1D unwrapping" or "2D unwrapping" may be misleading.

pixels and complicated deformation patterns.

It should be noted that the result of spatio-temporal unwrapping, is the unwrapped time-series per selected pixel with respect to a reference point in space. The choice of reference point is arbitrary, because the relative accuracy between points does not depend on the reference choice. However, for interpretation, it is more convenient to choose the reference point (or reference area) at stable locations that are assumed to be not affected by any deformation. As a consequence, the final results of TInSAR are always relative to the chosen reference. For absolute interpretation, the deformation time-series have to be connected to an external datum, see, e.g., Mahapatra et al. (2015).

2.3.3 Atmospheric-signal mitigation

The atmospheric signal of one interferogram is usually called the *atmospheric phase screen* (APS) in InSAR literature (Ferretti et al., 2001). The goal of atmospheric-signal mitigation is to estimate and subsequently filter out the APS for all the interferograms in an InSAR stack.

Generally speaking, atmospheric-signal mitigation is an optional step in TInSAR methodologies. While some methodologies (Kampes and Adam, 2006) maintain atmospheric signal in the final time-series and do not remove it, other methods (Ferretti et al., 2000; van Leijen, 2014) estimate and remove the APS from the final results and provide atmospheric time-series as additional by-product of TInSAR. Some methodologies, cf. Hooper et al. (2004) and Hooper (2008), filter out the atmospheric signal in the processing chain just in order to facilitate the unwrapping step, but after unwrapping add it back to the time-series and provide the final results containing atmospheric signal.

APS estimation is always done using a set of unwrapped data and some assumptions on the spatio-temporal characteristics of different signal components, mainly deformation and atmosphere. The most common approach is presented in Ferretti et al. (2000) and later adopted by Berardino et al. (2002); Mora et al. (2003); van Leijen (2014). Once the unwrapped phases are obtained for the set of coherent pixels (for example 1st order PS candidates), atmospheric delay phases can be filtered out. Topographic phase and modeled deformation (e.g., constant velocity) are estimated and subtracted from the time-series, resulting in residual phases including atmospheric signal, unmodeled deformation, orbit errors, and noise. In the filtering step, the contribution of atmosphere (and orbits) is separated from the unmodeled deformation using a high-pass filter on the residual phases per point time-series. This is based on the assumption that the atmospheric signal is uncorrelated in time, whereas the unmodeled deformation is temporally correlated. The result of the high-pass filter is a residual phase time-series containing atmospheric and orbital errors plus noise. Then, the APS for the whole scene per interferogram is estimated using an interpolation method such as Kriging, accounting for spatial correlation of the atmospheric signal by modeling the spatial dependency via a covariance function. This interpolation acts as a low pass filter in the spatial domain. As atmospheric signal is spatially correlated (in contrast to noise which has no spatial correlation), Kriging with nugget filtering is used to simultaneously interpolate and also

exclude the noise effect. The accuracy of the obtained APS mainly depends on the number of images and the density of the detected PS/DS-pixels (Liu, 2012).

Temporally uncorrelated atmosphere is the the key assumption in most atmospheric-signal mitigation methodologies. However, this assumption only holds for the turbulent-mixing component of the atmospheric signal, see sec. 2.1.2.2. In contrast, the vertical stratification component may show some degree of seasonal correlation. Taking advantage of strong correlation between vertical stratification and topography, some methodologies (Ferretti et al., 2005; Samiei-Esfahany et al., 2008; Liu, 2012) have been proposed to estimate vertical stratification as an additional parameter per interferogram using a known topographic model (DEM).

Note that generally for atmospheric-signal mitigation, not only assumptions on the spatio-temporal variability of APS are required, but also some a-priori information about the deformation signal (which is sometimes not available a-priori). This is important, because deformation is the main signal of interest in most of the TInSAR applications. Therefore, the potential over/under-estimation or over/under-smoothing of deformation time-series due to wrong assumptions on deformation signal in atmospheric-signal mitigation step is not desired. This is the main reason behind the idea of keeping (not removing) the atmospheric-signal in the final time-series in some methodologies and instead explaining the APS effect in a stochastic manner in the quality description of the results. Liu (2012) introduced an iterative algorithm in order to jointly estimate different signal components and also estimate the stochastic parameters of both deformation and atmospheric signals using variance component estimation.

In addition to methodologies which are based on estimating and filtering the atmospheric-signal, it is also possible to mitigate this signal using ancillary data. Examples of using meteorological data, optical remote sensing, and GPS measurements to evaluate InSAR atmospheric-signal can be found in Delacourt et al. (1998); Hanssen et al. (1998); Williams et al. (1998); Beauducel et al. (2000); van der Hoeven et al. (2002); Li et al. (2004, 2005, 2006b,a); Onn and Zebker (2006). The limitations of most of these methods is their limited coverage due to, e.g. obstruction by clouds, or their lower resolution compared to InSAR data. Recent developments in numerical weather modeling have provided a new source of auxiliary information for InSAR atmospheric-signal mitigation (Wadge et al., 2002; Webley et al., 2002; Foster et al., 2006; Puysségur et al., 2007; Rommen et al., 2009; Nico et al., 2011; Hobiger et al., 2010; Jolivet et al., 2011; Liu et al., 2011; Cimini et al., 2012). Comprehensive validation of APS estimates provided by numerical weather models (NWMs) shows effective APS signal estimation in mountainous regions, and hence good estimation of vertical stratification (Liu, 2012). Regarding turbulent mixing, the validation study showed that NWMs constantly underestimate the atmospheric delay variations, and are therefore not capable of providing an accurate and reliable APS prediction.

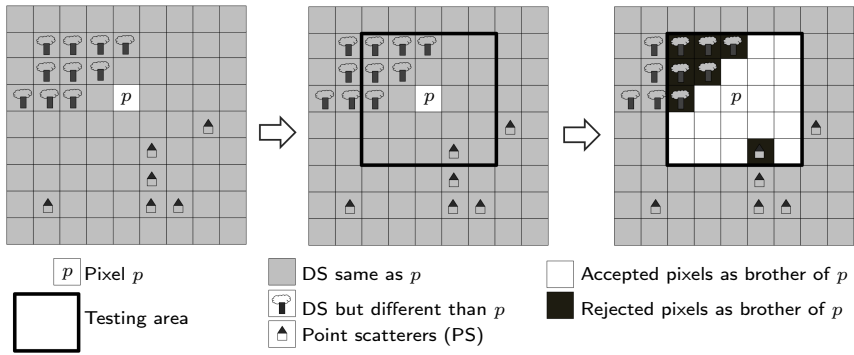


Figure 2.15: Schematic representation of the brotherhood selection algorithm for an arbitrary pixel p . A testing area is defined around p . Then all the pixels within the testing area are tested to see they have the same statistics as p . The pixels which pass the test are accepted as brothers of p and shape the averaging area used in multilooking.

2.4 Filtering: adaptive multilooking for distributed scatterers

The objective of filtering in TInSAR methodologies is to enhance the SNR of the observations by reducing decorrelation. As a consequence only TInSAR methodologies which exploit DS (e.g. SBAS and hybrid methodologies) incorporate a filtering step. Filtering approaches are either based on spectral filtering or spatial complex multilooking. Overview and details of both spectral filtering and complex multilooking were discussed in the sec. 2.1.3. Recent advances in multilooking are e.g. *adaptive multilooking* (Ferretti et al., 2011b). As discussed in sec. 2.1.3, complex multilooking is applied by spatial averaging over pixels that are assumed to be statistically homogeneous. In adaptive multilooking, a homogeneous area around each pixel is identified using a testing strategy. There are various testing strategies available for identification of statistically homogeneous pixels (SHP). Because adaptive multilooking is a crucial step for DS-pixels, we review the concept of adaptive multilooking and the details of different testing strategies in the following.

The idea of adaptive multilooking is to identify and use a representative and homogeneous estimation area (labeled *brotherhood* by Ferretti et al. (2011b)) around each pixel in spatial averaging. Adaptive multilooking is a common practice in amplitude-based SAR remote sensing and in polarimetric applications with the purpose of improving image quality without losing spatial details. For example, for application to only one interferogram, there are different space-adaptive filters introduced in literature (Lee et al., 2003; Deledalle et al., 2011; Vasile et al., 2004, 2006). Applying these methods on a stack of images may result in a different estimation window for each pixel in different interferograms, and therefore inconsistent multilooking.

New methods have been introduced in order to select homogeneous brotherhood area in a stack of images (Ferretti et al., 2011b; Parizzi and Brcic, 2011; Jiang et al., 2014b,a). Fig. 2.15 shows a schematic representation of a brotherhood selection algorithm for an arbitrary pixel p . First, a testing area is defined around p . All the pixels within the testing

area are tested to see whether they have the same amplitude statistics as p . The pixels which passed the test are accepted as brothers of p and collectively shape the averaging area used in multilooking. A brother pixel is identified by statistical hypothesis testing of the null hypothesis that the two pixels are a realization of the same stochastic process, against the alternative hypothesis that the pixels have different statistics. Different kind of parametric or non-parametric testing strategies exist for such a brotherhood selection. In this section we review some of these strategies.

2.4.1 Non-parametric tests for brotherhood selection

Non-parametric approaches for brotherhood selection are based on testing two data samples without any assumption on their probability distribution, such as the Kullback-Leibler divergence test (Bishop, 2006), the two sample Kolmogorov-Smirnov (KS) test (Stephens, 1970), and the Anderson-Darling (AD) test (Pettitt, 1976). Here, we discuss the latter two of these tests (i.e. KS and AD) which are applied most commonly in InSAR processing.

Two-sample Kolmogorov-Smirnov test

The Two-sample Kolmogorov-Smirnov (KS) test is a form of non-parametric test which tests the equality of the probability distributions of two data samples (i.e., the null hypothesis is that two samples have the same distribution) (Stephens, 1970; Press et al., 1989; Papoulis, 1991; Kvam and Vidakovic, 2007). This test has been proposed for InSAR adaptive multilooking by Ferretti et al. (2011b). If A_p and A_q are the amplitudes of pixels p and q , respectively, the null and alternative hypotheses are defined as:

$$H_0 : F_{\underline{A}_p}(A) = F_{\underline{A}_q}(A), \quad H_a : F_{\underline{A}_p}(A) \neq F_{\underline{A}_q}(A), \quad (2.29)$$

where $F_{\underline{\cdot}}(\cdot)$ is the *cumulative distribution function* (CDF). Assuming strict stationarity, in a stack of N images, the *empirical CDF* (ECDF) of the amplitude of pixel A_p can be computed over the range of amplitudes A as

$$\hat{F}_{\underline{A}_p}(A) = \frac{1}{N} \sum_{i=1}^N I_{A_p, i \leq A} \quad (2.30)$$

where $I_{A_p, i \leq A}$ is the indicator function, equal to 1 if $I_{A_p, i \leq A}$ and equal to 0 otherwise. The KS test statistic is defined as the maximum distance between the empirical distribution functions of the two samples. For two samples A_p and A_q with ECDF of $\hat{F}_{\underline{A}_p}(A)$ and $\hat{F}_{\underline{A}_q}(A)$, the KS test statistic is defined as:

$$T_{\text{ks}} = \sup_A |\hat{F}_{\underline{A}_p}(A) - \hat{F}_{\underline{A}_q}(A)| \quad (2.31)$$

where \sup_A is the supremum of the set of distances, see fig. 2.16. The distribution of test statistic T_{ks} converges to Kolmogorov distribution for $N > 8$ (Stephens, 1970). By setting a level of significance α , the null hypothesis is rejected if

$$T_{\text{ks}} > \sqrt{\frac{2}{N}} k_{\alpha}, \quad (2.32)$$

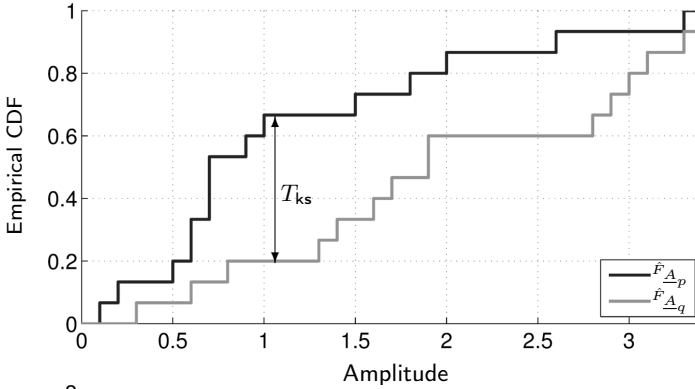


Figure 2.16: Visualization of the KS test statistic, for two pixels p and q . The maximum distance between these two lines, represented by the black arrow, is the KS test statistic T_{ks} .

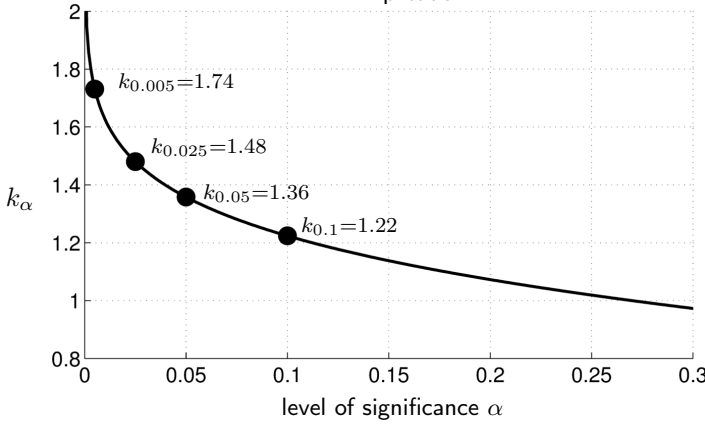


Figure 2.17: The values of α -percentile of Kolmogorov distribution (k_α) as a function of level of significance α . The values for $\alpha=0.1, 0.05, 0.025$ and 0.005 are highlighted.

where k_α is the α percentile of the Kolmogorov distribution (Stephens, 1970; Press et al., 1989; Kvam and Vidakovic, 2007). The threshold k_α is computed from the CDF of the Kolmogorov distribution in order to satisfy

$$\Pr(T_{ks} \leq k_\alpha) = 1 - \alpha. \quad (2.33)$$

where the Kolmogorov CDF is given by (Stephens, 1970):

$$\Pr(T_{ks} \leq k_\alpha) = 1 - 2 \sum_{n=1}^{\infty} (-1)^{n-1} \exp(-2n^2 k_\alpha^2). \quad (2.34)$$

Fig. 2.17 shows the values of k_α as a function of the level of significance α . In Ferretti et al. (2011b), it has been noted that the KS test is invariant under reparameterization of amplitudes, and so the same level of significance is obtained by using the KS test on amplitude, intensity, or their logarithmic units (in dB).

Anderson-Darling test

The Anderson-Darling (AD) test is another non-parametric test which applied for InSAR adaptive multilooking (Parizzi and Brcic, 2011; Wang et al., 2011; Goel and Adam, 2014). The AD test has the same null and alternative hypotheses as the KS test, see eq. (2.29). Similar to the KS test, the AD test statistic is also based on the difference

between the ECDF of two data samples (Pettitt, 1976):

$$T_{AD} = \frac{N}{2} \sum_A \frac{(\hat{F}_{\underline{A}_p}(A) - \hat{F}_{\underline{A}_q}(A))^2}{\hat{F}_{\underline{A}_{p,q}}(A)(1 - \hat{F}_{\underline{A}_{p,q}}(A))} \quad (2.35)$$

where $\hat{F}_{\underline{A}_{p,q}}(A)$ is the ECDF computed from combined dataset of two pixels p and q . The distribution of T_{AD} is more complicated than in the KS test, and there is no closed-form and exact solution for it. Detailed explanation on the approximation of the AD test statistics and how to choose a testing threshold based on level of significance can found in Pettitt (1976) and Scholz and Stephens (1987). Compared to the KS approach, the AD test gives more weight to the tails of distributions. It was demonstrated by Parizzi and Brcic (2011) that AD test has a better performance than other non-parametric tests for brotherhood selection in SAR stacks.

The main disadvantage of non-parametric tests like AD and KS is their high computational load due to computation of ECDF for each pixel. The ECDF computational load is increased by the number of images, and so can be cumbersome in large data stacks (e.g. $N > 100$). This is the main motivation to develop parametric tests with less computational burden for brotherhood selection.

2.4.2 Parametric tests for brotherhood selection

Contrary to non-parametric tests, parametric tests are designed assuming a known probability distribution function of data samples. The most common distribution for InSAR applications is the complex circular Gaussian distribution, assuming distributed scattering mechanism (Madsen, 1986; Sarabandi, 1992). The amplitude of a variable with a complex Gaussian distribution has Rayleigh distribution (Davenport and Root, 1987). Here we discuss two amplitude-based testing strategies assuming the Rayleigh distribution: testing the mean and testing the variance of amplitude.

Testing the amplitude mean

Assuming a distributed scattering mechanism with circular Gaussian distribution of variance σ_n^2 , the amplitude of SAR images has a Rayleigh distribution with probability distribution function (Papoulis, 1968; Abramowitz and Stegun, 1970)

$$f_{\underline{A}}(A) = \frac{A}{\sigma_n^2} \exp\left(-\frac{A^2}{2\sigma_n^2}\right), \quad (2.36)$$

having mean and variance

$$E\{\underline{A}\} = \mu_A = \sqrt{\frac{\pi}{2}}\sigma_n, \quad D\{\underline{A}\} = \sigma_A^2 = \frac{4 - \pi}{2}\sigma_n^2, \quad (2.37)$$

where $E\{\cdot\}$ and $D\{\cdot\}$ denote the expectation and dispersion operators, respectively. Based on this definition, the ratio between standard deviation and mean amplitude, called *coefficient of variation* (CV) (Jiang et al., 2014a), is constant:

$$CV_A = \frac{\sqrt{D\{\underline{A}\}}}{E\{\underline{A}\}} = \sqrt{\frac{4 - \pi}{\pi}} \approx 0.52. \quad (2.38)$$

If we have N SAR images, the mean amplitude \bar{A}_p for a pixel p is computed as

$$\bar{A}_p = \frac{1}{N} \sum_{i=1}^N A_{p,i}. \quad (2.39)$$

Assuming N to be a large number, according to the central limit theorem, the estimated mean \bar{A}_p has a Gaussian distribution with mean and variance

$$E\{\bar{A}_p\} = \mu_{A_p} = \sqrt{\frac{\pi}{2}} \sigma_n, \quad D\{\bar{A}_p\} = \frac{\sigma_{A_p}^2}{N} = \frac{4 - \pi}{2N} \sigma_n^2. \quad (2.40)$$

In order to test whether a pixel q is a brother of pixel p , the null and alternative hypotheses are defined as:

$$H_0 : E\{\bar{A}_q\} = \mu_{A_p}, \quad H_a : E\{\bar{A}_q\} \neq \mu_{A_p}. \quad (2.41)$$

Under the null hypothesis, the distribution of \bar{A}_q can be written as

$$\bar{A}_q \sim \mathcal{N}\left(\mu_{A_p}, \frac{\sigma_{A_p}^2}{N}\right). \quad (2.42)$$

By subtracting μ_{A_p} from \bar{A}_q and dividing by standard deviation $\sqrt{\frac{\sigma_{A_p}^2}{N}}$, the test statistic is defined as:

$$T_{\text{mean}} = \frac{(\bar{A}_q - \mu_{A_p})\sqrt{N}}{\sigma_{A_p}}, \quad (2.43)$$

where T_{mean} now has a standard normal distribution (i.e. $T_{\text{mean}} \sim \mathcal{N}(0, 1)$). Therefore the null hypothesis is rejected if

$$|T_{\text{mean}}| > k_{\alpha/2}, \quad (2.44)$$

where α is the level of significance and $k_{\alpha/2}$ the $\alpha/2$ percentile of the standard normal distribution. For the computation of T_{mean} , the values of μ_{A_p} and σ_{A_p} are required. Jiang et al. (2014a) proposed the following iterative algorithm for defining these values and selecting the brother pixels:

1. define a testing window around the pixel p ,
2. estimate μ_{A_p} as $\hat{\mu}_{A_p} = \bar{A}_p$ (see eq. (2.39)),
3. approximate σ_{A_p} as $\hat{\sigma}_{A_p} \approx 0.52\hat{\mu}_{A_p}$, (based on eq. (2.38))
4. evaluate the test statistics T_{mean} for all the pixels in the testing window (using eq. (2.43)), and select brother pixels by applying hypothesis testing (using eq. (2.44)),
5. re-estimate $\hat{\mu}_{A_p}$ by averaging the mean amplitudes of all the selected brothers, and
6. repeat steps 3 and 4 with the new estimate $\hat{\mu}_{A_p}$.

Table 2.1: Overview of testing methods for brotherhood selection in SAR stacks.

Method	Null hypothesis (H_0) Alternative hypothesis (H_a) Test statistics (T)	Properties
Kolmogorov-Smirnov (Ferretti et al., 2011b)	$H_0 : F_{A_p}^-(A) = F_{A_q}^-(A)$ $H_a : F_{A_p}^-(A) \neq F_{A_q}^-(A)$ T_{KS} : eq. (2.31)	- Non-parametric test - Not powerful for small stacks ($N < 10$) - Computationally expensive for very large stacks
Anderson-Darling (Parizzi and Brcic, 2011; Wang et al., 2011; Goel and Adam, 2014)	$H_0 : F_{A_p}^-(A) = F_{A_q}^-(A)$ $H_a : F_{A_p}^-(A) \neq F_{A_q}^-(A)$ T_{AD} : eq. (2.35)	- Non-parametric test - Not powerful for small stacks ($N < 10$) - Computationally expensive for very large stacks - Better performance than KS test - Recommended for stacks with medium size ($10 < N < 100$)
Testing the mean (Jiang et al., 2014a)	$H_0 : E\{\bar{A}_q\} = \mu_{A_p}$ $H_a : E\{\bar{A}_q\} \neq \mu_{A_p}$ T_{mean} : eq. (2.43)	- Parametric test - Assumes Rayleigh distribution - Computationally efficient even for large stacks - Valid only for large N - Recommended for large stacks ($N > 100$)
Testing the variance (Parizzi and Brcic, 2011)	$H_0 : \sigma_{A_p}^2 = \sigma_{A_q}^2$ $H_a : \sigma_{A_p}^2 \neq \sigma_{A_q}^2$ T_{var} : eq. (2.46)	- Parametric test - Assumes Rayleigh distribution - Computationally efficient even for large stacks - good performance on small stacks - Recommended for small stacks ($N < 10$)

This testing approach has lower computational complexity than non-parametric tests (e.g., KS and AD tests) because the test statistic (i.e. T_{mean} in eq. (2.43)) is only dependent on the amplitude mean and variance which can be computed faster and much more simply than the amplitude ECDF. The main assumption used in this testing approach is the Gaussianity of the test statistics which is valid only for large number of images (based on the central limit theorem). Therefore, this testing approach is recommended for large SAR stacks in which the computation of non-parametric tests is computationally expensive.

Testing the amplitude variance

Another parametric test is introduced for brotherhood selection in SAR stacks by Parizzi and Brcic (2011). Like the testing-the-mean concept, here also the Rayleigh distribution is assumed for SAR amplitudes. However, the null and alternative hypotheses are defined here based on the amplitude variance of the two pixels p and q (instead of the mean amplitude):

$$H_0 : \sigma_{A_p}^2 = \sigma_{A_q}^2, \quad H_a : \sigma_{A_p}^2 \neq \sigma_{A_q}^2. \quad (2.45)$$

Based on this formulation of hypotheses and by applying the the concept of *generalized likelihood ratio test* (GLRT) (Papoulis, 1991), the test statistic is introduced as (Parizzi and Brcic, 2011)

$$T_{\text{var}} = N \left(2 \ln(\hat{\sigma}_{A_{pq}}^2) - \ln(\hat{\sigma}_{A_p}^2) - \ln(\hat{\sigma}_{A_q}^2) \right), \quad (2.46)$$

where $\hat{\sigma}_{A_p}^2$ and $\hat{\sigma}_{A_q}^2$ are the estimated variances from the N amplitudes of pixels p and q , respectively. The variance factor $\hat{\sigma}_{A_{pq}}^2$ is the estimated variance from the pooled

amplitude samples (i.e., combined set of samples) of the two pixels and can be written as $\hat{\sigma}_{A_{pq}}^2 = (\hat{\sigma}_{A_p}^2 + \hat{\sigma}_{A_q}^2)/2$.

Based on both simulations and real case studies, Parizzi and Bricc (2011) demonstrated that for small SAR stacks (e.g. $N=10$), the *testing-the-variance* concept is more powerful than non-parametric tests. Regarding computational complexity, this testing approach, and generally parametric tests are simpler than non-parametric tests as they do not require the reconstruction of the amplitude ECDF for every pixel.

Table 2.1 summarizes all the parametric and non-parametric testing methods for brotherhood selection discussed here.

2.5 ESM-phase estimation for Distributed Scatterers

The equivalent single-master (ESM) phase estimation is another processing block performed only in TInSAR methodologies exploiting multi-master interferogram stacks. The objective is to estimate, for each detected DS-pixel, a phase time-series equivalent to a single-master stack from phase differences in a multi-master stack of interferograms. From a physical point of view, this phase estimation filters out the decorrelation noise and retrieves the (wrapped or unwrapped) phase time-series corresponding to the physical path differences between the targets and the sensor (i.e. the phase contributions of deformation, topography, atmosphere and orbital errors).

In principle this multi-master to single-master estimation can be done after unwrapping (e.g., in the SBAS method), or before unwrapping (e.g., in the SqueeSAR method), however with different estimation methodologies. This is because the functional relationship between the unknowns (i.e. SM phase time-series related to the physical path difference) and the observations (i.e. multi-master interferometric phases) is different for the unwrapped and wrapped cases. In the following the mathematical framework of post-unwrapping ESM-phase estimation is described, followed by a short review of pre-unwrapping ESM-phase estimation.

2.5.1 Post-unwrapping ESM-phase estimation

In TInSAR methodologies which apply ESM-phase estimation after unwrapping, e.g. SBAS, the expected value of every unwrapped multilooked interferometric phase ($\hat{\phi}_{-nm}^{\text{unw}}$) can be expressed as

$$E\{\hat{\phi}_{-nm}^{\text{unw}}\} = \varphi_{om}^{\text{unw}} - \varphi_{on}^{\text{unw}}. \quad (2.47)$$

where $\varphi_{om}^{\text{unw}}$ and $\varphi_{on}^{\text{unw}}$ are the true values of the single-master unwrapped interferometric phases corresponding to the physical path differences between the targets and the sensor. In a stack of N radar images, there are at most $N(N-1)/2$ interferometric combinations. For each pixel, writing eq. (2.47) for all the interferometric combinations defines a linear

system of observation equations as

$$E\left\{ \underbrace{\begin{bmatrix} \phi_{o1}^{\text{unw}} \\ \vdots \\ \phi_{o(N-1)}^{\text{unw}} \\ \vdots \\ \phi_{nm}^{\text{unw}} \\ \vdots \end{bmatrix}}_{\underline{y}} \right\} = \underbrace{\begin{bmatrix} 1 & & & & \\ & \ddots & & & \\ & & & & 1 \\ & & \vdots & & \\ & -1 & \dots & 1 & \\ & & \vdots & & \end{bmatrix}}_B \underbrace{\begin{bmatrix} \phi_{o1}^{\text{unw}} \\ \vdots \\ \phi_{o(N-1)}^{\text{unw}} \end{bmatrix}}_b, \quad (2.48)$$

where $n, m=1 \dots (N-1)$, y is the observation vector, b the vector of unknown parameters, and B the design matrix depending on the set of multi-master interferograms. This is the generic model for post-unwrapping ESM-phase estimation, originally introduced for SBAS (Berardino et al., 2002). Although the most generic case is presented here, in which all the interferometric combinations are used, the model can be written for any subset of interferograms. If M_{ifg} denotes the number used of interferograms in the SB subset (e.g. $M_{\text{ifg}}=N(N-1)/2$ in the most generic case if using all the possible interferograms), the matrix B will be an $M_{\text{ifg}} \times (N-1)$ matrix. For the set of connected interferograms, the matrix B is of full column rank and the solution of eq. (2.48) is given by least squares estimation as

$$\hat{\underline{b}} = (B^T B)^{-1} B^T \underline{y}. \quad (2.49)$$

For the cases of a disconnected network of interferograms, the matrix B has a rank deficiency and the least squares solution does not exist. In the original SBAS method (Berardino et al., 2002), a minimum norm solution based on singular value decomposition (SVD) has been proposed for ESM-phase estimation in the presence of a rank deficiency. Furthermore, a weight matrix can be introduced in the least squares solution to assign different weights to the multilooked observations, e.g. based on the coherence level of different interferograms.

As this inversion is applied after unwrapping, unwrapping errors may severely affect the solution. Hence the post-unwrapping ESM-phase estimation requires reliable phase unwrapping of every single interferogram prior to the estimation. Unwrapping errors can be seen as outliers in the estimation. In order to be less influenced by unwrapping errors (or outliers), Lauknes et al. (2011) have introduced a robust algorithm based on L_1 -norm minimization (instead of L_2 -norm least squares) for the model of eq. (2.48).

2.5.2 Pre-unwrapping ESM-phase estimation

Applying ESM-phase estimation before unwrapping has the advantage of improving the SNR ratio of the DS-pixels and hence yielding improved unwrapping. From an implementation point of view, the advantage is that the ESM-phase estimation can be applied independently of other processing steps such as unwrapping and atmosphere mitigation,

and in this way it can be simply added as an extension to other SM processing algorithms. For pre-unwrapping ESM-phase estimation, the functional relation between the observations and the unknown parameters is highly nonlinear due to the wrapping operation, and so a more advanced estimation methodology is required compared to post-unwrapping ESM-phase estimation.

There are different estimation methods in InSAR literature for pre-unwrapping ESM-phase estimation. Some solve the problem by maximum likelihood estimation based on a-priori/assumed knowledge on the statistical characteristics of DS pixels, e.g. in Monti-Guarnieri and Tebaldini (2008) and Ferretti et al. (2011b). Other methods describe the problem as a nonlinear weighted optimization in order to minimize the residuals between the observations (i.e. multilooked interferometric phase) and modeled observations (i.e. multi-baseline interferometric phases reconstructed from estimated SM phases) (Ferretti et al., 2011a; Pepe et al., 2015; Fornaro et al., 2015). In addition to these algorithms, a heuristic yet effective approach called *multi-link InSAR* has been also introduced in Pinel-Puysegur et al. (2012). The pre-unwrapping ESM-phase estimation is called *phase linking* by Monti-Guarnieri and Tebaldini (2008), as the estimated phases are results of linking or joint processing of all available interferometric phases, and the same concept is called *phase triangulation* in SqueeSAR (Ferretti et al., 2011b), as the estimation is done based on *phase consistency* (as will be described in chapter. 4).

2.6 Summary

In this chapter, we reviewed the basic concepts of InSAR and different time-series InSAR methodologies. We introduced a generic framework, consisting of five basic processing blocks, to describe different time-series processing methodologies in a unified manner. Detailed explanation of the main processing blocks was discussed. Specific processing steps for utilizing of distributed scatterers (DS), i.e. adaptive multilooking and ESM-phase estimation were emphasized and described in detail.

As the ESM-phase estimation is the key step for exploiting DS-pixels, a detailed mathematical explanation and comparison of different methods and a new proposal for pre-unwrapping ESM-phase estimation based on geodetic methodology shape the main body of this thesis (in chapters 4–6). Statistical properties of DS-pixels in SAR/InSAR stacks play an important role in both ESM-phase estimation and its quality description. We begin by reviewing the stochastic model for DS in the next chapter.

Stochastic model for Distributed Scatterers

This chapter focuses on the statistical properties of DS-pixels in SAR and InSAR stacks. We limit the scope of this chapter to single-point statistics (described in sec. 3.1). We revisit the complex statistics in SAR stacks (sec. 3.2), with special attention to the coherence matrix as a main metric in the stochastic model of SAR stacks, and to the different error sources influencing coherence values. In addition, the phase statistics in a single interferogram are reviewed (sec. 3.3), followed by the phase statistics in InSAR stacks in terms of second statistical moments or in the form of a covariance matrix (sec. 3.4). A Monte-Carlo methodology to compute a full covariance matrix for interferometric phase stacks is introduced (sec. 3.4.4), followed by the derivation of an analytical closed-form evaluation of InSAR second-order phase statistics (sec. 3.4.5).

3.1 Noise components in SAR/InSAR stacks

In general, the stochastic model of observations describes the uncertainty in the measurements by means of some statistical tools. Our main focus in this chapter is on the stochastic aspects of noise/error components in SAR and InSAR stacks with special attention to DS-pixels. The term "noise", however, may be interpreted loosely as its definition is application-dependent: *one man's signal is the other man's noise*. From the four main components of SAR/InSAR phase observations (i.e. the range-dependent component, atmospheric signal, the scattering effect, and noise, see Eqs. (2.4) and (2.6)), the range dependent phase is defined as a signal that includes information about the deformation and topography of the imaged area, and it is usually modeled functionally and is considered deterministic (or sometimes it is modeled as the summation of a deterministic model and stochastic deviations from the model), e.g., in Hanssen (2001), Ferretti et al. (2001), and Kampes and Hanssen (2004). The other components are usually modeled in a statistical sense by means of a probability distribution function (PDF) or its first two statistical moments.

Based on the different spatio-temporal behavior of SAR/InSAR stochastic components, we analyze and model them independently. The scattering effect and the system noise mainly affect every single resolution-cell independently, resulting in an insignificant spatial correlation among nonadjacent pixels. Therefore, the stochastic model for these components can be presented in the single-point level. In contrary, the atmospheric components (and the unmodeled deformation) have strong spatial correlation (Hanssen, 2001), and therefore, their stochastic model can be defined for multiple-points. As suggested by Hanssen (2001), focusing on 2nd statistical moments, the full covariance matrix of SAR/InSAR measurements Q can be approximated as summation of a covariance matrix Q_n influenced by single-point statistics and an atmospheric covariance matrix Q_{atmo} affected by multiple-point statistics as:

$$Q \doteq Q_n + Q_{\text{atmo}}. \quad (3.1)$$

Considering the exploitation of DS, the key focus in this chapter is on the evaluation/description of single-point statistics. The reason is two-fold. First, the multiple-point stochasticity mainly describes the variability in atmospheric effects and is the same for both PS and DS. It is described comprehensively in literature, see section 2.1.2.2. Second, the equivalent SM-phase estimation, which is the main TInSAR processing block on DS-pixels, is applied on a pixel-by-pixel basis, where the atmospheric signal is a part of the range-dependent components, shaping the set of unknown parameters of interest. Therefore in the equivalent SM-phase estimation, multiple-point statistics and the stochastic aspects of atmospheric signal are not relevant.

In the rest of this chapter, the analysis of single-point statistics, first for SAR (Sec. 3.2), and then for InSAR stacks (Sec. 3.3 and 3.4) are elaborated.

3.2 Single-point complex statistics for DS in SAR stacks

3.2.1 Physical origin of noise

The reflected signal received from a DS resolution cell is equal to the coherent summation of the reflections from multitude of elementary scatterers within the cell (see section 2.1.2.3 and fig. 2.3). In other words, the complex value (phasor) P of a pixel (with amplitude A and phase ψ) can be written as the complex summation of the phasors of all the elementary scatterers within the associated resolution cell:

$$P = A \exp(j\psi) = \sum_i S_i = \sum_i a_i \exp(j\varsigma_i) = \sum_i \text{Re}(S_i) + j \sum_i \text{Im}(S_i), \quad (3.2)$$

where S_i , a_i , and ς_i are the phasor, amplitude, and phase of the i th elementary scatterer within the cell. The elementary scattering phase ς_i is a function of the relative position and dielectric characteristics of each elementary scatterer. Although the complex phasor P and its phase and amplitude are intrinsically deterministic quantities, i.e. they are invariant if the measurements are repeated under the same condition, they are unpredictable and hence they cannot be described mathematically in a deterministic manner,

and so they are modeled stochastically. Assuming the location and distribution of elementary scatterers within a resolution cell to be random, the summation of S_i values should result in a phasor P with a Wiener (or random walk) process (Davenport, 1970; Sarabandi, 1992). For a large number of elementary scatterers, based on the central limit theorem¹, the phasor P is a complex random variable with a circular Gaussian distribution (Madsen, 1986; Sarabandi, 1992).

3.2.2 Circular Gaussian distribution

Goodman (1976) showed that, under certain assumptions, the complex SLC phasor P has a zero-mean² *circular Gaussian* distribution. These assumptions are (Goodman, 1976; Madsen, 1986; Bamler and Hartl, 1998):

1. the responses of all the elementary scatterers within the resolution cell are independent,
2. for each elementary scatterer, the amplitude A_i and phase ς_i are independent,
3. the phases ς_i are uniformly distributed between $-\pi$ and π , and
4. all the elementary scatterers produce comparable amplitudes A_i — there is no dominant scatterer within a resolution cell.

These assumptions generally hold for areas with a surface roughness comparable to the radar wavelength, and for DS-pixels over homogeneous natural landscapes such as agricultural fields, forests, and deserts.

Considering a single DS-pixel in a stack of N SAR images, the set of phasors in all the images can be seen as a multivariate complex random variable $\underline{y} = [P_1 \ P_2 \ \dots \ P_N]^T$. The zero-mean circular complex Gaussian PDF of \underline{y} is written as (Goodman, 1976; Hannan and Thomson, 1971; Lee et al., 1994)

$$f_{\underline{y}}(y) = \frac{1}{\pi^N |Q_y|} \exp(-y^* Q_y^{-1} y), \quad (3.3)$$

where $Q_y = D\{\underline{y}\} = E\{\underline{y} \underline{y}^*\}$ is an $N \times N$ complex covariance matrix defined by

$$Q_y = \begin{bmatrix} E\{|P_1|^2\} & \gamma_{12} \sqrt{E\{|P_1|^2\}E\{|P_2|^2\}} & \dots & \gamma_{1N} \sqrt{E\{|P_1|^2\}E\{|P_N|^2\}} \\ \gamma_{12}^* \sqrt{E\{|P_1|^2\}E\{|P_2|^2\}} & E\{|P_2|^2\} & \dots & \gamma_{2N} \sqrt{E\{|P_2|^2\}E\{|P_N|^2\}} \\ \vdots & \vdots & \ddots & \vdots \\ \gamma_{1N}^* \sqrt{E\{|P_1|^2\}E\{|P_N|^2\}} & \gamma_{2N}^* \sqrt{E\{|P_2|^2\}E\{|P_N|^2\}} & \dots & E\{|P_N|^2\} \end{bmatrix}. \quad (3.4)$$

¹Central limit theorem: Let $\underline{x}_1, \dots, \underline{x}_n$ be independent random variables/vectors and let $\underline{z} = \sum_{i=1}^n \underline{x}_i$. Then under general conditions, the distribution of \underline{z} approaches the (multivariate) normal distribution as n increases ($n \rightarrow \infty$).

²Here zero-mean refers to representation in real and imaginary components of the phasor.

In this formulation, the γ values are the complex correlation coefficients (called *coherence* values) between pair of images. The coherence value between P_i and P_j is defined as (Born et al., 1959; Foster and Guinzy, 1967; Papoulis, 1991)

$$\gamma_{ij} = \frac{\mathbb{E}\{P_i P_j^*\}}{\sqrt{\mathbb{E}\{|P_i|^2\}\mathbb{E}\{|P_j|^2\}}} = |\gamma_{ij}| \exp(j\phi_{0_{ij}}), \quad (3.5)$$

where the phase of the complex coherence, $\phi_{0_{ij}} \in [-\pi, \pi)$, is the phase of the expectation of the complex interferometric product $P_i P_j^*$. The absolute coherence $|\gamma_{ij}| \in [0, 1]$ is a measure of the correlation between the noise components of P_i and P_j . When the coherence is high, the noise components in P_i and P_j have a higher similarity, and so a large portion of the noise components will be canceled out in the interferometric phase. Consequently, the absolute coherence is also a normalized measure of the dispersion of the interferometric phase noise. The complex correlation matrix of the vector \underline{y} is called the *coherence matrix* and is defined as

$$\Gamma_y = \begin{bmatrix} 1 & \gamma_{12} & \cdots & \gamma_{1N} \\ \gamma_{12}^* & 1 & \cdots & \gamma_{2N} \\ \vdots & \vdots & \ddots & \vdots \\ \gamma_{1N}^* & \gamma_{2N}^* & \cdots & 1 \end{bmatrix}. \quad (3.6)$$

Note that the coherence matrix Γ_y is a Hermitian matrix³. Using the definition of the coherence matrix (Eq. (3.6)), the covariance matrix Q_y (see Eq. (3.4)) can be reformulated as:

$$Q_y = \Gamma_y \circ \underbrace{\begin{bmatrix} \mathbb{E}\{|P_1|^2\} & \sqrt{\mathbb{E}\{|P_1|^2\}\mathbb{E}\{|P_2|^2\}} & \cdots & \sqrt{\mathbb{E}\{|P_1|^2\}\mathbb{E}\{|P_N|^2\}} \\ \sqrt{\mathbb{E}\{|P_1|^2\}\mathbb{E}\{|P_2|^2\}} & \mathbb{E}\{|P_2|^2\} & \cdots & \sqrt{\mathbb{E}\{|P_2|^2\}\mathbb{E}\{|P_N|^2\}} \\ \vdots & \vdots & \ddots & \vdots \\ \sqrt{\mathbb{E}\{|P_1|^2\}\mathbb{E}\{|P_N|^2\}} & \sqrt{\mathbb{E}\{|P_2|^2\}\mathbb{E}\{|P_N|^2\}} & \cdots & \mathbb{E}\{|P_N|^2\} \end{bmatrix}}_{\bar{I}}, \quad (3.7)$$

where \circ represents the Hadamard (i.e., entry-wise) product, and the matrix \bar{I} is the expectation power matrix whose elements are defined by

$$\bar{I}_{[i,j]} = \zeta_{ij} = \sqrt{\zeta_{ii}\zeta_{jj}} = \sqrt{\mathbb{E}\{|P_i|^2\}\mathbb{E}\{|P_j|^2\}}. \quad (3.8)$$

In table 3.1, the complex PDF of \underline{y} , its first two statistical moments, and its coherence matrix are summarized.

In addition to the PDF formulation of eq. (3.3), some other alternative formulations can be also found in SAR literature. In the following, we review two alternative formulations which are used in the next chapters of this thesis.

³A Hermitian matrix is a complex square matrix that is equal to its own conjugate transpose. Hermitian matrices are the complex counterparts of symmetric matrices for real numbers. Note that the real part (and the absolute) of a Hermitian matrix is a symmetric matrix, but its imaginary part (and its phase) is a skew-symmetric matrix: its transpose is equal to its negative.

Table 3.1: Overview of the PDF, expectation, (co)variance, and coherence for single-pixel values in a SLC stack of N images (i.e, for $\underline{y} = [\underline{P}_1 \ \underline{P}_2 \ \cdots \ \underline{P}_N]^T$). All attributes in this table are complex-valued.

PDF: $f_{\underline{y}}(y)$	First moment (Expectation)	Second moment (Dispersion)	Coherence
$\frac{1}{\pi^N Q_y } \exp(-y^* Q_y^{-1} y)$	$E\{\underline{y}\} = [0 \ 0 \ \cdots \ 0]^T$ where $0 = 0 + j0$	$D\{\underline{y}\} = Q_y$ $Q_{y[i,i]} = E\{ \underline{P}_i ^2\}$ $Q_{y[i,j]} = \gamma_{ij} \sqrt{E\{ \underline{P}_i ^2\} E\{ \underline{P}_j ^2\}}$	$\text{Corr}\{\underline{y}\} = \Gamma_y$ $C_{y[i,i]} = 1$ $C_{y[i,j]} = \gamma_{ij}$

First Alternative formulation of PDF of \underline{y} :

The complex $N \times 1$ vector $\underline{y} = [\underline{P}_1 \ \underline{P}_2 \ \cdots \ \underline{P}_N]^T$, can be viewed as a $2N \times 1$ real valued random vector \underline{z} defined by:

$$\underline{z} = \left[\underbrace{\text{Re}(P_1), \text{Re}(P_2), \dots, \text{Re}(P_N)}_{\text{Re}(\underline{y}^T)} \ \underbrace{\text{Im}(P_1), \text{Im}(P_2), \dots, \text{Im}(P_N)}_{\text{Im}(\underline{y}^T)} \right]^T. \quad (3.9)$$

The complex circular Gaussian distribution satisfies the following conditions (Lee et al., 1994):

$$\begin{aligned} E\{\text{Re}(P_i)\} &= E\{\text{Im}(P_i)\} = 0 \\ D\{\text{Re}(P_i)\} &= D\{\text{Im}(P_i)\} \\ \text{Corr}\{\text{Re}(P_i), \text{Im}(P_i)\} &= 0 \\ \text{Corr}\{\text{Re}(P_i), \text{Re}(P_j)\} &= \text{Corr}\{\text{Im}(P_i), \text{Im}(P_j)\} = |\gamma_{ij}| \\ \text{Corr}\{\text{Re}(P_i), \text{Im}(P_j)\} &= -\text{Corr}\{\text{Re}(P_j), \text{Im}(P_i)\}. \end{aligned} \quad (3.10)$$

As all the real and imaginary components are normally distributed, the vector \underline{z} also has a multivariate Gaussian distribution. The PDF of the complex circular Gaussian distribution of vector $\underline{y} \in \mathbb{C}$ can be written as the joint PDF of its real and imaginary components, or, in other words, as the PDF of the random vector \underline{z} , with $\underline{z} \in \mathbb{R}$ (Dainty, 1975; Davenport and Root, 1987):

$$f_{\underline{y}}(y) = f_{\underline{z}}(z) = \frac{1}{\sqrt{(2\pi)^{2N} |Q_z|}} \exp\left\{-\frac{1}{2} z^T Q_z^{-1} z\right\}, \quad (3.11)$$

cf. eq. (3.3). The real-valued covariance matrix Q_z is then related to the complex-valued covariance matrix Q_y as

$$D\{\underline{z}\} = Q_z = \frac{1}{2} \begin{bmatrix} \text{Re}(Q_y) & -\text{Im}(Q_y) \\ \text{Im}(Q_y) & \text{Re}(Q_y) \end{bmatrix}, \quad (3.12)$$

where

$$\text{Re}(Q_y) = \bar{I} \circ \begin{bmatrix} 1 & |\gamma_{12}| \cos(\phi_{012}) & \cdots & |\gamma_{1N}| \cos(\phi_{01N}) \\ |\gamma_{12}| \cos(\phi_{021}) & 1 & \cdots & |\gamma_{2N}| \cos(\phi_{02N}) \\ \vdots & \vdots & \ddots & \vdots \\ |\gamma_{1N}| \cos(\phi_{0N1}) & |\gamma_{N2}| \cos(\phi_{02N}) & \cdots & 1 \end{bmatrix}, \quad (3.13)$$

and

$$\text{Im}(Q_y) = \bar{I} \circ \begin{bmatrix} 0 & |\gamma_{12}| \sin(\phi_{0_{12}}) & \cdots & |\gamma_{1N}| \sin(\phi_{0_{1N}}) \\ |\gamma_{12}| \sin(\phi_{0_{21}}) & 0 & \cdots & |\gamma_{2N}| \sin(\phi_{0_{2N}}) \\ \vdots & \vdots & \ddots & \vdots \\ |\gamma_{1N}| \sin(\phi_{0_{N1}}) & |\gamma_{2N}| \sin(\phi_{0_{N2}}) & \cdots & 0 \end{bmatrix}. \quad (3.14)$$

Note that, if the phase is zero (i.e., $\phi_{0_{ij}}=0$), the covariance matrix Q_z reduces to

$$Q_z = \frac{1}{2} \begin{bmatrix} \bar{I} & 0 \\ 0 & \bar{I} \end{bmatrix} \circ \begin{bmatrix} \Upsilon & 0 \\ 0 & \Upsilon \end{bmatrix}, \quad (3.15)$$

where Υ is an $N \times N$ absolute coherence matrix whose elements are given as $\Upsilon_{[i,j]} = |\gamma_{ij}|$. Equation 3.11 gives the first alternative formulation of the PDF of \underline{y} , cf. eq. (3.3).

Second Alternative formulation of PDF of \underline{y} :

By decomposing the phase of expectation of interferometric values ($\phi_{0_{ij}}$) into the separate contributions φ_i and φ_j from images i and j , the complex coherence values of eq.(3.5) can be written as

$$\gamma_{ij} = |\gamma_{ij}| \exp(j(\varphi_i - \varphi_j)). \quad (3.16)$$

Note that the phase values φ_i and φ_j should not be interpreted as the expectation value of SLC phases. In fact, the SLC phases are uniformly distributed between $-\pi$ and π and so they have zero expectation. The phase values φ_i and φ_j can be interpreted as the deterministic part of SLC phases (i.e., the summation of range dependent component and atmospheric signal). Based on the formulation of eq. (3.16), the coherence matrix Γ_y can be written in the following alternative form (Monti-Guarnieri and Tebaldini, 2007):

$$\Gamma_y = \Psi \Upsilon \Psi^*, \quad (3.17)$$

where Υ is the $N \times N$ absolute coherence matrix, and Ψ is an $N \times N$ diagonal complex matrix defined by

$$\Psi = \text{diag} \left(\exp(j\varphi_1), \exp(j\varphi_2), \dots, \exp(j\varphi_N) \right). \quad (3.18)$$

Now, the PDF of \underline{y} (see eq. (3.3)) can be formulated as

$$f_{\underline{y}}(y) = \frac{1}{\pi^N |\Psi \Upsilon \Psi^* \circ \bar{I}|} \exp \left(- y^* (\Psi \Upsilon \Psi^* \circ \bar{I})^{-1} y \right). \quad (3.19)$$

It is known that the determinant of the coherence matrix (i.e., $|\Gamma_y|$ or $|\Psi \Upsilon \Psi^*|$) is invariant with respect to the phase values in Ψ (Monti-Guarnieri and Tebaldini, 2008). Hence the conditional PDF of \underline{y} , conditioned on the phase values in Ψ , can be generally written as

$$f_{\underline{y}}(y|\Psi) = c \cdot \exp \left(- y^* (\Psi \Upsilon \Psi^* \circ \bar{I})^{-1} y \right), \quad (3.20)$$

where c is a constant value. For an SLC stack with normalized amplitudes, the matrix \bar{I} is an all-ones matrix, and therefore:

$$f_{\underline{y}}(y|\Psi) = c \cdot \exp \left(- y^* \Psi \Upsilon^{-1} \Psi^* y \right). \quad (3.21)$$

Equations (3.20), (3.11), and (3.3) are equivalent representations of the circular Gaussian PDF for DS-pixels in SLC stacks. In a single SLC image, this PDF reduces to a more simplified form and the marginal PDF of amplitude, intensity, and phase values can be also derived, as will be discussed in the following section.

3.2.3 Single-point statistics for a single SLC image

Assuming only one SAR image (i.e., $N=1$), eq. (3.3) is simplified and the PDF of the complex value \underline{y} of a single DS-pixel can be written as (Dainty, 1975; Davenport and Root, 1987)

$$f_{\underline{y}}(y) = \frac{1}{\pi 2\sigma^2} \exp\left(-\frac{\text{Re}(y)^2 + \text{Im}(y)^2}{2\sigma^2}\right), \quad (3.22)$$

where

$$\sigma^2 = \sigma_{\text{Re}(y)}^2 = \sigma_{\text{Im}(y)}^2 = \frac{\text{E}\{|y|^2\}}{2}. \quad (3.23)$$

The variance factor σ^2 is directly proportional to the expectation of intensity/power of the DS resolution cell, and subsequently the expectation of intensity is generally related to the radar cross section (i.e., σ^0) of elementary scatterers within the cell (Madsen, 1986; Bamler and Just, 1993; Bamler and Hartl, 1998).

Assuming $\underline{y} = \underline{A} \exp(j\underline{\psi})$, the joint PDF of amplitude \underline{A} and phase $\underline{\psi}$ is:

$$f_{\underline{A}, \underline{\psi}}(A, \psi) = \begin{cases} \frac{A}{2\pi\sigma^2} \exp\left(-\frac{A^2}{2\sigma^2}\right) & \text{for } A \geq 0 \text{ and } -\pi \leq \psi < \pi \\ 0 & \text{otherwise.} \end{cases} \quad (3.24)$$

By integrating $f_{\underline{A}, \underline{\psi}}(A, \psi)$ over ψ and A , the marginal PDF of amplitude \underline{A} and phase $\underline{\psi}$ is obtained as

$$f_{\underline{A}}(A) = \begin{cases} \frac{A}{\sigma^2} \exp\left(-\frac{A^2}{2\sigma^2}\right) & \text{for } A \geq 0 \\ 0 & \text{otherwise,} \end{cases} \quad (3.25)$$

and

$$f_{\underline{\psi}}(\psi) = \begin{cases} \frac{1}{2\pi} & \text{for } -\pi \leq \psi < \pi \\ 0 & \text{otherwise.} \end{cases} \quad (3.26)$$

The PDF of the amplitude \underline{A} (i.e., eq. (3.25)) is the *Rayleigh distribution* and the PDF of phase $\underline{\psi}$ (i.e., eq. (3.27)) is the *uniform distribution* between $-\pi$ and π . In the same way, the marginal PDF of intensity/power ($\underline{p}=\underline{A}^2$) is the *exponential distribution*:

$$f_{\underline{p}}(p) = \begin{cases} \frac{1}{2\sigma^2} \exp\left(-\frac{p}{2\sigma^2}\right) & \text{for } p \geq 0 \\ 0 & \text{otherwise.} \end{cases} \quad (3.27)$$

In table 3.2, these PDFs are visualized together with an overview of single-point statistics for single SAR image.

Table 3.2: Overview of statistics for a single DS resolution cell in a single SAR image: PDF, expectation, and variance of different components of complex variable $\underline{y} = \underline{A} \exp(j\underline{\psi}) = \text{Re}(\underline{y}) + j \text{Im}(\underline{y})$. The variance σ^2 is directly proportional to the averaged intensity/power of the DS resolution cell: $\sigma^2 = \frac{E\{\underline{A}^2\}}{2}$.

Parameter	PDF/Expectation/Variance	PDF
$\underline{r} = \text{Re}(\underline{y})$	$f_{\underline{r}}(r) = \frac{1}{\sqrt{2\pi\sigma^2}} \exp\left(-\frac{r^2}{2\sigma^2}\right)$ $E\{\underline{r}\} = 0$ $D\{\underline{r}\} = \sigma^2$	
$\underline{i} = \text{Im}(\underline{y})$	$f_{\underline{i}}(i) = \frac{1}{\sqrt{2\pi\sigma^2}} \exp\left(-\frac{i^2}{2\sigma^2}\right)$ $E\{\underline{i}\} = 0$ $D\{\underline{i}\} = \sigma^2$	
$\underline{A} = \underline{y} $	$f_{\underline{A}}(A) = \frac{A}{\sigma^2} \exp\left(-\frac{A^2}{2\sigma^2}\right)$ $E\{\underline{A}\} = \sigma^2 \frac{1}{2} \sqrt{2\pi}$ $D\{\underline{A}\} = 2\sigma^2 \left(1 - \frac{\pi}{4}\right)$	
$\underline{p} = \underline{y} ^2$	$f_{\underline{p}}(p) = \frac{1}{2\sigma^2} \exp\left(-\frac{p}{2\sigma^2}\right)$ $E\{\underline{p}\} = 2\sigma^2$ $D\{\underline{p}\} = (2\sigma^2)^2$	
$\underline{\psi} = \angle\{\underline{y}\}$	$f_{\underline{\psi}}(\psi) = \frac{1}{2\pi} \quad (-\pi \leq \psi < \pi)$ $E\{\underline{\psi}\} = 0$ $D\{\underline{\psi}\} = \frac{\pi^2}{3}$	

3.2.4 Coherence matrix

As we can see from eq. (3.3), single-point statistics in SAR stacks can be described by the covariance matrix Q_y , which itself is described by a Hadamard multiplication of the coherence matrix Γ_y with the intensity matrix \bar{I} (see eq. (3.7)). Regarding interferometric applications, the main focus is on phase measurements, and therefore, the intensity matrix \bar{I} is of less importance, as the intensities are invariant with respect to the phase values, see eq. (3.8). In contrary, the elements of the coherence matrix Γ_y are directly related to the expected interferometric phases (ϕ_0), while the absolute coherence values are a measure of decorrelation noise. Consequently, the computation and evaluation of the coherence matrix and its elements are of great importance for InSAR applications.

3.2.4.1 Estimation of coherence matrix from real data

For a single resolution cell P , observed by two or more SAR acquisitions, the elements of its coherence matrix C are defined by the complex coherence values γ_{ij} between circular Gaussian variables P_i and P_j (i.e. the representative pixel values in the i th and the j th image, respectively). The theoretical definition of γ_{ij} is given by eq. (3.5). However, as there is only one observation per image available for every resolution cell, the expectation values in eq. (3.5) (i.e., $E\{P_i P_j^*\}$, $E\{|P_i|^2\}$, and $E\{|P_j|^2\}$) cannot be obtained from the data by averaging over large samples of P_i and P_j . Therefore, the coherence values are conventionally computed based on the assumption of ergodicity which considers that the statistical properties of a uniform region (e.g., a set of neighboring pixels) to be equal, and thus the statistical properties (e.g., the mean or expectation) of one single pixel can be approximated from the set of neighboring pixels. Based on this assumption, the coherence values are estimated by spatial ensemble averaging as

$$\hat{\gamma}_{ij} = \frac{\sum_{n \in \Omega} P_{i_n} P_{j_n}^*}{\sqrt{\left(\sum_{n \in \Omega} |P_{i_n}|^2 \right) \left(\sum_{n \in \Omega} |P_{j_n}|^2 \right)}}, \quad (3.28)$$

where Ω is the set of surrounding/adjacent pixels. The set Ω can be selected as a square window around the pixel, or by adjacent pixels with a similar scattering mechanism (see section 2.4). The coherence estimator $\hat{\gamma}_{ij}$ is a complex value whose absolute value is the measure of interferometric correlation and is computed as

$$|\hat{\gamma}_{ij}| = \frac{\left| \sum_{n \in \Omega} P_{i_n} P_{j_n}^* \right|}{\sqrt{\left(\sum_{n \in \Omega} |P_{i_n}|^2 \right) \left(\sum_{n \in \Omega} |P_{j_n}|^2 \right)}}, \quad (3.29)$$

The phase of the estimator $\hat{\gamma}_{ij}$ is given by

$$\angle(\hat{\gamma}_{ij}) = \hat{\phi}_{0_{ij}} = \arctan \left(\frac{\sum_{n \in \Omega} \text{Im}(P_{i_n}) \text{Im}(P_{j_n}^*)}{\sum_{n \in \Omega} \text{Re}(P_{i_n}) \text{Re}(P_{j_n}^*)} \right), \quad (3.30)$$

where $\hat{\phi}_{0_{ij}}$ is called the *multilooked* interferometric phase estimator. Rodriguez and Martin (1992) showed that the phase $\hat{\phi}_{0_{ij}}$ is the maximum likelihood estimator of the interferometric phase. The interferometric phase estimator $\hat{\phi}_{0_{ij}}$ is unbiased provided the validity of the ergodicity assumption over the averaging area Ω . The statistical properties of the multilooked interferometric phases will be described in section 3.3. In the following, we review the statistical properties of the absolute coherence estimator $|\hat{\gamma}|$.

Absolute coherence estimator $|\hat{\gamma}|$

The absolute coherence is a metric for the interferometric noise (decorrelation) and is used intensively in interferometric studies as a quality descriptor, or to properly weight the interferometric observations. As $|\hat{\gamma}|$ is estimated from random variables, it itself is a random variable and its statistics can be obtained by propagation of the circular Gaussian statistics of the single-look SAR observations. Assuming the averaged samples within Ω are independent, the PDF of the absolute coherence estimator is obtained as a function of the true coherence $|\gamma|$ and the number of independent samples L (Touzi et al., 1996b)

$$f_{|\hat{\gamma}|}(|\hat{\gamma}|) = 2(L-1)(1-|\gamma|^2)^L |\hat{\gamma}| (1-|\hat{\gamma}|^2)^{L-2} {}_2F_1(L, L; 1; |\gamma|^2 \hat{\gamma}^2) \quad (3.31)$$

where ${}_2F_1(\cdot)$ is the classical standard hypergeometric function (Oberhettinger, 1970; Gradshteyn et al., 1994). An important property of the estimator $|\hat{\gamma}|$ is that it is biased and so its expectation is not equal to the true coherence value (i.e., $\mathbb{E}\{|\hat{\gamma}|\} \neq |\gamma|$). Touzi et al. (1999) have shown that the k -th statistical moment of the absolute coherence estimator (i.e., $M_k(|\hat{\gamma}|)$) can be computed as

$$M_k(|\hat{\gamma}|) = \frac{\Gamma(L)\Gamma(1+k/2)}{\Gamma(L+k/2)} {}_3F_2(1+k/2, L, L; L+k/2, 1; |\gamma|^2)(1-|\gamma|^2)^L, \quad (3.32)$$

where $\Gamma(\cdot)$ is the gamma function⁴, and ${}_3F_2(\cdot)$ the generalized hypergeometric function. Using $k=1$, the expectation $\mathbb{E}\{|\hat{\gamma}|\}$ is computed as the first statistical moment of $|\hat{\gamma}|$. Fig. 3.1 shows the $\mathbb{E}\{|\hat{\gamma}|\}$ as the function of the true coherence for the number of looks $L=5, 10, 20, 50$. We can see that the estimator $|\hat{\gamma}|$ is biased towards higher values for a small number of looks (i.e., small averaging area) and for low coherence values (i.e., areas with a high degree of decorrelation). The bias in the coherence estimation is a very well-known fact and has been addressed widely in InSAR literature (Joughin and Winebrenner, 1994; Tough et al., 1995; Touzi et al., 1996b, 1999; Bamler and Hartl, 1998; Hanssen, 2001; Zebker and Chen, 2005). In order to reduce this bias in low coherence areas, the number of looks should be large enough. There is also a possibility to approximate and correct for the bias using some approaches presented in (Touzi et al., 1996a; Zebker and Chen, 2005; Jiang et al., 2014b,a).

The influence of local signal-phase variation on absolute coherence estimation:

Absolute coherence values $|\hat{\gamma}|$ estimated by eq. (3.29) are affected by deterministic interferometric phase variation in the estimation area Ω . As far as the interferometric

⁴The gamma function is defined as: $\Gamma(x) = \int_0^\infty t^{x-1} \exp(-t) dt$, for $x \in \mathbb{R}$. The Gamma function can be simplified in the form of $\Gamma(x) = (x-1)!$, for $x-1 \in \mathbb{N}$ (Abramowitz and Stegun, 1965).

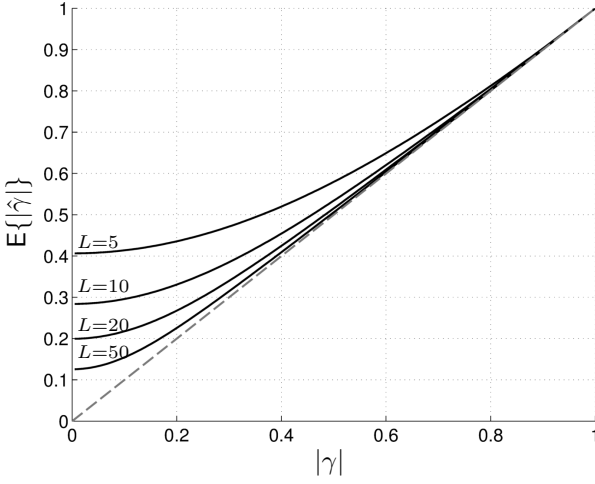


Figure 3.1: The expectation value $E\{|\hat{\gamma}|\}$ as a function of the true coherence value $|\gamma|$ for a number of looks $L=5, 10, 20, 50$ (The expectation values are computed by eq. (3.32) with $k=1$). The estimator $|\hat{\gamma}|$ is biased for small number of looks and low coherence values. After Touzi and Lopes (1996)

signal phase within Ω is stationary—that is all the signal components (e.g., deformation, topographic, and atmospheric phase) are constant in the estimation window and the phase variation is only due to the noise—the absolute coherence $|\hat{\gamma}|$ is a measure of phase (noise) statistics (although it is biased towards higher values for low coherence and a low number of looks). Obviously, if there still is a systematic phase variation in the estimation window due to deformation, topography, or atmosphere signals, the absolute coherence $|\hat{\gamma}|$ is underestimated, i.e., biased towards lower values. So if the phase within the estimation window still contains a systematic (signal) component, this phase variation should be compensated for. Assuming ϕ_{s_n} is the systematic phase component for the pixel n , the *phase corrected absolute coherence* $|\hat{\gamma}_{ij}^{\text{PC}}|$ is defined as (Hagberg et al., 1995; Monti-Guarnieri and Prati, 1997; Dammert, 1997)

$$|\hat{\gamma}_{ij}^{\text{PC}}| = \frac{|\sum_{n \in \Omega} P_{i_n} P_{j_n}^* \exp(-j\phi_{s_n})|}{\sqrt{\left(\sum_{n \in \Omega} |P_{i_n}|^2\right) \left(\sum_{n \in \Omega} |P_{j_n}|^2\right)}}. \quad (3.33)$$

Instead of using eq. (3.33) for compensation of the systematic phase, an alternative solution is to remove/filter-out the systematic signal prior to the coherence estimation. The expected variation can be either, if available, computed based on external/a-priori knowledge (e.g., flat-earth and topographic phase removal based on external DEM), or can be estimated directly from data and excluded by different kind of phase flattening or low-pass filters such as the adaptive multi-resolution *defringe* algorithm (Prati and Rocca, 1992; Davidson and Bamler, 1999; Wang et al., 2012), patch detrending (Zebker and Chen, 2005; Bamler and Hartl, 1998), and the low-pass filtering method presented by Hooper et al. (2004).

In addition to the aforementioned methodologies to correct for the systematic phase variation in the averaging area, Monti-Guarnieri and Prati (1997) have proposed a "quick and dirty" and amplitude-based coherence estimator which is independent of local systematic phase variations. The amplitude-based coherence estimate (denoted by $|\hat{\gamma}_{ij}^{\text{M}}|$) is defined as

$$|\hat{\gamma}_{ij}^{\text{M}}| = \begin{cases} \sqrt{2\hat{\rho}_{ij} - 1} & \hat{\rho}_{ij} > 1/2 \\ 0 & \hat{\rho}_{ij} \leq 1/2 \end{cases}, \quad (3.34)$$

where

$$\hat{\rho}_{ij} = \frac{\sum_{n \in \Omega} |P_{i_n}|^2 |P_{j_n}|^2}{\sqrt{\left(\sum_{n \in \Omega} |P_{i_n}|^4 \right) \left(\sum_{n \in \Omega} |P_{j_n}|^4 \right)}}. \quad (3.35)$$

The main advantage of $|\hat{\gamma}^M|$ estimation is that it does not require the stationarity of the local interferometric phase, and so it is independent of any phase estimation/compensation error. On the other hand, Monti-Guarnieri and Prati (1997) showed that the precision (variance) of the $|\hat{\gamma}^M|$ estimator is worse than the standard $|\hat{\gamma}|$ estimator if the same number of looks is applied. Assume L_1 and L_2 are the number of independent samples used to estimate $|\hat{\gamma}|$ and $|\hat{\gamma}^M|$, respectively, then in order to have the same precision for both estimators the following ratio between L_1 and L_2 should be held (Monti-Guarnieri and Prati, 1997):

$$\frac{L_2}{L_1} = \frac{\gamma^8 + 6\gamma^6 - 12\gamma^4 + 2\gamma^2 + 3}{4\gamma^2(1 - \gamma^2)^2}. \quad (3.36)$$

In general, despite the lower precision, the $|\hat{\gamma}^M|$ estimator is computationally more efficient than the standard $|\hat{\gamma}|$ estimator, and it is more reliable in cases when there is still a considerable amount of signal variation in the estimation window (e.g., due to high topographic variations in interferograms with large baseline).

3.2.4.2 Model-based absolute coherence matrix

The elements of the absolute coherence matrix (i.e. Υ) can be either estimated directly from data based on the ergodicity/stationary assumption via eqs. (3.29), (3.33), and (3.34), or alternatively they can be evaluated theoretically based on models of coherence loss. Here we briefly discuss some of the common theoretical models for evaluation of absolute coherence values.

The five sources of coherence loss (see sections 2.1.2.3 and 2.1.2.4 for detailed explanation of different sources of decorrelation) can be listed as:

1. *System noise decorrelation*: the influence of thermal noise on system coherence depends on the signal-to-noise (SNR) ratio as (Zebker and Villasenor, 1992):

$$\gamma_{\text{thermal}} = \frac{1}{1 + \text{SNR}^{-1}}. \quad (3.37)$$

The value for SNR is dependent on system parameters and the radar scene's radar cross section (SCR), where the latter is varying subject to terrain characteristics. For example for the system parameters of the ERS satellite (as reported in Zebker et al. (1994a) and Hanssen (2001)) and a SCR of -14 dB, the SNR will be 12 dB, resulting in a γ_{thermal} of 0.92. The detailed computation of SNR based on SAR system parameters is explained by Hanssen (2001) and Zebker and Villasenor (1992).

2. *Processing noise decorrelation*: this is mainly a function of the accuracy of image coregistration and resampling/interpolation steps. For coregistration with subpixel accuracy of $\sigma_{\text{coreg},a}$ and $\sigma_{\text{coreg},r}$ in azimuth and range directions, respectively, the decorrelation induced by coregistration γ_{coreg} is computed as (Just and Bamler, 1994; Hanssen, 2001):

$$\gamma_{\text{coreg}} = \begin{cases} \text{sinc}(\sigma_{\text{coreg},a}) \cdot \text{sinc}(\sigma_{\text{coreg},r}) & \sigma_{\text{coreg},r} \leq 1 \text{ and } \sigma_{\text{coreg},a} \leq 1 \\ 0 & \sigma_{\text{coreg},r} > 1 \text{ or } \sigma_{\text{coreg},a} > 1 \end{cases} \quad (3.38)$$

It is obvious that a misregistration equal to a full resolution cell (or bigger) results in complete decorrelation and therefore zero coherence. It has been demonstrated by Hanssen (2001) that the coherence does not improve significantly for a misregistration smaller than 0.1 resolution cell (or 1/8th of a pixel). For this coregistration accuracy in both azimuth and range direction, the γ_{coreg} will be equal to 0.96. In addition to coregistration, the resampling step (i.e., the interpolation of slave image on the master image grid) causes the loss of coherence as well, depending on the kind of interpolation kernel used. The detailed overview of different interpolation kernels and their influence on coherence loss is explained in Laakso et al. (1996) and Hanssen and Bamler (1999). Assuming that γ_{int} describes the decorrelation induced by resampling, the total processing coherence can be computed as

$$\gamma_{\text{proc}} = \gamma_{\text{coreg}} \cdot \gamma_{\text{int}}. \quad (3.39)$$

3. *Baseline decorrelation*: The baseline decorrelation is the result of different incidence angles between the two radar paths at the earth's surface. For an interferometric pair of two radar images, baseline decorrelation is approximated as (Zebker and Villasenor, 1992; Gatelli et al., 1994; Hanssen, 2001):

$$\gamma_{\text{geom}} = \max\left(1 - \frac{|B_{\perp}|}{B_{\perp\text{max}}}, 0\right). \quad (3.40)$$

where B_{\perp} is the perpendicular baseline between two images, and $B_{\perp\text{max}}$ the critical baseline at which the decorrelation is maximum and the coherence will be zero. The critical baseline is a function of the radar wavelength λ , the incidence angle θ_{inc} , and the topographic slope ζ as:

$$B_{\perp\text{max}} = \frac{\lambda B_{\text{rg}} R_{\text{M}} \tan(\theta_{\text{inc}} - \zeta)}{c}, \quad (3.41)$$

where c is the speed of light, and B_{rg} is the range bandwidth.

4. *Doppler-centroid decorrelation*: This decorrelation is a result of varying viewing geometry in azimuth direction, and its coherence factor can be modeled as (Hanssen, 2001):

$$\gamma_{\text{dc}} = \max\left(1 - \frac{\Delta f_{\text{DC}}}{B_{\text{az}}}, 0\right), \quad (3.42)$$

where Δf_{DC} is the difference in Doppler-centroid frequencies between master and slave images, and B_{az} is the bandwidth in azimuth direction.

5. *Temporal decorrelation*: Temporal decorrelation is the result of temporal changes in position or scattering characteristics of all elementary scatterers within a resolution cell. As the range of physical mechanisms causing temporal decorrelation is too wide, there is no single analytical model to evaluate coherence loss induced by this effect. Nevertheless there are some experimental models for processes which induce natural and gradual changes within resolution cells. If all the elementary scatterers within a cell move independently but in a homogeneous manner (i.e., their motions can be modeled statistically with the same distribution), temporal coherence can be described by (Zebker and Villasenor, 1992; Rocca, 2007)

$$\gamma_T = \exp\left(-\frac{1}{2}\left(\frac{4\pi}{\lambda}\right)^2 \sigma_r^2\right), \quad (3.43)$$

where σ_r^2 is the variance of the motion of scatterers in the LOS direction. The motion variance σ_r^2 can be modeled in different manners as a function of time, depending on real physical characteristics of the scattering surface. For example, Rocca (2007) modeled the motion of the elementary scatterers as Brownian motion which causes a linear increase of σ_r^2 in time:

$$\sigma_r^2 = \sigma_n^2 \Delta t, \quad (3.44)$$

where Δt is the time difference between two acquisitions and σ_n^2 represents the motion variance for the unit of time. Then the temporal coherence γ_T of eq. (3.43) can be written as

$$\gamma_T = \exp\left(\frac{-\Delta t}{\tau}\right), \quad (3.45)$$

where

$$\tau = \frac{2}{\sigma_n^2} \left(\frac{\lambda}{4\pi}\right)^2. \quad (3.46)$$

The parameter τ can be considered as the *temporal decorrelation range* with dimension time.

In principle, if the motion of scatterers for a homogeneous resolution cell is induced by N different mechanisms with total variance σ_r^2 , using the fact that the summation variances of different mechanisms is equal to $\sigma_r^2 = \sum_{i=1}^N \sigma_{r_i}^2$, eq. (3.43) is written as

$$\gamma_T = \prod_{i=1}^N \exp\left(-\frac{1}{2}\left(\frac{4\pi}{\lambda}\right)^2 \sigma_{r_i}^2\right). \quad (3.47)$$

An example of such a model with $N = 2$ is proposed by Morishita and Hanssen (2015b) for pasture areas, where it is assumed that the motion of elementary scatterers is due to short and long term mechanisms. The short term mechanism explains sudden movements of scatterers due to for example wind (Lavalle et al., 2012), while the long term process causes the increase in variance as a function of time (similar to the Brownian motion model) due to for example vegetation growth. Then the σ_r^2 can be expressed as

$$\sigma_r^2 = \sigma_{r,\text{short}}^2 + \sigma_{r,\text{long}}^2 \Delta t, \quad (3.48)$$

where $\sigma_{r,\text{short}}^2$ is the variance of sudden motions, and $\sigma_{r,\text{long}}^2$ is the variance of long term motion for the unit of time. Assuming the model of eq. (3.48) and using eq. (3.47) with $N = 2$, the total temporal coherence can be expressed as

$$\gamma_T = \underbrace{\exp\left(-\frac{1}{2}\left(\frac{4\pi}{\lambda}\right)^2 \sigma_{r,\text{short}}^2\right)}_{\gamma_{t,\text{short}}} \exp\left(\frac{-\Delta t}{\tau_{\text{long}}}\right) = \gamma_{t,\text{short}} \exp\left(\frac{-\Delta t}{\tau_{\text{long}}}\right), \quad (3.49)$$

where $\tau_{\text{long}} = \frac{2}{\sigma_{r,\text{long}}^2} \left(\frac{\lambda}{4\pi}\right)^2$. Note that in all the aforementioned models for temporal coherence, the motion variances describe the variance of scatterers motion in LOS direction. Assuming σ_h^2 and σ_v^2 are the variance of the motion in horizontal and vertical directions, the σ_r^2 in the LOS direction can be computed as (Zebker and Villasenor, 1992)

$$\sigma_r^2 = \sigma_h^2 \sin^2(\theta_{\text{inc}}) + \sigma_v^2 \cos^2(\theta_{\text{inc}}), \quad (3.50)$$

where θ_{inc} is the incidence angle.

As the coherence terms are multiplicative (Zebker and Villasenor, 1992), the total coherence can be evaluated by the multiplication of all the coherence terms as

$$\gamma_{\text{total}} = \gamma_{\text{thermal}} \cdot \gamma_{\text{procc}} \cdot \gamma_{\text{geom}} \cdot \gamma_{\text{dc}} \cdot \gamma_T. \quad (3.51)$$

By computing the γ_{total} for all the interferometric combinations, the full model-based absolute coherence matrix (i.e., $\Upsilon = \text{abs}(\Gamma_y)$) can be constructed.

3.3 Single-point phase statistics for single interferogram

In the previous section the single-point phase statistics of distributed scatterers in SAR stacks were discussed. In order to evaluate the single-point *interferometric* phase statistics, the SAR statistics should be propagated through the interferogram generation process which includes complex conjugate multiplication of pairs of SAR images. Here, we first look at the phase statistics for a single interferogram, followed in Sec. 3.4, by the extension of the stochastic model to the multi-interferogram case, i.e., for a vector of single-point interferometric phases in InSAR stacks.

Assuming two SLC pixels P_1 and P_2 with zero-mean complex circular Gaussian distribution (see eqs. (3.3) and (3.4)), with complex coherence γ (see eq. (3.5)), the joint PDF of the amplitude and the phase of the multilooked interferogram constructed from the two SLC images is given by (Goodman, 1963; Barber, 1993; Lee et al., 1994; Tough et al., 1995)

$$f_{\underline{A},\underline{\phi}}(A, \phi) = \frac{2L(LA)^L}{\pi\zeta^{L+1}(1-|\gamma|^2)\Gamma(L)} \exp\left(\frac{2|\gamma|LA \cos(\phi - \phi_0)}{\zeta(1-|\gamma|^2)}\right) K_{L-1}\left(\frac{2LA}{\zeta(1-|\gamma|^2)}\right), \quad (3.52)$$

where L is the number of looks, $K_{L-1}(\cdot)$ the modified Bessel function of the third kind (Gradshteyn et al., 1994), $\Gamma(\cdot)$ the Gamma function, and $\zeta = \sqrt{\text{E}\{|P_1|^2\}\text{E}\{|P_2|^2\}}$.

By integrating over amplitudes A , the marginal PDF of the interferometric phase ϕ is computed as (Tough et al., 1995)

$$\begin{aligned} f_{\underline{\phi}}(\phi) = & \frac{(1 - |\gamma|^2)^L}{2\pi} \left\{ \frac{\Gamma(2L - 1)}{(\Gamma(L))^2 2^{2(L-1)}} \right. \\ & \times \left(\frac{(2L - 1)\beta}{(1 - \beta^2)^{L+0.5}} \left(\frac{\pi}{2} + \arcsin(\beta) \right) + \frac{1}{(1 - \beta^2)^L} \right) \\ & \left. + \frac{1}{2(L - 1)} \sum_{r=0}^{L-2} \frac{\Gamma(L - 0.5)}{\Gamma(L - 0.5 - r)} \frac{\Gamma(L - 1 - r)}{\Gamma(L - 1)} \frac{1 + (2r + 1)\beta^2}{(1 - \beta^2)^{r+2}} \right\}, \end{aligned} \quad (3.53)$$

with $\beta = |\gamma| \cos(\phi - \phi_0)$, where ϕ_0 is the expected interferometric phase. An equivalent formulation of $f_{\underline{\phi}}(\phi)$ has been presented in different publications (Barber, 1993; Lee et al., 1994; Joughin and Winebrenner, 1994)

$$f_{\underline{\phi}}(\phi) = \frac{\Gamma(L + 0.5)(1 - |\gamma|^2)^L \beta}{2\sqrt{\pi}\Gamma(L)(1 - \beta^2)^{L+0.5}} + \frac{(1 - |\gamma|^2)^L}{2\pi} {}_2F_1(L, 1; 0.5; |\gamma|^2 \beta^2) \quad -\pi \leq \phi < \pi, \quad (3.54)$$

where ${}_2F_1(\cdot)$ is the classical standard hypergeometric function (Oberhettinger, 1970; Gradshteyn et al., 1994). For single-look pixels (i.e., $L=1$), the interferometric phase PDF reduces to (Just and Bamler, 1994; Lee et al., 1994; Tough et al., 1995)

$$f_{\underline{\phi}}(\phi|L=1) = \frac{(1 - |\gamma|^2) \left((1 - \beta^2)^{0.5} + \beta(\pi - \cos^{-1}(\beta)) \right)}{2\pi(1 - \beta^2)^{1.5}} \quad -\pi \leq \phi < \pi, \quad (3.55)$$

Figs. 3.2A, B, and C show examples of $f_{\underline{\phi}}(\phi)$ for coherence values 0.2, 0.5, and 0.8, evaluated for different number of looks $L=1, 5, 10, 20,$ and 50 . We can see that the higher L is, the more peaked the PDF is. For the extreme case of $|\gamma|=0$, $f_{\underline{\phi}}(\phi)$ reduces to

$$f_{\underline{\phi}}(\phi| |\gamma|=0) = \frac{1}{2\pi} \quad \text{for } -\pi \leq \phi < \pi, \quad (3.56)$$

which is equivalent to the PDF of uniformly distributed phases between $-\pi$ and π . For another extreme scenario of $|\gamma|=1$ (i.e., zero decorrelation or zero noise), the interferometric phase PDF reduces to the Dirac delta function:

$$f_{\underline{\phi}}(\phi| |\gamma|=1) = \begin{cases} \infty & \phi = \phi_0 \\ 0 & \phi \neq \phi_0. \end{cases} \quad (3.57)$$

First and second statistical moments of interferometric phase

With the PDFs of eqs. (3.53) or (3.54), the mean and the variance of the interferometric phases can be computed by evaluating the first two statistical moments of $f_{\underline{\phi}}(\phi)$ as

$$E\{\underline{\phi}\} = \mu_{\underline{\phi}} = \int_{-\pi}^{\pi} \phi f_{\underline{\phi}}(\phi) d\phi, \quad (3.58)$$

$$D\{\underline{\phi}\} = \sigma_{\underline{\phi}}^2 = \int_{-\pi}^{\pi} (\phi - E\{\underline{\phi}\})^2 f_{\underline{\phi}}(\phi) d\phi. \quad (3.59)$$

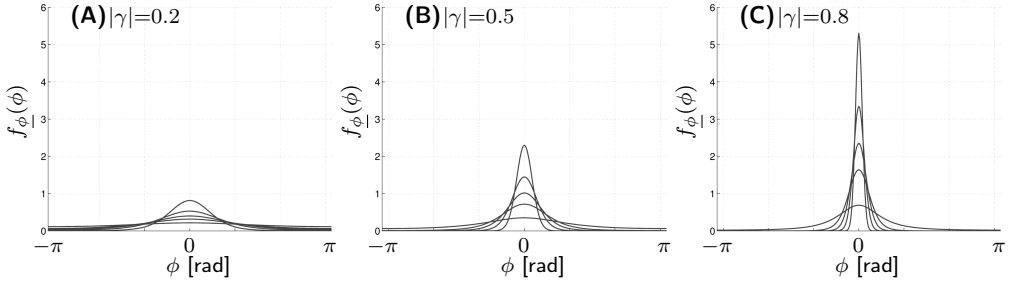


Figure 3.2: Probability density function of interferometric phase for coherence levels **(A)** $|\gamma|=0.2$, **(B)** $|\gamma|=0.5$, and **(C)** $|\gamma|=0.8$ evaluated for different number of looks $L=1, 5, 10, 20$, and 50 (the higher the L , the more peaked PDF). It is evident that multilooking improves the precision of the interferometric phase. All the PDFs were computed based on eq. (3.54) assuming $\phi_0 = 0$. After Hanssen (2001)

For the single-look case (i.e., $L=1$), Tough et al. (1995) evaluate the integrals of eqs. (3.58) and (3.59) in a closed form as

$$\mu_{\phi, L=1} = \frac{|\gamma| \sin(\phi_0)}{\sqrt{1 - |\gamma|^2 \cos^2(\phi_0)}} \arcsin(|\gamma| \cos(\phi_0)) \quad (3.60)$$

$$\sigma_{\phi, L=1}^2 = \frac{\pi^2}{3} - \pi \arcsin(|\gamma| \cos(\phi_0)) + \left(\arcsin(|\gamma| \cos(\phi_0)) \right)^2 - \text{Li}_2(|\gamma|^2) \quad (3.61)$$

where $\text{Li}_2(\cdot)$ is Euler's dilogarithm⁵. Note that both aforementioned evaluations of the mean and variance are not only related to $|\gamma|$, but they are also a function of ϕ_0 . This fact challenges the interpretation of mean and variance as a metric for the central tendency and spread of the interferometric phase. Ideally we are interested in a measure of central tendency which can characterize ϕ_0 , and a measure of dispersion which characterizes the spread of the phase around ϕ_0 . However in above equations, for example if ϕ_0 (and consequently the mode of the PDF) deviates from zero, the bounded PDF between $-\pi$ and π becomes non-symmetric around the mode, and consequently the mean of eq. (3.59) is not representative of the central tendency, while the mode is a better measure. In the same manner, the variance is not representative of phase dispersion around ϕ_0 , but it is a measure of non-symmetric dispersion around the mean (See Quegan et al. (1994) for more discussion). In fact we are interested in a measure of dispersion which is invariant with respect to ϕ_0 and which depends only on the coherence as a measure of noise. So the central tendency and the measure of phase dispersion ideally should be defined relative to the mode and account for the 2π symmetry of the PDF (Tough et al., 1995). In order to solve this problem, considering the fact that the phase PDF is periodic with a 2π cycle, it is suggested to evaluate the integration of eqs. (3.58) and (3.59) in the interval $(\phi_0 - \pi, \phi_0 + \pi)$ instead of $(-\pi, \pi)$, resulting in the following definition of phase mean and variance (Just and Bamler, 1994):

$$\mathbb{E}\{\phi\} = \mu_{\phi} = \int_{\phi_0 - \pi}^{\phi_0 + \pi} \phi f_{\phi}(\phi) d\phi = \phi_0, \quad (3.62)$$

$$\mathbb{D}\{\phi\} = \sigma_{\phi}^2 = \int_{\phi_0 - \pi}^{\phi_0 + \pi} (\phi - \phi_0)^2 f_{\phi}(\phi) d\phi = \int_{-\pi}^{\pi} (\phi)^2 f_{\phi}(\phi + \phi_0) d\phi. \quad (3.63)$$

⁵Euler's dilogarithm is defined as: $\text{Li}_2(x) = \sum_{k=1}^{\infty} \frac{x^k}{k^2}$ (Abramowitz and Stegun, 1970).

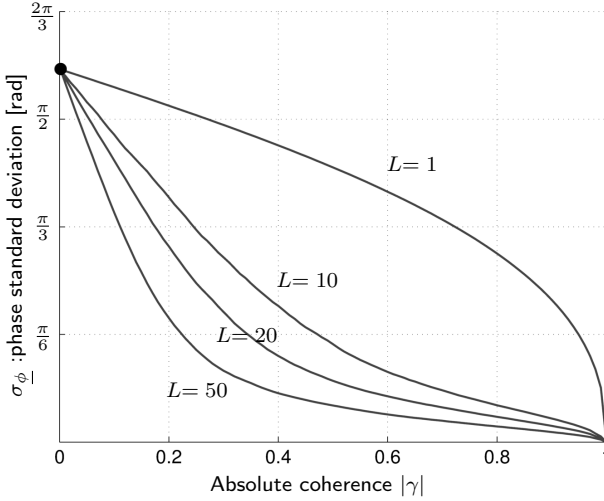


Figure 3.3: Evaluation of standard deviation of the interferometric phase (σ_{ϕ}) as a function of coherence $|\gamma|$, for four different number of looks $L=1, 10, 20$, and 50 . The standard deviations are computed by numerical evaluation of eq. (3.63). The upper-bound of standard deviation (visualized by the black dot \bullet) is equivalent to $\frac{2\pi}{\sqrt{12}}$ (or $\approx 104^\circ$), which is the standard deviation of uniformly distributed phase between $-\pi$ and π . After Just and Bamler (1994)

It should be pointed out that changing the integration interval to $(\phi_0 - \pi, \phi_0 + \pi)$, is equivalent to evaluating the integral in the interval $(-\pi, \pi)$ under the assumption of $\phi_0 = 0$. With this new definition of the mean (i.e. eq. (3.62)), μ_{ϕ} directly characterizes ϕ_0 and it is independent of the coherence values. Equivalently, the variance of eq. (3.63) is now dependent on $f_{\phi}(\phi + \phi_0)$ which is invariant with respect to ϕ_0 , and so the evaluated variance is exclusively a function of coherence. In general there is no closed-form evaluation of eq. (3.63) (except for single-look cases), and therefore the integral should be evaluated numerically. For single-look cases, the closed-form evaluation of eq. (3.63) results in (Bamler and Hartl, 1998):

$$\sigma_{\phi, L=1}^2 = \frac{\pi^2}{3} - \pi \arcsin(|\gamma|) + \left(\arcsin(|\gamma|) \right)^2 - \text{Li}_2(|\gamma|^2), \quad (3.64)$$

which is equivalent to eq. (3.61) if $\phi_0=0$. In fig. 3.3, the standard deviation of the interferometric phase (i.e., $\sqrt{\sigma_{\phi}^2}$) is evaluated as a function of coherence $|\gamma|$ and for different number of looks $L=1, 10, 20$, and 50 . It is evident that a higher multilooking factor reduces the phase standard deviation, assuming ergodicity. Note that in the highest dispersion case (i.e., $|\gamma|=0$), the standard deviation reaches an upper bound which is the standard deviation of uniformly distributed phase between $-\pi$ and π .

Note on information content of multilooked interferometric phase

A common measure of the information content that a random variable carries about an unknown parameter is the *Fisher information* (Rice, 2001). If we consider ϕ_0 to be the primary unknown parameter of interest in interferometric applications (as ϕ_0 contains all the geometric information about deformation, topography, and atmosphere), the amount of information included in the multilooked interferometric phase ϕ (or in the two SLC windows constructing ϕ) about ϕ_0 can be quantified by the Fisher information of interferometric phase as (Seymour and Cumming, 1994)

$$\mathcal{I}_{\phi}(\phi_0) = \frac{2L|\gamma|^2}{1 - |\gamma|^2}, \quad (3.65)$$

which results in zero information for $|\gamma|=0$ and maximum information of infinity when

$|\gamma|=1$. In other words, the Fisher information $\mathcal{I}_\phi(\phi_0)$ accounts for the loss of information about ϕ_0 due to decorrelation. The lower bound, or *Cramér-Rao bound* (CRB), of the interferometric phase variance is given by the inverse of the Fisher information (Rodriguez and Martin, 1992; Seymour and Cumming, 1994):

$$\sigma_{\phi_{\text{CRB}}}^2 = \left(\mathcal{I}_\phi(\phi_0) \right)^{-1} = \frac{1 - |\gamma|^2}{2L|\gamma|^2}. \quad (3.66)$$

We should note the fundamental difference between non-Gaussian random variables (such as interferometric phase) and Gaussian variables. While for the latter, variance/dispersion is truly the measure of information loss (as the PDF of normally distributed variables can be completely characterized by its dispersion), for interferometric phases, the variance is always bounded (see the upper bound in fig. 3.3) and it is not completely representative for loss of information. In fact a zero coherence interferometric phase conveys no information (corresponding to infinite information loss), while its variance is at most equal to $\frac{(2\pi)^2}{12}$, which is the variance of uniformly distributed phase between $-\pi$ and π .

Note on interferometric phase dispersion of point scatterers

The dispersion/variance of eqs. (3.63) and (3.64) was derived based on the assumption of a distributed scattering mechanism with complex circular Gaussian distribution (see section 3.2.2). For resolution cells with a dominant point scatterer, the true variance is smaller than the one given by eq. (3.64) (Bendat and Piersol, 1986). For point scatterers which can be assumed to be a superposition of distributed scattering and a deterministic signal (reflected from the dominant scatterer within a resolution cell), the variance of the interferometric phase is given by (Just and Bamler, 1994)

$$\sigma_{\phi_{PS}}^2 = \frac{1 - |\gamma|^2}{2|\gamma|^2}, \quad (3.67)$$

which is equivalent to the CRB lower bound ($\sigma_{\phi_{\text{CRB}}}^2$ in eq. (3.66)) for $L=1$. Note that eq. (3.67) only holds for $|\gamma|$ close to 1.

3.4 Single-point phase statistics for interferogram stack

In the previous section, we discussed the statistical properties of interferometric phases for single pixels in single interferograms. Thus, the interferometric phase is a univariate random variable, with a one-dimensional PDF whose dispersion is given by the phase variance. However, in order to evaluate phase statistics for one pixel in a stack of interferograms, we are dealing with a multivariate vector of interferometric phases, with a multi-dimensional PDF (or a joint PDF of all the interferometric phases for one pixel) and the dispersion in the form of a full covariance matrix. If the decorrelation noise components in different interferograms are assumed independent, the joint PDF can be evaluated simply by multiplication of the univariate phase PDFs given by eqs. (3.53) or (3.54), and the phase dispersion can be described by a diagonal covariance matrix

whose diagonal elements are equal to univariate variance factors evaluated by eq. (3.61). However the assumption of independency may not hold due to different reasons. In this section, we first discuss the reasons of dependency/correlation between the noise components, followed by reviewing different concepts for the analytical and numerical evaluation of multivariate interferometric phase PDFs and their dispersion.

3.4.1 Causes of correlation between interferograms

Assume two interferograms I_{12} and I_{34} constructed from a set of four SLC images P_1 , P_2 , P_3 , and P_4 . In order to evaluate the correlation between the phases of the two interferograms, the noise statistics of the complex multivariate vector $y = [P_1, P_2, P_3, P_4]^T$, which can be described by a circular complex Gaussian distribution (see eqs. (3.3) and (3.5)), should be propagated to the 2×2 covariance matrix of the vector $[\phi_{12}, \phi_{34}]^T$. As the SLC values in the vector y are likely to be correlated (as described by coherence values in the 4×4 coherence matrix Γ_y), there is no reason in principle to assume that the two interferometric phases are independent. In fact, the interferometric phases can be correlated or uncorrelated as expressed by different sets of coherence values in Γ_y . In order to get more insight on the physical origin of the correlation between noise components, we discuss three main sources of this dependency in the following⁶.

1. *Common master/slave image*: If two interferograms share a common master/slave image, the decorrelation noise terms in the common image (e.g. the thermal and system noise terms in the shared image) appear in the interferometric phases of both interferograms, introducing correlation between them.
2. *Common geometrical or Doppler-centroid decorrelation component*: Even if there is no shared image between interferograms, the imaging geometry of the four acquisitions which produce the two interferograms, can cause correlation in the phase components of geometrical decorrelation, see e.g. Agram and Simons (2015). Assume the four SLC images P_1 , P_2 , P_3 , and P_4 with the viewing geometry demonstrated in fig. 3.4. Then the total geometrical decorrelation noise affecting the interferometric phase ϕ_{34} also affects ϕ_{12} because of the overlap in the object spectrum, introducing correlation between the two interferometric phases. The same rationale can be also used for Doppler-centroid decorrelation, where an overlap in Doppler-baseline space can result in correlation between Doppler-centroid decorrelation phases in two interferograms.
3. *Common temporal decorrelation component*: An overlap between the time-period covered by two interferograms can cause correlation between components of temporal decorrelation. In other words, the changes in scattering characteristics of the surface during the common period of time affect the both interferograms in the

⁶Note that in this chapter, we are discussing the statistics of noise terms due to different decorrelation mechanisms (i.e., single-point statistics, see section 3.1 for more information on discrimination between different noise components). Therefore, when we talk about correlation or dependency, we mean correlation or statistical dependency between different noise terms for one pixel in two interferograms. This should not be mistakenly interpret as the correlation between other signal/noise components such as atmospheric or deformation phase.

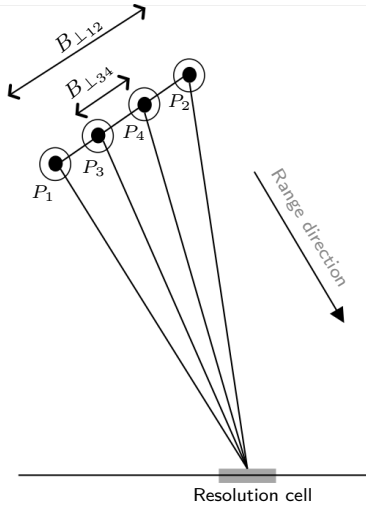


Figure 3.4: Example of InSAR acquisition geometry for four acquisitions P_1 , P_2 , P_3 , and P_4 : demonstration of the cause of correlation between geometrical decorrelation phases in two interferograms. The total geometrical decorrelation noise affecting the interferometric phase ϕ_{34} also affects ϕ_{12} because of the overlap in the baseline space, introducing correlation between the two interferometric phases. Figure adapted from Agram and Simons (2015).

same manner and may introduce a correlation between the temporal decorrelation phases.

3.4.2 Phase statistics for interferograms with a common image

In the case of only two interferometric phases constructed from three SLCs (i.e. ϕ_{12} and ϕ_{13} constructed from three SLCs in $y = [P_1, P_2, P_3]^T$ with absolute coherence matrix Υ), Lucido et al. (2010) evaluated a closed form expression for the joint PDF of the two interferometric phases as

$$f_{\phi_{12}, \phi_{13}}(\phi_{12}, \phi_{13}) = \frac{q}{(2\pi)^2 |\Upsilon|^{1/2} \prod_{i=1}^3 \lambda_{ii}} \left(1 + q(I_{1,2,3} + I_{2,3,1} + I_{3,1,2}) \right) \quad (3.68)$$

with the following variables:

- elements of the inverse of the absolute coherence matrix λ_{ij} defined as

$$\Upsilon^{-1} = \begin{bmatrix} 1 & |\gamma_{12}| & |\gamma_{13}| \\ |\gamma_{12}| & 1 & |\gamma_{23}| \\ |\gamma_{13}| & |\gamma_{23}| & 1 \end{bmatrix}^{-1} = \begin{bmatrix} \lambda_{11} & \lambda_{12} & \lambda_{13} \\ \lambda_{12} & \lambda_{22} & \lambda_{23} \\ \lambda_{13} & \lambda_{23} & \lambda_{33} \end{bmatrix}, \quad (3.69)$$

- parameter q defined as

$$q = \frac{1}{1 - r_{12}^2 - r_{13}^2 - r_{23}^2 + 2r_{12}r_{13}r_{23}} \quad (3.70)$$

where

$$r_{ik} = r_{ki} = \frac{\lambda_{ik} \cos(\phi_{ik} - \phi_{0_{ik}})}{\sqrt{\lambda_{ii} \lambda_{kk}}}, \quad (3.71)$$

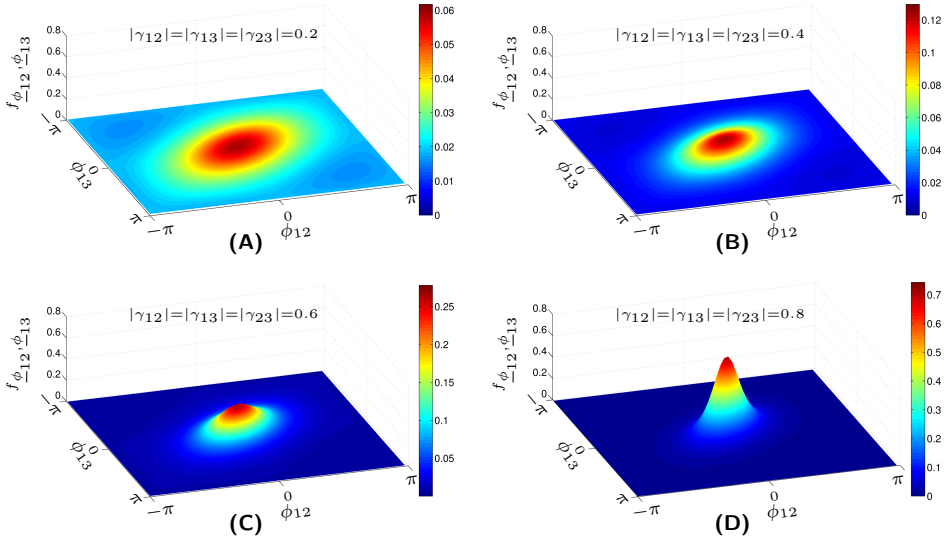


Figure 3.5: Examples of joint probability distribution function of two (single-look) interferometric phases ϕ_{12} and ϕ_{13} generated from three SLCs P_1, P_2 , and P_3 with mutual coherence between all pairs of SLCs equal to (A) 0.2, (B) 0.4, (C) 0.6, and (D) 0.8, assuming $\phi_{012}=0$ and $\phi_{013}=0$. The PDFs are evaluated based on the closed form expression of eq. (3.68). Colors denote the probability density. Note the difference in color scales.

- and $I_{i,k,l}$ given by

$$I_{i,k,l} = \frac{r_{ik}^3 + 2r_{il}r_{kl} - r_{ik}(1 + r_{il}^2) + r_{kl}^2}{\sqrt{(1 - r_{ik}^2)}} \left(\frac{\pi}{2} - \arctan\left(\frac{r_{ik}}{\sqrt{(1 - r_{ik}^2)}}\right) \right) \quad (3.72)$$

Note that the PDF of eq. (3.68) is periodic with 2π cycles in two dimensions. Considering wrapped phases in the interval $[-\pi, \pi)$, the peak/mode of the PDF is located at $[\phi_{012}, \phi_{013}]^T$.

Fig. 3.5 shows examples of 2D representation of the joint PDF given by eq. (3.68) for cases where the coherence between all SLC pairs assumed to be equal (i.e., $|\gamma_{12}|=|\gamma_{13}|=|\gamma_{23}|$), and for four different coherence values. Based on eq. (3.68), the joint PDF of two interferometric phases sharing the same master image depends not only on the coherence values of the two interferograms, but also depends on the coherence of the third interferogram constructed by the two slave images. Fig. 3.6 demonstrates this fact. In the plot, the coherence of two interferometric phases ϕ_{12} and ϕ_{13} is assumed to be constant and equal to $|\gamma_{12}|=|\gamma_{13}|=0.6$, but the coherence of the third interferogram (i.e. $|\gamma_{23}|$) is gradually increasing from 0.1 to 0.9. We can clearly see that the joint PDF of (and so the correlation between) the two interferometric phases varies depending on the value of the $|\gamma_{23}|$. Summarizing, in order to evaluate phase statistics of two interferometric phases constructed from three SLC values, the full 3×3 absolute coherence matrix Υ is required.

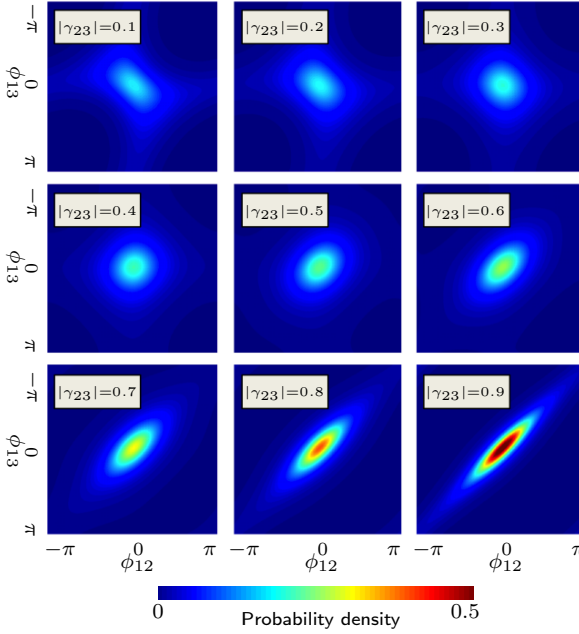


Figure 3.6: Examples of joint probability distribution function of two (single-look) interferometric phases ϕ_{12} and ϕ_{13} generated from three SLCs $P_1, P_2,$ and P_3 . In all the plots, the coherence of ϕ_{12} and ϕ_{13} is assumed to be constant and equal to $|\gamma_{12}|=|\gamma_{13}|=0.6$, but the coherence of the connecting interferogram is gradually increasing from 0.1 to 0.9. This is the demonstration of the fact that the joint PDF of and the correlation between two interferometric phases (sharing a common master image) not only depends on the coherence of two interferograms but also depends on the coherence of the interferometric phase between the two slave images. (Colors denote the probability density).

Note that eq. (3.68) evaluates the joint PDF for two connected interferograms — sharing a common master/slave image — and only for single-look pixels. For more general cases, i.e., for two interferograms without a common image and for different multilooking factors, there is no closed-form expression available. For these cases, we will discuss the first two statistical moments of the joint-PDF in the next section.

3.4.3 First and second statistical moments

The expected value of the random vector of two interferometric phases (i.e., $\underline{y} = [\phi_{12}, \phi_{34}]^T$) is defined as a vector whose elements are the expected values of each interferometric phase, and so (see eq. (3.62))

$$\mathbb{E}\{\underline{y}\} = \mathbb{E}\left\{\begin{bmatrix} \phi_{12} \\ \phi_{34} \end{bmatrix}\right\} = \begin{bmatrix} \mathbb{E}\{\phi_{12}\} \\ \mathbb{E}\{\phi_{34}\} \end{bmatrix} = \begin{bmatrix} \phi_{012} \\ \phi_{034} \end{bmatrix}. \quad (3.73)$$

The second statistical moment or dispersion of the vector $\underline{y} = [\phi_{12}, \phi_{34}]^T$ is defined as a 2×2 covariance matrix Q_y :

$$\begin{aligned} \mathbb{D}\{\underline{y}\} &= \mathbb{D}\left\{\begin{bmatrix} \phi_{12} \\ \phi_{34} \end{bmatrix}\right\} = Q_y = \begin{bmatrix} \sigma_{\phi_{12}}^2 & \sigma_{\phi_{12}, \phi_{34}} \\ \sigma_{\phi_{12}, \phi_{34}} & \sigma_{\phi_{34}}^2 \end{bmatrix} \\ &= \int_{\underline{y}} (\underline{y} - \mathbb{E}\{\underline{y}\})(\underline{y} - \mathbb{E}\{\underline{y}\})^T f_{\underline{y}}(\underline{y}) d\underline{y}, \end{aligned} \quad (3.74)$$

where $f_{\underline{y}}(y)$ represents the multivariate PDF of \underline{y} , i.e. $f_{\underline{y}}(y) = f_{\phi_{12}, \phi_{34}}(\phi_{12}, \phi_{34})$. The diagonal elements of this covariance matrix or the variance of the interferometric phases can be computed by numerical evaluation of eq. (3.63) for multilooked pixels, or by evaluation of eq. (3.64) for single-look cases. However, evaluation of the off-diagonal element or the covariance between interferometric phases requires numerical integration over the joint PDF :

$$\text{Cov}\{\phi_{12}, \phi_{34}\} = \sigma_{\phi_{12}, \phi_{34}} = \int_{-\pi}^{\pi} \int_{-\pi}^{\pi} \phi_{12} \phi_{34} f_{\phi_{12}, \phi_{34}}(\phi_{12}, \phi_{34}) d\phi_{12} d\phi_{34}. \quad (3.75)$$

Because the generic closed-form expression of the joint PDF is not available, eqs. (3.75) or (3.74) cannot be evaluated. Therefore, the evaluation of the full phase covariance matrix requires an alternative approach. In the following, we present two approaches for this purpose: one based on the numerical Monte-Carlo integration and the other based on an analytical approximation using nonlinear error propagation.

3.4.4 Evaluation of phase covariance matrix: Monte-Carlo method

Monte-Carlo methods were originally developed for numerical evaluation of integrals by generating random numbers (Ripley, 1987; Kalos and Whitlock, 2008; Liu, 2001). More specifically for the computation of second statistical moment of interferometric phases, the integral of eq. (3.74) can be numerically estimated by the Monte-Carlo integration as (Gundlich et al., 2003; Alkhatib, 2007)

$$D\{\underline{y}\} = Q_y = \frac{1}{M} \sum_{i=1}^M (y^{(i)} - E\{\underline{y}\})(y^{(i)} - E\{\underline{y}\})^T, \quad (3.76)$$

where $y^{(i)}, i = 1 \dots M$ are the M random realizations of vector \underline{y} generated from multivariate PDF $f_{\underline{y}}(y)$. In order to generate random realizations of the vector of interferometric phases $y^{(i)}$, in the first step, random realizations of vector of SLC values (i.e., $\underline{y}_{\text{slc}}$) are simulated from the multivariate circular Gaussian distribution specified by a coherence matrix. Subsequently, the sample vectors of interferometric phases are computed from the simulated SLC realizations. Finally the empirical covariance matrix is computed by eq. (3.76) based on the simulated realizations. The algorithm to compute the covariance matrix Q_y can be summarized as:

- **Inputs:** the $N \times N$ absolute coherence matrix Υ (assuming a stack of N SLC images), the multilooking factor L , and the number of realizations M , which should be chosen as a large number.
- **Step 1:** generate $M \times L$ vectors of samples $\underline{y}_{\text{slc}}^{(j)}, j = 1 \dots M \times L$ of the form of $\underline{y}_{\text{slc}}^{(j)} = [\text{Re}_1^j \dots \text{Re}_N^j \text{Im}_1^j \dots \text{Im}_N^j]^T$ from a zero-mean multivariate normal distribution⁷ with absolute coherence matrix $Q_{\underline{y}_{\text{slc}}} = \frac{1}{2} \begin{bmatrix} \Upsilon & 0 \\ 0 & \Upsilon \end{bmatrix}$ (see eq. (3.15)),

⁷Generating random samples from a multivariate normal distribution is a standard practice in numer-

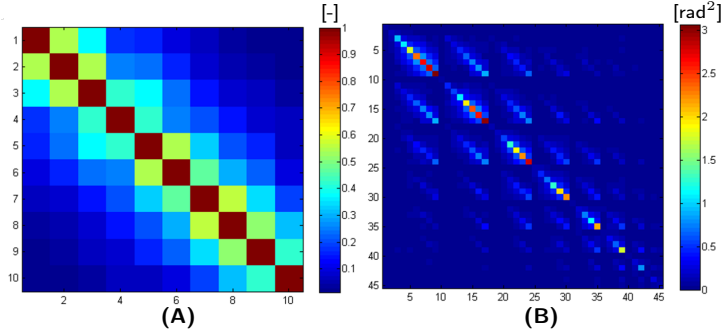


Figure 3.7: Demonstration of the Monte-Carlo method to propagate an absolute coherence matrix to interferometric phase covariance matrix: **(A)** An arbitrary 10×10 absolute coherence matrix Υ , **(B)** corresponding 45×45 covariance matrix Q_y computed by the Monte-Carlo method for the vector of all the 45 interferometric combinations constructed from the 10 SLC images, for multilooking factor $L = 25$. The 45 interferometric combinations in the vector \underline{y} are assumed to be ordered as $[\phi_{12} \dots \phi_{1N} \ \phi_{23} \dots \phi_{2N} \ \dots \ \phi_{(N-1)N}]$, where $N=10$.

- **Step 2:** compute M realizations of multilooked interferometric phase vectors $\underline{y}^{(i)}, i = 1 \dots M$ from $M \times L$ generated samples of SLC vectors $y_{\text{slc}}^{(j)}$,
- **Step 3:** compute the empirical covariance matrix by evaluation of eq. (3.76), where the expectation $E\{y\}$ can be estimated as the average of the simulated samples as $\hat{E}\{y\} = 1/M \sum_{i=1}^M y^{(i)}$.

Note that, although the integral of eq. (3.74) was written for the vector of only two interferometric phases (i.e., $\underline{y} = [\phi_{12}, \phi_{34}]^T$), the Monte-Carlo algorithm is generic and can be applied, in principle, to any stack of interferometric phases provided that an $N \times N$ absolute coherence matrix Υ is available. As a demonstration, for a stack of 10 SLC images, fig. 3.7 shows an arbitrary 10×10 coherence matrix Υ and its corresponding 45×45 covariance matrix Q_y computed by the Monte-Carlo method for the vector \underline{y} which includes all the 45 interferometric combinations constructed from the 10 SLC images (assuming multilooking factor $L = 25$). Note that the unit of interferometric phases is radian, so the unit of the elements of the covariance matrix is squared radians ($[\text{rad}^2]$).

3.4.5 Evaluation of phase covariance matrix: Analytical approximation

The closed-form evaluation of the second statistical moment of the vector of interferometric phases is challenging to derive due to the highly nonlinear relation between SLC values and multilooked interferometric phases (see eq. (2.23)), and hence such a closed-form expression has not been derived so far. In this section, we derive such an expression

ical simulations, and there are various libraries and packages for it in different programming/statistical environments. An example is the function `mvnrnd.m` in the MATLAB statistical toolbox (MATLAB, 2014). For more information concerning methods and algorithms of generating random vectors from multivariate normal distribution, see, for example, the textbooks by Gentle (2003) and Fishman (2003).

using the concept of nonlinear error propagation in order to propagate the dispersion of SLC values described by coherence matrix to the dispersion of interferometric phases.

Assume two complex interferograms \underline{I}_{12} and \underline{I}_{34} constructed from the set of four SLC values (i.e., $\underline{y}_{\text{slc}} = [\underline{P}_1, \underline{P}_2, \underline{P}_3, \underline{P}_4]^T$) with a circular complex Gaussian distribution described by a 4×4 absolute coherence matrix Υ

$$\Upsilon = \begin{bmatrix} 1 & |\gamma_{12}| & |\gamma_{13}| & |\gamma_{14}| \\ |\gamma_{12}| & 1 & |\gamma_{23}| & |\gamma_{24}| \\ |\gamma_{13}| & |\gamma_{23}| & 1 & |\gamma_{34}| \\ |\gamma_{14}| & |\gamma_{24}| & |\gamma_{34}| & 1 \end{bmatrix}. \quad (3.77)$$

We are interested in the dispersion or covariance matrix of the vector of interferometric phases $\underline{y} = [\underline{\phi}_{12}, \underline{\phi}_{34}]^T$. We assume, without loss of generality, that the amplitude of SLC images are normalized in the way that $E\{A_i^2\} = 1$ (Note that the final goal is the computation of the phase dispersion, which is invariant with respect to normalization of amplitudes).

In the complex plain, every multilooked interferometric phase can be computed as the ratio between the multilooked interferometric imaginary component over the real component, and so:

$$\phi_{i,j} = \arctan\left(\frac{\text{Im}(\langle I_{i,j} \rangle)}{\text{Re}(\langle I_{i,j} \rangle)}\right), \quad (3.78)$$

where $\langle \cdot \rangle$ denotes spatial complex averaging or complex multilooking. So the relationship between the vector of two interferometric phases (i.e., $\underline{y} = [\underline{\phi}_{12}, \underline{\phi}_{34}]^T$) and interferometric real/imaginary components can be written as

$$\underline{y} = \begin{bmatrix} \underline{\phi}_{12} \\ \underline{\phi}_{34} \end{bmatrix} = \begin{bmatrix} \arctan\left(\frac{\text{Im}(\langle I_{1,2} \rangle)}{\text{Re}(\langle I_{1,2} \rangle)}\right) \\ \arctan\left(\frac{\text{Im}(\langle I_{3,4} \rangle)}{\text{Re}(\langle I_{3,4} \rangle)}\right) \end{bmatrix}. \quad (3.79)$$

For simplicity, we express the vector of interferometric real and imaginary components as

$$\underline{x} = \begin{bmatrix} \underline{x}_1 \\ \underline{x}_2 \\ \underline{x}_3 \\ \underline{x}_4 \end{bmatrix} = \begin{bmatrix} \text{Re}(\langle I_{1,2} \rangle) \\ \text{Re}(\langle I_{3,4} \rangle) \\ \text{Im}(\langle I_{1,2} \rangle) \\ \text{Im}(\langle I_{3,4} \rangle) \end{bmatrix}. \quad (3.80)$$

the functional relationship between the the vector of two interferometric phases (i.e., $\underline{y} = [\underline{\phi}_{12}, \underline{\phi}_{34}]^T$) and the vector \underline{x} can be described as a multivariate function $F(\underline{x})$:

$$\underline{y} = \begin{bmatrix} \underline{\phi}_{12} \\ \underline{\phi}_{34} \end{bmatrix} = F(\underline{x}) = \begin{bmatrix} F_1(\underline{x}) \\ F_2(\underline{x}) \end{bmatrix} = \begin{bmatrix} \arctan\left(\frac{\underline{x}_3}{\underline{x}_1}\right) \\ \arctan\left(\frac{\underline{x}_4}{\underline{x}_2}\right) \end{bmatrix}. \quad (3.81)$$

Based on the nonlinear error propagation law, the dispersion of vector $\underline{y} = [\underline{\phi}_{12}, \underline{\phi}_{34}]^T$ can be approximated as:

$$Q_y = D\left\{ \begin{bmatrix} \underline{\phi}_{12} \\ \underline{\phi}_{34} \end{bmatrix} \right\} \approx J_F(\underline{x}|x_0) Q_x J_F(\underline{x}|x_0)^T, \quad (3.82)$$

where $J_F(\underline{x}|x_0)$ is the Jacobian of the multivariate function $F(\underline{x})$ with respect to the vector \underline{x} evaluated at an expected value x_0 . For zero-mean⁸ phases (i.e., $E\{\underline{\phi}_{1,2}\}=E\{\underline{\phi}_{3,4}\}=0$), and assuming x_0 equal to the expected values of the interferometric real and imaginary components, eq. (3.82) is evaluated and the dispersion or covariance matrix of the interferometric phase vector is approximated as (the explicit derivation is provided in Appendix A.1.1)

$$D\left\{\begin{bmatrix} \phi_{12} \\ \phi_{34} \end{bmatrix}\right\} \approx \begin{bmatrix} \frac{1-|\gamma_{12}|^2}{2L|\gamma_{12}|^2} & \frac{|\gamma_{13}||\gamma_{24}|-|\gamma_{14}||\gamma_{23}|}{2L|\gamma_{12}||\gamma_{34}|} \\ \frac{|\gamma_{13}||\gamma_{24}|-|\gamma_{14}||\gamma_{23}|}{2L|\gamma_{12}||\gamma_{34}|} & \frac{1-|\gamma_{34}|^2}{2L|\gamma_{34}|^2} \end{bmatrix}. \quad (3.83)$$

From eq. (3.83), the general equation for the interferometric phase variance and the covariance between interferometric phases are expressed as

$$D\{\underline{\phi}_{ij}\} = \sigma_{\underline{\phi}_{ij}}^2 \approx \frac{1-|\gamma_{ij}|^2}{2L|\gamma_{ij}|^2}, \quad (3.84)$$

and

$$\text{Cov}\{\underline{\phi}_{ij}, \underline{\phi}_{kl}\} = \sigma_{\underline{\phi}_{ij}, \underline{\phi}_{kl}} \approx \frac{|\gamma_{ik}||\gamma_{jl}| - |\gamma_{il}||\gamma_{jk}|}{2L|\gamma_{ij}||\gamma_{kl}|}. \quad (3.85)$$

Note that eq. (3.84) is in agreement with the CRB lower bound of eq. (3.66). Also for two interferometric phases with the same master image, equation (3.85) is reduced to

$$\text{Cov}\{\underline{\phi}_{ij}, \underline{\phi}_{ik}\} = \sigma_{\underline{\phi}_{ij}, \underline{\phi}_{ik}} \approx \frac{|\gamma_{jk}| - |\gamma_{ij}||\gamma_{ik}|}{2L|\gamma_{ij}||\gamma_{ik}|}. \quad (3.86)$$

In a stack of N SLC images, for the vector of any subset of interferometric phases, all the elements of the full covariance matrix of interferometric phases can be approximated by eqs. (3.84), (3.85), and (3.86) provided that the $N \times N$ absolute coherence matrix is available. In summary, with these two equations, the absolute coherence matrix Υ can be approximately propagated to the full covariance matrix of the multilooked interferometric phases. It should be pointed out that the approximation via nonlinear error propagation is valid when the dispersion of interferometric real/imaginary components is relatively small with respect to nonlinearity of the function $F(\underline{x})$ around its expectation. This assumption holds for high coherence values or a large number of looks. This is in fact the reason that the variance of eq. (3.84) gives exactly the variance of interferometric phase of point scatterers (see eq. (3.67)), which have a relatively large interferometric amplitude compared to dispersion of their interferometric real/imaginary components. As a demonstration for covariance evaluation between two interferometric phases ϕ_{12} and ϕ_{34} , we simulate some numerical examples. The setting of the simulation has been captured in fig. 3.8. Four SLC images P_1 , P_2 , P_3 , and P_4 are considered, with absolute coherence values $|\gamma_{ij}|$. Four of the coherence values are assumed to be constant and equal to an arbitrary value of 0.3, and the coherence values $|\gamma_{13}|$ and $|\gamma_{24}|$ are gradually increased in the simulation from 0 to 1. The results of the simulation for four different multilooking factors $L = 1, 5, 20$ and 50 are visualized in fig. 3.9. We can clearly see that eq. (3.85) provides an good approximation for high number of looks. This is expected as, for larger L , the dispersion of interferometric real and imaginary components gets smaller and so the nonlinear error propagation gives a better approximation.

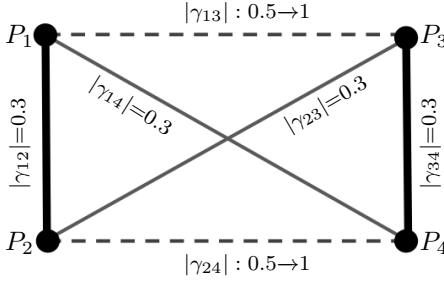


Figure 3.8: Stylized setting for the demonstration of covariance evaluation between two interferometric phases ϕ_{-12} and ϕ_{-34} (the results of simulation are visualized in fig. 3.9). Four SLC images P_1 , P_2 , P_3 , and P_4 are considered, with absolute coherence values $|\gamma_{ij}|$. Four of the coherence values assumed to be constant and equal to an arbitrary value 0.3, and the coherence values $|\gamma_{13}|$ and $|\gamma_{24}|$ are gradually increased in the simulation from 0.5 to 1.

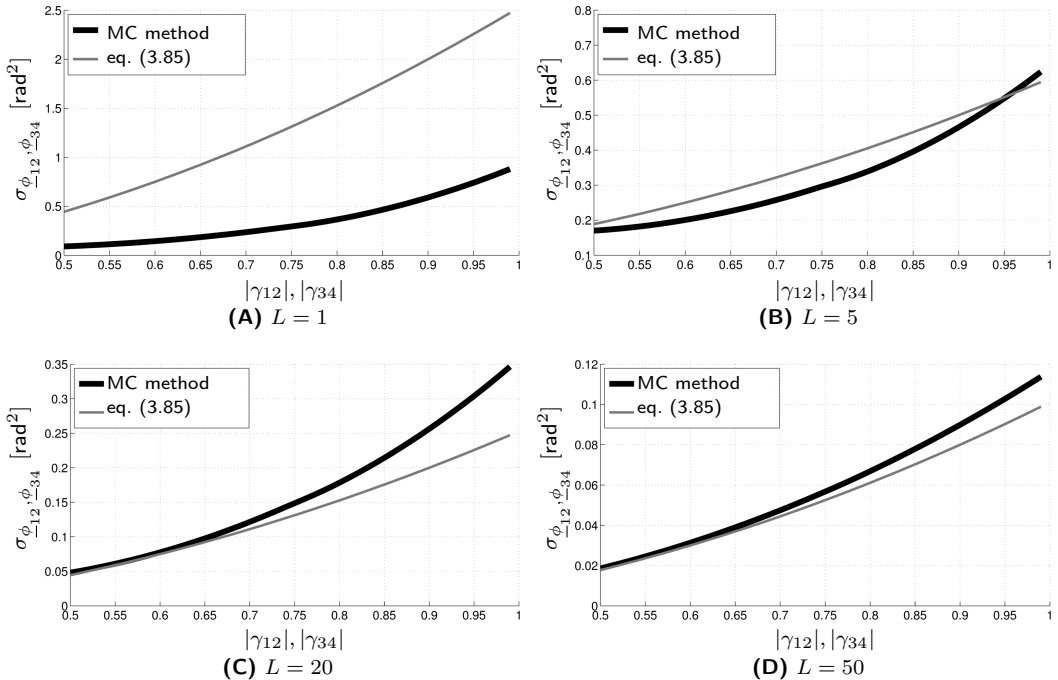


Figure 3.9: Demonstration of covariance evaluation between two interferometric phases ϕ_{-12} and ϕ_{-34} and comparison between evaluations by the Monte-Carlo approach and the closed-form evaluation of eq. (3.85), for four different multilooking factors: **(A)** $L = 1$, **(B)** $L = 5$, **(C)** $L = 20$, and **(D)** $L = 50$. The stylized setting of the demonstration have been visualized in fig. 3.8. We can see for higher number of looks, eq. (3.85) provides an good approximation.

Rocca (2007) and De Zan et al. (2015) also have reported an equation for the evaluation of covariance between interferometric phases as

$$\text{Cov}\{\phi_{ij}, \phi_{kl}\} \approx \frac{|\gamma_{il}||\gamma_{jk}| - |\gamma_{ij}||\gamma_{kl}|}{2L|\gamma_{ij}||\gamma_{kl}|}. \quad (3.87)$$

Note the difference between the numerators of eqs. (3.87) and (3.85). It is possible to show that eq. (3.87) derived by Rocca (2007) and De Zan et al. (2015) has been derived based on the simplified assumption that complex interferograms have a circular complex distribution, which is an invalid assumption as the Hermitian product of circularly Gaussian distributed SLC values does not generally follow a circular distribution (see Appendix A.1.1). Furthermore, we can see that eq. (3.85) is truly the function of all the six absolute coherence values in Υ , in contrast with eq. (3.87) which is invariant with respect to the coherence values $|\gamma_{ik}|$ and $|\gamma_{jl}|$. For example, for the demonstration setting of fig. 3.8, eq. (3.87) evaluates the covariance values equal to zero which is clearly wrong compared to the results of the Monte-Carlo simulation (see fig. 3.9). Hence, we conclude that eq. (3.85) is more generic than eq. (3.87) and is a better approximation for the phase covariance of interferometric phases.

3.5 Summary and conclusions

This chapter gave an overview of single-point statistics for distributed scatterers in both SAR and InSAR stacks. For stacks of SAR images, a comprehensive review of the associated probability distribution functions and their first and second statistical moments have been given in section 3.2, with the main focus on the coherence matrix as the main descriptor of SAR stack statistics. Different aspects of the evaluation of coherence matrices and the influence of different error sources on coherence values have been elaborated. We also reviewed the single-point statistics of interferometric phase values, for both cases of a single interferogram (section 3.3) and a stack of interferograms (section 3.4). For a vector of (multilooked) interferometric phases associated with a single DS-pixel, the stochastic model has been given in terms of second statistical moments or the covariance matrix. We have introduced a Monte-Carlo numerical approach to evaluate the covariance matrix of interferometric phases (section 3.4.4). As an alternative, an analytical approximation for evaluation of the variances and covariances of interferometric phases has been also derived by nonlinear propagation of SAR statistics (i.e., coherence matrix) into the dispersion of interferometric phases (section 3.4.5).

The covariance matrices constructed either by the proposed Monte-Carlo approach or by the analytical approximation of eq. (3.85) can serve as the stochastic part of the mathematical model for the ESM-phase estimation problem. In the next chapter, we discuss the functional model and different existing estimators for ESM-phase estimation.

⁸Note that the assumption of zero mean phase is equivalent to changing the integration interval of eqs. (3.58) and (3.59) to $(\phi_0 - \pi, \phi_0 + \pi)$ instead of $(-\pi, \pi)$ (see section 3.3 and eq. (3.63)).

ESM-Phase Estimation: Complex optimization methods

4

This chapter is about Equivalent Single Master (ESM) phase estimation. The concept of phase consistency is elaborated as the basic constraint imposed in all ESM-phase estimation methodologies (sec. 4.1). A generic mathematical model for ESM-phase estimation is introduced (sec. 4.2), and three different objective functions are given for this problem, one in the real-valued phase domain and the other two in the complex domain. The focus of this chapter is mainly on the ESM-phase estimation by optimization in the complex domain, while the next chapter will focus on the optimization in the phase domain. The existing estimators are revisited, and it is shown that all complex-domain estimators are a particular case of a generic mathematical model (sec. 4.3). Practical considerations about the solution of different estimators are discussed (sec. 4.4), followed by an elaboration of the lower Cramér-Rao Bound for the dispersion of ESM-phase estimation (sec. 4.5).

Equivalent Single Master (ESM) phase estimation is the key processing step for information extraction from DS-pixels (cf. sec. 2.5). This estimation filters out the decorrelation noise, while estimating, for each pixel, the SM-phase time-series corresponding to the physical path length differences between the targets and the sensor by exploiting a stack of multi-master interferometric phases.

In principle, ESM-phase estimation can be applied either after unwrapping or before unwrapping (see sec. 2.5). The details of the post-unwrapping ESM-phase estimation were discussed in section 2.5.1. The focus of this chapter is on pre-unwrapping estimation. In contrary to the post-unwrapping procedure, which is formulated by a linear model (eq. (2.48)), the functional relation between observations and unknown parameters is highly nonlinear in the case of pre-unwrapping estimation, and so it requires a more advanced estimation methodology compared to the post-unwrapping estimation.

Although various estimation methods can be found in InSAR literature (Monti-Guarnieri and Tebaldini, 2008; Ferretti et al., 2011b,a; Pepe et al., 2015; Fornaro et al., 2015; Cao et al., 2016) for pre-unwrapping ESM-phase estimation with different concepts and

mathematical formulation, there is strong similarities between them (Cao et al., 2015). Irrespective of the mathematical formulation, the ESM-phase estimation methodologies are all based on the principle of *phase consistency*. In brief, phase consistency¹ for each pixel means that for each set of three interferometric phases, obtained from three SLC images, each of the interferometric phases can be reconstructed from the other two interferometric phases. In the following sections, we first describe, in detail, the concept of phase consistency (sec. 4.1), followed by an introduction to a generic functional model for ESM-phase estimation (sec. 4.2), and a review of different existing methodologies in the framework of the proposed generic mathematical model (sec. 4.2.2).

4.1 Concept of phase consistency

Assume that P_m , P_n , and P_o are three SLC values corresponding to a pixel P in three different SAR images. (see fig. 4.1 as a simplistic example) in the form of

$$P_m = A_m \exp(j\psi_m), \quad (4.1)$$

where j is the imaginary unit, and $A_m \in \mathbb{R}^+$ and $\psi_m \in [-\pi, \pi)$ represent the amplitude and phase of P_m , respectively. Then the single-look interferometric values I_{om} , I_{on} and I_{nm} constructed from these SLC values can be written as

$$I_{om} = P_o P_m^*, \quad I_{on} = P_o P_n^*, \quad I_{nm} = P_n P_m^*, \quad (4.2)$$

where $*$ denotes the complex conjugate. It is trivial that the phase of these interferometric values follows (deterministically) from the other two, e.g.

$$\phi_{nm} = W\{\phi_{om} - \phi_{on}\}, \quad (4.3)$$

where ϕ_{nm} is the wrapped interferometric phase of I_{nm} , and $W\{\cdot\}$ the wrapping (modulo- 2π) operator. The equality of eq. (4.3) is called phase consistency, which holds by definition for single pixels.

However, for multilooked interferometric pixels, phase consistency does not necessarily hold, see fig. 4.1 as a numerical demonstration of phase consistency for single- and multilooked phases. The main source of inconsistency among multilooked phases is the random noise. For example, in the demonstration of fig. 4.1, we assume the signal to be zero, and random noise simulated based on a complex Gaussian distribution. Hence, the observed inconsistency among the multilooked phases is purely induced by the random noise. Apart from the noise, all other interferometric signal components (e.g. the atmospheric phase, topographic phase, and ground deformation phase) follow the phase consistency condition (even for multilooked phases) if they are constant within the averaging window².

¹The concept of *phase consistency* is called *phase triangularity* in some literature, e.g. in Ferretti et al. (2011b).

²However, it has been shown, see (De Zan et al., 2015; Zwieback et al., 2016), that there are also some scattering mechanisms which can induce systematic phase inconsistencies unrelated to the effect of random noise. Examples of these mechanisms are the volume scattering in the presence of perpendicular baselines or variation in the soil moisture. To limit the scope of this study, these mechanisms and their effects on phase estimation are not elaborated further, see the recommendations of sec. 7.3

Under certain statistical conditions, the phase consistency for multilooked pixels can be expressed in terms of phase expectation. Assuming a distributed scattering mechanism (i.e. each SAR pixel as a superposition of contributions from many elementary scatterers in a resolution cell), SLC pixels have a zero-mean circular Gaussian distribution (Madsen, 1986; Bamler and Hartl, 1998). Under this assumption, the expectation of complex interferometric observations can be written as (cf. eq. (3.16))

$$E\{\underline{I}_{nm}\} = \zeta_{nm} |\gamma_{nm}| \exp(j(\varphi_n - \varphi_m)), \quad (4.4)$$

where $E\{\cdot\}$ is the expectation operator, $|\gamma_{nm}|$ the absolute value of normalized interferometric coherence, and $\zeta_{nm} = \sqrt{E\{\underline{A}_n^2\}E\{\underline{A}_m^2\}}$ is the expected power of the two SLC pixels. The phase terms $\varphi_n \in [-\pi, \pi)$ and $\varphi_m \in [-\pi, \pi)$ are the deterministic components of ψ_i and ψ_j , respectively, and they are defined as the phase contributions related to the physical path difference between the target and the sensor (i.e. the phase contributions of deformation, topography, atmosphere and orbital errors). We can rewrite eq. (4.4) by adding and subtracting the true phase value of another image P_o from the argument of the complex interferogram \underline{I}_{nm} :

$$\begin{aligned} E\{\underline{I}_{nm}\} &= \zeta_{nm} |\gamma_{nm}| \exp(j(\varphi_n - \varphi_m)) \\ &= \zeta_{nm} |\gamma_{nm}| \exp(j(\varphi_n - \varphi_o - \varphi_m + \varphi_o)) \\ &= \zeta_{nm} |\gamma_{nm}| \exp(j(\varphi_{om} - \varphi_{on})), \end{aligned} \quad (4.5)$$

where φ_{om} and φ_{on} are now the true values of the interferometric phases, and \underline{A}_{nm} the interferometric amplitude. If $\hat{\phi}_{nm}$ denotes the multilooked phase, under the assumption that the signal components φ are constant within the averaging window, we obtain (Just and Bamler, 1994)

$$E\{\exp(j\hat{\phi}_{nm})\} = E\{\exp(j\hat{\phi}_{nm})\} = \exp(j(\varphi_{om} - \varphi_{on})), \quad (4.6)$$

or in alternative formulation in the phase domain:

$$E\{\underline{\phi}_{nm}\} = E\{\hat{\phi}_{nm}\} = W\{\varphi_{om} - \varphi_{on}\}. \quad (4.7)$$

In contrast to eq. (4.3), we call the eq. (4.6) or (4.7) the *expected phase consistency* condition, which is the same as the phase consistency but defined on the expected value of interferometric phases.

Based on this formulation, ESM-phase estimation is defined as the estimation of a set of *consistent* interferometric phases (i.e. where phase consistency holds for every combination of three interferograms) from a stack of *inconsistent* multilooked interferograms. In other words, ESM-phase estimation is the extraction of a deterministic signal φ from stochastic multilooked observations $\hat{\phi}_{nm}$ under the expected phase consistency condition.

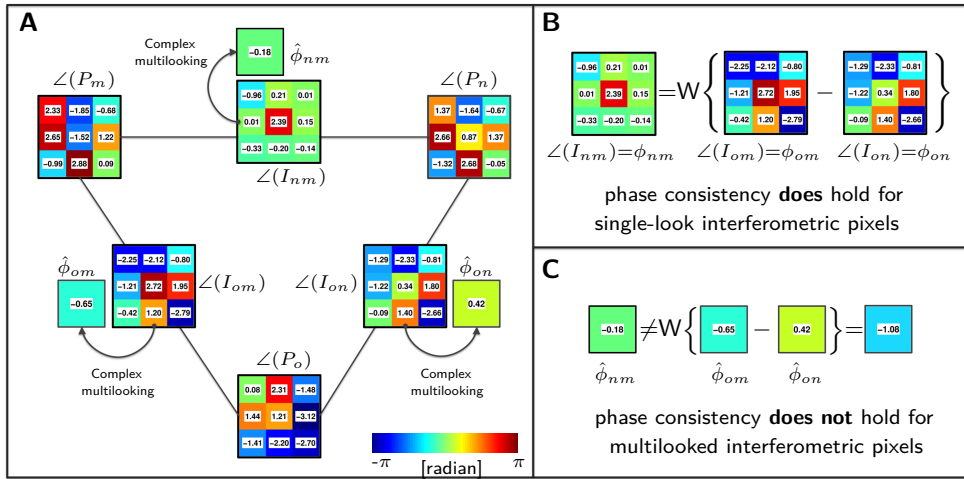


Figure 4.1: Numerical demonstration of phase inconsistency: **(A)** Three 3×3 phase interferograms constructed from the 3×3 SLC phases ($\angle(P_o), \angle(P_m), \angle(P_n)$), and the corresponding multilooked interferometric phases ($\hat{\phi}_{om}, \hat{\phi}_{on}, \hat{\phi}_{nm}$), **(B)** demonstration of the phase *consistency* condition for single-look pixels, **(C)** demonstration of the phase *inconsistency* for multilooked pixels. Note that, in this context, multilooking is always complex (i.e., it is applied by coherent averaging). Figure taken from Samiei-Esfahany et al., 2016.

4.2 Generic mathematical model

4.2.1 Functional model

In a stack of N SLC images, for each pixel, the observation vector contains M_{ifg} potential multilooked wrapped interferometric phases. In the most generic, case where all the interferometric combinations are used, the observation vector is a vector of size $M_{\text{ifg}} = N(N-1)/2$, containing the total number of multilooked wrapped interferometric phases $\hat{\phi}_{nm}$, where n and m are the radar image indices. The unknown parameters are the *true* SM wrapped interferometric phases ϕ_{oi} , where the o -index indicates the master acquisition. Then, eqs. (4.6) and (4.7) can be regarded as nonlinear observation equations with ϕ_{nm} as observations, and ϕ_{on} and ϕ_{om} as the unknown parameters of interest. In matrix notation, the nonlinear system of observation equations in the phase

domain (based on eq. 4.7) can be written as

$$E \left\{ \underbrace{\begin{bmatrix} \hat{\phi}_{o1} \\ \vdots \\ \hat{\phi}_{o(N-1)} \\ \vdots \\ \hat{\phi}_{nm} \\ \vdots \end{bmatrix}}_{\underline{y}} \right\} = W \left\{ \underbrace{\begin{bmatrix} 1 & & & & \\ & \ddots & & & \\ & & & & 1 \\ & & \vdots & & \\ -1 & \dots & 1 & & \\ & & \vdots & & \end{bmatrix}}_{B} \underbrace{\begin{bmatrix} \varphi_{o1} \\ \vdots \\ \varphi_{o(N-1)} \end{bmatrix}}_b \right\}, \quad (4.8)$$

or in a compact form as

$$E\{\underline{y}\} = W\{Bb\}, \quad (4.9)$$

where $n, m=1 \dots (N-1)$, \underline{y} is the observation vector, b the vector of unknown parameters, and B the design matrix depending on the set of multi-master interferograms. Instead of formulating the problem in the real number domain (the phase domain) and using a wrapping operator, the same functional model can be formulated in the complex domain (based on eq. (4.6)), using the complex phasors as

$$E\{\exp^\circ(j\underline{y})\} = \exp^\circ(jBb), \quad (4.10)$$

where $\exp^\circ(\cdot)$ is Hadamard (entry-wise) exponential function (Horn and Johnson, 1990, 1991). Equations (4.9) or (4.10) can be considered as the generic functional model for pre-unwrapping SM-phase estimation with M_{ifg} observations and $N-1$ unknowns.

4.2.2 Objective functions

In order to solve the inconsistent system of equations in eq. (4.9) and find an optimal estimate \hat{b} , we require a metric as a measure of difference between the phase observations in \underline{y} and the predicted observations $\hat{\underline{y}}$ that are given by the forward model $\hat{\underline{y}} = W\{B\hat{b}\}$. As the values in both \underline{y} and $\hat{\underline{y}}$ are wrapped phases, the difference between them should be also wrapped. This difference is called the *residual vector* and defined as $e = W\{\underline{y} - \hat{\underline{y}}\}$. In principle, it is possible to define different metrics (or objective function) for ESM-phase estimation based on the length of the residual vector e or its complex phasor $\exp^\circ(je)$.

A common metric in estimation theory is the weighted L2-norm of the residual vector:

$$\|e\|_W^2 = e^T W e, \quad (4.11)$$

where W is a weight matrix assigning weights to different observations. Based on this metric, the least squares (LS) solution of ESM-phase estimation can be defined as a nonlinear minimization problem:

$$\hat{b}_{\text{LS}} = \underset{b}{\operatorname{argmin}} \|e\|_W^2 = \underset{b}{\operatorname{argmin}} \|W\{\underline{y} - W\{Bb\}\}\|_W^2. \quad (4.12)$$

Although the LS principle provides the optimal solution for many estimation problems, its application for ESM-phase estimation requires coping with the strong nonlinearity and discontinuity that is induced by the wrapping operator in eq. (4.12). We introduce a new methodology for solving the nonlinear LS problem of eq. (4.12) in chapter 5. In the rest of this chapter, we focus on alternative objective functions that are defined over complex residual phasors instead of real residual phases. We define the vector of residual phasors as

$$r = \exp^\circ(je) = \exp^\circ\left(j(y - W\{\hat{B}\hat{b}\})\right) = \exp^\circ\left(j(y - \hat{B}\hat{b})\right). \quad (4.13)$$

The vector of residual phasors r can be considered as the complex counterpart of the real-valued residual vector e . For minimizing the residual phase values in e , two different metrics can be defined over the complex vector r : one is based on the circular variance of the phase values of the phasor elements in r , while the other is based on the real value of the vector summation over r . We describe these two metrics and their corresponding objective functions for ESM-phase estimation in the following.

Circular variance of residual phases

For circular variables³ like wrapped residual phases in e , a measure for the dispersion around the mean is the (weighted) ensemble circular variance s_e^2 which has been defined as (Fisher, 1995; Mardia and Jupp, 2000):

$$s_e^2 = 1 - \left| \frac{\sum_{i=1}^M w_i \exp(je_i)}{\sum_{i=1}^M w_i} \right| = 1 - \left| \frac{\sum_{i=1}^M w_i r_i}{\sum_{i=1}^M w_i} \right|, \quad (4.14)$$

where e_i ($i = 1 \dots M$) are the residual phases, r_i ($i = 1 \dots M$) are the elements of the vector of residual phasors r , and w_i ($i = 1 \dots M$) are the weighting factors. Note that the second term in the right hand side of eq. (4.14) is the normalized length of the resultant vector that is computed from weighted summation of residual phasors r_i . The weighted circular variance s_e^2 has a minimum value of zero and a maximum value of 1. We can write eq. (4.14) in matrix form as

$$s_e^2 = 1 - \left| \frac{\text{sum}(Wr)}{\text{tr}(W)} \right|, \quad (4.15)$$

where W is the $M \times M$ diagonal weight matrix whose i th diagonal element is equal to w_i , and $\text{sum}(\cdot)$ and $\text{tr}(\cdot)$ denote the sum of the vector elements and the trace of the matrix, respectively.

For solving the ESM-phase estimation problem, the objective function can be defined as the ensemble weighted circular variance of residual phases and the solution can be found

³Circular (or angular) variables are variables whose their possible highest and lowest values are approaching together, while the definition of the higher and lower values for them is arbitrary. A particular class is the wrapped interferometric phase whose lowest value $-\pi$ is approaching to its highest value $\pi - \epsilon$ (where ϵ is a small positive infinitesimal quantity). For more information about circular variables and their statistics, see Fisher (1995); Mardia and Jupp (2000), and Jammalamadaka and SenGupta (2001).

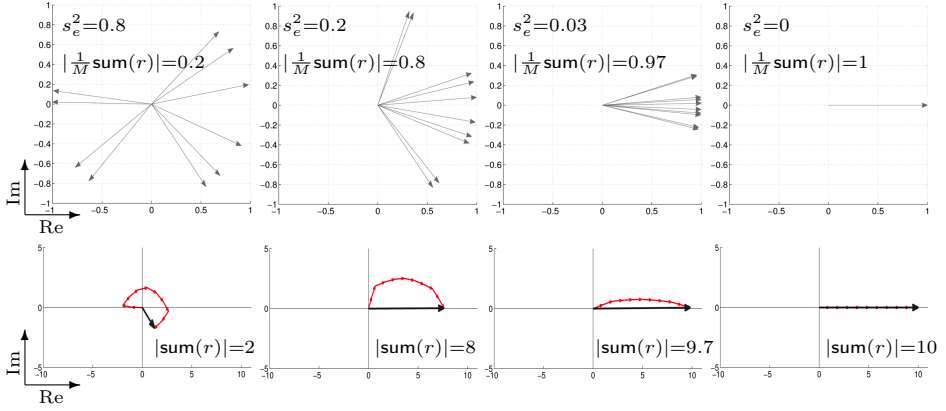


Figure 4.2: Demonstration of the relation between phase variance and the length of the resultant vector (i.e., $|\text{sum}(r)|$) in the complex domain: assuming 10 number of residual phases, we simulated four different sets of residual phases from high to low dispersion, i.e., from left to right respectively. In the latest set, the phase dispersion is zero, and so all the 10 phasors are identical and they are super-imposed on each other. The resultant vector $\text{sum}(r)$ is visualized in the bottom row plots by the solid black lines. Maximizing the length of the resultant vector is equivalent to minimizing the phase dispersion.

by the following nonlinear optimization

$$\begin{aligned}
 \hat{b}_{\text{LCV}} &= \underset{b}{\operatorname{argmin}} \left(1 - \left| \frac{\text{sum}(Wr)}{\operatorname{tr}(W)} \right| \right) \\
 &= \underset{b}{\operatorname{argmin}} \left(1 - \left| \frac{\text{sum}\left(W \exp^\circ(j(y - Bb))\right)}{\operatorname{tr}(W)} \right| \right) \\
 &= \underset{b}{\operatorname{argmax}} \left| \frac{\text{sum}\left(W \exp^\circ(j(y - Bb))\right)}{\operatorname{tr}(W)} \right| \\
 &= \underset{b}{\operatorname{argmax}} \left| \text{sum}\left(W \exp^\circ(j(y - Bb))\right) \right|, \tag{4.16}
 \end{aligned}$$

where LCV is the acronym for *least circular variance*. We see that minimizing the weighted circular variance is equivalent to maximizing the length of the resultant vector $\text{sum}(r)$. In fig. 4.2, this fact is demonstrated. Assuming $M = 10$ number of residual phases, we simulated four different sets of residual phases from high to low dispersion (from left to right respectively). The resultant vector is visualized in the bottom row plots. We observe that maximizing the length of the resultant vector results in the minimization of the residual phase dispersion. It should be noted that the same metric has been used by Pepe et al. (2015) for ESM-phase estimation with weights equal to the estimated pixel coherence in every interferograms, see more details in sec. 4.3.4. A discussion on different algorithms for solving the nonlinear optimization of eq. (4.16) is given in sec. 4.4.

Real value of the resultant vector of r

An alternative metric for ESM-phase estimation can be defined based on the real value of

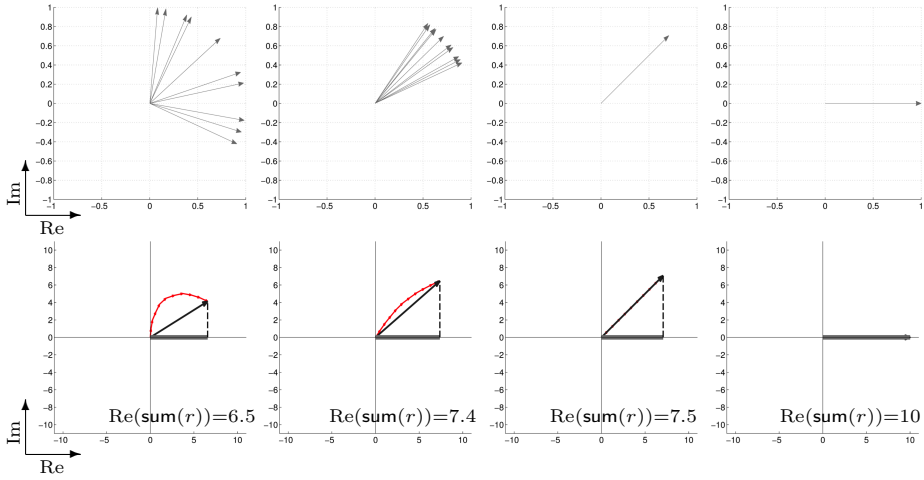


Figure 4.3: Demonstration of the relation between residual phase values and the real part of the resultant vector in the complex domain: assuming 10 residual phases, we simulated four different sets of residual phases. The phase dispersion is reduced from left to right. The phase dispersion is zero and identical for the third and the fourth set, but all the phases are equal to zero in the fourth set. The resultant vector and its real part are visualized in the bottom row plots (the solid lines/vectors). Maximizing the real part of the resultant vector is equivalent to minimizing the residual phase values. Although the phase dispersion is identical in the third and fourth cases, the real part of the resultant vector is larger for zero phases.

the resultant vector $\text{sum}(r)$. In fig. 4.3, it is demonstrated that the resultant vector that contains phasors with minimum residual phases gives the maximum real value. Based on this metric, the solution of the ESM-phase estimation is given by

$$\hat{b}_{\text{RR}} = \underset{b}{\operatorname{argmax}} \operatorname{Re} \left(\operatorname{sum} \left(W \exp^{\circ} \left(j(y - Bb) \right) \right) \right), \quad (4.17)$$

where RR is the acronym for *Real value of the Resultant vector*. Note the conceptual difference between maximization of eq. (4.17) and the one of eq. (4.16): by maximizing the real part of the resultant vector, the optimization of eq. (4.17) not only inserts the condition of minimum phase variance (i.e, the same as eq. (4.16)), but also it constrains the phasors r_i to have minimum absolute phase values (see fig. 4.3). In other words, in contrast to the objective function of eq. (4.16) which is invariant for a common offset in the residual phases, eq. (4.17) has a maximum value when the phase offset is also minimum.

It is possible to show that all the existing ESM-phase estimators are special cases of one of the two optimization problems of eq. (4.16) or eq. (4.17), as elaborated in the following section.

4.3 A review of existing estimators

In this section, we revise the existing estimators and formulate them based on the generic mathematical framework introduced in sec. 4.2. Note that in this section, we only focus on the mathematical formulation of different estimators. Practical issues concerning the solution of these estimators are discussed later in sec. 4.4.

4.3.1 Maximum Likelihood method

The maximum likelihood (ML) estimator for ESM-phase estimation was originally introduced by Monti-Guarnieri and Tebaldini (2008), who referred to this estimation as *phase linking*. Later, a similar ML concept was used in the framework of the SqueeSAR algorithm (Ferretti et al., 2011b). The ML estimation is based on maximizing the multivariate joint-probability distribution of SLC values within the averaging/brotherhood area that used for multi-looking. In order to formulate this joint PDF, the point of departure is to consider the multivariate PDF of the $N \times 1$ SLC vector d_k for a pixel k (see eq. (3.21)):

$$f_{\underline{d}_k}(d_k|\Psi) = c \cdot \exp(-d_k^* \Psi \Upsilon^{-1} \Psi^* d_k), \quad (4.18)$$

which is conditioned on the unknown phase values in Ψ . Here, c is a constant value, Υ is the $N \times N$ absolute coherence matrix, and Ψ is an $N \times N$ diagonal complex matrix defined by:

$$\Psi = \text{diag}\left\{\exp(j\varphi_0), \exp(j\varphi_1), \dots, \exp(j\varphi_{(N-1)})\right\}, \quad (4.19)$$

where φ_i is the true phase value in the i th image. Assuming the true phases φ_i are constant within the multilooking area (denoted by Ω), and assuming statistical independence between adjacent pixels, the multivariate joint-PDF of L number of pixels in Ω is proportional to the multiplication of PDFs of individual pixels within Ω :

$$f_{\underline{d}_\Omega}(d_\Omega|\Psi) \propto \prod_{k=1}^L \exp(-d_k^* \Psi \Upsilon^{-1} \Psi^* d_k), \quad (4.20)$$

where $d_\Omega = [d_1^T, d_2^T, \dots, d_L^T]^T$. Equation (4.20) can be re-arranged as (see the proof in sec. A.2.1)

$$f_{\underline{d}_\Omega}(d_\Omega|\Psi) \propto \exp(-\text{tr}(\Psi \Upsilon^{-1} \Psi^* \hat{\Gamma})), \quad (4.21)$$

where $\hat{\Gamma}$ is the complex coherence matrix estimated based on the pixels within Ω . Based on this formulation, the ML estimates for the φ_i values in Ψ can be computed by maximizing the conditional PDF of eq. (4.21). However, as only phase differences (or interferometric phases) appear in $\hat{\Gamma}$, the problem is under-determined considering N unknown parameters, and the φ_i values can be estimated only up to an arbitrary constant. Without loss of generality, to deal with this under-determined problem, the ML methods set the φ_i of one of the images (e.g., master image) to zero (Monti-Guarnieri and Tebaldini, 2008; Ferretti et al., 2011b). By doing so, in fact the phase differences (or interferometric phases) with respect to the assumed master image are estimated. Therefore, although the ML mathematical model is formulated explicitly

based on SLC phases, by setting the master image phase to zero, the ESM-phases are implicitly estimated. If we denote the master image by the index "o", the constraint $\varphi_o = 0$ in Ψ is equivalent to subtracting the φ_o from all φ_i phases, and by doing so, a new vector Φ can be defined as

$$\Phi = \left[\exp(j(\varphi_o - \varphi_o)), \exp(j(\varphi_o - \varphi_1)), \dots, \exp(j(\varphi_o - \varphi_{(N-1)})) \right]^T \quad (4.22)$$

$$= \left[1, \exp(-j\varphi_{o1}), \dots, \exp(-j\varphi_{o(N-1)}) \right]^T \quad (4.23)$$

$$= \left[1, \exp^\circ(-jb) \right]^T, \quad (4.24)$$

where b is the $N-1$ vector of unknown parameters of the ESM-phase estimation problem (see eq. (4.8)). With this formulation, the ML estimates of the unknown parameters in b are computed by the following maximization problem (Monti-Guarnieri and Tebaldini, 2008; Ferretti et al., 2011b):

$$\hat{b}_{\text{ML}} = \arg \max_b \left\{ \Phi^* (-\Upsilon^{-1} \circ \hat{\Gamma}) \Phi \right\}. \quad (4.25)$$

As the true coherence matrix Υ is always unknown, the ML methods use the inverse of the estimated absolute coherence matrix $\hat{\Upsilon} = \text{abs}(\hat{\Gamma})$, and therefore (Monti-Guarnieri and Tebaldini, 2008; Ferretti et al., 2011b):

$$\hat{b}_{\text{ML}} = \arg \max_b \left\{ \Phi^* (-\hat{\Upsilon}^{-1} \circ \hat{\Gamma}) \Phi \right\}. \quad (4.26)$$

It is possible to show that the maximization problem of eq. (4.26) can be expressed in the following form (see the proof in sec. A.2.2):

$$\hat{b}_{\text{ML}} = \arg \max_b \left\{ \text{Re} \left(\sum_{m=1}^N \sum_{n>m}^N -[\hat{\Upsilon}^{-1}]_{[m,n]} |\hat{\gamma}_{mn}| \exp(j(\hat{\phi}_{mn} - \varphi_{om} + \varphi_{on})) \right) \right\}, \quad (4.27)$$

where $[\hat{\Upsilon}^{-1}]_{[m,n]}$ is the element of matrix $\hat{\Upsilon}^{-1}$ at row m and column n . Note that the exponent of eq. (4.27) is equivalent to the complex residual phasors of the generic model of the ESM-phase estimation problem (see eq. (4.13)). Therefore, by writing eq. (4.27) in a vector form based on eq. (4.13), we get:

$$\hat{b}_{\text{ML}} = \arg \max_b \text{Re} \left(\text{sum} \left(W_{\text{ML}} \exp^\circ(j(y - Bb)) \right) \right), \quad (4.28)$$

where W_{ML} is an $M \times M$ diagonal weight matrix (M is the number of interferograms, in this case $M=N(N-1)/2$). The i th diagonal element of W_{ML} is defined as

$$[W_{\text{ML}}]_{[i,i]} = -[\hat{\Upsilon}^{-1}]_{[m,n]} |\hat{\gamma}_{mn}|, \quad i = 1 \dots M, \quad (4.29)$$

where the i factor denotes the interferogram-index corresponding the the interferometric combination mn .

We can see that eq. (4.27) is a specific case of the objective function of eq. (4.17), with the weight matrix equal to W_{ML} . The main property of the ML mathematical

model is that by exploiting the complex coherence matrix $\hat{\Gamma}$, it uses all the $N(N - 1)/2$ possible interferometric combinations. Also it requires the inverse of the absolute coherence matrix $\hat{\Upsilon}$, which is, in general, not positive-definite due to the biased coherence estimation, and therefore the ML algorithms require the introduction of a damping factor to remove small negative or null eigenvalues of $\hat{\Upsilon}$ prior to the matrix inversion (Ferretti et al., 2011b).

4.3.2 Maximum coherence-based-weighted sum of residual phasors (MCSR)

Ferretti et al. (2011a) introduced an alternative objective function for the ESM-phase estimation problem based on maximizing the real value of the coherence-based-weighted sum of the residual phasors r_i (see eq. (4.17)). In this approach, the $N-1$ unknown SM-phases in vector b are estimated by the following maximization problem

$$\hat{b}_{\text{MCSR}} = \arg \max_b \left\{ \text{Re} \left(\sum_{m=1}^N \sum_{n=1}^N |\hat{\gamma}_{mn}|^p \exp(j(\hat{\phi}_{mn} - \varphi_{om} + \varphi_{on})) \right) \right\}, \quad (4.30)$$

where the exponent p is a positive real number used to assign different weights to the coherence values $|\hat{\gamma}_{mn}|$. The summations in eq. (4.30) can be also re-written as (the proof is similar to the proof of eq. (4.30), see sec. A.2.2)

$$\hat{b}_{\text{MCSR}} = \arg \max_b \left\{ \text{Re} \left(\sum_{m=1}^N \sum_{n>m}^N |\hat{\gamma}_{mn}|^p \exp(j(\hat{\phi}_{mn} - \varphi_{om} + \varphi_{on})) \right) \right\}, \quad (4.31)$$

which in the vectorized form can be expressed as

$$\hat{b}_{\text{MCSR}} = \arg \max_b \text{Re} \left(\text{sum} \left(W_{\text{MCSR}} \exp^\circ(j(y - Bb)) \right) \right), \quad (4.32)$$

where W_{MCSR} is an $M \times M$ diagonal weight matrix. The i th diagonal element of W_{MCSR} is defined as

$$[W_{\text{MCSR}}]_{[i,i]} = |\hat{\gamma}_{mn}|^p \quad (4.33)$$

where the i -factor ($i = 1 \dots M$) denotes the interferogram-index corresponding to the interferometric combination mn . We can see that—similar to the ML estimator—the MCSR estimator of eq. (4.32) is a specific case of the objective function of eq. (4.17), but with the weight matrix equal to W_{MCSR} . In contrast to the ML estimator, the MCSR method does not require the inversion of the absolute coherence matrix. This property can be considered as a computational advantage of this approach. Although the original MCSR formulation uses all the possible interferograms, it is easy to exclude interferograms in this method by assigning zero weights to them. In this way, the MCSR formulation, in contrary to ML estimator, has the flexibility to digest also a subset of interferograms.

4.3.3 Eigendecomposition-based methods

The eigendecomposition-based method for ESM-phase estimation was originally introduced by Fornaro et al. (2015) in the framework of the CAESAR algorithm. This ESM-phase estimation is based on an eigenvalue decomposition (EVD) of the SLC data covariance matrix, which is estimated for each pixel by

$$\hat{Q}_{y_{slc}} = \frac{1}{L} \sum_{k \in \Omega} d_k d_k^*, \quad (4.34)$$

where d_k is the $N \times 1$ vector of SLC values for pixel k , Ω is the pixel multilooking/brotherhood area, and L is the number of samples within Ω . Note that the $[m, n]$ elements of $\hat{Q}_{y_{slc}}$ are equal to:

$$[\hat{Q}_{y_{slc}}]_{[m,n]} = \hat{I}_{mn} \hat{\gamma}_{mn} = \hat{I}_{mn} |\hat{\gamma}_{mn}| \exp(j \hat{\phi}_{mn}), \quad (4.35)$$

where \hat{I}_{mn} denotes the $[m, n]$ element of the average power matrix \bar{I} , see eq. (3.7).

$$\hat{I}_{mn} = \frac{1}{N} \sqrt{\left(\sum_{k \in \Omega} |d_{k_m}|^2 \right) \left(\sum_{k \in \Omega} |d_{k_n}|^2 \right)}. \quad (4.36)$$

The ESM-phases are estimated by extracting the complex eigenvector corresponding to the largest eigenvalue of the complex covariance matrix $\hat{Q}_{y_{slc}}$. The phases of this eigenvector are the estimates for the ESM-phase estimation. Assuming \hat{u}_1 to be the first eigenvector corresponding to the largest eigenvalue of $\hat{Q}_{y_{slc}}$, the \hat{u}_1 is the result of the following maximization problem (Fornaro et al., 2015)

$$\hat{u}_1 = \arg \max_u \{ u^* \hat{Q}_{y_{slc}} u \}, \quad \text{subject to} \quad u^* u = 1. \quad (4.37)$$

Because for the ESM-phase estimation the only free parameters are the SM-phase values, the maximization of eq. (4.37) can be considered as a maximization over vector u whose absolute values are fixed to the absolute value of the largest eigenvector \hat{u}_1 but its phases are variable. Therefore, eq. (4.37) can be reformulated as (Cao et al., 2015)

$$\hat{u}_1 = \arg \max_{u_1} \{ u_1^* \hat{Q}_{y_{slc}} u_1 \}, \quad \text{subject to} \quad u_1^* u_1 = 1, \quad (4.38)$$

where u_1 is defined as

$$\begin{aligned} u_1 &= \left[|u_1|_1 \exp(j(\varphi_o - \varphi_o)), |u_1|_2 \exp(j(\varphi_1 - \varphi_o)), \dots, |u_1|_{N-1} \exp(j(\varphi_{N-1} - \varphi_o)) \right]^T, \\ &= |u_1| \circ \left[\exp(j0), \exp(j(\varphi_1 - \varphi_o)), \dots, \exp(j(\varphi_{N-1} - \varphi_o)) \right]^T \\ &= |u_1| \circ [1, \exp^\circ(-jb)]^T. \end{aligned} \quad (4.39)$$

By inserting the u_1 of eqs. (4.39) and (4.35) in eq. (4.38), the maximization problem can be written over phase differences in b as (Cao et al., 2015)

$$\hat{b}_{EVQ} = \arg \max_b \left\{ \text{Re} \left(\sum_{m=1}^N \sum_{n>m}^N [|u_1| |u_1^T|]_{[m,n]} \hat{I}_{mn} |\hat{\gamma}_{mn}| \exp(j(\hat{\phi}_{mn} - \varphi_{om} + \varphi_{on})) \right) \right\}, \quad (4.40)$$

which in the vectorized form can be formulated as

$$\hat{b}_{\text{EVQ}} = \arg \max_b \operatorname{Re} \left(\sum \left(W_{\text{EVQ}} \exp^\circ (j(y - Bb)) \right) \right), \quad (4.41)$$

where W_{EVQ} is a $M \times M$ diagonal weight matrix with diagonal elements as

$$[W_{\text{EVQ}}]_{[i,i]} = [|u_1| |u_1^T|]_{[m,n]} \hat{I}_{mn} |\hat{\gamma}_{mn}|, \quad (4.42)$$

where the i -factor ($i = 1 \dots M$) denotes the interferogram-index corresponding to the interferometric combination mn . This formulation shows that the Eigendecomposition-based estimator \hat{b}_{EVQ} is a specific case of the objective function of eq. (4.17), but this time with the weight matrix equal to W_{EVQ} .

It should be noted that the Eigendecomposition-based method can also be applied to the full complex coherence matrix $\hat{\Gamma}$, instead of the covariance matrix $\hat{Q}_{y_{slc}}$ (Cao et al., 2016). If $\hat{\Gamma}$ is used, a new estimator can be defined, denoted by EVC and written as (Cao et al., 2016):

$$\hat{b}_{\text{EVC}} = \arg \max_b \left\{ \operatorname{Re} \left(\sum_{m=1}^N \sum_{n>m}^N [|v_1| |v_1^T|]_{[m,n]} |\hat{\gamma}_{mn}| \exp(j(\hat{\phi}_{mn} - \varphi_{om} + \varphi_{on})) \right) \right\}, \quad (4.43)$$

where v_1 is the first eigenvector corresponding to the largest eigenvalue of $\hat{\Gamma}$. In the vectorized form, eq. (4.43) is

$$\hat{b}_{\text{EVC}} = \arg \max_b \operatorname{Re} \left(\sum \left(W_{\text{EVC}} \exp^\circ (j(y - Bb)) \right) \right), \quad (4.44)$$

where W_{EVC} is a $M \times M$ diagonal weight matrix with diagonal elements

$$[W_{\text{EVC}}]_{[i,i]} = [|v_1| |v_1^T|]_{[m,n]} |\hat{\gamma}_{mn}|, \quad (4.45)$$

where the i -factor ($i = 1 \dots M$) denotes the interferogram-index corresponding to the interferometric combination mn . Similar to the EVQ estimator, the EVC estimator \hat{b}_{EVC} is a specific case of the objective function of eq. (4.17), but this time with the weight matrix W_{EVC} . Note that in practice, the solution for EVQ/EVC estimators is computed by eigenvalue decomposition of the full covariance matrix $\hat{Q}_{y_{slc}}$, and therefore these estimators require the computation of all the possible interferometric phase combinations.

4.3.4 Least circular variance estimator

The least circular variance (LCV) estimator has been introduced in sec. 4.2.2. This estimator for ESM-phase estimation has been introduced by Pepe et al. (2015) in the framework of the *improved EMCF-SBAS* processing chain. In this algorithm, the ESM-phases are estimated by the following maximization problem (see eq. (4.16)):

$$\hat{b}_{\text{LCV}} = \arg \max_b \left| \sum \left(W_{\text{LCV}} \exp^\circ (j(y - Bb)) \right) \right|, \quad (4.46)$$

where W_{LCV} is the diagonal weight matrix whose elements are defined based on the absolute coherence values as

$$[W_{\text{LCV}}]_{[i,i]} = |\hat{\gamma}_{mn}|, \quad (4.47)$$

where the i -factor ($i = 1 \dots M$) denotes the interferogram-index corresponding to the interferometric combination mn . It should be noted that the LCV maximization problem does not require the full coherence matrix, and so it has the flexibility of also digesting a subset of interferograms.

4.3.5 Summary of the review of ESM-phase estimators

In summary, we saw that all the existing ESM-phase estimators are special cases of either maximization of eq. (4.17) or eq. (4.16). The LCV estimator of eq. (4.46) is the only one which is based on eq. (4.16), while the others are the special cases of the objective function of eq. (4.17).

The key difference among the discussed estimators are the weight factors which they assign to the multi-looked interferometric phases. Table 4.1 summarizes all the discussed estimators and their properties. In this section, we only discussed the mathematical formulation of different estimators. In the next section, we discuss the practical considerations to solve the nonlinear maximization problems of different estimators.

4.4 Practical considerations

In this section, we discuss the practical considerations regarding the solution for the nonlinear optimization problem of different ESM-phase estimators, which have been described in sec. 4.3.

4.4.1 Solution of different estimators

As we discussed in sec. 4.3, all the existing ESM-phase estimators can be formulated into one of the nonlinear maximization problems of eq. (4.17) or eq. (4.16). Except the eigendecomposition-based estimators (see sec. 4.3.3) for which the solution can be easily computed by an eigenvalue decomposition of coherence/covariance matrices, the other estimators require a nonlinear optimization method in order to obtain the solution. In principle, for the ESM-phase estimation, any nonlinear optimization routine (e.g. Newton's or quasi-Newton methods, simulated annealing, etc.) can be applied. The common method is the Broyden-Fletcher-Goldfarb-Shanno (BFGS) algorithm (Press et al., 2007)⁴, which is frequently used for ESM-phase estimation in InSAR literature (Ferretti et al., 2011b,a; Pepe et al., 2015).

⁴The BFGS algorithm is an iterative quasi-Newton method for nonlinear optimization, and different open-source BFGS solvers are available, e.g. the Fortran-based limited-memory BFGS subroutine for large-scale optimization problems (Zhu et al., 1997), which has been used for ESM-phase estimation by Pepe et al. (2015)

Table 4.1: Overview of complex-domain ESM-phase estimators, based on the generic mathematical framework introduced in this study.

Estimator	Optimization problem	Weight factors	Comments
Maximum Likelihood (ML) Original name: Phase-linking (Monti-Guarnieri and Tebaldini, 2008), or Phase-triangulation in the framework of SqueesSAR algorithm (Ferretti et al., 2011b)	eq. (4.28) : $\hat{b}_{\text{ML}} = \arg \max_b \operatorname{Re} \left(\sum_b \left(W_{\text{ML}} \exp^{\circ} \left(j(y - Bb) \right) \right) \right)$	eq. (4.29) : $[W_{\text{ML}}]_{[i,i]} = -[\hat{\Upsilon}^{-1}]_{[m,n]} \hat{\gamma}_{mn} $	<ul style="list-style-type: none"> - solution via non-linear optimization methods - requires all the possible interferometric combinations
Maximum coherence-based-weighted sum of residual phasors (MCSR) (Ferretti et al., 2011a)	eq. (4.32) : $\hat{b}_{\text{MCSR}} = \arg \max_b \operatorname{Re} \left(\sum_b \left(W_{\text{MCSR}} \exp^{\circ} \left(j(y - Bb) \right) \right) \right)$	eq. (4.33) : $[W_{\text{MCSR}}]_{[i,i]} = \hat{\gamma}_{mn} ^p$	<ul style="list-style-type: none"> - solution via non-linear optimization methods - flexible to digest subset of interferograms
Eigendecomposition of covariance matrix (EVQ) Used in the CAESAR algorithm (Fornaro et al., 2015)	eq. (4.41) : $\hat{b}_{\text{EVQ}} = \arg \max_b \operatorname{Re} \left(\sum_b \left(W_{\text{EVQ}} \exp^{\circ} \left(j(y - Bb) \right) \right) \right)$	eq. (4.42) : $[W_{\text{EVQ}}]_{[i,i]} = \begin{bmatrix} u_1 \ u_1^T \end{bmatrix}_{[m,n]} \hat{J}_{mn} \hat{\gamma}_{mn} $	<ul style="list-style-type: none"> - solution eigenvalue decomposition of the full complex covariance matrix - requires all the possible interferometric combinations
Eigendecomposition of coherence matrix (EVC) Used in the PD-InsAR algorithm (Cao et al., 2016)	eq. (4.44) : $\hat{b}_{\text{EVC}} = \arg \max_b \operatorname{Re} \left(\sum_b \left(W_{\text{EVC}} \exp^{\circ} \left(j(y - Bb) \right) \right) \right)$	eq. (4.45) : $[W_{\text{EVC}}]_{[i,i]} = \begin{bmatrix} u_1 \ u_1^T \end{bmatrix}_{[m,n]} \hat{\gamma}_{mn} $	<ul style="list-style-type: none"> - solution eigenvalue decomposition of the full complex coherence matrix - requires all the possible interferometric combinations
Least circular variance (LCV) Used in the improved EMCF-SBAS algorithm (Pepe et al., 2015)	eq. (4.46) : $\hat{b}_{\text{LCV}} = \arg \max_b \left \sum_b \left(W_{\text{LCV}} \exp^{\circ} \left(j(y - Bb) \right) \right) \right $	eq. (4.47) : $[W_{\text{LCV}}]_{[i,i]} = \hat{\gamma}_{mn} $	<ul style="list-style-type: none"> - solution via non-linear optimization methods - flexible to digest subset of interferograms

In addition to nonlinear optimization algorithms (e.g., BFGS), Monti-Guarnieri and Tebaldini (2008) proposed an iterative closed-form solution for the ML ESM-phase estimation. This closed-form solution computes the ML estimates of each individual SLC phase $\hat{\varphi}_n$ as (Monti-Guarnieri and Tebaldini, 2008):

$$\hat{\varphi}_n^{(k)} = \angle \left\{ \sum_{m \neq n}^N [\hat{\mathbf{Y}}^{-1}]_{[m,n]} |\hat{\gamma}_{mn}| \exp(j(\hat{\phi}_{mn} + \hat{\varphi}_n^{(k-1)})) \right\}, \quad (4.48)$$

where k is the iteration step. Then the estimate for the ESM-phases is computed as

$$\hat{\varphi}_{on}^{(k)} = \angle \left\{ \exp(j(\hat{\varphi}_n^{(k)} - \hat{\varphi}_o^{(k)})) \right\}, \quad (4.49)$$

where the index o denotes the index of the master image. Note that, although the closed-form evaluation of eq. (4.48) has been introduced for the ML method, it can be, in principle, applied for all methods that are based on the maximization of eq. (4.17). To do so, for a specific estimator, the weight factors of the ML estimator (i.e., $([\hat{\mathbf{Y}}^{-1}]_{[m,n]} |\hat{\gamma}_{mn}|)$ in eq. (4.48)) can be set to the weight factors of the other estimators (see Table. 4.1).

In general, all the iterative non-linear optimization algorithms (e.g. BFGS or eq. (4.48)) require initial values of unknown parameters for starting the iteration. For ESM-phase estimation, a simple choice for the initial values is the original multilooked SM-phase. The other option, suggested by Ferretti et al. (2011a), is to use the estimates of one of the eigen-decomposition estimators as the initial values.

4.4.2 Conditions for multilooking

The observation vector for ESM-phase estimation is the vector \underline{y} , which contains multilooked interferometric phases (see eq. (4.9)). The multilooked phases are computed by spatial coherent averaging over statistically homogeneous pixels (SHP). To satisfy the homogeneity condition, we should use a spatially adaptive averaging window. See sec. 2.4 for an overview of different methods for adaptive multilooking.

Another assumption in the computation of multilooked phases for each pixel is that the signal components of φ are constant in the averaging area. This assumption may be reasonable for relatively small areas with spatially correlated signals. However, if high spatial variation of signal components is expected this phase variation should be removed beforehand. Examples of variable signals are high topography gradients or orbital errors. These kinds of spatially-variable signals can be removed by different kinds of phase flattening or low-pass filters such as the adaptive multi-resolution defringe algorithm in Davidson and Bamler (1999); Wang et al. (2012); Jiang et al. (2014b), patch detrending in Zebker and Chen (2005); Bamler and Hartl (1998), or low-pass filtering in Hooper et al. (2004).

4.4.3 Posterior assessment

After SM-phase estimation, the quality of the estimated phase values should be assessed. In Ferretti et al. (2011b), an ensemble temporal coherence $\hat{\gamma}_{\text{PTA}}$ has been introduced as a goodness-of-fit measure for SM-phase estimation:

$$\hat{\gamma}_{\text{PTA}} = \frac{2}{N(N-1)} \operatorname{Re} \left(\sum_{m=1}^N \sum_{n>m}^N \exp(j(\hat{\phi}_{mn} - \hat{\phi}_{om} + \hat{\phi}_{on})) \right). \quad (4.50)$$

This parameter can be written in the vectorized notation, and for a more generic case, using a subset of interferograms, as:

$$\hat{\gamma}_{\text{PTA}} = \frac{1}{M_{\text{ifgs}}} \operatorname{Re} \left(H^T \exp(j(y - B\hat{b})) \right), \quad (4.51)$$

where M_{ifgs} is the number of interferograms in the subset, and H is an all-ones column vector with length of M_{ifgs} . If all the possible interferometric combinations are used M_{ifgs} will equal to $N(N-1)/2$. The coherence $\hat{\gamma}_{\text{PTA}}$ can be used for the final selection of DS with reliable phase estimation (Ferretti et al., 2011b).

In addition to $\hat{\gamma}_{\text{PTA}}$ as an indicator of the general quality of the estimates, it is desirable to describe the quality of the results in the form of the second statistical moment or a covariance matrix. To do so, the uncertainty of the multilooked observations in \underline{y} should be propagated to the final estimates \hat{b} . However, as all the described estimators are nonlinear, and their solution is derived based on different nonlinear optimization routines, there is no single recipe or no closed-form expression for the evaluation of the covariance matrix of the estimates. In the following section, a lower bound for the precision (or covariance matrix) of the ESM-phase estimators is given.

4.5 Cramér-Rao Bound for ESM-phase estimation

Monti-Guarnieri and Tebaldini (2007, 2008) have proposed a generic formulation for the evaluation of the lower Cramér-Rao bound (CRB) of the covariance matrix for the ESM-phase estimation. This CRB evaluates the highest achievable precision (or the lowest variance) for ESM-phase estimators given a stack of SAR values for a pixel with a particular absolute coherence matrix, independent of the applied algorithm for the estimation. Given the $N \times N$ absolute coherence matrix Υ , the CRB for ESM-phase estimation is evaluated as (Monti-Guarnieri and Tebaldini, 2007) (see sec. A.2.3 for the proof and more discussion):

$$Q_{\hat{b}} \geq (\Theta^T X \Theta)^{-1}, \quad (4.52)$$

where the inequality (\geq) indicates that the difference between the left and the right side of the inequality should be a non-negative definite matrix, and the matrices Θ and X are defined as follows:

- the matrix $\Theta = [0 \ I_{N-1}]^T$ is the $N \times (N-1)$ Jacobian matrix of the first-order partial derivative of SLC phases with respect to the unknown parameters, and

- the matrix \mathbf{X} is the Fisher Information Matrix (FIM) associated with the estimates and is defined as (Monti-Guarnieri and Tebaldini, 2007):

$$\mathbf{X} = 2L(\Upsilon \circ \Upsilon^{-1} - I_N), \quad (4.53)$$

where \circ means the entry-wise product, L is the number of looks, and I_N is a $N \times N$ identity matrix.

Note that for the specific case of having only one interferogram constructed from two SLC images (i.e., $N = 2$), the CRB of eq. (4.52) is reduced to

$$Q_{\hat{b}, \{N=2\}} = \sigma_{\varphi_{12}}^2 \geq \frac{1 - |\gamma_{12}|^2}{2L|\gamma_{12}|^2}, \quad (4.54)$$

which has been already derived for single interferometric phases, see eq. (3.66). The CRB of eq. (4.52) can be used to assess the efficiency of an estimator (for example, the simulation study of sec. 5.3), or can be used as an approximation of the precision of the ESM-phase estimators.

4.6 Conclusions

In this chapter, we introduced a generic functional model for ESM-phase estimation problem in the form of a system of observation-equations (sec. 4.2). Based on this formulation, different objective functions for SM-phase estimation were discussed (sec. 4.2.2).

We reviewed the ESM-phase estimators that are based on optimization in the complex domain (sec. 4.3). A theoretical comparison of different estimators was given (see Table. 4.1), and it was shown that all the estimators are particular solutions for the proposed generic functional model. The fundamental difference among the estimators is in the approach in which they assign weight factors to the interferometric observations. Practical considerations that are important for solving the nonlinear optimization of different estimators were elaborated (sec. 4.4). We also discussed a generic lower Cramér-Rao bound of the variance of ESM-phase estimators (sec. 4.5). The CRB bound can be used as the quality (precision) descriptor of estimated ESM-phases .

As an alternative to the estimators which are based on complex optimization, we briefly discussed another objective function that can be directly applied on interferometric phase residuals (see eq. (4.12)) based on the least squares (LS) principle. The LS formulation results in a highly nonlinear minimization problem due to the wrapping operator in the functional model. In the next chapter, we propose a methodology for solving the nonlinear LS problem of eq. (4.12), followed by a synthetic study and a numerical comparison of different ESM-phase estimators.

ESM-Phase Estimation: Integer least squares method

In this chapter, we propose a new method for ESM-phase estimation based on the integer least squares (ILS) principle. We model the ESM-phase estimation problem in a linear form by introducing additional integer ambiguities (sec. 5.1), and use a bootstrap estimator for the joint estimation of ESM-phases and the integer unknowns (sec. 5.2). For validation, the proposed estimator is applied on synthetic datasets, and the results are compared with the ESM-phase estimators that were reviewed in the previous chapter (sec.5.3). A case study over the Torfajökull volcano in Iceland demonstrates the performance of the proposed method (sec.5.4).

5.1 Hybrid functional model for ESM-phase estimation

In the previous chapter, a generic functional model for ESM-phase estimation has been formulated both in the real-valued phase domain (eq. (4.9)) as well as in the complex domain (eq. (4.10)). For the latter, different objective functions were discussed, and the existing estimators were reviewed. In this chapter, we will focus on the ESM-phase estimation in the real-valued phase domain.

The main challenge to solve the problem in the phase domain is the nonlinearity imposed by the wrapping operator. The basic building block of the functional model is the *expected phase consistency condition* (cf. eq. (4.7)):

$$E\{\hat{\phi}_{nm}\} = W\{\varphi_{om} - \varphi_{on}\}, \quad (5.1)$$

where $\hat{\phi}_{nm}$ is the multilooked wrapped interferometric phase between radar images n and m . The unknown parameters are the *true* SM wrapped interferometric phases φ_{om} and φ_{on} , where the o -index indicates the master acquisition. Equation (5.1) can be

¹This chapter has, in extended form, been published in the IEEE Transaction on Geoscience and Remote Sensing 2016 (Samiei-Esfahany et al., 2016).

regarded as nonlinear observation equation with $\hat{\phi}_{nm}$ as observable, and φ_{on} and φ_{om} as unknown parameters of interest. We reformulate eq. (5.1) and write the nonlinear wrapping operator in a linear form by introducing an integer ambiguity term a_{nm} as

$$E\{\hat{\phi}_{nm}\} = \begin{cases} \varphi_{om} - \varphi_{on} + a_{nm}(2\pi) & \text{if } n, m \neq 0 \\ \varphi_{om} & \text{if } n = 0 \\ -\varphi_{on} & \text{if } m = 0 \end{cases}, \quad (5.2)$$

where $a_{nm} \in \{-1, 0, 1\}$. Since the φ terms are wrapped phases, the value of $(\varphi_{nm} - \varphi_{on})$ can only lie between -2π and 2π , and therefore the only possible values for the ambiguity terms are 1, -1 , or 0. In matrix notation, this linear system of observation equations is written as

$$E\left\{ \underbrace{\begin{bmatrix} \hat{\phi}_{o1} \\ \vdots \\ \hat{\phi}_{o(N-1)} \\ \vdots \\ \hat{\phi}_{nm} \\ \vdots \end{bmatrix}}_y \right\} = \underbrace{\begin{bmatrix} 0 & \dots & 0 \\ \vdots & \ddots & \vdots \\ 0 & \dots & 0 \\ 2\pi & & \\ & \ddots & \\ & & 2\pi \end{bmatrix}}_A \underbrace{\begin{bmatrix} \vdots \\ a_{nm} \\ \vdots \\ \vdots \end{bmatrix}}_a + \underbrace{\begin{bmatrix} 1 & & & & \\ & \ddots & & & \\ & & & & 1 \\ & & -1 & \dots & 1 \\ & & \vdots & & \\ & & \vdots & & \end{bmatrix}}_B \underbrace{\begin{bmatrix} \varphi_{o1} \\ \vdots \\ \varphi_{o(N-1)} \end{bmatrix}}_b, \quad (5.3)$$

where $n, m=1 \dots (N-1)$. Although the most generic case is presented here, in which all the interferometric combinations are used, the model is flexible and can be written for any subset of interferograms. With the model of eq. (5.3), we describe the ESM-phase estimation problem in a hybrid system of linear equations with real unknowns φ_{on} and integer unknowns a_{nm} . The solution of this system of equations is given by ILS estimation, as described in the next section.

5.2 Integer Least Squares (ILS) for ESM-phase estimation

In order to solve the hybrid system of equations (eq. (5.3)) with both integer and real values unknowns, we use the concept of Integer Least Squares (ILS) estimation. ILS is a geodetic estimation method, originally designed for GPS applications (Teunissen, 1995; Teunissen and Kleusberg, 1998), and later also applied to InSAR temporal phase unwrapping (Hanssen et al., 2001; Hanssen and Ferretti, 2002; Kampes and Hanssen, 2004; Teunissen, 2006).

5.2.1 ILS Estimator

Consider a hybrid system of linear observation equations with n integer and p real-valued unknown parameters:

$$E\{y\} = Aa + Bb, \quad (5.4)$$

where $E\{\cdot\}$ is the expectation operator, $y \in \mathbb{R}^m$ the vector of observations, and $a \in \mathbb{Z}^n$ and $b \in \mathbb{R}^p$ the vectors of integer and real-valued unknown parameters, respectively. The matrix $[A \ B]$ is given and assumed to be a full column rank matrix. Equation (5.4) is called the *functional model* as it describes the functional relation between the observations and the unknown parameters. The weighted integer least squares solution of eq. (5.4) is (Teunissen, 1995)

$$\check{a}, \check{b} = \underset{a \in \mathbb{Z}, b \in \mathbb{R}}{\operatorname{argmin}} \|y - Aa - Bb\|_W^2, \quad (5.5)$$

where W is the weight matrix, and $\|\cdot\|_W^2$ a quadratic norm defined as $\|\cdot\|_W^2 = (\cdot)^T W (\cdot)$. The weight matrix W is used to assign different weights to different observations. In sec. 5.2.2, we discuss the implication of the weight matrix for ILS ESM-phase estimation. To account for the integer constraint of vector a , it has been shown by Teunissen (1995); Teunissen and Kleusberg (1998) that the objective function of eq. (5.5) can be orthogonally decomposed into the sum of three L_2 -norm components:

$$\|y - Aa - Bb\|_W^2 = \underbrace{\|y - A\hat{a} - B\hat{b}\|_W^2}_1 + \underbrace{\|\hat{a} - a\|_{W_a}^2}_2 + \underbrace{\|\hat{b}|_a - b\|_{W_b}^2}_3, \quad (5.6)$$

where \hat{a} and \hat{b} are the real-valued unconstrained weighted least-squares estimates of the a and b vectors, and $\hat{b}|_a$ the conditional least squares estimates of vector b , conditioned on a . The matrices W_b and W_a are defined as:

$$W_b = B^T W B, \quad (5.7)$$

and

$$W_a = F^T W F, \quad (5.8)$$

where

$$F = A - B(B^T W B)^{-1} B^T W A. \quad (5.9)$$

Because of the orthogonality condition among the three L_2 -norm components, as soon as \hat{a} and \hat{b} are computed using ordinary least squares, the minimization problem of eq. (5.5) can be regarded as two individual minimization problems of :

$$\check{a} = \underset{a \in \mathbb{Z}}{\operatorname{argmin}} \|\hat{a} - a\|_{W_a}^2, \quad (5.10)$$

and

$$\check{b} = \underset{b \in \mathbb{R}}{\operatorname{argmin}} \|\hat{b}|_a - b\|_{W_b}^2. \quad (5.11)$$

As a consequence the solution of eq. (5.5) can be derived in three steps as follows (Teunissen, 1993).

1. The standard weighted least-squares estimation is performed disregarding the integer constraint $a \in \mathbb{Z}^n$ in order to compute \hat{a} and \hat{b} :

$$\begin{bmatrix} \hat{a} \\ \hat{b} \end{bmatrix} = ([A \ B]^T W [A \ B])^{-1} [A \ B]^T W y. \quad (5.12)$$

These solutions are called *float solutions*.

2. To solve the minimization of eq. (5.10), the integer unknowns in vector \check{a} are estimated by mapping the float solution \hat{a} to the corresponding integer (fixed) solution using a mapping operator $S: \mathbb{R}^n \mapsto \mathbb{Z}^n$, i.e. $\check{a} = S(\hat{a})$. In this mapping, the float solution vector \hat{a} is mapped to the *nearest* integer vector. However, *nearest* must be measured in the metric of matrix W_a in order to account for the correlation among float solutions in vector \hat{a} .

To estimate \check{a} , there exist two common integer estimators. The *integer least-squares* estimator accounts for all the correlation among float solutions, and the *integer bootstrapping* estimator considers some of the correlations among the entries of \hat{a} . Although the ILS estimator is more optimal, its solution cannot be given in a closed form and its computational time is larger compared to the bootstrapping method. Here we use the bootstrapping approach. A detailed explanation of these algorithms can be found in Teunissen (1995); Teunissen and Kleusberg (1998). We also briefly describe the bootstrapping algorithm in Appendix B.1.

3. Solving the minimization of eq. (5.11)) is the most straightforward as it is a well-determined problem (same number of unknowns as equations). So in principle, the solution is given as:

$$\check{b} = \hat{b}|_a. \quad (5.13)$$

However the true value a is unknown. Assuming that the \check{a} is the correct estimation of a , we have $a = \check{a}$. Based on this assumption, once the fixed solution \check{a} is obtained, the fixed solution of real parameters \check{b} is computed as

$$\check{b} = \hat{b}|_{\check{a}} = (B^T W B)^{-1} B^T W (y - A \check{a}). \quad (5.14)$$

Assuming Q_y as the covariance matrix of observation vector y , the covariance matrix of the fixed solution \check{b} can be obtained as

$$Q_{\check{b}} = Q_{\hat{b}|_{\check{a}}} = (B^T W B)^{-1} B^T W Q_y W B (B^T W B)^{-1}. \quad (5.15)$$

Note that, although we formulate the ILS problem with a generic weight matrix W (not with $W = Q_y^{-1}$), we use the covariance matrix Q_y in eq. (5.15) to propagate the dispersion of the observations to the final estimates and to obtain $Q_{\check{b}}$, which is a full covariance matrix describing the precision of the final real-valued estimates \check{b} .

Having the functional model of eq. (5.3) for each pixel in an interferogram stack, the three ILS steps can be applied to estimate the ESM-phases. For the evaluation of eqs. (5.12), (5.14), and (5.15), two more ingredients are required: the covariance matrix of the phase observations, Q_y , and the proper weight matrix W . The covariance matrix Q_y can be constructed either by a Monte-Carlo approach as proposed in sec. 3.4.4, or by the analytical approximation of eq. (3.85). In the following, we address the choice of the weight matrix W for the ESM-phase estimation.

5.2.2 The choice of weight matrix

ILS problem has been conventionally formulated with a weight matrix equal to the inverse of the covariance matrix of the observations. This is logical for observations with a Gaussian distribution, because using $W=Q_y^{-1}$ provides the maximum likelihood estimation. As the multilooked interferometric phases are not normally distributed, their statistics cannot be explained fully by the phase covariance matrix. Also, an accurate covariance matrix may not always be available (e.g. due to biased coherence estimation). Therefore, we express ILS with a generic weight matrix W , increasing the flexibility of the method to digest different kinds of weight matrices.

Focusing on the fundamental difference between non-Gaussian random variables (such as interferometric phases) and Gaussian variables: while for the latter, the variance/dispersion is truly the measure of information loss (as the PDF of Gaussian variables can be completely characterized by the dispersion or the covariance matrix in multivariate cases), for interferometric phases, the variance is always bounded and is not representative of information loss. In fact, a zero coherence interferometric phase conveys no information (corresponding to infinite information loss), while its variance is equal to $\frac{(2\pi)^2}{12}$, which is the variance of uniformly distributed phase between $-\pi$ and π .

In the case of ESM-phase estimation, a reasonable choice for weighting the observations is the coherence of each interferometric phase in observation vector y (cf. eq. (5.3)). In this case, W is defined as a diagonal matrix in which the weight of an observation $\hat{\phi}_{mn}$ is defined as

$$w_{\hat{\phi}_{mn}} = \gamma_{mn}, \quad (5.16)$$

where γ_{mn} is the absolute coherence value.

Another weighting strategy is based on the information content of interferometric multilooked phases. A common measure for the information content that a random variable carries about an unknown parameter is the *Fisher information* index (Rice, 2001). If we consider φ_{mn} to be the expected interferometric phase of the multilooked observation $\hat{\phi}_{mn}$, the amount of information included in $\hat{\phi}_{mn}$ about φ_{mn} can be quantified by the Fisher information index of the interferometric phase as (cf. eq. (3.65))

$$\mathcal{I}_{\hat{\phi}_{mn}} \{ \varphi_{mn} \} = \frac{2L\gamma_{mn}^2}{1 - \gamma_{mn}^2}, \quad (5.17)$$

which results in zero information for $\gamma_{mn}=0$ and maximum information (of infinity) when γ_{mn} approaches 1. In other words, $\mathcal{I}_{\hat{\phi}_{mn}} \{ \varphi_{mn} \}$ accounts for the loss of information about φ_{mn} due to noise and decorrelation. So the diagonal elements of a Fisher-information-based weight matrix W is defined as:

$$w_{\hat{\phi}_{mn}} = \mathcal{I}_{\hat{\phi}_{mn}} \{ \varphi_{mn} \}. \quad (5.18)$$

In sec. 5.3.2.3, we will compare the influence of different weighting strategies on the precision or efficiency¹ of the ILS ESM-phase estimator.

¹In this section the term "efficiency" indicates the closeness of the estimator precision to the Cramér-Rao bound.

5.2.3 Practical Considerations

With the functional model of eq. (5.3), the covariance matrix Q_y , and the weight matrix of eq. (5.18), we have all the required ingredients to apply ILS. Here, we list some practical considerations for the proposed ESM-phase estimation:

- **Float solution:** In eq. (5.3), if all the SM interferograms are included in the observation vector y , the number of equations and unknowns are equal and hence the solution of the first ILS step (the float solution) can be simply computed as

$$\begin{bmatrix} \hat{a} \\ \hat{b} \end{bmatrix} = [A \ B]^{-1} y. \quad (5.19)$$

However, if we use a smaller subset of interferograms and if this subset does not include all the SM interferograms, the number of unknowns will exceed the number of equations, and the float solution is not computable as the matrix $[A \ B]$ is rank-deficient and not invertible. As a consequence, the limitation of the proposed model is that the subset should always include all the SM interferograms. If some of the SM interferograms are not available, pseudo-observations can be introduced in the model to overcome rank-deficiency (e.g., a pseudo-observation equal to zeros can be used).

- **Constraints on integer unknowns:** The application of the ILS method for ESM-phase estimation requires a modification in the original ambiguity resolution algorithm (e.g. in the integer bootstrapping algorithm) regarding the constraints on integer unknowns. For ESM-phase estimation, each ambiguity a is constrained to $a \in \{-1, 0, 1\}$. Therefore, in the second step of ILS, when the float solutions are fixed to their nearest integers, this constraint should be exerted.
- **Statistical homogeneity of the averaging area:** The multilooked phases in vector y are computed by spatial averaging over statistically homogeneous pixels (SHP). In order to satisfy the homogeneity condition, we use a spatially adaptive averaging window. Ferretti et al. (2011b) introduced a spatially adaptive filtering algorithm in order to, for each pixel, define a *brotherhood area* including neighboring SHP based on Kolmogorov-Smirnov test. Alternative approaches with different tests and implementations are also given in (Parizzi and Brcic, 2011; Wang et al., 2012; Goel and Adam, 2014; Jiang et al., 2014b,a). To reduce the influence of non-homogeneous pixels (outliers) in the averaging areas, the concept of robust coherence estimation can be also used (Wang and Zhu, 2016).
- **Signal consistency in the averaging area:** Another assumption in the computation of multilooked phases for each pixel is that the signal components of φ are constant in the averaging area. This assumption is reasonable for relatively small areas with spatially correlated signals. However, if high spatial variation of

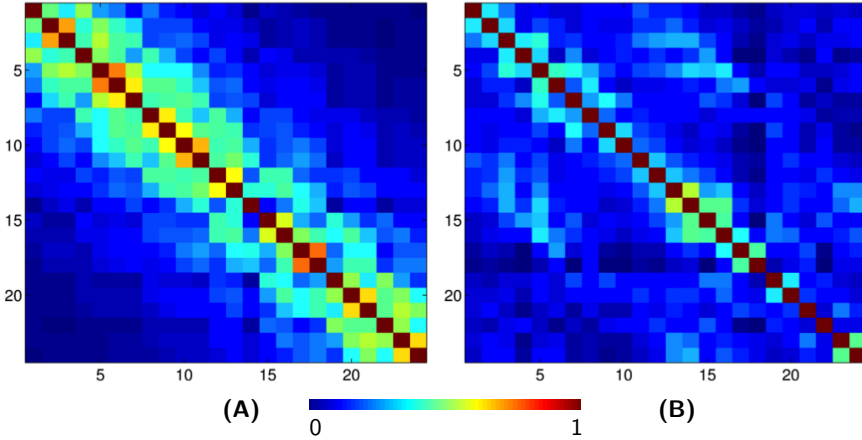


Figure 5.1: Coherence matrices of the synthetic data for two scenarios: - (A) exponential decay C_e , (B) seasonal periodicity C_s . The images are ordered based on their acquisition dates, equidistantly spaced in time with a revisit time of 35 days.

signal components is expected this phase variation should be removed beforehand. Examples of variable signals are high topography gradients or orbital errors. These kinds of spatially variable signals can be removed by different kinds of phase flattening or low-pass filters such as the adaptive multi-resolution defringe algorithm (Davidson and Bamler, 1999; Wang et al., 2012; Jiang et al., 2014b), patch detrending (Zebker and Chen, 2005; Bamler and Hartl, 1998), or low-pass filtering (Hooper et al., 2004).

- **Posterior assessment:** After ESM-phase estimation, the quality of the estimated phase values should be assessed. Ferretti et al. (2011b) introduced an extended temporal coherence $\hat{\gamma}_{\text{PTA}}$ as a goodness-of-fit measure for ESM-phase estimation. This parameter can be written in our model notation as (cf. eq.(4.51)):

$$\hat{\gamma}_{\text{PTA}} = \left| \frac{1}{N_{\text{ifgs}}} H^T \exp\left(j(y - B\check{b})\right) \right|, \quad (5.20)$$

where j is the imaginary unit, and N_{ifgs} the number of interferograms in the stack, H is an all-ones column vector with length N_{ifgs} . If all the possible interferometric combinations are used, $N_{\text{ifgs}} = N(N-1)/2$. The coherence $\hat{\gamma}_{\text{PTA}}$ is used for the final selection of DS with reliable phase estimation.

5.3 Synthetic Data Processing

In order to validate the ILS ESM-phase estimation and evaluate its performance, we test it on a set of synthetic datasets. Here, we describe the simulation settings, followed by results and discussion.

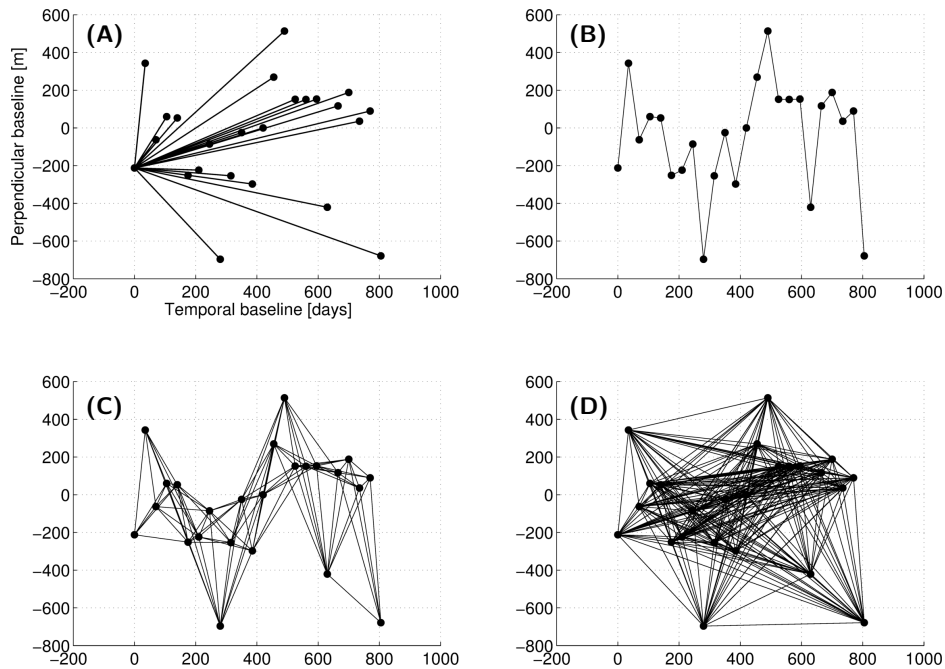


Figure 5.2: Example of baseline configurations used in the synthetic experiment - (A) Single master (SM), (B) small temporal baselines (STB), (C) Small baseline subset (SB), (D) all interferometric combinations.

5.3.1 Simulation setting

We generated two radar data stacks with different noise behavior. Each dataset included 24 SLC images with a revisit time of 35 days. A deformation signal was simulated assuming a simple Gaussian deformation bowl with a maximum line-of-sight deformation rate of 3 cm/year at the center, and a radius of 600 m. We assumed a flat area resulting in zero topographic signal. Atmospheric signal was simulated assuming the power law behavior presented by Hanssen (2001). A crop of 1000×1000 m, a radar wavelength of 56 mm, and a pixel size of 20×20 m were also assumed. For noise simulation, we assume that all the pixels have the same statistics. The noise components are simulated based on the assumption of a zero-mean multivariate circular Gaussian distribution. For the simulation of noise components in interferometric phases, only a coherence matrix is required. In this synthetic study, we have assumed two arbitrary scenarios for temporal decorrelation: exponential decay and seasonal periodicity. The corresponding coherence matrices are constructed for the two scenarios as explained in Appendix B.2 and shown in fig. 5.1. The noise time-series for each pixel is simulated by generating a random vector of complex numbers which have a multivariate zero-mean circular Gaussian distribution with the associated coherence matrix. The noise-free and noisy simulated datasets are visualized in figs. 5.3-5.4A and B, respectively.

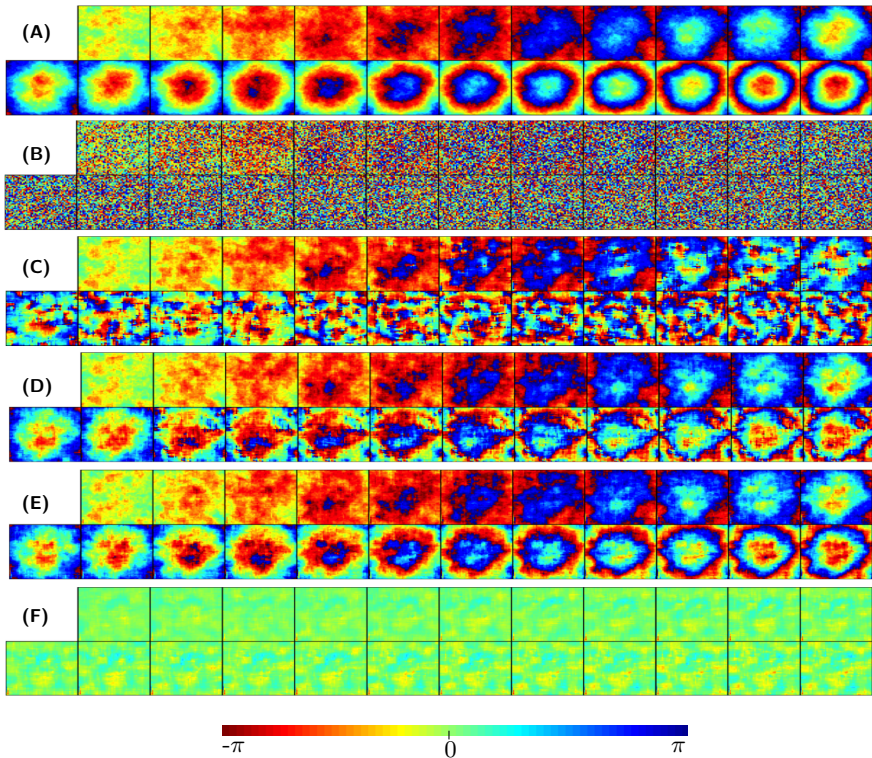


Figure 5.3: Synthetic example (exponential decay scenario)- **(A)** simulated signal (deformation and atmosphere) for SM interferograms using the first acquisition as the master image, **(B)** interferograms after adding decorrelation noise. **(C)** SM interferograms after multi-looking, **(D)** reconstructed SM interferograms from consecutive multilooked small temporal baseline (STB) interferograms, **(E)** results of the ILS method using all interferograms, **(F)** residuals of the ILS method (i.e. the difference between sub-figures A and E).

5.3.2 Simulation results

We first analyse the overall results, before discussing the specific aspects that influence the simulation results.

5.3.2.1 Overall analysis

We applied the ILS ESM-phase estimation on the two simulated datasets. In order to construct the observation vector y for each pixel, the simulated phases were multilooked by coherent phase averaging over 5×5 windows. As discussed in sec. 5.2.3, to meet the signal consistency assumption in the averaging windows, the spatially variable signal within an averaging area should be removed by a defringing/detrending algorithm. In this simulation, in order not to be affected by the sub-optimality of detrending algorithms, the spatially variable signal (or the trend) in the averaging windows is computed and corrected based on the known noise-free simulated signal.

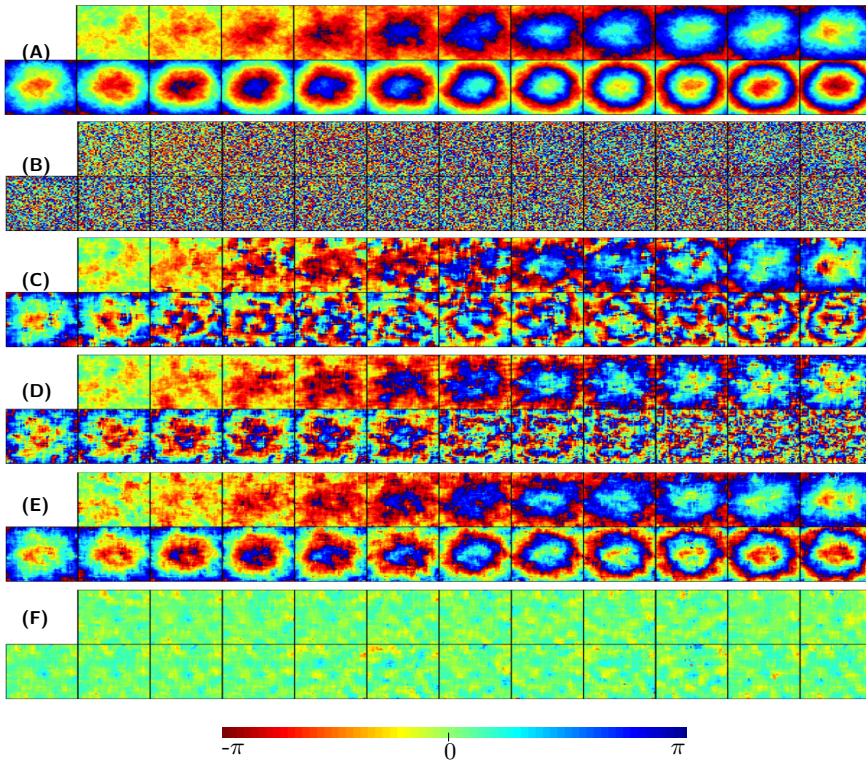


Figure 5.4: Synthetic example (seasonal periodicity scenario)- simulated data results: **(A)** simulated signal (deformation and atmosphere) for SM interferograms using the first acquisition as the master image, **(B)** interferograms after adding decorrelation noise, **(C)** SM interferograms after multilooking, **(D)** reconstructed SM interferograms from consecutive multilooked small temporal baseline (STB) interferograms, **(E)** results of the ILS method using all interferograms, **(F)** residuals of the ILS method (i.e. the difference between sub-figures A and E).

The weight matrix for each dataset is constructed using the Fisher information of multilooked phases computed from the true coherence values based on eq. (5.18). To provide a generic comparison with conventional *ad hoc* phase retrieval methods, we also examined the ESM-phase construction by multilooking the original (SM) interferograms (fig. 5.2B), and by consecutive integration of the temporally adjacent multilooked interferograms, denoted as the small temporal baseline (STB) configuration, see fig. 5.2B.

The results are summarized in figs. 5.3–5.4 for the two scenarios. Figures 5.3–5.4A and B show the noise-free and noisy simulated SM phases, respectively. Figures 5.3–5.4C show the reconstructed phases computed by multilooking the original SM phases, and figs. 5.3–5.4D show the reconstructed phases from STB interferograms. The results of ILS ESM-phase estimation using all the interferograms (i.e. the baseline configuration in fig. 5.2D) are presented in figs. 5.3–5.4E. Finally, the difference between the original simulated signal and the ILS estimates is plotted in figs. 5.3–5.4F.

Initial qualitative evaluation shows that in both scenarios, ILS can effectively filter out noise and is able to reconstruct the original signal. The results indicate better phase

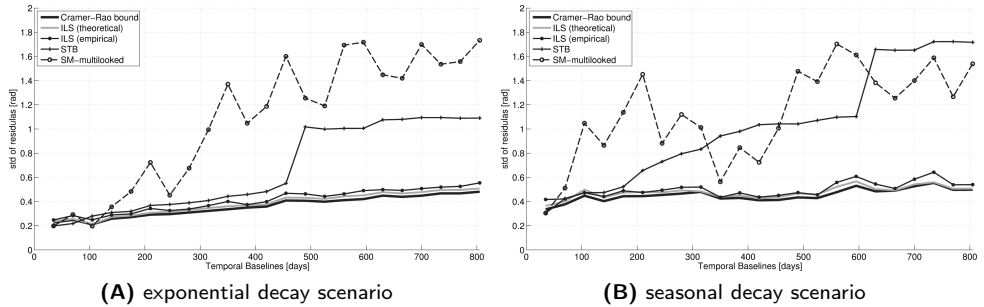


Figure 5.5: Empirical standard deviation of the residuals for three different reconstruction approaches (the multilooked SM stack, the STB reconstructed stack, and the ILS ESM-phase estimation for the two simulation scenarios: **(A)** exponential decay, **(B)** seasonal periodicity. For comparison, we also plotted the theoretical standard deviation computed as square root of the diagonal elements of $Q_{\hat{b}_i}$, and also the lower Cramer-Rao bound of ESM-phase estimation. In both scenarios, the results of ILS ESM-phase estimation outperforms the STB and SM reconstruction methods. There is a good agreement between the theoretical and empirical standard deviations. The empirical standard deviations are close to CRB, indicating the efficiency of the ILS ESM-phase estimation.

reconstructions than SM and STB methodologies, demonstrating the generic added value of using the ESM-phase estimation procedure. In both scenarios, the residuals between the ILS-reconstructed signal and the true signal have zero mean, indicating an unbiased estimation.

Figures 5.5A-B provide a more quantitative evaluation. We calculated the standard deviation of the residuals (i.e. the difference between the constructed interferograms and the true values) for the multilooked SM, the STB reconstructed, and the ILS estimated stacks. For comparison, we also computed the theoretical standard deviations of ILS results from diagonal elements of $Q_{\hat{b}_i}$, see eq. (5.15). To assess the efficiency of the ILS estimator, we also calculated the lowest achievable standard deviation as the square-root of the Cramér-Rao bound (CRB) for ESM-phase estimation, cf. sec. 4.5 (Monti-Guarnieri and Tebaldini, 2008).

In both scenarios, we see that the results of ILS ESM-phase estimation outperforms the STB and SM reconstruction methods. The residual standard deviations of the STB reconstruction increases with temporal baseline, because of the accumulation of noise in the reconstruction process. For SM multilooking, as expected, the standard deviations are variable and dependent on the coherence level; the higher the coherence, the lower the phase standard deviation. For ILS, there is a good agreement between the theoretical and empirical standard deviations. Note that in general, for Gaussian observations, least squares is a minimum-variance estimator, and its variance is equivalent to the CRB. However, interferometric phases are not Gaussian, and empirical standard deviations are hence compared with the analytical CRB. In both scenarios, the empirical standard deviations approach the CRB with an average difference of ~ 0.07 rad or 4° (equivalent to 0.3 mm for C-band) which is negligible compared to the standard deviation expected for high SNR point targets. The closeness to the CRB is an indicator of the efficiency of the ILS estimator.

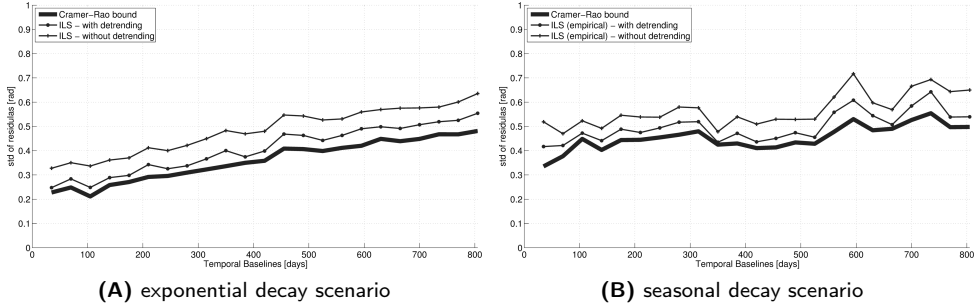


Figure 5.6: The effect of non-stationary signal within averaging windows on the empirical standard deviation of the residuals for (A) exponential decay, (B) seasonal periodicity. For comparison, we also plotted the lower Cramer-Rao bound of ESM-phase estimation.

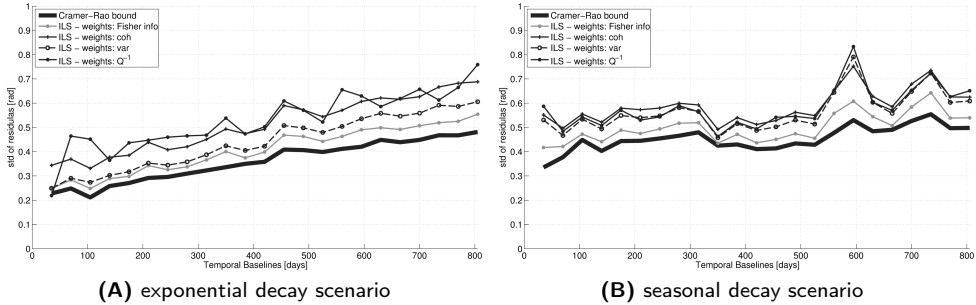


Figure 5.7: The effect of assigned weights on empirical standard deviation of the residuals for (A) exponential decay, (B) seasonal periodicity. For comparison, we also plotted the lower Cramer-Rao bound of ESM-phase estimation.

5.3.2.2 On the influence of non-stationary signal within averaging windows

As mentioned before, we computed and corrected for the spatially variable signal (trend) in the multilooking windows using the known noise-free simulated signal. To evaluate the effect of the trend on the efficiency of ESM-phase estimation, we applied the ILS estimation on both the detrended dataset and the one with the trend included. The results are summarized in fig. 5.6. We observe that trend removal reduces the standard deviation of the residuals significantly. The ratio between the CRB and the standard deviations is approximately two times smaller for the detrended datasets. This indicates the importance of applying a defringing/detrending algorithm during the multilooking/averaging process.

5.3.2.3 On the influence of assigned weights

We applied ILS ESM-phase estimation on the two simulated scenarios with four different weighting strategies (see sec. 5.2.2): (i) setting W as the inverse of the observation

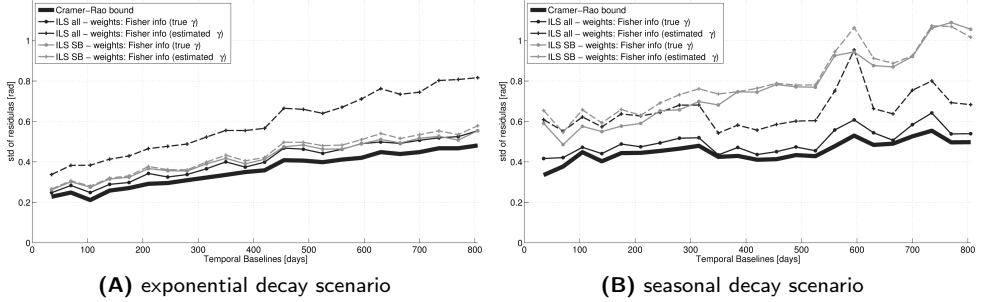


Figure 5.8: The effect of coherence bias and using interferogram subsets for two simulation scenarios: (A) exponential decay, (B) seasonal periodicity.

covariance matrix (i.e., $W = Q_y^{-1}$), (ii) with diagonal elements as inverse variance, (iii) coherence, and (iv) the Fisher information index. The resulting effects on the precision of the phase estimation is summarized in fig. 5.7. We observe that the Fisher-information-based weight matrix is the most efficient. This demonstrates that the dispersion-based weighting strategies (i.e., the inverse of the covariance matrix, or the inverse of the variances) are not optimal for multi-looked phase observations, which have a non-Gaussian distribution. In other comparison of this section, we only show the results of ILS estimation based on the Fisher-information weighting strategy.

5.3.2.4 On the influence of coherence bias and interferogram selection

All the aforementioned weighting strategies require coherence values for calculating W . The coherence values for each pixel can be practically computed from interferograms by spatial coherent averaging (Seymour and Cumming, 1994; Hanssen, 2001). It has been shown that the estimated coherence is biased, particularly for low coherence and small averaging areas (Joughin and Winebrenner, 1994; Tough et al., 1995; Touzi et al., 1996b, 1999; Bamler and Hartl, 1998; Hanssen, 2001; Zebker and Chen, 2005). Increasing the number of looks reduces this bias. Here, we evaluate the effect of the coherence bias on estimation precision. We applied ILS ESM-phase estimation using the Fisher-information-based weight matrix computed both from the true coherence values (i.e. the one used in the simulation) and the estimated coherence values. The results are shown in figs. 5.8A-B. In addition to using all the interferometric combinations, we also applied the ILS estimation on a small baseline subset (SB) of interferograms. Figures 5.2C and D demonstrate the baseline configuration for SB and all interferograms, respectively.

We notice that in both scenarios, using all the interferograms with the true coherence gives the best results. When using all the interferograms with the estimated coherences, the precision deteriorates (approximately with a factor of two) due to the biased coherence estimation. However, in case of SB, there is no significant difference between using the true or the estimated coherences in the weight matrix. This is because we only use interferograms with a relatively high coherence (i.e. a low bias in the coherence estimation), and hence the results are minimally affected by the coherence bias. We also

observe that in the exponential-decay scenario (fig. 5.8A), using the SB subset provides results with the same precision as using all the interferograms with the true coherences. This is expected because, in this scenario, the large temporal baseline interferograms have zero coherence and do not convey any information. Therefore, they do not have any added value on the estimation precision or efficiency. This is an important conclusion: for SAR stacks with a large number of images, where the computation of all the interferometric combinations can be cumbersome, using an SB subset of interferograms can provide the same phase precision for ESM-phase estimation as using the set of all the interferograms. It should be noted, however, that selecting the most informative subset of interferograms is a challenging task, for which currently no generic methodology exists, as it requires *a priori* knowledge on the coherence behavior of DS targets.

5.3.2.5 Comparison with other ESM-phase estimation methods

We compared the results of the ILS method with the results obtained by application of three other ESM-phase estimation methodologies (see sec. 4.3). These three methodologies are:

- the maximum likelihood (ML) ESM-phase estimation used in the phase-linking method (Monti-Guarnieri and Tebaldini, 2008) and SqueeSAR (Ferretti et al., 2011b) (see sec. 4.3.1).
- the ESM-phase estimation methods based on eigenvalue decomposition (EVD) of the full complex coherence matrix as in Fornaro et al. (2015) and in Cao et al. (2015) (see sec. 4.3.3),
- the ESM-phase estimation method based on the minimization of the weighted circular variance of the complex interferometric residuals, as presented in the framework of an improved-SBAS (ISB) algorithm (Pepe et al., 2015) (see sec. 4.3.4).

The first two methods (ML and EVD) exploit the full complex coherence matrix, and hence they use all the interferometric combinations. For a fair comparison, we use all the interferometric combinations for both ILS and ISB as well. To study the influence of biased coherence estimation on the efficiency of different methods, we apply all the methods both with the true absolute coherences and with the estimated coherences; fig. 5.9 shows the results of this comparison. Using the true coherence values (figs. 5.9A and B), all the methods show comparable performance. Using the true coherence values, the ML method gives the most efficient results, approaching the CRB. The ILS and ISB methods show comparable efficiency, which is slightly lower than the ML estimation, and EVD provides the lowest efficiency. However, when we look at the results based on the estimated coherences (figs. 5.9C and D), the results vary significantly, showing different sensitivities of the methods to the biased estimation of coherence values. The ML estimator is affected the most by the biased coherences. This is logical as the ML is the only estimator that requires the inversion of the coherence matrix, and hence small numerical biases in coherence estimation are amplified during the matrix inversion, and severely affect the estimation efficiency. In fact, it has been discussed in the SqueeSAR

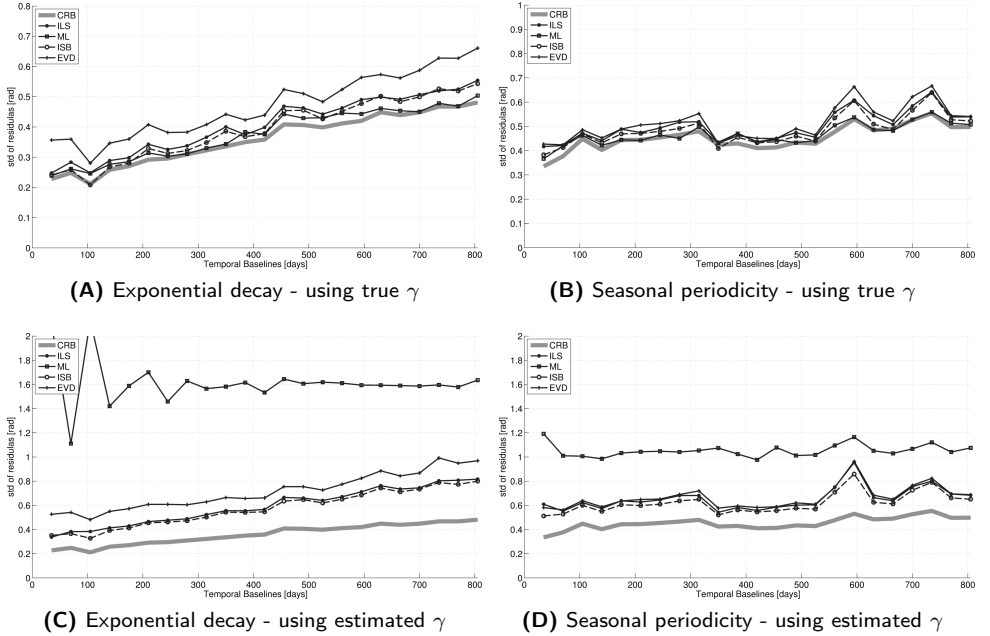


Figure 5.9: Empirical standard deviation of the residuals for different ESM-phase estimation methodologies **(A)** exponential decay scenario with true coherence values, **(B)** seasonal periodicity scenario with true coherence values, **(C)** exponential decay scenario with estimated coherence values, **(D)** seasonal periodicity scenario with estimated coherence values. For comparison, the lower Cramer-Rao bound of ESM-phase estimation is also plotted. The ILS and ISB methods provide comparable efficiency and they are less sensitive to the biased estimation of coherence values. The ML estimator is the most efficient method when the true coherences are used, but it is severely affected by biased coherence estimation and numerical instabilities in the matrix inversion. Generally EVD method shows a lower efficiency than the ILS and ISB methods.

algorithm that the estimated coherence matrix is not, in general, positive definite and is ill-conditioned, requiring the use of a pseudo-inverse or a damping factor before the matrix inversion (Ferretti et al., 2011b). In our implementation of ML estimation, we use the pseudo-inverse. Among other methods, when using estimated coherences, ILS and ISB show comparable results, and once again EVD provides relatively low efficiency.

To summarize, the results of the comparison among different methods (see fig. 5.9) show that the ILS and ISB methods provide comparable efficiency, and they are less sensitive to the biased estimation of coherence values. Even though the ML estimation is theoretically the most efficient method, it is severely affected by biased coherence estimation and numerical instabilities in the matrix inversion. Generally EVD shows lower efficiency than the ILS and ISB methods. However, EVD has an additional functionality compared to other methods. In case of DS with multiple scattering mechanisms, recent studies have showed that EVD is capable of decomposing the contribution of different mechanisms (Fornaro et al., 2015; Cao et al., 2015; De Zan et al., 2015). However, in our specific simulation based on a single scattering mechanism, the efficiency of EVD is lower than other methods.

Method	ILS	ML	ISB	EVD
Exponential decay scenario	42.1	6.2	6.2	2.8
Seasonal periodicity scenario	42.5	6.3	6.4	3.1

Table 5.1: Comparison of the computation time (in seconds) of different ESM-phase estimation methods applied on the two simulation scenarios.

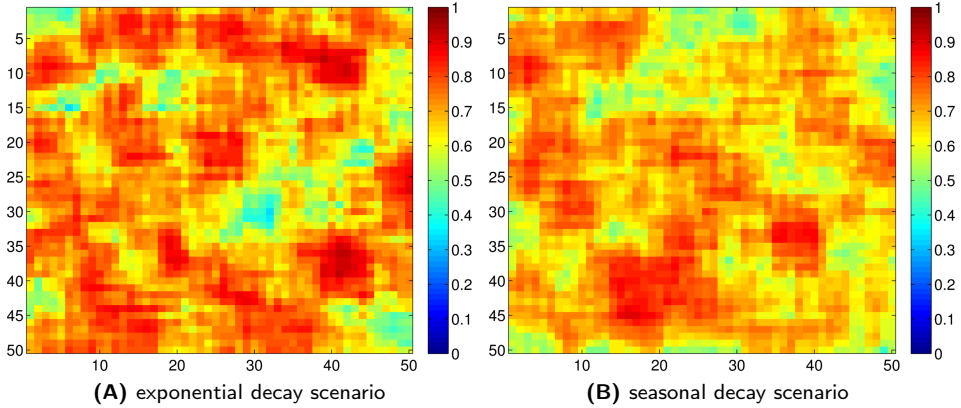


Figure 5.10: Temporal coherence $\hat{\gamma}_{PTA}$ for the two simulation scenarios: **(A)** exponential decay, **(B)** seasonal periodicity, over the simulated area of 50×50 pixels. A low value of $\hat{\gamma}_{PTA}$ indicates large disagreement between observations and the estimated parameters.

Regarding the computational time of different methods, it is difficult to give an accurate and fair analysis, as it strongly depends on the implementation of the different methods. An indication of the relative computational times of different estimators applied on the simulation of this study is summarized in table 5.1. We see that the main drawback of ILS with respect to other estimators is its high computational time, which is approximately seven times higher than the ML and ISB methods in our implementation. In this context, recent numerical improvements in the implementation of fast ILS estimation algorithms, as for example in Jazaeri et al. (2011), can be considered.

5.3.2.6 On the posterior assessment of the results

Figure 5.10 shows the temporal coherence $\hat{\gamma}_{PTA}$ (see equation (5.20)) for both simulation scenarios. A low value of $\hat{\gamma}_{PTA}$ indicates a large disagreement between the observations and the estimated parameters and so sub-optimal ESM-phase estimation. The source of these large residuals may be related to the erroneous estimation of ambiguities in the second step of ILS ESM-phase estimation. When ambiguities are mapped to the wrong integers, the quality of the final estimation will be lower and it will result in a low $\hat{\gamma}_{PTA}$. Therefore, by excluding the pixels with low $\hat{\gamma}_{PTA}$, we can remove unreliable pixels with erroneous ESM-phase estimation. Figure 5.11 shows the effect of this exclusion on the final precision. The threshold of $\hat{\gamma}_{PTA} < 0.7$ was used. We can see that the standard

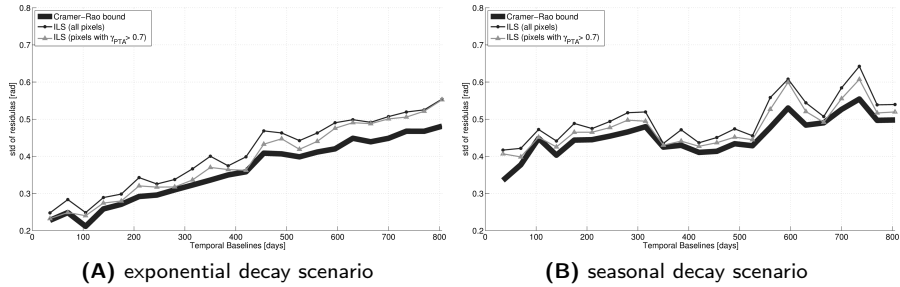


Figure 5.11: The effect of the exclusion of unreliable estimates with $\hat{\gamma}_{PTA} < 0.7$ on the final precision of ILS ESM-phase estimation for the two simulation scenarios: **(A)** exponential decay, **(B)** seasonal periodicity. By excluding the unreliable pixels, the standard deviations are reduced and approaching the CRB, confirming that the extended temporal coherence $\hat{\gamma}_{PTA}$ can be used effectively for the final selection of DS with reliable phase estimation.

deviations were reduced and are approached the CRB. These results confirm that the temporal coherence $\hat{\gamma}_{PTA}$ can be used effectively for the final selection of DS with reliable phase estimation.

5.4 Case study

We applied the ILS ESM-phase estimation method to a stack of 20 Envisat SAR images (track 324), covering the period between 03 Sep 2003 and 28 Jul 2010 over Torfajökull volcano, Iceland (see fig. 5.12). Torfajökull's latest eruption was in the 15th century, but the volcano caldera has been subsiding with linear rates in recent years (Scheiber-Enslin et al., 2011). We coregistered all slave images to a single master (4 Jul 2007), which was chosen to minimize the average value of perpendicular and temporal baselines. The distribution of both temporal and perpendicular baselines of the radar images is depicted in fig. 5.13. The crop used in the study is approximately 40×26 kilometer wide, see fig. 5.12.

The multilooked phases for each pixel are computed by spatial averaging over statistically homogeneous pixels (SHP) detected by the Kolmogorov-Smirnov test (Ferretti et al., 2011b). The weight matrix was constructed based on estimated coherence values, using eq. (5.18). In order to reduce the spatially variable signal within the multilooking areas, the topographic phase component is computed and subtracted from all the interferograms, using a 25 m digital elevation model from the national land survey of Iceland. We also apply the defringe algorithm presented in Jiang et al. (2014b) during the multilooking step. After SHP selection and multilooking, we applied the ILS ESM-phase estimation using all the interferometric combinations. Then, for pixels with more than 50 SHP (in order to have a large number of looks), we replaced the phase of the original SM interferograms with the phase estimates of ILS ESM-phase estimation. In order to evaluate where the ESM-phase estimation is more effective, we plotted the $\hat{\gamma}_{PTA}$ for all pixels in fig. 5.14. The higher values (e.g., $\hat{\gamma}_{PTA} \geq 0.7$) indicate pixels with

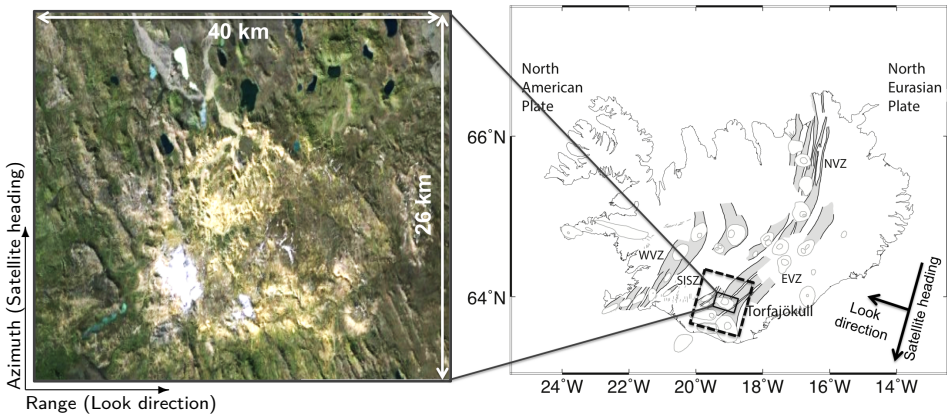


Figure 5.12: Right: Study area over Torfajökull volcano, Iceland. Torfajökull is located at the Eastern Volcanic Zone (EVZ). The black dashed rectangle is the location of the Envisat SAR scenes, while the black solid rectangle is the 40×26 km crop used in this study. Left: Google map view of the 40×26 km area of interest.

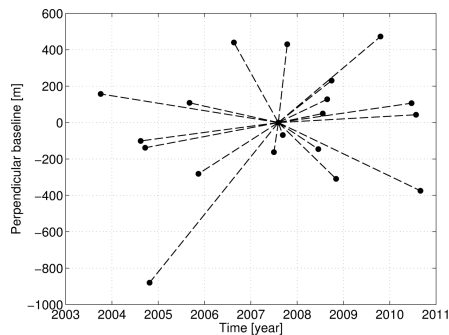


Figure 5.13: The distribution of temporal and perpendicular baselines of the radar images used in the case study over Torfajökull volcano.

reliably estimated SM phases, hence candidates to be selected as coherent distributed scatterers. Figure 5.15 shows four examples of *reconstructed* interferograms compared with the original single-looked interferograms. Visual investigation of these examples shows that ESM-phase estimation can significantly improve the coherence by effectively filtering the noise components.

In order to evaluate the added value of ESM-phase estimation, we compare the results with the results with standard PSI processing when no ESM-phase estimation is applied. For PSI processing, the StaMPS software was used (Hooper, 2006; Hooper et al., 2012). Both methods estimate a deformation of ~ 10 cm in 7 years. Within the volcano caldera the surface is subsiding with rate of ~ 15 mm/y (attributed to a possible crystallization of the magma reservoir (Scheiber-Enslin et al., 2011)). In order to have fair comparison, the same processing setup and selection criteria were used for both methods, except that for the processing with ESM-phase estimation, we also used an additional selection

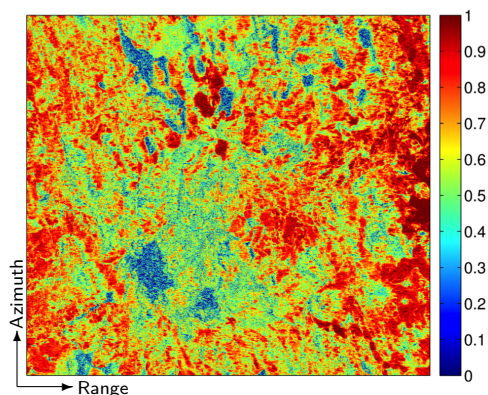


Figure 5.14: Temporal coherence $\hat{\gamma}_{PTA}$ for all pixels over the Torfajökull area. Higher values (≥ 0.7) indicate pixels with reliable ESM-phase estimation. These pixels are selected as candidate coherent distributed scatterers.

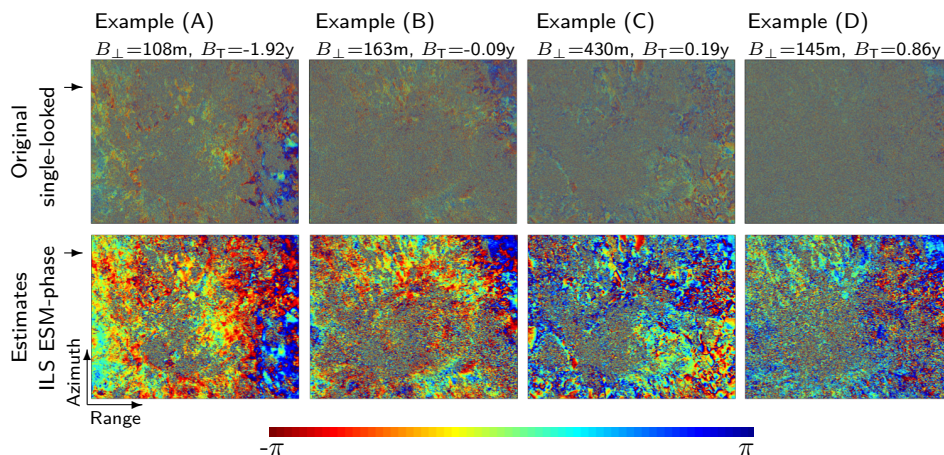


Figure 5.15: Four examples of reconstructed interferograms by ILS ESM-phase estimation (bottom row) compared with the original single-looked interferograms (top row). These examples show that the ESM-phase estimation can significantly improve the coherence by effectively filtering the noise components.

criterion, i.e. $\hat{\gamma}_{PTA} \geq 0.7$, on pixels with a number of SHP larger than 50. The final results are shown in fig. 5.16 where the line of sight (LOS) velocity maps are plotted. These velocities are relative with respect to the average velocity of the whole crop. Using the standard method with single-looked interferograms, ~ 32000 coherent pixels were identified in contrast with ~ 72000 identified coherent pixels via ILS ESM-phase estimation. Over the main deforming area (the white rectangles in fig. 5.16), the number of coherent pixels improved from 3300 to 13000. Improvements in point density increase redundancy, leading to better precision, enhance the quality of the phase unwrapping or atmospheric removal, and allow for the detection of spatially high-frequency deformation signal. Moreover, a higher density in the deforming areas can introduce more constraints in geophysical interpretation and subsurface modeling.

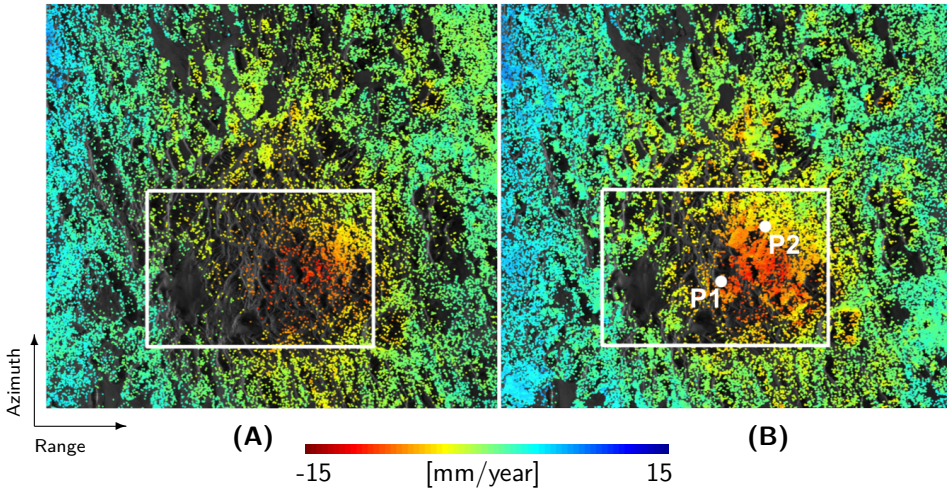


Figure 5.16: Comparison between the velocity map applying StaMPS PS processing using (A) original single-look SM interferograms, and (B) SM interferograms after ILS ESM-phase estimation. The average velocity of the whole crop was used as a reference. The white rectangle shows the main subsiding area. The density of points improved from 32000 to 72000 (3300 to 13000 in the deforming area). The deformation time-series of points P1 and P2 are plotted in fig. 5.17 (A)-(B).

One of the main advantages of the ILS method is that it provides the precision, or the full covariance matrix (i.e., $Q_{\hat{b}}$) of the inverted interferometric phases via eq. (5.15). These matrices can be used as a proper weight matrix in further post-processing or geophysical modeling of time-series InSAR results. Figures 5.17A–B demonstrate two deformation time-series associated with the two pixels P1 and P2 identified with white dots in fig. 5.16B. The coherence matrix and the full covariance matrix of the inverted phases of these two pixels are visualized in figs. 5.17C–D and figs. 5.17E–F, respectively. We should note that $Q_{\hat{b}}$ in eq. (5.15) is a function of the baseline configuration used in the estimation (via the B matrix), the weight matrix (W), and the covariance matrix of multilooked interferometric phase (Q_y), the latter itself is a function of the target coherence matrix and the number of looks. The difference in the covariance matrix of the inverted phases for the pixels P1 and P2 is due to the different coherence matrices and different number of looks, which are 113 and 76 for P1 and P2, respectively. The higher the number of looks is, the smaller the variances are. The variable coherence structures and number of looks among detected DS results in deformation time-series with variable quality in time and space. Consequently, with DS, we are dealing with a set of deformation estimates with highly variable precision in time and space. This important fact should be considered in further interpretation of the DS results.

5.5 Conclusion

We proposed a new method for ESM-phase estimation based on integer least squares (ILS) principle. The main advantages of ILS ESM-phase estimation is the flexibility to be applied on any subset of interferograms and the quality description via the provision

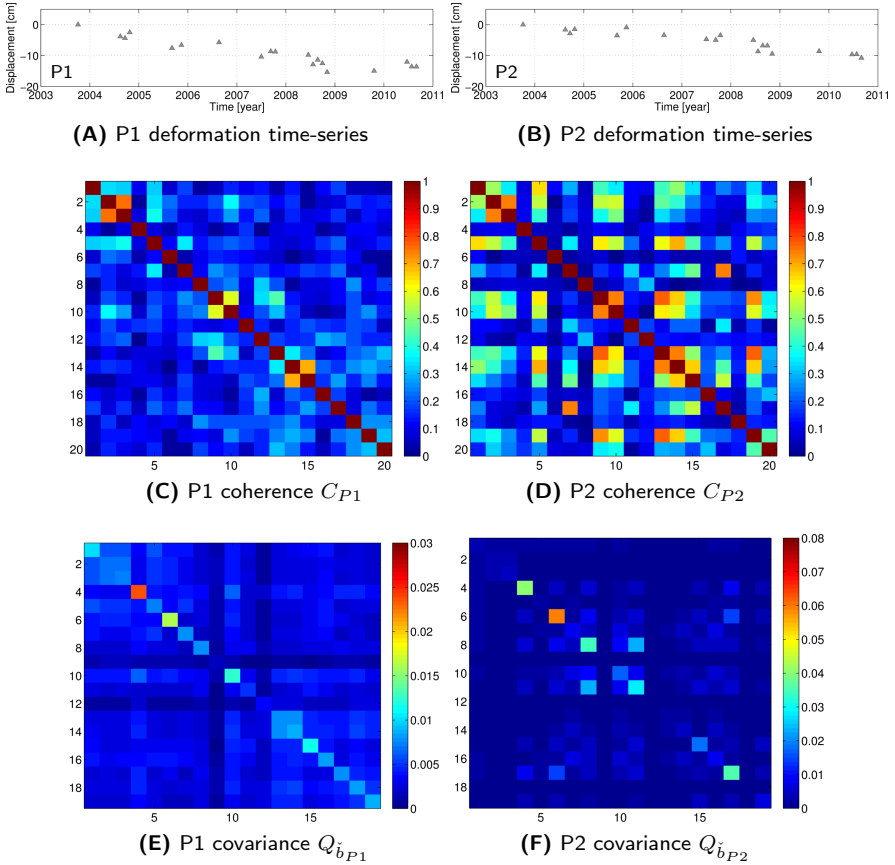


Figure 5.17: Two example deformation time-series associated with (A) point P1 and (B) point P2 identified with white dots in fig. 5.16(B). The coherence matrix of these two pixels are visualized in (C) and (D) and their full covariance matrix are visualized in (E) and (F), respectively. The phase covariances in (E) and (F) has been converted to [cm²]. The master image for construction of covariance matrices in (E) and (F) is the master image indicated in fig. 5.13

of a full covariance matrix of the estimates. The obtained covariance matrices can be further propagated to other InSAR derived parameters and can play an important role in the further post-processing or geophysical modeling of time-series InSAR products. Via a simulation study, we have shown that the ILS ESM-phase estimator is unbiased, and the closeness of the variance of its residuals to the lower Cramér-Rao bound demonstrates the high precision of the proposed estimator. We have also discussed the influence of different factors such as detrending, weighting, and coherence bias on the precision of the ILS method. The efficiency of the ILS method has been compared to alternative estimators. The results show comparable or higher precision for ILS compared to other estimators. The main drawback of the ILS approach is its high computational time, which needs to be improved. The proposed method has been successfully applied to a stack of interferograms over Torfajökull volcano in Iceland, resulting in double the number of detected coherent pixels with respect to conventional PSI.

6

Feasibility analysis of DS exploitation: A case study over Veendam subsidence field

This chapter presents the results obtained for a case study on the subsidence of Veendam in northern Netherlands. We first give some background information on the importance of subsidence monitoring (sec. 6.1), followed by an introduction of the Veendam study area (sec. 6.2). The processing settings and the used dataset are described, followed by a prior feasibility analysis of exploiting DS in this area (sec. 6.3). The results of applying combined PS and DS processing are given, including the comparison with PS processing (sec. 6.4). A new model is introduced for temporal decorrelation of agricultural and pasture areas as a stochastic process with non-stationary but periodic increments, and the parameters of the proposed model are estimated for the typical observed coherence behavior around Veendam (sec. 6.5). Finally, using the estimated decorrelation model parameters, the feasibility of exploiting DS-pixels is assessed for different satellite missions (sec. 6.6).

6.1 Introduction

Land subsidence can cause serious socio-economic problems. Damage to infrastructure and buildings can be mentioned as examples. In coastal and low-lying areas such as the Netherlands, land subsidence is a highly consequential phenomenon with a great societal importance due to its impact on water management and ecological systems, and most importantly on flood risk. During the last decade, InSAR, particularly PSI, has been applied to study different subsiding areas in the Netherlands, e.g., the subsidence induced by hydrocarbon production in Groningen (Ketelaar, 2008), fault-related surface deformation in the Roer Valley Graben (Caro-Cuenca, 2012), and the subsidence induced by both gas and salt extraction in Noordwest-Friesland (Muntendam Bos et al., 2009). Despite the challenging factors such as slow deformation rates (smaller than 1 cm/year) and rural/agricultural landscapes, the results of these studies have proven the feasibility of the technique for subsidence monitoring in the Netherlands. The majority of buildings and structures appear to serve as reliable measurement points (i.e. PS), the accuracy of PSI has been quantified by combining multiple satellite tracks, and a correlation of 94%

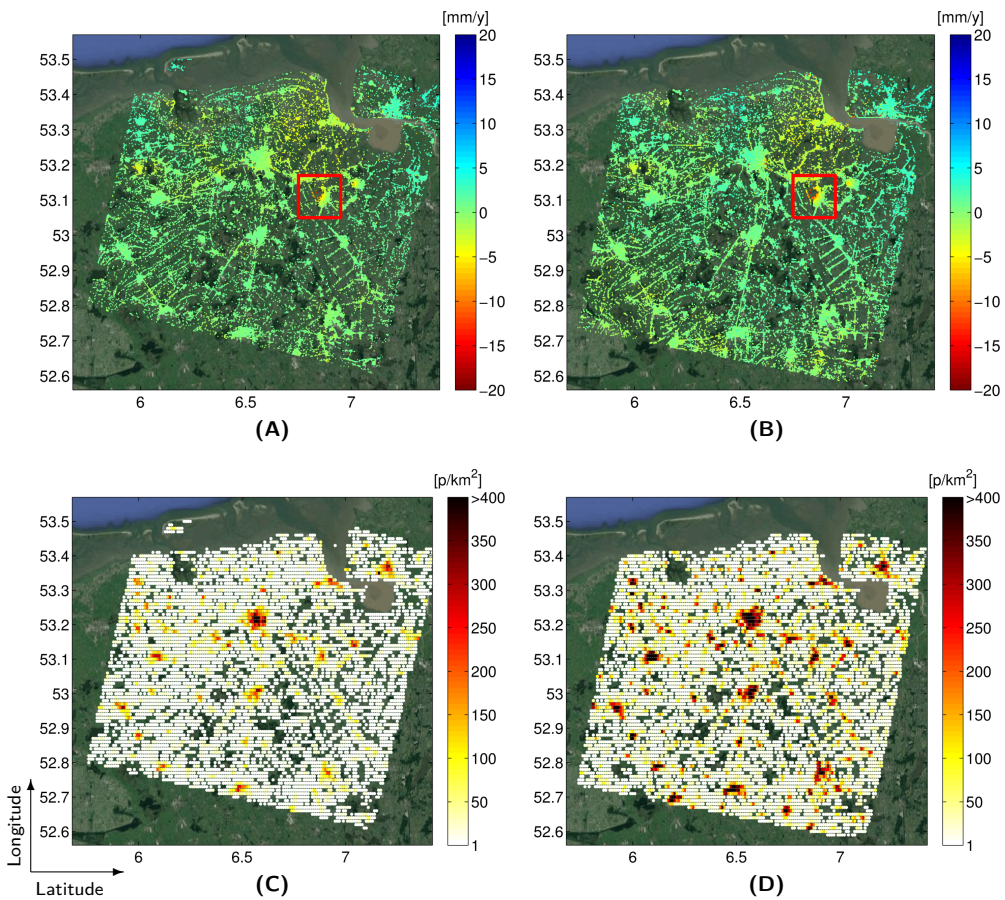


Figure 6.1: PSI results of the Groningen area using the DePSI processing (A) based on an Envisat dataset acquired between December 2003 and September 2010, and (B) based on a RadarSAT2 dataset acquired between July 2009 and June 2013. Figures (C) and (D) show the PS density for the two datasets, Envisat and RadarSAT2, respectively. The red box, in figures A and B, outlines the Veendam salt mining area, which is the case study area of this chapter.

with ground optical leveling measurements was achieved for the Groningen subsidence area (Ketelaar, 2008; Muntendam Bos et al., 2009). Nowadays PSI is operationally used for various subsidence monitoring projects in the Netherlands.

Although PSI has been successfully applied for subsidence monitoring (e.g. over the Groningen gas field, see the figs. 6.1A and B, there are still areas with a limited number of PS targets. Especially smaller subsidence fields in rural areas may be sparsely covered with PS measurements compared to the extent of the subsiding area. Figures 6.1C and D show the PS density in the Groningen region based on two different datasets from two C-band radar mission Envisat and RadarSAT2, respectively. We can see that the PS density in urban areas reaches 500 PS/km², while in some rural areas we have very few PSs. Therefore, in order to improve the observation density in rural areas, there is a potential value in methodologies that exploit DS. In addition to the density improvement, the

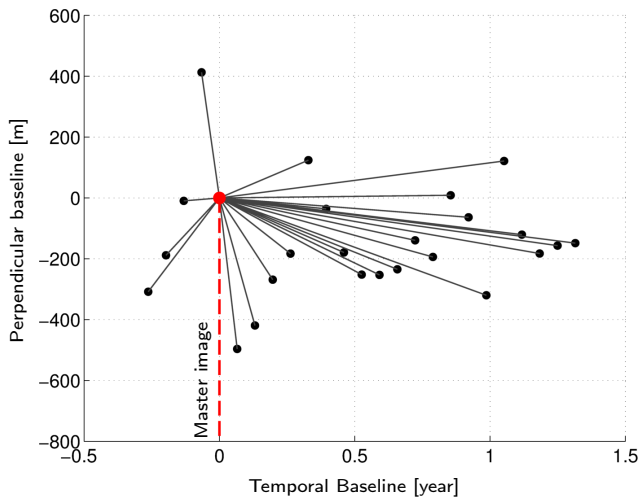


Figure 6.2: The baseline configuration of the used dataset, containing 25 radar images acquired between October 2011 and May 2013. The acquisition of 24 January 2012 has been used as the master image.

information extraction from DS in rural areas can be useful for hydrological applications, for example with the aim of studying the soil properties of different kinds of agricultural fields (te Brake et al., 2013), or for water management and monitoring water table variations (van Leijen and Hanssen, 2008).

Despite the potential value in methodologies exploiting DS, the feasibility of such methods for subsidence monitoring over rural areas in the Netherlands with a pasture and vegetation landscape, which has a high phase-decorrelation rate (Morishita and Hanssen, 2015b), is still a pending question. Our objective, in this chapter, is to investigate the feasibility of DS exploitation in these rural areas. To limit the scope, we chose a case study area over a solution salt mining-induced subsidence field in Veendam, which is explained in more details in the next section.

6.2 The Veendam test case

To evaluate the DS processing, a test site around a salt mining area close to the city of Veendam in the north part of The Netherlands is chosen, see the red box in the fig. 6.1A,B. The combination of having different kinds of landscape (e.g., both rural and urban, see fig. 6.3B), and its high deformation rate together with the low density of PSs in agricultural fields make this region a relevant case study area.

The salt extraction in the area started in 1981. Solution mining is used for the withdrawal of magnesium chloride. This technique is based on the addition of a solvent (e.g., water) to the mineral, following by pumping and separating the minerals from the solvent. The salt production has induced a land subsidence in this region in the order of 17 mm/year (van Leijen and Hanssen, 2007). The PSI results of the area show the PS density of approximately 300 PS/km² over city of Veendam, and a much lower density over agricultural fields.

A RadarSAT2 dataset containing 25 radar images acquired between October 2011 and

May 2013 is used for the study. Figure 6.2 shows the baseline configuration of the used dataset, using the image of 24 January 2012 as the master image for PSI processing.

In the following sections we present the results and discuss the findings of this case study. We divide the discussion into two parts:

1. A-priori analysis (Section 6.3). Here, with *a-priori*, we mean the study of the characteristics of pixels prior to applying the ESM-phase estimation and PSI processing. In this analysis, we evaluate the coherence behavior of different landscapes in the area-of-interest (AOI), followed by an assessment of the feasibility of exploiting DS based on the observed coherence histories.
2. A-posteriori analysis (Section 6.4). In a-posteriori analysis, we look at the final results of applying the DS processing over the AOI, compare the results with standard PSI processing, study the quality of the detected DS, and evaluate the density improvements over different landscapes.

6.3 A priori analysis

The feasibility and the quality of the phase information extracted from DS-pixels depends mainly on their coherence behavior. For example, in a case of high temporal/spatial/volume decorrelation in dense forest area (or in the extreme case of water areas), it is almost impossible to extract any reliable phase information from DS-pixels regardless of the applied methodology. On the other hand, over a dry and desert landscape, DS-pixels may be minimally affected by decorrelation and their quality can even be comparable with the quality of point scatterers. In-between these two extreme scenarios, whether or not we can reliably estimate/extract phase time-series from DS-pixels depends on the coherence behavior of the pixels in a given stack of images with particular temporal and perpendicular baselines.

To study the coherence behavior over different landscapes in the Veendam case, we estimated the coherence matrix of all the pixels in this area. Figure 6.3A and B show the multi-reflectivity map and land-use map of the area of interest. For coherence estimation, an adaptive *brotherhood* area is selected around each pixel based on the two-sample Kolmogorov-Smirnov (KS) test (see sec. 2.4 for details of adaptive brotherhood selection). The brother pixels are selected within a window of 25×25 pixels, so the maximum number of brothers is $25^2 = 225$. Figure 6.3C shows the number of selected brothers for each pixel. We can see that the pixels over urban areas generally have a lower number of brothers. This is expected due to the variable nature of pixels in urban areas. Also it is well known that PS-pixels (e.g., pixels associated with buildings) have a low number of brothers, i.e. less than 20 (Ferretti et al., 2011b). On the other hand, over agricultural fields, most of the pixels within the surrounding 25×25 windows show the same amplitude statistics and are selected as brother pixels. Consequently the pixels over agricultural/pasture lands generally have a large number of brothers (more than 200).

Based on selected brotherhood area around each pixel, the coherence matrices have been estimated. In order to reduce the bias in the coherence estimation, the coherence matrices have been estimated by the bootstrap estimator (Jiang et al., 2014b). Figure 6.3D shows, for each pixel, the mean coherence over 300 possible interferogram combinations (i.e., there are 25 SLC images, and so the total number of possible interferograms is $(25 \times 24)/2 = 300$). As a general observation, we see a high variability of the mean coherence in agricultural/pasture lands, varying between 0 and 0.4. In urban areas, the mean coherence is much higher compared to other terrain areas. Excluding the potential PS from the analysis¹, the mean coherence in urban areas is on average 0.53. In order to get more detailed information and a quantitative assessment about the coherence behavior over different classes of land use, we analyze example coherence matrices for three typical classes (urban areas, agricultural/pasture lands, and road surfaces) in the following.

6.3.1 Coherence behavior over urban areas

We analyze three typical examples of coherence behavior in urban areas in and around the city of Veendam. The location of these three cases (denoted by U_A , U_B , and U_C) is indicated in fig. 6.4, and their corresponding coherence matrices are shown in figs. 6.5A, B, and C, respectively. To get more precise coherence estimation, the matrices presented here are the average of the estimated coherence matrices of the neighboring pixels in a 300×300 meter surrounding. To compute the average coherence, we only use pixels with approximately same number of brothers and same coherence-mean (whose values \bar{N}_{br} and $\bar{\gamma}$ are mentioned in the caption of figs. 6.5A-C).

In the coherence matrices, we observe as a general pattern that the interferograms with a shorter temporal baseline have a relatively high coherence value, reaching to ~ 0.65 (Note that the images are sorted based on the acquisition date, so the close-to-diagonal elements represent interferograms with shorter temporal baselines.). The other interferometric combinations show on average values around $\sim 0.3 - 0.4$, which is still high considering the large number of brothers of these pixels (100 – 150). This almost-constant behavior of coherence over large temporal baselines indicates that these pixels preserve some degree of coherence within the 1.5 years span of this data stack. Figures 6.5D-F show the CRB standard deviations (σ_{CRB} computed by eq.(4.52)) of the ESM-phase estimation for these three examples. For relative comparison, we also plot the standard deviation of zero-coherence noise (i.e., $\sigma_{\gamma=0} \sim 104^\circ$, corresponding to the uniform distribution between $-\pi$ and π), and the assumed typical standard deviation of a point scatterer ($\sigma_{ps} \sim 25^\circ$). The CRB standard deviation can be interpreted as an indicator of the amount of information that exists in the data stack about each SM-phase. A high σ_{CRB} (close to $\sim 104^\circ$) means almost no information, and a low σ_{CRB} (close to or smaller than σ_{ps}) indicates that the information content (or the quality) of the corresponding ESM-phase is comparable with PS-pixels. For these three cases, all the σ_{CRB} are smaller than the typical PS standard deviation. These results show that, by

¹In order to focus on DS in the statistical analysis of this section, we consider pixels which have less than 25 brothers, a mean coherence larger than 0.7, or an amplitude dispersion smaller than 0.4 as potential PS pixels and exclude them from the rest of the a-priori analysis.

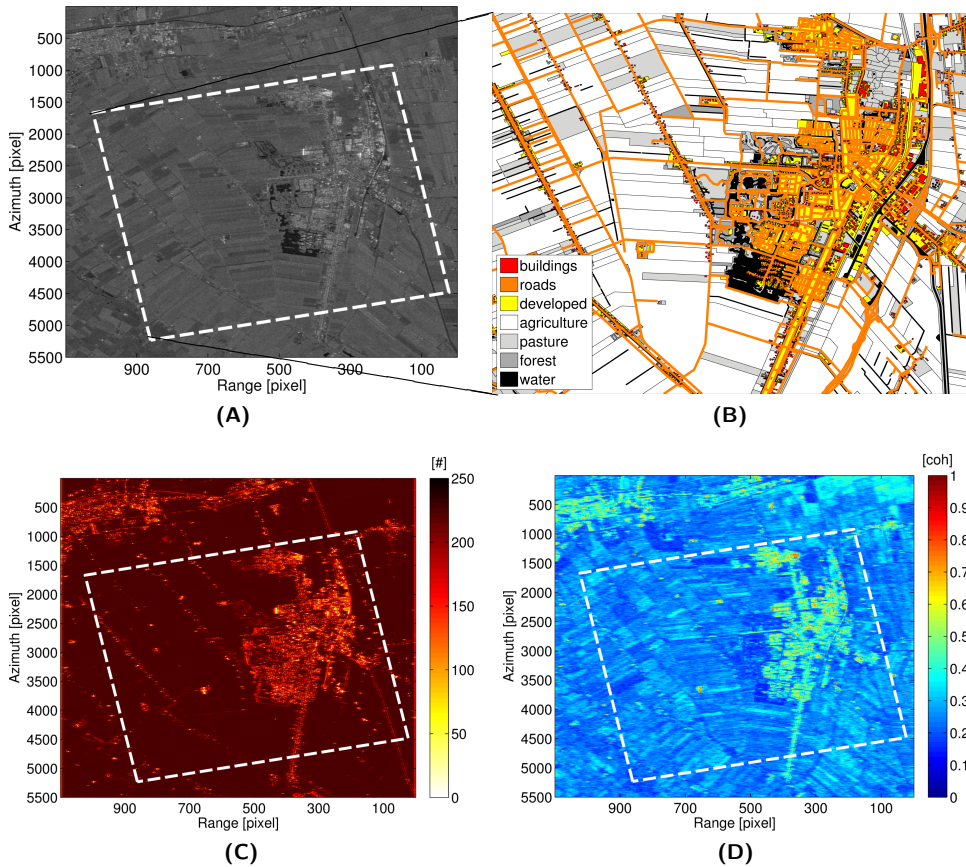


Figure 6.3: The Veendam case study: (A) multi-image reflectivity map of the AOI (i.e., the incoherently averaged amplitude of the 25 RadarSAT2 SLC images acquired between October 2011 and May 2013), (B) Land-use map of the AOI, (C) Number of detected interferometric pixels as statistically homogeneous pixels (SHP), (D) the mean coherence over 300 possible interferogram combinations. The outline of the land-use map (B) is shown as a white dashed box in the other sub-figures. (Land-use map of (B) is copyrighted: © Cadastre, Geoinformation, Zwolle, 2014).

applying the ESM-phase estimation, the phase quality of these kinds of DS-pixels in the urban areas of Veendam reaches to the quality of a typical PS-pixel, and therefore, it is feasible to utilize these pixels for further TInSAR processing and deformation estimation.

6.3.2 Coherence behavior over agricultural and pasture areas

We study the coherence behavior of three examples in agricultural and pasture areas around Veendam. The locations of these cases are marked as P_A , P_B , and P_C in fig. 6.4. The coherence matrices of these examples are shown in figs. 6.6A, B, and C, respectively.

The first observation is that the interferograms with a short temporal-baseline show a relatively high coherence in the winter period. In contrast, in the summer period

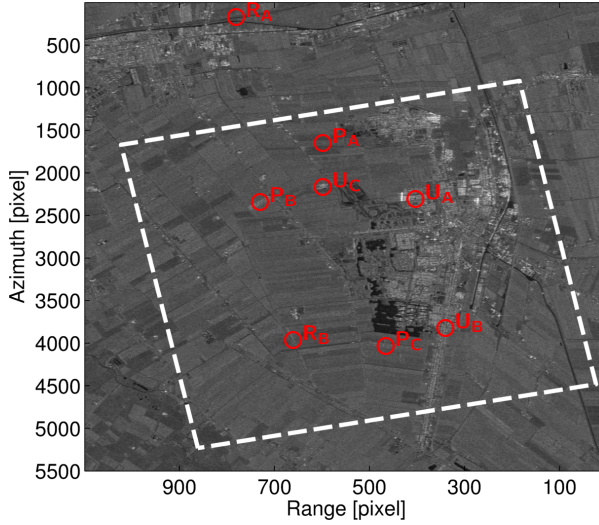


Figure 6.4: The location of eight example coherence matrices from three typical land-use classes: $U_{A,B,C}$ in urban areas, $P_{A,B,C}$ in agricultural/pasture lands, and $R_{A,B}$ on roads. The coherence matrices of these eight examples are shown/analyzed in figs. 6.5-6.7,

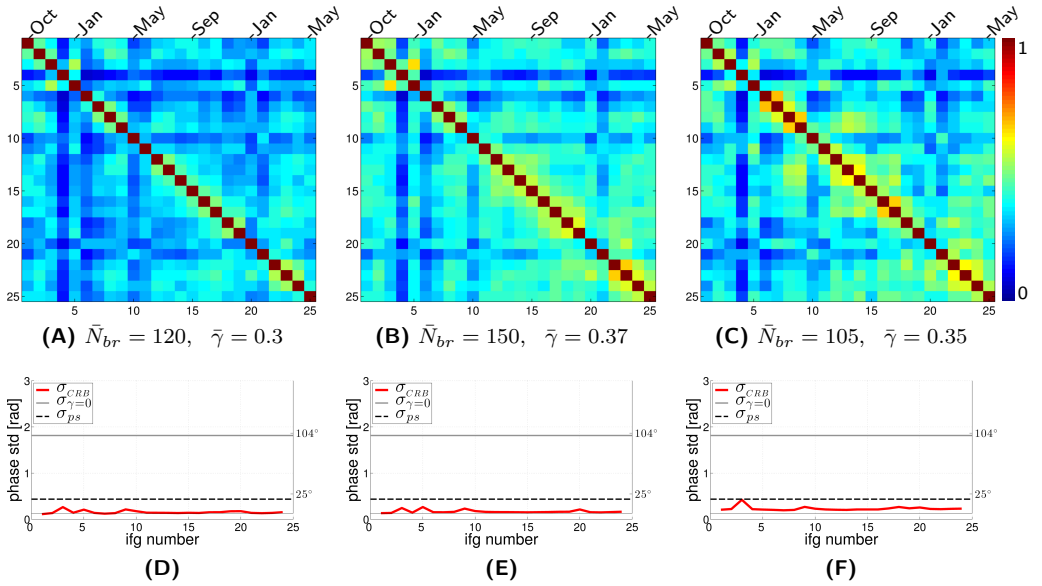


Figure 6.5: (A), (B), and (C) are three examples of coherence matrices in urban areas, corresponding to the locations U_A , U_B , and U_C in fig. 6.4. In the coherence matrices, the images are sorted based on the acquisition date (the months of acquisitions are indicated above the matrices). These matrices are the result of averaging the coherence matrices of surrounding pixels. The average number of brothers and mean coherence of averaged pixels is indicated by \bar{N}_{br} and $\bar{\gamma}$, respectively. The bottom row plots (D), (E), and (F) show the CRB standard deviations of ESM-phase estimation. The standard deviation of zero-coherence noise ($\sim 104^\circ$), and the standard deviation of a typical point scatterer ($\sim 25^\circ$) are also plotted. For these three cases, all the σ_{CRB} are smaller than the typical PS standard deviation, indicating the feasibility of utilizing these pixels for further TInSAR processing.

(between May and October), the coherence values are almost zero even for consecutive acquisitions with a 24 days temporal baseline. These results indicate that the temporal decorrelation in these cases is faster in summer than in winter, possibly as a result of crop growth and tillage of agricultural lands during the summer period. For pasture areas in the Netherlands, it has been shown by Morishita and Hanssen (2015b) that the coherence level of C-band interferograms with repeat intervals of 24-35 days (for RadarSAT2 and ERS/Envisat) is quite low. Even with a multilook factor of $L = 200$, the information content of such interferograms is not significant. In fact, due to the loss of coherence, the summer-acquisitions do not convey any useful geometrical information. The results of fig. 6.6 also reveal that, although the coherence level of short-baseline interferograms in winters is high, there is almost no coherence between two winter periods (as indicated by the low coherence values in the upper-right and the lower-left part of the coherence matrices). Such a coherence pattern results in sub-optimal ESM-phase estimation as demonstrated by the CRB standard deviations in figs. 6.6D-F. The σ_{CRB} values do not reach the PS standard deviation, indicating that the information content in the stack may not be sufficient for the precise estimation of phase time-series for these pixels.

It should be noted that, in this study, we did not consider the option of exploiting temporally coherent PS or DS. We only studied the feasibility of the exploitation of the entire timeseries. Consequently, for correct parameter estimation and unwrapping of DS-pixels after ESM-phase estimation, it is required that DS-pixels have a good phase stability in the entire ESM-phase time-series. To obtain such a stable time-series, it is important to have a *connected path* through all the acquisitions of the dataset, via relatively high-coherence interferometric phases. The results of fig. 6.6 over agricultural/pasture areas around Veendam, show that the summer-acquisitions cause a disconnect time-series, and so the further PSI processing and reliable exploitation of these kinds of pixels in agricultural/pasture areas is not feasible.

6.3.3 Coherence behavior over roads

In order to study the coherence behavior over roads, we analyzed two examples as shown in figs. 6.7A and B. The location of these cases are denoted by R_A and R_B in fig. 6.4. The coherence pattern of these two cases are significantly different compared to each other. The point R_A shows the coherence behavior similar to the DS-pixels in urbanized areas with small CRB standard deviation (fig. 6.7C), whereas the point R_B shows the coherence pattern more similar to the pasture areas with seasonal coherence behavior and low ESM-phase quality (see CRB standard deviation in fig. 6.7D). In order to get a better understanding of the reason of these two different coherence behavior, we provide an optical photo of the location of these two road examples in figs. 6.8A-B. For the R_A case, the road is a main highway with $\sim 40\text{m}$ width, elongated in the east-west direction (i.e., almost in the radar-look direction). Considering the pixel-size of approximately $\sim 20\text{m}$ by $\sim 4\text{m}$ in range and azimuth direction (the white box in fig. 6.8A), the east-west direction can result in a large number ($\bar{N}_{br} \sim 120$) of pixels whose area is fully covered by hard material of the road pavement, and consequently, results in relatively higher coherence values. On the other hand, the R_B is a local road with $\sim 6\text{m}$ width, in an almost north-south direction (and so perpendicular to the radar-look direction). This

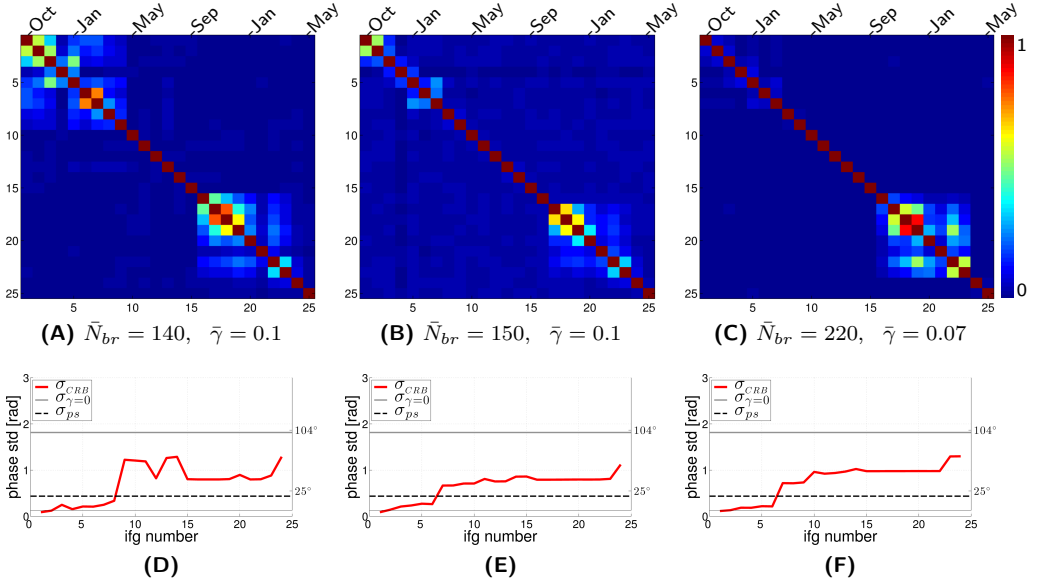


Figure 6.6: (A), (B), and (C) are three examples of coherence matrices in rural/pasture areas, corresponding to the locations P_A , P_B , and P_C in fig. 6.4. In the coherence matrices, the images are sorted based on the acquisition date (the months of acquisitions are indicated above the matrices). These matrices are the result of averaging coherence matrices of surrounding pixels. The average number of brothers and mean coherence of averaged pixels is indicated by \bar{N}_{br} and $\bar{\gamma}$, respectively. The bottom row plots (D), (E), and (F) show the CRB standard deviations of ESM-phase estimation. The standard deviation of zero-coherence noise ($\sim 104^\circ$), and the standard deviation of a typical point scatterer ($\sim 25^\circ$) are also plotted. For these three cases, the σ_{CRB} values do not reach to the PS standard deviation, indicating that the information content in the stack is not sufficient to estimate reliable phase time-series for these pixels.

particular geometry results in resolution cells that are partially covered by the road surface and the surrounding vegetation. Furthermore, the brotherhood area used in coherence estimation may be contaminated by the adjacent pixels from agricultural areas. This situation causes the coherence pattern of fig. 6.7D that is very similar to the pattern we observed over agricultural and pasture areas. We can conclude that, for DS-pixels over roads, the feasibility of extracting useful information and reliable phase estimation is case-dependent and varies road-by-road, depending on different factors such as the width and direction of the roads.

6.3.4 Cramèr-Rao bound study of the whole area

In the examples that we analyzed so far, we used the CRB bound of ESM-phase estimation as the indicator for feasibility of extracting useful information from DS-pixels. For a feasibility assessment over the entire Veendam area, we performed similar analyses and estimate the σ_{CRB} -time-series for all the pixels. Then for each pixel we took the maximum of CRB standard deviations (i.e., $\max(\sigma_{CRB})$). The results are shown in fig. 6.9. The pixels with $\max(\sigma_{CRB})$ smaller or equal to the standard deviation of a typical point scatterer ($\sigma_{ps} \sim 25^\circ$) are the potential DS-pixels with sufficient coherence,

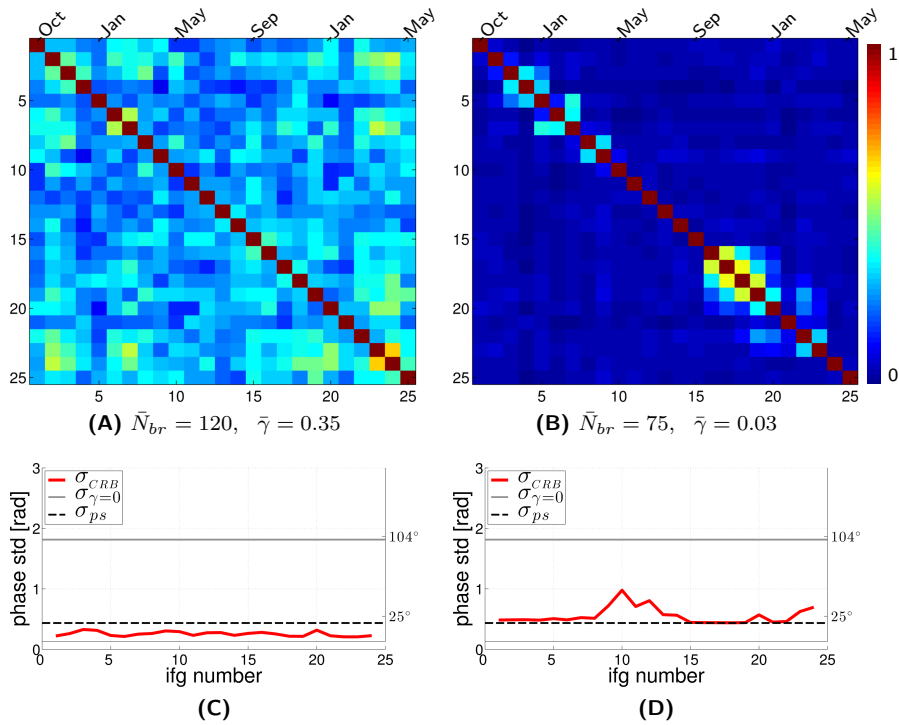


Figure 6.7: (A) and (B) are two examples of coherence matrices of roads, corresponding to the locations R_A and P_B in fig. 6.4. In the coherence matrices, the images are sorted based on the acquisition date (the months of acquisitions are indicated above the matrices). These matrices are the result of averaging coherence matrices of surrounding pixels. The average number of brothers and mean coherence of averaged pixels is indicated by \bar{N}_{br} and $\bar{\gamma}$, respectively. The bottom row plots (C) and (D) show the CRB standard deviations of ESM-phase estimation. The standard deviation of zero-coherence noise ($\sim 104^\circ$), and the standard deviation of a typical point scatterer ($\sim 25^\circ$) are also plotted. For these two examples, we observe entirely different coherence behaviors due to the geometry of the road. Optical images of these two roads are shown in figs. 6.8A-B).

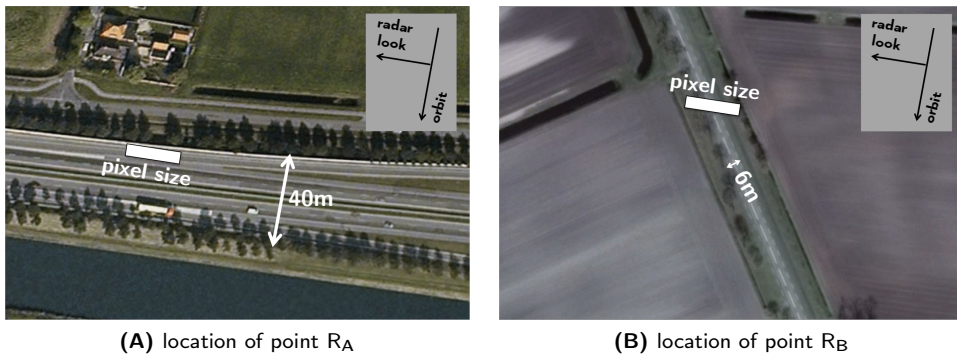
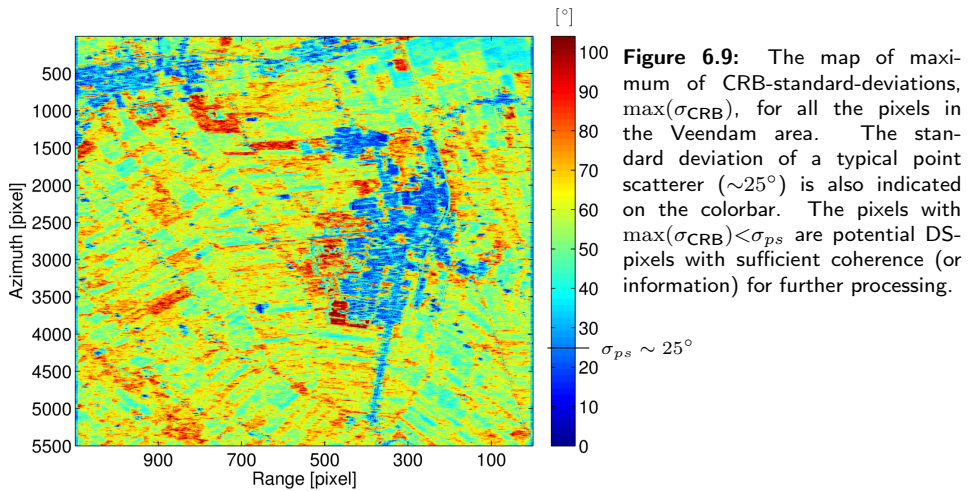


Figure 6.8: Optical (Google-Earth) photo of the roads (A) R_A and (B) P_B . The satellite geometry and the pixel size of approximately 20×4 m are also visualized for comparison with the direction and the width of the roads.



hence information, for further processing. The majority of these kinds of pixels are located in urbanized/developed areas. The agricultural and pasture fields do not generally show a sufficient level of information for reliable phase estimation. These results can be considered as feasibility indicators, which are based on the coherence analysis of the data before any ESM-phase estimation or other processing steps such as unwrapping and parameter-estimation. In the next section, we will discuss the results obtained by ESM-phase estimation and further combined PS-DS processing.

6.4 A posteriori analysis

With "a-posteriori analysis" we mean the analysis of the results of applying ESM-phase estimation combined with a standard PSI processing to the RadarSAT2 stack over Veendam. We will compare the results of the combined PS-DS processing with the results obtained by standard PSI processing, and evaluate the density improvements over different landscapes.

6.4.1 Processing setting

We applied a two-step hybrid methodology similar to the *SqueeSAR* approach by Ferretti et al. (2011b) (see sec. 2.2.2.3 for more information). The flowchart of the algorithm is depicted in fig. 6.10. The particular settings that we used in each step are described in the following.

- **Adaptive multilooking:** The multilooked phases for each pixel are computed by spatial averaging over statistically homogeneous pixels (SHP) detected by the Kolmogorov-Smirnov test (see sec. 2.4 for details of adaptive brotherhood selection). The brother pixels are selected within a window of 25×25 pixels. figure 6.3C

shows the number of selected brothers for each pixel. In order to reduce the spatially variable signal within the multilooking areas, the topographic phase component is computed and subtracted from all the interferograms, using the SRTM digital elevation model.

- **EMS-phase estimation:** After SHP selection and multilooking, we applied the ILS SM-phase estimation using all the possible interferometric combinations. This step is applied on all the pixels in the used crop (see fig. 6.3A). The weight matrix for ILS estimation is constructed based on the Fisher information index (eq. (5.18)), using the estimated coherence matrix of each pixel.
- **Selection of DS candidates:** After ESM-estimation, the posterior coherence factor $\hat{\gamma}_{PTA}$ (see eq. (5.20)) was estimated for each pixel. Pixels with a $\hat{\gamma}_{PTA}$ larger than 0.4 and with more than 25 brothers were selected as potential DS. In order to make the final ESM-stack of interferograms, for the selected pixels, we replaced the phase of the original SM interferograms with the phase estimates of ILS ESM-phase estimation. By using the pixels with more than 25 brothers, the phase time-series of PS-pixels are not affected by ILS-phase estimation. In fact, in the new ESM-stack the PS-pixels get their original phase, whereas for the selected DS-pixels, the ESM-phases are used.
- **Conventional PSI processing:** For PSI processing, we used the *Delft implementation of persistent scatterer interferometry* (DePSI) (van Leijen, 2014). We made a modification to DepSI regarding the combined PS-DS processing by changing the initial PS-candidate selection method. The PS candidates were selected using the standard amplitude dispersion method (see eq. (2.24)), while the DS-candidates, which had been selected in the previous step, were added to the set of PS-candidates. The combined set of PS and DS pixels was processed by DePSI². The final selection of coherent points (both PS and DS) was abstained by thresholding on the estimated *ensemble coherence* (see eq. (2.25)) of the pixels. The threshold of 0.7 was used for the final selection. In addition, pixels with an absolute estimated velocity larger than 3 cm/year and an estimated height larger than 100 meter were selected as false-detections, and were removed from the final results.

In the next section, we analyze the final results obtained by applying the aforementioned algorithm.

6.4.2 Results

The results of applying the hybrid PS-DS processing on the Veendam case are shown in fig. 6.11. We applied both the standard DePSI processing with the original SM interferograms, and also with the estimated equivalent SM interferograms. The obtained

²Specific settings of DePSI processing used in this study: a linear model and the bootstrapping approach have been used for temporal phase unwrapping, a Gaussian kernel with a length of one year has been used for atmosphere filtering, and the pixels associated with side-lobes of PS-pixels have been detected and removed before further processing (van Leijen, 2014).

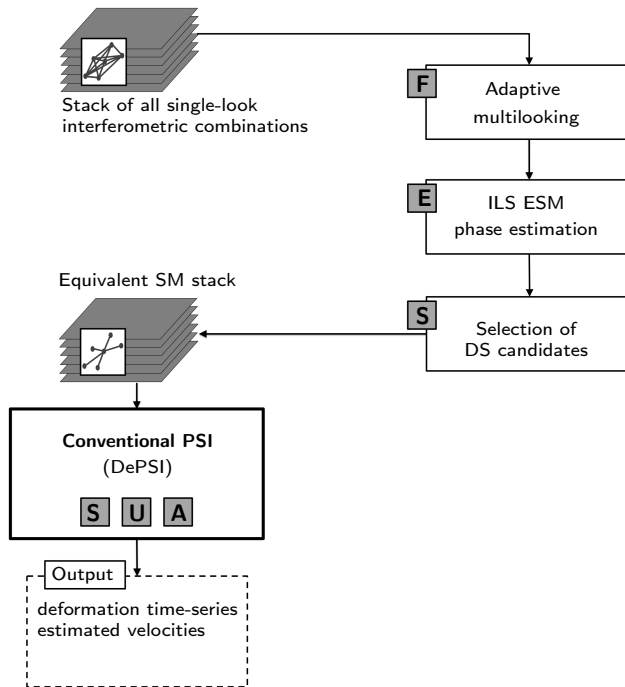


Figure 6.10: Generic flowchart of the hybrid methodology used for the Veendam case study. The processing steps are classified into the five basic TInSAR processing blocks as introduced in sec. 2.3 (S: pixel selection, U: unwrapping, A: atmospheric-signal mitigation, F: filtering, and E: equivalent SM-phase estimation.)

velocity maps are presented in figs. 6.11A and B, respectively. The same processing setup has been used for both cases. Also, the density of detected PS/DS-pixels is shown in figs. 6.11C and D. The results show a significant increase in the number of scatterers, especially in urban areas (see fig. 6.3B for the land-use map of the Veendam area). Although the general density is also improved in the rural areas, most of the new detected DSs are in areas around buildings or on the roads. Only a very low number of DS-pixels is detected over agricultural fields or pasture areas. In fact, this low density was expected based on the a-priori analysis of the temporal-coherence behavior over agricultural/pasture landscapes (sec. 6.3.2). In these areas, the coherence is almost entirely lost during the summer period, and the phase quality of DS-pixels in ESM-phase timeseries is not sufficient to detect these points as being persistent in the PSI processing.

Based on the land-use map of fig. 6.3B, we classified the detected PS/DS-pixels into two classes of urban/roads and agricultural/pasture. While the number of points in urban/road areas increased from 12594 to 144815 (almost 12 times larger), it improved from 1709 to 11003 pixels in the agricultural/pasture areas (i.e., four times more). As stated in sec.6.3.1, the limited relative improvement in point density for agriculture regions is mainly due to the fact that the entire timeseries is used, rather than focusing on coherent subsets in time. Another important remark is that the phases, and consequently

all other phase-derived estimates (e.g. velocities), of adjacent DS-pixels have some degree of correlation. This is due to the overlap between DS brotherhood areas that have been used in the adaptive multilooking. Therefore, the effective density-improvement is less than what we observe just by counting the detected DS-pixels independently and assuming no correlation between them.

Nevertheless the main message of these results is that the added-value of DS processing, in areas with similar landscape, is mainly in urbanized areas. The DS-pixels over agricultural and pasture regions do not generally have sufficiently consistent phase quality in order to be successfully exploited over multiple years in the PSI processing. Based on the a-priori analysis of sec. 6.3.2 over these areas, the main reason for this low phase quality is the seasonal behavior of the temporal coherence, which causes almost zero coherence during summer periods. In the next section, we will look further into the observed coherence pattern over agricultural and pasture areas.

6.5 Analytical model for seasonal temporal decorrelation

Both the a-priori and the a-posteriori analyses of previous sections—using C-band data with repeat time of 24 days—show limited improvement of measurement density in rural areas by exploiting DS-pixels in agricultural/pasture fields. In these areas, the results of the analyses indicate a seasonally varying coherence behavior of DS-pixels, resulting in a different temporal-decorrelation rate between summer and winter periods. Such a pattern has also been observed in other areas in the Netherlands. For example, Morishita and Hanssen (2015b) reported the same seasonal pattern over pasture areas based on an integrated analysis of radar data from various radar satellite missions.

To study the effect of different factors, such as satellite revisit time, radar wavelength, or multilooking factor, on phase quality of DS-pixels and the feasibility of their exploitation, it is useful to have an analytical model for the observed seasonal temporal decorrelation pattern. Such a model helps to parametrize the coherence behavior over agricultural/pasture landscapes. The available models for temporal decorrelation (see, for example, the models described in sec. 3.2.4.2), are usually based on a stationary behavior. For example, the common coherence model of exponential decay (see eq.(3.45)) is based on the assumption that scatterers within resolution cells are moving in a random-walk manner (Rocca, 2007) with certain variance and with stationary increments. Such a random process results in the same decorrelation rate in different periods, and therefore, it cannot account for the observed periodic pattern in the agricultural/pasture areas. In the following, we introduce a new model for the temporal decorrelation based on a random processes with non-stationary but periodic increments.

6.5.1 Model for periodic temporal decorrelation

In principle, due to the wide range of physical mechanisms that cause temporal decorrelation, there is no one single analytical model that can explain the coherence loss induced

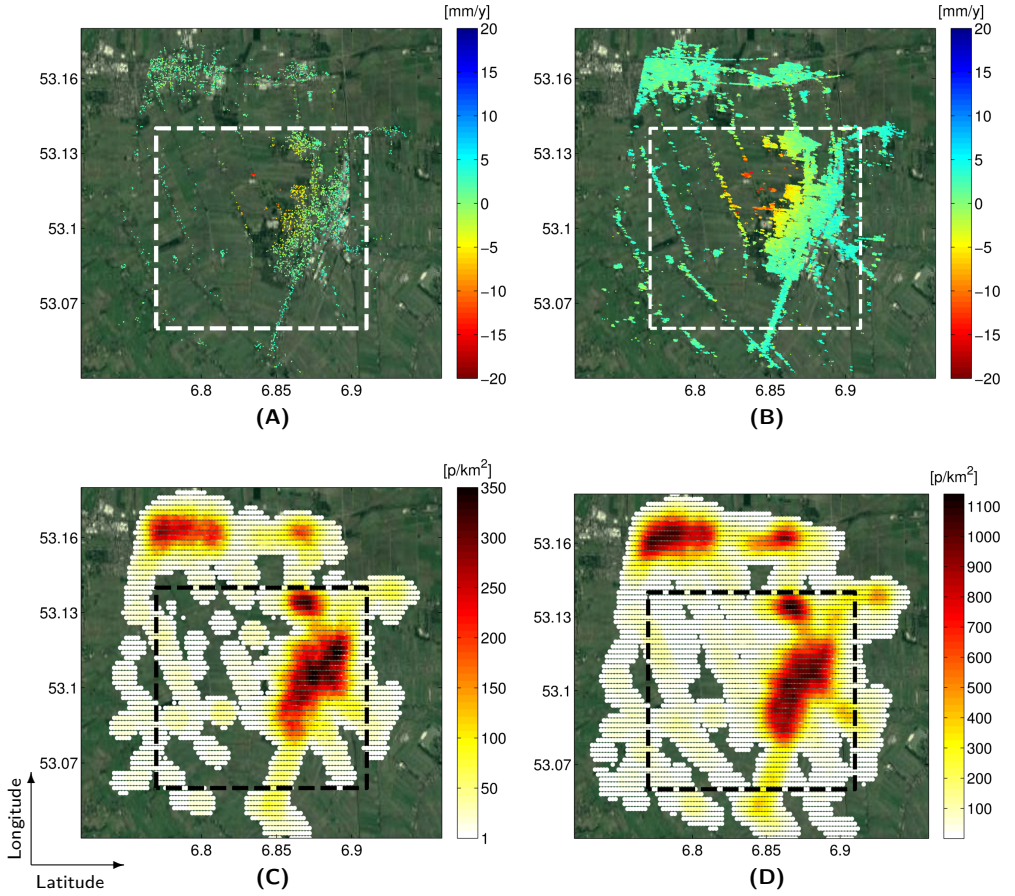


Figure 6.11: Comparison between the velocity maps obtained by applying DePSI processing using **(A)** original single-look SM interferograms, and **(B)** SM interferograms after ILS ESM-phase estimation. Figures **(C)** and **(D)** show the density of the detected PS/DS for the two processing methods, respectively. Note the different color scales of the density maps. The main density improvement is observed around buildings in the urbanized areas.

by these effects. There are some models, however, for processes which induce natural and gradual changes within resolution cells. Hypothetically, if all the elementary scatterers within a cell stay intact, but move independently but in a homogeneous manner, the temporal correlation can be described as (Zebker and Villasenor, 1992; Rocca, 2007)

$$\gamma_T = \exp\left(-\frac{1}{2}\left(\frac{4\pi}{\lambda}\right)^2 \sigma_r^2\right), \quad (6.1)$$

where σ_r^2 is the variance of the LOS motion of the elementary scatterers within the resolution cells. The motion variance σ_r^2 can be modeled in different manners as a function of time. The most common model assumes that the elementary scatterers move in a Brownian motion (or random-walk) manner with stationary increments that have certain variance. For example, see fig. 6.12A, which shows the stationary variance (σ_0^2) of the increments. For such a motion, the variance of the total motion between

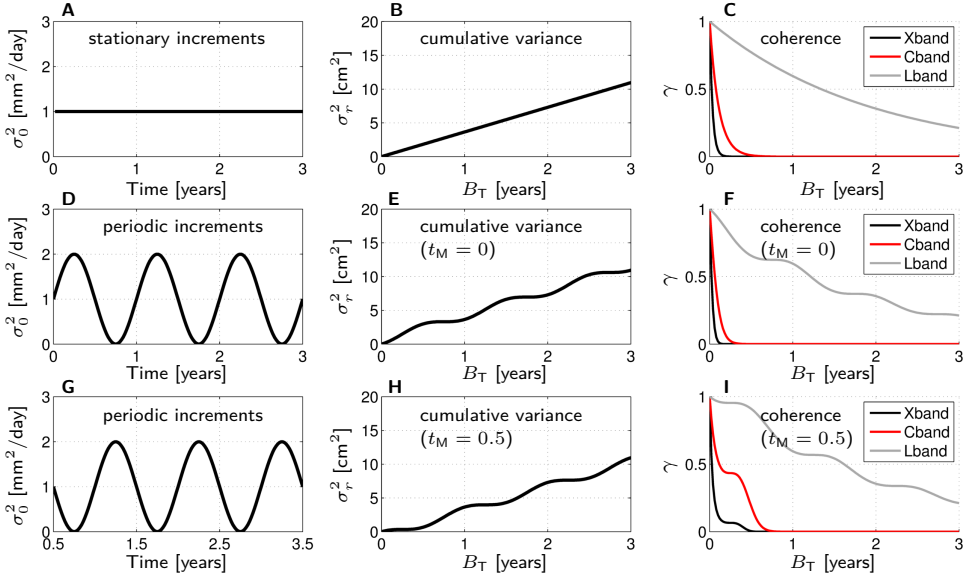


Figure 6.12: Demonstration of different temporal decorrelation models. Top row (A), (B), and (C): Random walk model with stationary increments of $\sigma_0^2 = 1 \text{ mm}^2/\text{day}$. Middle row (D), (E), and (F) seasonal random process with non-stationary and periodic increments with period $T = 1$ year, $t_0 = 0$, $\sigma_1^2 = \sigma_2^2 = 1 \text{ mm}^2/\text{day}$ (see eq. (6.5)), and the master time $t_M = 0$. Bottom row (G), (H), and (I): the same as the middle row but with the master time $t_M = 0.5$. First column: the variance of the motion increments. Second column: the variance of the cumulative motion. Third column: coherence as the function of B_T .

two acquisitions with dates t_M and t_S increases linearly as

$$\sigma_r^2 = \int_{t_M}^{t_S} \sigma_0^2 dt = \sigma_0^2 B_T, \quad (6.2)$$

where $B_T = t_S - t_M$ is the temporal baseline, and σ_0^2 represents the motion variance for the unit of time. Figure 6.12B shows, as an example, the temporal increase of σ_r^2 as a function of B_T for σ_0^2 of $1 \text{ mm}^2/\text{day}$. Inserting eq. (6.2) in eq. (6.1) gives the well-known exponential decay model for temporal coherence γ_T as

$$\gamma_T = \exp\left(\frac{-B_T}{\tau}\right), \quad (6.3)$$

where

$$\tau = \frac{2}{\sigma_0^2} \left(\frac{\lambda}{4\pi}\right)^2. \quad (6.4)$$

The parameter τ can be considered as the *temporal decorrelation range*. Figure 6.12C shows, for X, C, and L bands, the decorrelation pattern derived by eq. (6.3) for the stationary-increments motion with σ_0^2 of $1 \text{ mm}^2/\text{day}$. Note that the τ parameter is proportional to λ^2 . So, for example, with the wavelength of $\lambda_L = 23.5 \text{ cm}$ and $\lambda_C = 5.6 \text{ cm}$, the decorrelation rate for L-band is the factor of $\left(\frac{23.5}{5.6}\right)^2 \approx 17$ slower than the the decorrelation rate of C-band. These factors hold under the assumption that the "physical" elementary scatterers are equal for, e.g., C and L-band observations. Most likely this is not the case.

The decorrelation model of eq.(6.3) is a function of B_T only, and it cannot account for a periodic decorrelation. For example, an interferogram with B_T of one month in winter results in the same predicted decorrelation as one month in summer. In order to model the periodic behavior, we assume that elementary scatterers move in a similar manner as the Brownian motion but with increments that have non-stationary variance, which develops in time periodically with period T (e.g., for annual signal $T = 1$ year). For such a process we can write the increment variance as a function of time

$$\sigma_0^2(t) = \sigma_1^2 + \sigma_2^2 \sin(\omega(t - t_0)), \quad (6.5)$$

where $\omega = \frac{2\pi}{T}$ is the angular frequency, t_0 the initial time, σ_1^2 the variance factor which is constant in time, and σ_2^2 the variance of the periodic component. The introduction of two different variance factors σ_1^2 and σ_2^2 is necessary to guarantee that we always get positive (or zero) variance³, provided that $\sigma_1^2 \geq \sigma_2^2$. As an example, see figs. 6.12D and G, which show the non-stationary variance $\sigma_0^2(t)$ with $t_0 = 0$, $T = 1$ year, and $\sigma_1^2 = \sigma_2^2 = 1 \text{ mm}^2/\text{day}$. The difference between the plots D and G is that the $\sigma_0^2(t)$ has been evaluated for two different time intervals of $[0 - 3]$ and $[0.5 - 3.5]$, respectively. For such a random process with periodic-variance increments, we derive the variance of the total movement between two time instants t_M and $t_S = t_M + B_T$ by the integration over eq. (6.5) as

$$\begin{aligned} \sigma_r^2 &= \int_{t_M}^{t_M+B_T} \sigma_0^2(t) dt = \int_{t_M}^{t_M+B_T} (\sigma_1^2 + \sigma_2^2 \sin(\omega(t - t_0))) dt \\ &= \sigma_1^2 t - \frac{\sigma_2^2}{\omega} \cos(\omega(t - t_0)) \Big|_{t_M}^{t_M+B_T} \\ &= \sigma_1^2 B_T + \frac{\sigma_2^2}{\omega} \left(\cos(\omega(t_M - t_0)) - \cos(\omega(t_M + B_T - t_0)) \right). \end{aligned} \quad (6.6)$$

Note that eq. (6.6) is an extension of the random-walk model of eq. (6.2). The first component in the left-hand side of eq. (6.6) is the same as the random-walk model, and the second term is the periodic component. Unlike the random-walk model which is only dependent on the temporal baseline B_T , the periodic component also depends on the master acquisition time t_M . Figure 6.12E and H shows, as examples, the annual variation of σ_r^2 as a function of B_T for two different master time $t_M = 0$ and $t_M = 0.5$ years, respectively. By inserting eq. (6.6) in eq. (6.1), we obtain a new model for the temporal coherence as a function of B_T and t_M ,

$$\gamma_T = \exp\left(\frac{-B_T}{\tau_1}\right) \exp\left(\frac{\cos(\omega(t_M + B_T - t_0)) - \cos(\omega(t_M - t_0))}{\omega\tau_2}\right), \quad (6.7)$$

where τ_1 and τ_2 are

$$\tau_1 = \frac{2}{\sigma_1^2} \left(\frac{\lambda}{4\pi}\right)^2, \quad \text{and} \quad \tau_2 = \frac{2}{\sigma_2^2} \left(\frac{\lambda}{4\pi}\right)^2, \quad (\sigma_1^2 \geq \sigma_2^2, \tau_2 \geq \tau_1). \quad (6.8)$$

³In eq. (6.5), if we only consider the second term (i.e., the periodic component), the $\sigma_0^2(t)$ can get negative values, which is contradictory with the very definition of variance. In order to solve this problem, we introduce the constant variance of σ_1^2 . In this way, the $\sigma_0^2(t)$ is always positive or zero if $\sigma_1^2 \geq \sigma_2^2$.

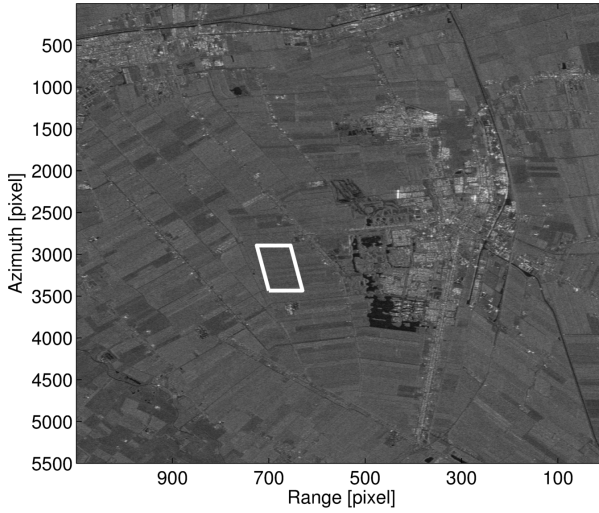


Figure 6.13: The white box shows the location of a 1 km² area that has been used for estimating the coherence matrix used for the temporal decorrelation modeling. The obtained coherence matrix, and the results of the modeling are presented in fig. 6.14.

The conditions of $\sigma_1^2 \geq \sigma_2^2$, and $\tau_2 \geq \tau_1$ are necessary in order to get positive-definite covariance matrices and coherence values smaller than 1. Examples of the decorrelation model of eq. (6.7) as a function of B_T are shown in figs. 6.12F and I, for X-, C-, and L-bands, and for two different master dates (i.e., $t_M = 0$ and $t_M = 0.5$ years). First of all we can see that the proposed model provides two different coherence-loss mechanisms for the two master timings. For example, if we assume t_0 is within summer, the case of $t_M = t_0 = 0$ shows the coherence behavior in summers, and the second case of $t_M = t_0 + T/2 = 0.5$ demonstrates the coherence loss during the winter period, in which the pixels lose their coherence much slower than in summer.

The model of eq. (6.7) can be considered as the extension of the random-walk model of eq. (6.3). When the τ_2 parameter becomes very large (i.e., the variance of the periodic motion σ_2^2 is very small), the periodic part of the model will vanish as

$$\lim_{\tau_2 \rightarrow \infty} \exp\left(\frac{-B_T}{\tau_1}\right) \exp\left(\frac{\cos(\omega(t_M + B_T - t_0)) - \cos(\omega(t_M - t_0))}{\omega\tau_2}\right) = \exp\left(\frac{-B_T}{\tau_1}\right), \quad (6.9)$$

and only the random-walk part remains.

With the proposed model of eq. (6.7), it may be possible to describe the observed seasonal coherence behavior in agricultural and pasture areas. Assuming that the period T is one year, the model has three free parameters τ_1 , τ_2 , and t_0 . In the next section, we estimate these model parameters based on the observed coherence matrices in the Veendam case study.

6.5.2 Estimation of coherence model parameters

For the modeling of temporal-decorrelation, it is helpful to have timeseries of images, which are as long as possible. For this analysis, we used a stack of 74 RadarSAT2 SLC images acquired between July 2009 and July 2014 (i.e., 5 years of data with a 24 days

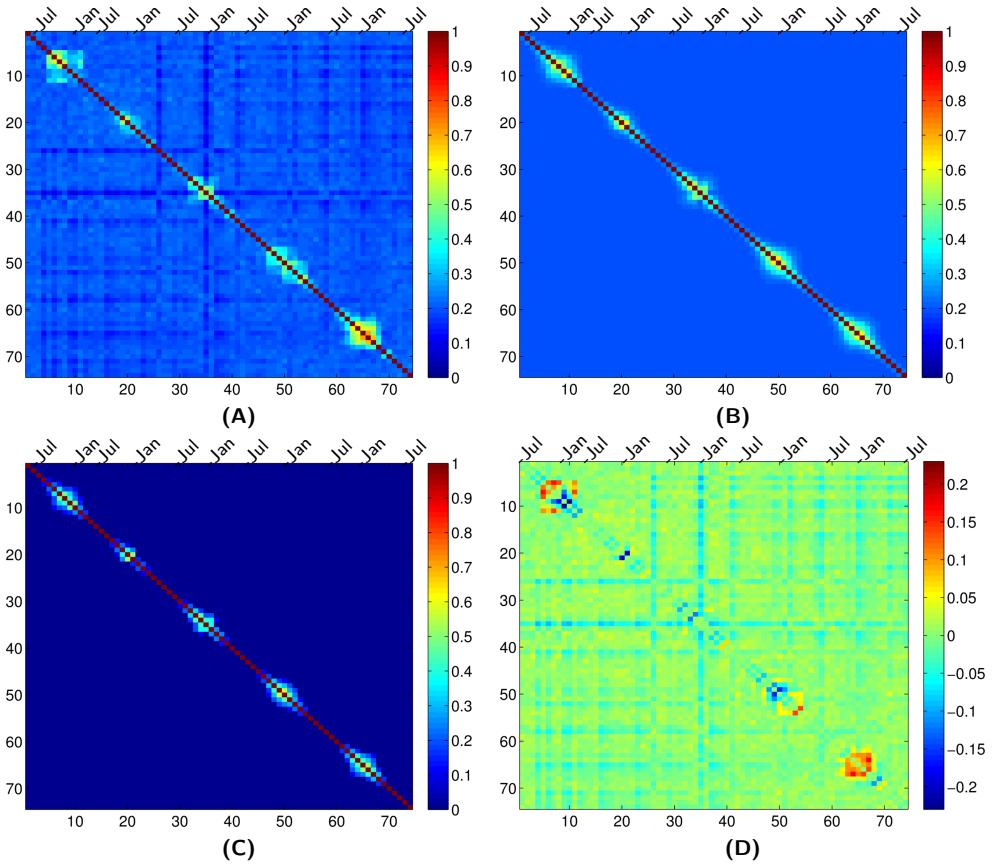


Figure 6.14: Results of the coherence modeling: **(A)** observed coherence matrix in a sample agricultural/pasture area, west of Veendam (see fig. 6.13), **(B)** model of the biased coherence matrix based on the estimated parameters, **(C)** model of the unbiased coherence matrix based on the estimated parameters, and **(D)** the modeling residuals or misfit between observations and the model (note the different color-scale).

revisit time). An approximately 1 km^2 area west of Veendam is chosen as visualized in fig. 6.13.

The coherence values have been estimated by the conventional coherence estimator (see eq. (3.28)). To get a more precise coherence estimation, we averaged the coherence values over the whole selected area. To compute the average coherence, we only use pixels with approximately the same number of brothers and the same mean coherence. The estimated coherence matrix is shown in fig. 6.14A. The seasonal pattern is clearly visible in the estimated coherence matrix. In order to estimate the model parameters of temporal decorrelation, the other decorrelation mechanisms, such as geometrical and thermal decorrelation, should be also included in the model. The total coherence can be written as

$$\gamma = \gamma_{\text{others}} \gamma_T \quad (6.10)$$

where γ_{others} accounts for other decorrelation mechanisms as

$$\gamma_{\text{others}} = \gamma_{\text{thermal}}\gamma_{\text{procc}}\gamma_{\text{geom}}\gamma_{\text{dc}}. \quad (6.11)$$

The γ_{others} is evaluated by analytical models reviewed in sec. 3.2.4.2 and based on the RadarSAT2 satellite parameters. As a result, the final total coherence is only a function of the three unknown parameters of the temporal decorrelation model of eq. (6.7) (i.e., τ_1 , τ_2 , and t_0):

$$\gamma(\tau_1, \tau_2, t_0) = \gamma_{\text{others}} \cdot \exp\left(\frac{-B_T}{\tau_1}\right) \cdot \exp\left(\frac{\cos(\omega(t_M + B_T - t_0)) - \cos(\omega(t_M - t_0))}{\omega\tau_2}\right) \quad (6.12)$$

The parameters of the model of eq. (6.12) can now be estimated against the estimated coherence values $\hat{\gamma}$. The estimated coherences are results of the standard coherence estimation. It is well-known that the coherence estimator is biased especially for small coherence values (Touzi et al., 1999; Hanssen, 2001). The expectation of the estimated coherence⁴ (i.e., $E\{\hat{\gamma}\}$) is not equal to the true coherence γ , but is a function of it (Touzi et al., 1999):

$$E\{\hat{\gamma}\} = G(\gamma) = \frac{\Gamma(L)\Gamma(3/2)}{\Gamma(L+1/2)} {}_3F_2(3/2, L, L; L+1/2, 1; \gamma^2)(1-\gamma^2)^L, \quad (6.13)$$

where L is the number of looks, $\Gamma(\cdot)$ is the gamma function, and ${}_3F_2(\cdot)$ the generalized hypergeometric function (for more information about eq.(6.13), see eq.(3.32) and fig. 3.1). For simplicity, we used the function $G(\gamma)$ to denote the function of eq.(6.13). To estimate the model parameters τ_1 , τ_2 , and t_0 based on the biased coherence observations $\hat{\gamma}$, we used eq. (6.13) as the functional model, and minimize the following objective function

$$\hat{\tau}_1, \hat{\tau}_2, \hat{t}_0 = \underset{\tau_1, \tau_2, t_0}{\operatorname{argmin}} \left\| \hat{\gamma}_{\text{vec}} - G(\gamma_{\text{vec}}(\tau_1, \tau_2, t_0)) \right\|^2, \quad (6.14)$$

where $\hat{\gamma}_{\text{vec}}$ and γ_{vec} are the vectors of all the $\hat{\gamma}$ values and the corresponding $\gamma(\tau_1, \tau_2, t_0)$ functions, respectively. A nonlinear least squares algorithm⁵ was used for the estimation, resulting in the following estimates for the three parameters

$$\begin{aligned} \hat{\tau}_1 &= 13.5 \text{ days,} \\ \hat{\tau}_2 &= 17 \text{ days,} \\ \hat{t}_0 &= 78 \approx 18\text{th of March.} \end{aligned}$$

Figure 6.14B shows the modeled observations, and fig. 6.14D shows the residuals of the modeling (note the different color scales of the residual plot). Despite some small differences, the results show reasonable agreement between the "observations" and the model. Using eq. (6.12), the unbiased coherences were also computed, and the results are presented in fig. 6.14C.

⁴In this section, for simplicity, we use γ as indicator of the absolute coherence $|\gamma|$.

⁵For nonlinear least squares estimation, we used the trust-region-reflective algorithm (Coleman and Li, 1996), as implemented in Matlab2014A.

	Satellite Wavelength [mm]	R2 56	Env/ERS 56	SenA 56	SenA/B 56	TSX 31	ALOS 236
Constant components $\gamma_{\text{thermal}} = \frac{1}{1+\text{SNR}^{-1}}$	SNR [db]	12	12	12	12	12	12
$\gamma_{\text{procc}} = \text{sinc}^2(\sigma_{\text{coreg},a,r})$	$\sigma_{\text{coreg},a,r}$ [pixel]	0.1	0.1	0.1	0.1	0.1	0.1
Geometrical dec. $\gamma_{\text{geom}} = \max(1 - \frac{ B_{\perp} }{B_{\perp\text{max}}}, 0)$	$\sigma_{B_{\perp}}$ [m] $B_{\perp\text{max}}$ [km]	200 1.3	200 1.1	50 1.2	50 1.2	50 3.8	100 7.0
Temporal dec. eq.(6.7)	Repeat interval [days]	24	35	12	6	11	46
	$\hat{\tau}_1$ [days]	13.5	13.5	13.5	13.5	4.1	239
	$\hat{\tau}_2$ [days]	17	17	17	17	5.2	301
	\hat{t}_0 (date)	18Mar	18Mar	18Mar	18Mar	18Mar	18Mar

Table 6.1: Parameters used in the synthetic feasibility study for different radar satellite missions.

The estimated parameters $\hat{\tau}_1$, $\hat{\tau}_2$, \hat{t}_0 can be used to simulate synthetic coherence matrices for datasets with a different number of images, a different number of looks, and different radar wavelengths. In the next section, we use these estimated parameters to assess the feasibility of exploiting DS-pixels in agricultural/pasture areas for different satellite missions.

6.6 Feasibility study

We used the estimated seasonal temporal-decorrelation for agricultural and pasture areas to simulate the corresponding coherence matrix for different satellite missions. Using this setting, the important question to answer is whether the DS exploitation method is capable to extract the high quality phase timeseries in these areas. In addition to the temporal decorrelation, other coherence components also are simulated. Table. 6.1 shows the used parameters for each satellite. Note that the decorrelation rate components τ was estimated, in the previous section, only for the C-band data. For other bands these parameters can be simply computed as

$$\tau_{\text{X-band}} = \left(\frac{\lambda_{\text{X}}}{\lambda_{\text{C}}}\right)^2 \tau_{\text{C-band}}, \quad \tau_{\text{L-band}} = \left(\frac{\lambda_{\text{L}}}{\lambda_{\text{C}}}\right)^2 \tau_{\text{C-band}}, \quad (6.15)$$

assuming that the elementary scatterers are the same for different wavelengths. The estimated $\hat{\tau}_1$ and $\hat{\tau}_2$ components are presented in the last two rows of table. 6.1 for different missions.

For simulation of the coherence matrices, a period of three years data was considered. In other words, we want to assess the feasibility of the utilization of DS-pixels if we have three years of data from each satellite. Consequently the number of images for each satellite is different due to the different repeat intervals. The simulated coherence matrices are visualized in fig. 6.15. The number of SLCs is also indicated in the plots. The seasonal pattern is clear, and the relatively high coherence for L-band ALOS and

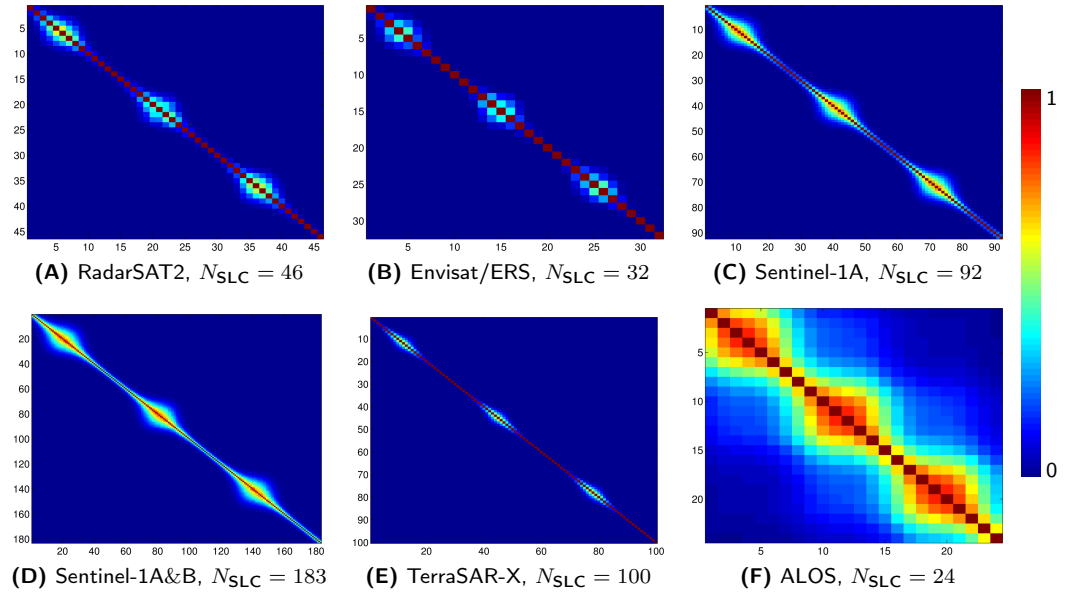


Figure 6.15: Predicted coherence matrices for studying the feasibility of DS exploitation for different radar satellite missions over agricultural/pasture areas, based on the estimated and assumed model parameters in table 6.1. Three years of data are assumed, resulting in different number of images for each mission (due to their different repeat interval).

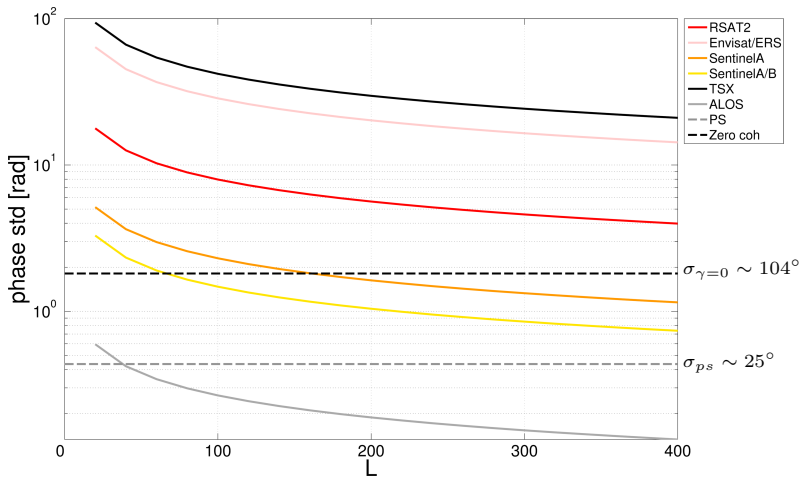


Figure 6.16: Predicted $\max(\sigma_{CRB})$ for different multilooking factor L for different satellite missions in the case of three years data and for simulated coherence matrices of fig. 6.15. The standard deviation of typical PS-pixels (25°), and the maximum possible standard deviation (104°) are also plotted. Note the logarithmic scaling of y -axis.

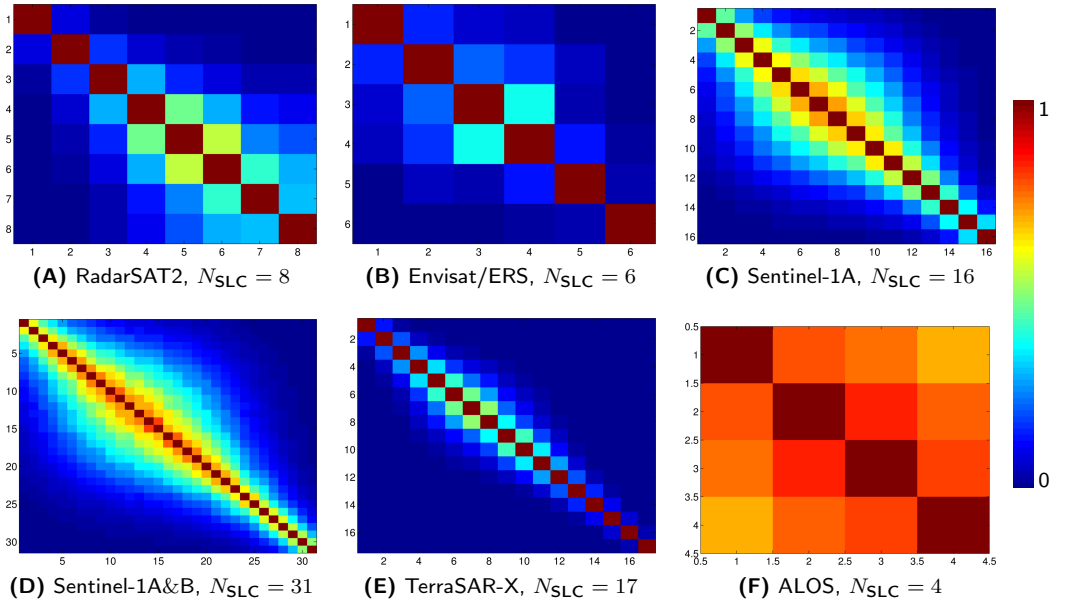


Figure 6.17: Predicted coherence matrices for studying the feasibility of DS exploitation for different radar satellite missions over agricultural and pasture areas, based on the estimated and assumed model parameters in table. 6.1. Six months of data are assumed, resulting in a different number of images for each mission (due to their different repeat interval).

the low coherence for X-band TSX is evident. To assess the feasibility, we compute the maximum CRB bound of ESM-phase estimation $\max(\sigma_{\text{CRB}})$ (similar to the a-priori analysis of sec. 6.3) based on different simulated coherence matrices. The closeness of $\max(\sigma_{\text{CRB}})$ to the expected standard deviation of typical PS-pixels (in this case 25°) is used as an indicator that the information content of DS-pixels is sufficient to exploit their associated phase timeseries. As the $\max(\sigma_{\text{CRB}})$ is dependent to the number of looks (L), we evaluated $\max(\sigma_{\text{CRB}})$ for a number of looks L in the range of 20-400. The results are shown in fig. 6.16 for different satellite missions. The standard deviation of typical PS-pixels (25°), and the maximum possible standard deviation (104°) are also plotted. Note the logarithmic scaling of the computed $\max(\sigma_{\text{CRB}})$ parameters.

We see that the CRB bound can possibly be larger than the maximum possible standard deviation of 104° . For interpretation, we should consider the CRB bound as the inverse of the Fisher information content. Unlike the phase standard deviation (or variance) which has the upper-bound of 104° , the CRB bound (or its inverse, the Fisher information) can be between zero to infinity by definition. In fact, a zero coherence phase has standard deviation of 104° , while it has no information and consequently its CRB bound is infinity. For high information, the square root of the CRB bound approaches to the expected standard deviation. The results show that, except for the L-band ALOS mission, non of the other sensors can provide sufficient information for the exploitation of DS-pixels with the assumed coherence behavior. Although different coherence components are simulated, the main driving mechanism behind the observed pattern in these results is the temporal decorrelation which is mainly affected by the repeat time interval. For example,

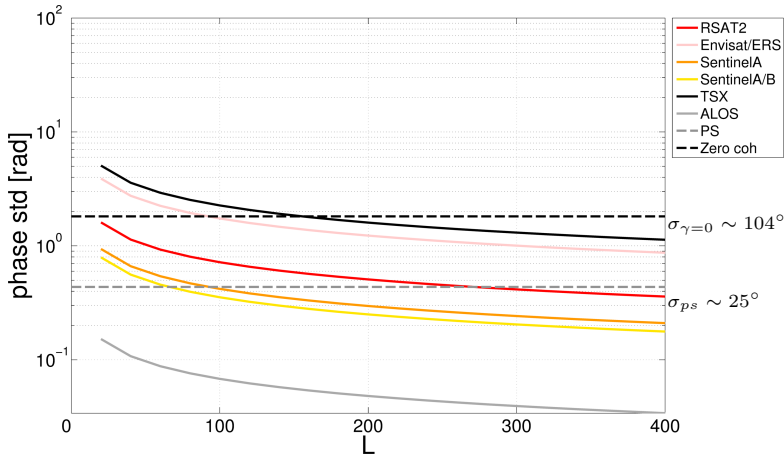


Figure 6.18: Predicted $\max(\sigma_{\text{CRB}})$ for different multilooking factor L for different satellite missions in the case of six months data and for simulated coherence matrices of fig. 6.17. The standard deviation of typical PS-pixels (25°), and the maximum possible standard deviation (104°) are also plotted. Note the logarithmic scaling of y -axis.

between Sentinel-1A case and the Sentinel-1A/B combination, the only difference is the repeat interval (i.e., 12 and 6 days, respectively), resulting in a better performance of Sentinel-1A/B. Based on these results we conclude that the information content of DS-pixels in three years datasets from these missions (except ALOS) is not enough for a successful utilization of these kinds of DS pixels, at least upto an L -factor of 400, which is already very large. Note that, in theory, if we continue to increase the L -factor, at some point we will approach to the quality of typical persistent scatterers and even better. However, for large multilooking factor we require a valid assumption of ergodicity over extremely large areas, which is not practical in real cases.

The results of fig. 6.16 are an indication of the information content of DS-pixels within the entire phase timeseries of three years. One would ask what would happen if we only process the coherent seasons (in this case winters). By processing the individual winter periods, it may be possible to use these kinds of DS-pixels. To assess this possibility, we repeat the experiment but, this time, using only 6 months of data during the winter period. The corresponding coherence matrices are shown in fig. 6.17, and the evaluated $\max(\sigma_{\text{CRB}})$ parameters are presented in fig. 6.18. These results show a quite promising capability of Sentinel-1 data, which reach to the desired quality (i.e., σ_{ps}) with an L -factor of approximately 100 or higher (approximately 100×100 m), which is practical in real scenarios. For TSX data, the information content is still very poor. For other C-band data, i.e., RadarSAT2, Envisat, and ERS, the phase quality is still not sufficient if we only process six months of data during the high coherence season. It should also be noted that, in addition to a sufficient phase quality, the number of images is also an important factor for a final feasibility study. By limiting the period of the full stack, we in fact reduce the number of final SM interferograms significantly. For example, for Envisat/ERS/RadarSAT2, over six months we get less than 10 images which is too low for standard timeseries processing. However the Sentinel-1 datasets have enough images for proper time-series processing even over six months. In summary, the high revisit time

of Sentinel-1 data shows a promising expectation regarding DS exploitation by C-band data over agricultural and pasture areas. The X-band data have a limited potential over these kinds of landscapes, and L-band ALOS data have very good performance, however with limitations of a lower resolution and a long repeat interval.

7

Conclusions and Outlook

In this study, we formulated and applied ESM-phase estimation of DS-pixels in a standard geodetic methodology. Additionally, we assessed the feasibility of exploiting distributed scatterers for deformation monitoring over a typical rural landscape in the Netherlands. Here, we present the main conclusions (sec. 7.1), and the contributions (sec. 7.2) of this study, followed by recommendations for further research (sec. 7.3).

7.1 Conclusions

The main conclusions of this study relate to the four research questions, as listed in chapter 1, are given in the following.

7.1.1 Mathematical model for ESM-phase estimation

How to formulate the functional and the stochastic part of the mathematical model for ESM-phase estimation in the form of a Gauss-Markov model of observation-equations?

Equivalent single-master (ESM) phase estimation is the key processing step for information extraction from DS-pixels. The objective of this processing step is to estimate, for each DS-pixel, a phase time-series equivalent to a single-master stack from phase differences in a multi-master stack of interferograms. From a physical point of view, this estimation reduces the decorrelation noise, while estimating, for each pixel, the equivalent SM-phase time-series corresponding to the physical path length differences between the targets and the sensor. The Gauss-Markov model for this estimation comprises a functional and a stochastic model. The functional model has been established and discussed in chapters 4 and 5, while the stochastic model has been established and elaborated on in chapter 3.

Functional model. The basic building block of the functional model for ESM-phase estimation is the *expected phase consistency condition*. This condition provides a functional relation between the expectation of the wrapped, multi-looked, and multi-master phases (or "observations") and ESM-phases (or "unknowns"). The most challenging property of the ESM-phase estimation is that the functional relation between the observations and unknown parameters is highly nonlinear due to the wrapping operation. The nonlinear model has been converted to a linear form by introducing additional integer ambiguity unknowns, resulting in a linear system of observation equations, as commonly used in geodetic methodology. This new model is a *hybrid* model as it comprises both *real-valued* unknowns (i.e. ESM-phases) and additional *integer* unknowns (i.e., ambiguities). The functional model is flexible to digest different subsets of interferograms. An important property of this hybrid model is the constraint on the integer ambiguities: due to the arithmetic properties of the wrapping operation, the possible values for the ambiguities are limited to 1, -1, and 0.

Stochastic model. In the Gauss-Markov framework, the stochastic model is described by the second statistical moment of observations. In the case of ESM-phase estimation, the stochastic model has been given in terms of the full covariance matrix of the wrapped multi-looked and multi-master phases associated to each DS-pixel. In case of independent observations, the covariance matrix would be diagonal. However the assumption of independency does not hold due to different reasons, e.g., due to a common master or slave image, or an overlap between the object spectra or time-periods covered by two interferograms.

In order to evaluate the full covariance matrix for each DS-pixel, the SAR statistics described by the pixel coherence matrix should be propagated into the dispersion of multilooked interferometric phases. We proposed a numerical Monte-Carlo approach to evaluate the full covariance matrix of DS-pixels. Also, we derived a closed-form approximation for all the elements of the covariance matrix. The closed-form approximation is computationally much more efficient than the Monte-Carlo approach, but it is only precise for DS-pixels with a large number of looks (e.g. $L > 50$). The covariance matrices constructed either by the Monte-Carlo approach or by the analytical approximation serve as the stochastic part of the Gauss-Markov model for the ESM-phase estimation problem.

7.1.2 ILS ESM-phase estimator

How to estimate ESM-phases using the weighted least squares estimator and how does it compare to other existing methods?

Integer Least Squares Estimator. The solution for the ESM-phase estimation, as formulated by the Gauss-Markov hybrid model, is given by the integer least squares (ILS) estimator (discussed in chapter 5). For this estimator, the weighted least squares objective function is defined as the L_2 -norm of the interferometric phase residuals.

The application of the ILS method for ESM-phase estimation requires two main modifications in the original ILS approach. The first modification is about inserting the constraints on integer unknowns. For ESM-phase estimation, each ambiguity a is con-

strained to $a \in \{-1, 0, 1\}$. Therefore, in the second step of ILS, when the float solutions are fixed to their nearest integers, this constraint should be exerted.

The second modification regards the choice of the weight matrix for ILS estimation. The ILS problem has been conventionally formulated with a weight matrix equal to the inverse of the covariance matrix of the observations. This is logical for observations with a Gaussian distribution because it provides the maximum likelihood estimation. As the multilooked interferometric phases are not normally distributed, their data statistics cannot be explained fully by the phase covariance matrix. Moreover, an accurate covariance matrix may not always be available (e.g. due to a bias and uncertainties in coherence estimation), and the numerical uncertainties in the evaluation of the covariance matrix may be amplified by the matrix inversion. Therefore, in the theoretical formulation, we expressed the ILS objective function with a generic weight matrix W , increasing the flexibility of the method to digest different kinds of weight matrices. However, an increase in flexibility also increases the subjectivity of the method. Therefore, for practical applications, we proposed and validated a weighting strategy based on the Fisher information index of multilooked interferometric phases. Via synthetic studies, we compared the performance of using the Fisher-information-based weight matrices with three other weighting strategies: (i) the inverse of the full covariance matrix of multilooked phases, (ii) a weight matrix with diagonal elements equal to the inverse of the phase variances, and (iii) a weight matrix with diagonal elements equal to the absolute coherence values. The results demonstrate that the Fisher-information-based weight matrix provides more precise ESM-phase estimates, compared to the other weight matrices (see sec. 5.3). In addition, using Fisher-information-based weight matrices has an advantage regarding the computational complexity of the ILS method, as it does not require a matrix inversion.

One of the advantages of ILS ESM-phase estimation is the quality description via the provision of a full covariance matrix of the estimates. These covariance matrices can be further propagated to other InSAR derived parameters and can play an important role in the further post-processing or geophysical modeling of time-series InSAR products.

Via a simulation study, we have shown that the ILS SM-phase estimator is unbiased, and the closeness of the variance of its residuals with the lower Cramér-Rao bound demonstrates the *minimum-variance* property (or "efficiency") of the proposed approach. The method has been successfully applied to a stack of interferograms over Torfajökull volcano in Iceland, resulting in doubling the number of detected coherent pixels with respect to conventional PSI.

Comparison of different estimators. The main difference between ILS ESM-phase estimation and all the other existing methodologies is that the ILS method is an optimization in the real-valued phase domain, while all the other five existing methods (as listed in sec. 4.3) have been formulated as optimizations in the complex domain. In order to situate both the ILS estimator and the other estimators in a unified mathematical framework and provide a theoretical comparison among them, a generic functional model, in the form of a system of observation equations is proposed. The observations of this unified model—i.e. the multilooked phases—can be expressed either by the phases themselves in the real-valued phase domain (i.e. $\hat{\phi} \in \mathbb{R}$) or by their associated phasors in the complex domain (i.e. $\exp(j\hat{\phi}) \in \mathbb{C}$). The ILS estimator gives a solution to the real-valued version of this unified model. We showed that all the other five discussed

methods provide specific solutions for the complex-valued representation of this model. The only difference between these methods are the objective function that they utilize to solve the unified functional model (see an overview in table 4.1). An important conclusion is that, despite some minor differences in their objective functions, the fundamental difference among the complex-domain estimators is in the approach that they use to assign weights to the interferometric observations.

The comparison between the efficiency and performance of four methods (i.e. maximum likelihood estimation (ML), eigendecomposition-based methods, least circular variance estimator, and the ILS approach) has been performed via a synthetic-data experiment. Two main aspects have been considered: (i) computational cost, and (ii) optimality of the estimators in terms of precision.

Regarding the computation time, the eigendecomposition-based estimators are much faster than the other estimators, as their solution can be simply computed by eigen-value decomposition which does not require any iterative algorithm, while the other methods (including ILS) require iteration. However there is a trade-off between the computational cost and the precision. While it is a faster estimator, the eigendecomposition-based method provides the lowest precision compared to the others. Among all the investigated estimators, the ILS method has the highest computational time, almost seven times slower than the maximum likelihood and circular variance estimator, and 15 times slower than the eigendecomposition-based estimators. This is the main drawback of the ILS EMS-phase estimation compared to other methods¹.

Regarding the precision of different estimators, the results show that the maximum likelihood estimator provides the best (minimum-variance) solution when the true coherence values are used in the estimation. However, in practice, the ML estimator suffers from instabilities induced by uncertainties and biases in the coherence estimation (as the ML estimator requires the inverse of the coherence matrix). Based on the results of the synthetic-data experiment, when the estimated coherences are used in the estimation, the ILS and the least circular variance estimator have comparable precision and show a better performance than the other estimators. The main conclusion is that the estimators that do not require the coherence matrix inversion and use direct coherence factors—or a function of coherence factors—as the weights provide a more stable solution than the ML estimator.

7.1.3 DS density over rural landscapes

How much can the DS-exploitation methods improve the spatial density of time-series InSAR measurements over a typical rural landscape in the Netherlands?

We performed a case study on a mining area close to the city of Veendam, the Netherlands. The combination of having different kinds of landscape and its high deformation rate together with the low PS density in agricultural areas makes this region a relevant

¹It should be noted that the comparison on computational cost is subjective as it is strongly dependent on the algorithmic implementation. In this study, a simple prototype implementation of the ILS algorithm was used, with a strong potential for improvement. Nevertheless, the results of the comparison provide a relative measure of computational complexity among different ESM-phase estimators.

case study area. The assessment of point density improvement by exploiting DS-pixels has been performed in two steps: (i) a-priori analysis based on studying coherence behavior of different kinds of landscape prior to applying the ESM-phase estimation (see sec. 6.3), and (ii) a-posteriori analysis based on actual point density obtained by applying ESM-phase estimation together with PSI processing.

The a-priori feasibility analysis of exploiting DS-pixels in the test area shows that the majority of DS-pixels with sufficient coherence over the entire time-series are located in urbanized and developed areas, and the agricultural and pasture fields do not show an adequate level of information (i.e., comparable to typical PS targets with phase standard deviation of 25 degree) for optimal phase estimation. Note that we did not consider the option of temporally correlated targets.

In the a-posteriori analysis, a combined PS and DS processing has been applied on the Veendam test site. The results confirm the conclusions derived from the a-priori analysis. The main added-value of DS processing is in urbanized and developed landscapes, with almost a factor of 5-10 in density improvement in developed areas. It should be noted that, due to the overlapping windows, used in multilooking, neighboring DS-pixels are not independent, and therefore, the effective density improvement is less than the numbers that we report just by counting the detected DS-pixels. Nevertheless, these numbers provide a qualitative measure of relative density improvement among different landscapes. Based on the number of detected DS-pixels, the agricultural and pasture areas show very limited improvement in the point density compared to the PS density in the conventional PSI processing. The main reason for this limited improvement is the seasonal behavior of the temporal coherence, which causes almost complete drop in coherence during summer periods. Therefore, the ESM-phase timeseries of DS-pixels in these areas do not have persistent coherence in the entire stack and cannot be exploited for the estimation of deformation time-series. Although, the scope of the study has been limited to the feasibility of the exploitation of the entire timeseries, the results show that, in temporally coherent subsets, there is still some unexploited information that cannot be extracted from processing the entire timeseries. In this regard, the potential of temporally coherent targets (TCS) should be evaluated (as applied e.g. by Ferretti et al., 2012).

7.1.4 Temporal decorrelation model

How to model the coherence behavior and its temporal variations over agricultural and pasture areas in the Netherlands? With such a model, what is the performance of different existing satellite missions regarding the exploitation of distributed scatterers?

A new model was introduced to describe the temporal decorrelation of agricultural and pasture areas. The hypothetical movements of elementary scatterers in a resolution cell were modeled as a stochastic process with non-stationary but periodic increments. The proposed periodic model results in a new temporal decorrelation model as a function of the temporal baseline and the date of the master image of each interferogram. This model is the extension of the exponential decay model, which is commonly used to

describe the temporal decorrelation. The main difference to the exponential decay model is that the proposed model is also capable of describing a seasonal coherence-loss.

The parameters of the proposed decorrelation model have been estimated for the Veen-dam data. The results showed a good agreement between the observed coherence behavior and the model. The estimated model shows an almost entire loss of coherence in the summer periods for C-band RadarSAT2 data over agricultural areas.

The estimated parameters of the decorrelation model have been used to simulate synthetic coherence matrices that are used to assess the feasibility of exploitation of DS-pixels in agricultural areas by different satellite missions. The results show that assuming a three years stack of data, the information content of DS-pixels from current C-band and X-band missions is not enough for successful utilization of these kinds of pixels, considering the condition that the entire timeseries is used. However, the L-band data show a good phase quality over agricultural/pasture area.

By processing the individual coherent periods/subsets (i.e. six months from October-March), the feasibility study also shows that it may be possible to exploit DS-pixels over agricultural areas. For C-band data of RadarSAT2, Envisat, and ERS, the phase quality is not sufficient even in individual seasons due to the relatively long revisit time. In contrast, the short revisit time of Sentinel-1 data shows a promising expectation regarding DS exploitation by C-band data over agricultural and pasture areas. The X-band data generally have a very limited potential for these kinds of landscapes, and L-band ALOS data have very good performance, however with limitations of a lower resolution and a long repeat interval.

7.2 Contributions

The contributions of this research are:

- We introduced a generic framework, consisting of five basic processing blocks, to describe different time-series processing methodologies in a unified manner (chapter 2).
- We proposed a Monte-Carlo approach to evaluate the full covariance matrix of DS-pixels (chapter 3).
- We derived a closed-form approximation to evaluate the second-order statistics of interferometric phases (chapter 3).
- We gave a theoretical comparison of existing ESM-phase estimators, and showed that the main difference between them is only in the used weight matrix in the estimation (chapter 4).
- We introduced a mathematical model for ESM phase estimation in the form of a linear system of observation-equations (chapter 5) and (Samiei-Esfahany et al., 2016).
- We introduced the weighted ILS ESM-phase estimator (chapter 5).

- We compared different ESM-phase estimators on synthetic datasets (chapter 5).
- We analyzed the effect of different factors, such as detrending, the multilooking factor, weighting, and subset selection, on the efficiency and precision of the ILS ESM-phase estimator (chapter 5).
- We analyzed the temporal coherence behavior of three different landscapes (urbanized, agricultural and pasture, and roads) in the Netherlands (chapter 6).
- We applied a hybrid PS-DS processing on the Veendam subsidence. Results show a maximum subsidence rate of -17 mm/year in this area (chapter 6).
- We introduced a new model for the temporal decorrelation of agricultural and pasture areas as a stochastic process with non-stationary but periodic increments (chapter 6).
- We estimated the temporal decorrelation parameters for the agricultural/pasture areas around Veendam (chapter 6).
- We assessed the feasibility of complete timeseries exploitation of DS-pixels for different satellite missions over typical agricultural and pasture areas in the Netherlands (chapter 6).
- We designed, implemented, and validated DS software as an extension to the Delft Persistent Scatterer Interferometry (DePSI) software.

7.3 Recommendations

Regarding the exploitation of DS-pixels in InSAR stacks, there are still complications and improvements that we did not address in this study. A few topics for further research are listed in the following.

- In this study, we only studied the exploitation of DS-pixels that show a good phase stability over the entire timeseries. However, over agricultural areas, as tillage and harvesting are known to destroy coherence completely, this approach is sub-optimal. The observed seasonal coherence behavior over agricultural areas shows the potential of extracting information from subsets of interferograms (for example subsets in the coherent seasons). In this regard, the potential of exploiting temporally coherent targets needs to be studied (e.g., see Ferretti et al., 2012).
- The focus in this study, and also in most of the other existing DS algorithms, is to process single-track data acquired from an individual satellite mission. However, recent research demonstrates the potential of joint processing of data stemming from different sensors to better estimate small deformation signals in pasture areas (Morishita and Hanssen, 2015a). The feasibility of this kind of multi-sensor estimation over different landscapes should be assessed. It should be evaluated how the ESM-phase estimation can be integrated into a multi-sensor processing.

- The periodic temporal decorrelation model proposed in this study has been validated against data from a limited area around Veendam. It is desirable to estimate the parameters of this model over different kinds of landscapes. The results can be used for land-use classification based on the coherence behavior. Such an analysis allows a more precise feasibility study and error budget assessment for DS-pixels over different landscapes.
- The fundamental assumption behind all ESM-phase estimators is the validity of the expected phase consistency condition. That is, it is assumed that all the inconsistencies are purely induced by random noise. However, it has been recently shown that there are also some mechanisms that can induce systematic phase inconsistencies, for example, due to volume scattering or due to variation in soil moisture (De Zan et al., 2015; Zwieback et al., 2016). The indication of the existence of such inconsistencies raises a question regarding the extent to which the ESM-phase estimators are affected by them. It should be investigated what would happen to the soil moisture effect by postulating the expected phase consistency in the estimation process, and whether the systematic phase inconsistencies are optimally or partially filtered out, or may leak into the final ESM-phase estimates. The sensitivity of different ESM phase estimators to these systematic effects should be assessed.
- The main limiting factor of using the proposed ILS ESM-phase estimation is its computational time, especially in the step of ambiguity resolution. It is desirable to speed-up the ILS algorithm. In this context, recent advances in numerical improvements in the implementation of fast ILS estimation algorithms, as in Jazaeri et al. (2011), should be considered.
- One of the attractive properties of the geodetic methodology is the special attention to the quality aspects of the obtained results in terms of precision and reliability of the estimated parameters. Although some aspects of quality description—e.g. the error propagation in the ILS method and the precision of the ESM-phase estimator—were utilized in this study, the geodetic quality description was not exploited to full extent. The possibility of using by-products of the ILS estimator, e.g. the *success rate*, or the *a-posteriori variance factor* as a quality indicator of DS-pixels should be considered. These by-products can be used for optimal detection of high quality DS-pixels. Also, the body of knowledge about hypothesis testing in an ILS framework can be used to detect/remove low-quality interferograms ("outliers") in the ESM-phase estimation. Another aspect is the full error propagation through the entire time-series processing. It is desirable to design an algorithm to propagate all the error sources from SLC observations to final InSAR timeseries and to final derived products such as deformation rates. Due to the large number of points and images, an efficient error propagation scheme through all the processing steps should be designed.
- From a computational perspective, DS processing algorithms are computationally much more expensive than the PSI algorithms. The reason is twofold: (i) the number of DS-pixels is generally much larger than the number of PS, and (ii) a multi-master set of interferograms (or all the possible interferometric combinations

in some algorithms) should be constructed compared to SM-stacks of PSI algorithms. The second condition can be relaxed. The results of synthetic examples in this study show that there is redundant information in the set of all possible interferograms. The same amount of information may be possible to extract from smaller subsets. A design methodology should be defined to optimally select the most informative subset of interferograms. The feasibility of recursive ESM-phase estimation should be investigated, to speed-up the DS algorithms in case of near real-time processing.

Appendices



Derivations

A.1 Derivations of Chapter 3

A.1.1 Derivation of the covariance matrix of eq. (3.83)

Objective:

The objective is to evaluate the covariance matrix of the vector $\underline{y} = [\underline{\phi}_{12}, \underline{\phi}_{34}]^T$ via the approximation (nonlinear error propagation):

$$Q_y = D\left\{ \begin{bmatrix} \underline{\phi}_{12} \\ \underline{\phi}_{34} \end{bmatrix} \right\} \approx J_F(x|x_0) Q_x J_F(x|x_0)^T, \quad (\text{A.1})$$

where

- x is the vector of interferometric real and imaginary components as

$$\underline{x} = \begin{bmatrix} \underline{x}_1 \\ \underline{x}_2 \\ \underline{x}_3 \\ \underline{x}_4 \end{bmatrix} = \begin{bmatrix} \text{Re}(\langle \underline{I}_{1,2} \rangle) \\ \text{Re}(\langle \underline{I}_{3,4} \rangle) \\ \text{Im}(\langle \underline{I}_{1,2} \rangle) \\ \text{Im}(\langle \underline{I}_{3,4} \rangle) \end{bmatrix}, \quad (\text{A.2})$$

- $F(\underline{x})$ is the multivariate function describing the relationship between the vector of two interferometric phases (i.e., $\underline{y} = [\underline{\phi}_{12}, \underline{\phi}_{34}]^T$) and \underline{x} :

$$\underline{y} = \begin{bmatrix} \underline{\phi}_{12} \\ \underline{\phi}_{34} \end{bmatrix} = F(\underline{x}) = \begin{bmatrix} F_1(\underline{x}) \\ F_2(\underline{x}) \end{bmatrix} = \begin{bmatrix} \arctan\left(\frac{\underline{x}_3}{\underline{x}_1}\right) \\ \arctan\left(\frac{\underline{x}_4}{\underline{x}_2}\right) \end{bmatrix}, \quad (\text{A.3})$$

and

- $J_F(\underline{x}|x_0)$ is the Jacobian of the multivariate function $F(\underline{x})$ with respect to the vector \underline{x} evaluated at an initial value x_0 .

Derivation of $J_F(\underline{x}|x_0)$:

The Jacobian of $J_F(\underline{x})$ is computed by taking the partial derivatives of F with respect to the elements of \underline{x} , so

$$J_F(\underline{x}) = \begin{bmatrix} \frac{-x_3}{x_1^2+x_2^2} & 0 & \frac{x_1}{x_1^2+x_3^2} & 0 \\ 0 & \frac{-x_4}{x_2^2+x_4^2} & 0 & \frac{x_2}{x_2^2+x_4^2} \end{bmatrix} \quad (\text{A.4})$$

The initial value x_0 can be selected at the expected value of the elements of \underline{x} :

$$x_0 = \begin{bmatrix} x_{01} \\ x_{02} \\ x_{03} \\ x_{04} \end{bmatrix} = \begin{bmatrix} \text{E} \left\{ \text{Re}(\langle I_{1,2} \rangle) \right\} \\ \text{E} \left\{ \text{Re}(\langle I_{3,4} \rangle) \right\} \\ \text{E} \left\{ \text{Im}(\langle I_{1,2} \rangle) \right\} \\ \text{E} \left\{ \text{Im}(\langle I_{3,4} \rangle) \right\} \end{bmatrix}. \quad (\text{A.5})$$

Assuming zero-mean interferometric phase (i.e. $\text{E}\{\phi_{1,2}\}=\text{E}\{\phi_{3,4}\}=0$), the elements of x_0 are evaluated as:

$$x_0 = \begin{bmatrix} x_{01} \\ x_{02} \\ x_{03} \\ x_{04} \end{bmatrix} = \begin{bmatrix} |\gamma_{12}| \\ |\gamma_{34}| \\ 0 \\ 0 \end{bmatrix}. \quad (\text{A.6})$$

Evaluating the Jacobian of eq. A.4 at x_0 gives

$$J_F(\underline{x}|x_0) = \begin{bmatrix} 0 & 0 & \frac{1}{|\gamma_{12}|} & 0 \\ 0 & 0 & 0 & \frac{1}{|\gamma_{34}|} \end{bmatrix}. \quad (\text{A.7})$$

Derivation of Q_x :

First, it should be noted that, generally speaking, complex interferograms that are computed by the Hermitian product of circularly Gaussian distributed SLC values, do not follow a circular distribution, and hence, the multivariate PDF of the vector of complex interferometric values may not be circular. In general, for a non-circularly distributed random vector z , the dispersion or covariance matrix defined as $\text{D}\{z\} = \text{E}\{zz^*\}$ does not entirely describe the second order statistics of z (Mandic and Goh, 2009). This is due to the fact that the vector z and its conjugate transpose z^* are correlated in case of non-circularity. For a full description of the second statistical moment of non-circularly distributed complex vectors, a complementary quantity called *pseudo-covariance* or *complementary covariance* needs to be taken into account (Neeser and Massey, 1993; Picinbono and Bondon, 1997; Schreier and Scharf, 2003; Mandic and Goh, 2009). The complementary covariance is defined as $\text{E}\{zz^T\}$ where the $.^T$ denotes the standard transpose operation. In agreement with the terminology *complementary covariance*, we introduce the term *complementary dispersion* denoted by $\tilde{\text{D}}$ which is defined as $\tilde{\text{D}}\{z\} = \text{E}\{zz^T\}$. It is known that the dispersion of the vector of real and imaginary component of z can be computed as (Neeser and Massey, 1993)

$$\text{D} \left\{ \begin{bmatrix} \text{Re}(z) \\ \text{Im}(z) \end{bmatrix} \right\} = \begin{bmatrix} \frac{1}{2} \text{Re}(\text{D}\{z\} + \tilde{\text{D}}\{z\}) & \frac{1}{2} \text{Im}(\text{D}\{z\} + \tilde{\text{D}}\{z\}) \\ -\frac{1}{2} \text{Im}(\text{D}\{z\} - \tilde{\text{D}}\{z\}) & \frac{1}{2} \text{Re}(\text{D}\{z\} - \tilde{\text{D}}\{z\}) \end{bmatrix} \quad (\text{A.8})$$

Assuming the complex vector of the interferometric phases $\underline{z} = [\underline{I}_{12}, \underline{I}_{34}]^T$, the vector \underline{x} can be reformulated as

$$\underline{x} = \begin{bmatrix} \text{Re}(\underline{z}) \\ \text{Im}(\underline{z}) \end{bmatrix}, \quad (\text{A.9})$$

and so the dispersion of \underline{x} (i.e., Q_x) can be evaluated by eq. (A.8). In order to evaluate eq. (A.8), the dispersion and the complementary dispersion of $\underline{z} = [\underline{I}_{12}, \underline{I}_{34}]^T$ should be derived.

The dispersion of $\underline{z} = [\underline{I}_{12}, \underline{I}_{34}]^T$ is written as

$$D\{\underline{z}\} = D\left\{ \begin{bmatrix} \underline{I}_{12} \\ \underline{I}_{34} \end{bmatrix} \right\} = D\left\{ \begin{bmatrix} \underline{P}_1 \underline{P}_2^* \\ \underline{P}_3 \underline{P}_4^* \end{bmatrix} \right\} \quad (\text{A.10})$$

$$= E\left\{ \begin{bmatrix} \underline{P}_1 \underline{P}_2^* \\ \underline{P}_3 \underline{P}_4^* \end{bmatrix} \begin{bmatrix} \underline{P}_2 \underline{P}_1^* & \underline{P}_4 \underline{P}_3^* \end{bmatrix} \right\} \quad (\text{A.11})$$

$$= \begin{bmatrix} E\{\underline{P}_1 \underline{P}_2^* \underline{P}_2 \underline{P}_1^*\} & E\{\underline{P}_1 \underline{P}_2^* \underline{P}_4 \underline{P}_3^*\} \\ E\{\underline{P}_2 \underline{P}_1^* \underline{P}_3 \underline{P}_4^*\} & E\{\underline{P}_3 \underline{P}_4^* \underline{P}_4 \underline{P}_3^*\} \end{bmatrix} \quad (\text{A.12})$$

Using the Gaussian moment factoring theorem¹ (Reed, 1962; Krishnan and Chandra, 2006), eq. (A.12) is written as

$$D\{\underline{z}\} = \begin{bmatrix} E\{\underline{P}_1 \underline{P}_2^*\} E\{\underline{P}_2 \underline{P}_1^*\} + E\{\underline{P}_1 \underline{P}_1^*\} E\{\underline{P}_2 \underline{P}_2^*\} & E\{\underline{P}_1 \underline{P}_2^*\} E\{\underline{P}_4 \underline{P}_3^*\} + E\{\underline{P}_1 \underline{P}_3^*\} E\{\underline{P}_2 \underline{P}_4^*\} \\ E\{\underline{P}_2 \underline{P}_1^*\} E\{\underline{P}_3 \underline{P}_4^*\} + E\{\underline{P}_2 \underline{P}_2^*\} E\{\underline{P}_1 \underline{P}_3^*\} & E\{\underline{P}_3 \underline{P}_4^*\} E\{\underline{P}_4 \underline{P}_3^*\} + E\{\underline{P}_3 \underline{P}_3^*\} E\{\underline{P}_4 \underline{P}_4^*\} \end{bmatrix} \quad (\text{A.14})$$

Assuming amplitude-normalized SLC images (i.e. $E\{\underline{A}_i^2\}=1$) and zero-mean interferometric phases (i.e. $E\{\phi_{i,j}\}=0$), the expected value of the interferograms is equal to the absolute coherence values (i.e., $E\{\underline{P}_i \underline{P}_j^*\} = E\{\underline{P}_j \underline{P}_i^*\} = |\gamma_{ij}|$, see eq. (3.5)), and so eq. (A.14) can be evaluated as

$$D\{\underline{z}\} = D\left\{ \begin{bmatrix} \underline{I}_{12} \\ \underline{I}_{34} \end{bmatrix} \right\} = \begin{bmatrix} 1 + |\gamma_{12}|^2 & |\gamma_{12}||\gamma_{34}| + |\gamma_{13}||\gamma_{24}| \\ |\gamma_{12}||\gamma_{34}| + |\gamma_{13}||\gamma_{24}| & 1 + |\gamma_{34}|^2 \end{bmatrix}. \quad (\text{A.15})$$

In the same manner the complementary dispersion of \underline{z} is computed as

$$\begin{aligned} \tilde{D}\{\underline{z}\} &= \tilde{D}\left\{ \begin{bmatrix} \underline{I}_{12} \\ \underline{I}_{34} \end{bmatrix} \right\} = \tilde{D}\left\{ \begin{bmatrix} \underline{P}_1 \underline{P}_2^* \\ \underline{P}_3 \underline{P}_4^* \end{bmatrix} \right\} \\ &= E\left\{ \begin{bmatrix} \underline{P}_1 \underline{P}_2^* \\ \underline{P}_3 \underline{P}_4^* \end{bmatrix} \begin{bmatrix} \underline{P}_1 \underline{P}_2^* & \underline{P}_3 \underline{P}_4^* \end{bmatrix} \right\} \\ &= \begin{bmatrix} E\{\underline{P}_1 \underline{P}_2^* \underline{P}_1 \underline{P}_2^*\} & E\{\underline{P}_1 \underline{P}_2^* \underline{P}_3 \underline{P}_4^*\} \\ E\{\underline{P}_1 \underline{P}_2^* \underline{P}_3 \underline{P}_4^*\} & E\{\underline{P}_3 \underline{P}_4^* \underline{P}_3 \underline{P}_4^*\} \end{bmatrix} \\ &= \begin{bmatrix} E\{\underline{P}_1 \underline{P}_2^*\} E\{\underline{P}_1 \underline{P}_2^*\} + E\{\underline{P}_1 \underline{P}_2^*\} E\{\underline{P}_2 \underline{P}_1^*\} & E\{\underline{P}_1 \underline{P}_2^*\} E\{\underline{P}_3 \underline{P}_4^*\} + E\{\underline{P}_1 \underline{P}_4^*\} E\{\underline{P}_2 \underline{P}_3^*\} \\ E\{\underline{P}_1 \underline{P}_2^*\} E\{\underline{P}_3 \underline{P}_4^*\} + E\{\underline{P}_1 \underline{P}_4^*\} E\{\underline{P}_2 \underline{P}_3^*\} & E\{\underline{P}_3 \underline{P}_4^*\} E\{\underline{P}_3 \underline{P}_4^*\} + E\{\underline{P}_3 \underline{P}_4^*\} E\{\underline{P}_4 \underline{P}_3^*\} \end{bmatrix} \\ &= \begin{bmatrix} 2|\gamma_{12}|^2 & |\gamma_{12}||\gamma_{34}| + |\gamma_{14}||\gamma_{23}| \\ |\gamma_{12}||\gamma_{34}| + |\gamma_{14}||\gamma_{23}| & 2|\gamma_{34}|^2 \end{bmatrix}. \end{aligned} \quad (\text{A.16})$$

¹Gaussian moment factoring theorem: if \underline{X}_1 , \underline{X}_2 , \underline{X}_3 , and \underline{X}_4 are zero mean variables with a complex jointly Gaussian distribution, the following relationship holds:

$$E\{\underline{X}_1 \underline{X}_2^* \underline{X}_3 \underline{X}_4^*\} = E\{\underline{X}_1 \underline{X}_2^*\} E\{\underline{X}_3 \underline{X}_4^*\} + E\{\underline{X}_1 \underline{X}_4^*\} E\{\underline{X}_2 \underline{X}_3^*\} \quad (\text{A.13})$$

Substituting eqs. (A.15) and (A.16) into eq. (A.8) gives the dispersion of \underline{x} (for single-look pixels)

$$D\{\underline{x}\} = Q_x = \frac{1}{2} \begin{bmatrix} 3|\gamma_{12}|^2+1 & 2|\gamma_{12}||\gamma_{34}|+\dots & 0 & 0 \\ |\gamma_{13}||\gamma_{24}|+|\gamma_{14}||\gamma_{23}| & 3|\gamma_{34}|^2+1 & 0 & 0 \\ 0 & 0 & 1-|\gamma_{12}|^2 & |\gamma_{13}||\gamma_{24}|-|\gamma_{14}||\gamma_{23}| \\ 0 & 0 & |\gamma_{13}||\gamma_{24}|-|\gamma_{14}||\gamma_{23}| & 1-|\gamma_{34}|^2 \end{bmatrix}, \quad (\text{A.17})$$

Finally for multilooked pixels computed by coherent averaging over L independent homogeneous pixels with covariance matrix Q_x , the covariance matrix of the vector of interferometric real and imaginary components is computed by linear error propagation as

$$Q_{x|L} = \frac{1}{L} Q_x. \quad (\text{A.18})$$

Derivation of Q_y :

By substituting eqs. (A.18), (A.17), and (A.7) into eq. A.1, the covariance matrix of the interferometric phase vector is approximated as

$$D\left\{ \begin{bmatrix} \phi_{12} \\ \phi_{34} \end{bmatrix} \right\} \approx \begin{bmatrix} \frac{1-|\gamma_{12}|^2}{2L|\gamma_{12}|^2} & \frac{|\gamma_{13}||\gamma_{24}|-|\gamma_{14}||\gamma_{23}|}{2L|\gamma_{12}||\gamma_{34}|} \\ \frac{|\gamma_{13}||\gamma_{24}|-|\gamma_{14}||\gamma_{23}|}{2L|\gamma_{12}||\gamma_{34}|} & \frac{1-|\gamma_{34}|^2}{2L|\gamma_{34}|^2} \end{bmatrix}. \quad (\text{A.19})$$

A.2 Derivation of Chapter 4

A.2.1 Proof of eq. (4.21)

Eq. (4.20) can be written as:

$$f_{d_\Omega}(d_\Omega|\Psi) \propto \prod_{k=1}^L \exp(-d_k^* \Psi \Upsilon^{-1} \Psi^* d_k) \quad (\text{A.20})$$

$$= \exp\left(-\sum_{k=1}^L d_k^* \Psi \Upsilon^{-1} \Psi^* d_k\right). \quad (\text{A.21})$$

Based on the property of quadratic forms that $b^* A b = \text{tr}(A b b^*)$, eq. (A.21) can be written as

$$f_{d_\Omega}(d_\Omega|\Psi) \propto \exp\left(-\sum_{k=1}^L \text{tr}(\Psi \Upsilon^{-1} \Psi^* d_k d_k^*)\right). \quad (\text{A.22})$$

Using the fact that $\sum_i (\text{tr}(A_i)) = \text{tr}(\sum_i(A_i))$, eq. (A.22) is written as

$$f_{\underline{d}_\Omega}(d_\Omega|\Psi) \propto \exp\left(-\text{tr}\left(\sum_{k=1}^L \Psi \Upsilon^{-1} \Psi^* d_k d_k^*\right)\right) \quad (\text{A.23})$$

$$= \exp\left(-\text{tr}\left(\Psi \Upsilon^{-1} \Psi^* \sum_{k=1}^L d_k d_k^*\right)\right). \quad (\text{A.24})$$

Considering that the estimated coherence matrix $\hat{\Gamma} \propto \frac{1}{L} \sum_{k=1}^L d_k d_k^*$, eq. (A.24) can be written as

$$\boxed{f_{\underline{d}_\Omega}(d_\Omega|\Psi) \propto \exp\left(-\text{tr}(\Psi \Upsilon^{-1} \Psi^* \hat{\Gamma})\right)}, \quad (\text{A.25})$$

which is equivalent to eq. (4.21).

A.2.2 Proof of eq. (4.27)

Based on the property of quadratic forms that $a^* A a = \sum_i^N \sum_j^N A_{[i,j]} a_i^* a_j$ (where a is the $N \times 1$ vector, and A is the $N \times N$ Hermitian matrix), the objective function of equation (4.26) can be written as

$$\begin{aligned} \Phi^*(-\hat{\Upsilon}^{-1} \circ \hat{\Gamma})\Phi &= \\ &= \sum_m^N \sum_n^N -[\hat{\Upsilon}^{-1}]_{[m,n]} |\hat{\gamma}_{mn}| \exp(j\hat{\phi}_{mn}) \Phi_{[m]}^* \Phi_{[n]}. \end{aligned} \quad (\text{A.26})$$

Based on the fact that

$$\sum_i^N \sum_j^N A_{[i,j]} a_i^* a_j = \quad (\text{A.27})$$

$$= \sum_{i=1}^N A_{[i,i]} a_i^* a_i + \sum_{i=1}^N \sum_{j>i}^N A_{[i,j]} a_i^* a_j + \left(\sum_{i=1}^N \sum_{j>i}^N A_{[i,j]} a_i^* a_j\right)^* \quad (\text{A.28})$$

$$= \sum_{i=1}^N A_{[i,i]} a_i^* a_i + 2 \text{Re} \left(\sum_{i=1}^N \sum_{j>i}^N A_{[i,j]} a_i^* a_j \right), \quad (\text{A.29})$$

the double summation in Ee. (A.26) can be decomposed in two terms as:

$$\Phi^*(-\hat{\Upsilon}^{-1} \circ \hat{\Gamma})\Phi = \sum_{m=1}^N -[\hat{\Upsilon}^{-1}]_{[m,m]} + \dots \quad (\text{A.30})$$

$$\dots + 2 \text{Re} \left(\sum_{m=1}^N \sum_{n>m}^N -[\hat{\Upsilon}^{-1}]_{[m,n]} |\hat{\gamma}_{mn}| \exp(j\hat{\phi}_{mn}) \Phi_{[m]}^* \Phi_{[n]} \right). \quad (\text{A.31})$$

Based on eq. (4.22), we have $\Phi_{[m]} = \exp(-j\psi_{om})$. By inserting this definition to eq. (A.31), we get:

$$\begin{aligned} \Phi^*(-\hat{\Upsilon}^{-1} \circ \hat{\Gamma})\Phi &= \sum_{m=1}^N -[\hat{\Upsilon}^{-1}]_{[m,m]} + \dots \\ &\dots + 2 \operatorname{Re} \left(\sum_{m=1}^N \sum_{n>m}^N -[\hat{\Upsilon}^{-1}]_{[m,n]} |\hat{\gamma}_{mn}| \exp(j\hat{\phi}_{mn} + \psi_{om} - \psi_{on}) \right). \end{aligned} \quad (\text{A.32})$$

The first term in eq. (A.32) is invariant with respect to the unknown parameters ψ_{om} . Therefore, the maximization problem of equation (4.26) can be written as

$$\begin{aligned} \hat{b}_{\text{ML}} &= \arg \max_b \left\{ \Phi^*(-\hat{\Upsilon}^{-1} \circ \hat{\Gamma})\Phi \right\} \\ &= \arg \max_b \left\{ \operatorname{Re} \left(\sum_{m=1}^N \sum_{n>m}^N -[\hat{\Upsilon}^{-1}]_{[m,n]} |\hat{\gamma}_{mn}| \exp(j(\hat{\phi}_{mn} - \psi_{om} + \psi_{on})) \right) \right\}, \end{aligned} \quad (\text{A.33})$$

which is equivalent to eq. (4.27).

A.2.3 Explanation and proof of eq. (4.52)

Monti-Guarnieri and Tebaldini (2007) and Monti-Guarnieri and Tebaldini (2008) gave a general formulation for the computation of the hybrid Cramér-Rao bound (HCRB) for estimators which use InSAR stacks as observations to estimate any set of unknown (and deterministic) parameters, e.g. $x = [x_1, x_2, \dots, x_K]^T$ (where K is the number of unknown parameters). Assume we have a vector of N focused SAR SLC images, and ϕ_n ($n=0, 1, \dots, N-1$) is the multilooked interferometric phase for the n th image with respect to an arbitrary reference, expressed as:

$$\phi_n = \psi_n(x) + \alpha_n, \quad (\text{A.34})$$

where $\psi_n(x)$ is a known function of x describing the functional relation between the interferometric phases and the unknown parameters. The parameter α_n represents the (stochastic) atmospheric component affecting the n th image.

The HCRB formulation is based on the assumption of scattering with a multivariate circular Gaussian distribution with absolute coherence matrix Υ , and atmospheric noise ($\underline{\alpha}$) as a zero-mean normal stochastic process: $\underline{\alpha} \sim \mathcal{N}(0, Q_\alpha)$, where Q_α is the $N \times N$ covariance matrix of the atmospheric signal. If \hat{x} is the unbiased estimator of x , the dispersion or variance matrix of \hat{x} is bounded from below as (Monti-Guarnieri and Tebaldini, 2008)

$$\begin{aligned} \text{D}\{\hat{x}\} &= \text{E}\{(\hat{x} - x)(\hat{x} - x)^T\} = Q_{\hat{x}} \geq \\ &\lim_{\epsilon \rightarrow 0} \left(\Theta^T \left((X + \epsilon I_N)^{-1} + Q_\alpha \right)^{-1} \Theta \right)^{-1}. \end{aligned} \quad (\text{A.35})$$

where the matrix Θ and X are defined as the follows.

- The matrix Θ is the $N \times K$ Jacobian matrix of the first-order partial derivatives of the interferometric phases with respect to the unknown parameters. The elements of Θ are defined as:

$$\{\Theta\}_{np} = \frac{\partial \psi_n(x)}{\partial x_p}. \quad (\text{A.36})$$

- The matrix X is the Fisher Information Matrix (FIM) associated to the estimates of $\psi_n(x)$ and is defined as (Monti-Guarnieri and Tebaldini, 2007):

$$X = 2L(\Upsilon \circ \Upsilon^{-1} - I_N), \quad (\text{A.37})$$

where \circ means the entry-wise product, L is the number of looks, and I_N is a $N \times N$ identity matrix.

The inequality \geq in eq. (A.35) indicates that the difference between the left and the right side of the inequality is a non-negative definite matrix.

For the problem of equivalent SM-phase estimation, the unknown vector $x = b$ includes the *true* interferometric phases with respect to the master image:

$$b = [\varphi_{o1} \ \varphi_{o2} \ \dots \ \varphi_{o(N-1)}]^T. \quad (\text{A.38})$$

Assuming the first image as the master image (and deterministic), the Jacobian Θ is evaluated as

$$\Theta = \begin{bmatrix} \frac{\partial \psi_o}{\partial \varphi_{o1}} & \frac{\partial \psi_o}{\partial \varphi_{o2}} & \dots & \frac{\partial \psi_o}{\partial \varphi_{o(N-1)}} \\ \frac{\partial \psi_1}{\partial \varphi_{o1}} & \frac{\partial \psi_1}{\partial \varphi_{o2}} & \dots & \frac{\partial \psi_1}{\partial \varphi_{o(N-1)}} \\ \frac{\partial \psi_2}{\partial \varphi_{o1}} & \frac{\partial \psi_2}{\partial \varphi_{o2}} & \dots & \frac{\partial \psi_2}{\partial \varphi_{o(N-1)}} \\ \vdots & \vdots & \vdots & \vdots \\ \frac{\partial \psi_N}{\partial \varphi_{o1}} & \frac{\partial \psi_N}{\partial \varphi_{o2}} & \dots & \frac{\partial \psi_N}{\partial \varphi_{o(N-1)}} \end{bmatrix} = \begin{bmatrix} 0 & 0 & \dots & 0 \\ 1 & 0 & \dots & 0 \\ 0 & 1 & \dots & 0 \\ \vdots & \vdots & \vdots & \vdots \\ 0 & 0 & \dots & 1 \end{bmatrix} = [0 \ I_{N-1}]^T. \quad (\text{A.39})$$

Furthermore, for equivalent SM-phase estimation, the atmospheric effect is treated as deterministic and is part of the signal of interest and so the atmosphere covariance matrix is set to zero. Then, the CRB for SM-phase estimation can be computed by eq. (A.35) by inserting eq. (A.39) and setting $Q_\alpha = 0$ as

$$Q_{\hat{x}} \geq (\Theta^T X \Theta)^{-1}, \quad (\text{A.40})$$

which is equivalent to eq. (4.52).

B

Integer bootstrapping estimator, and the simulation setting

B.1 Integer Bootstrapping Estimator

Integer bootstrapping (IB) is an estimator to solve integer minimization problems with the form of

$$\check{a} = \operatorname{argmin}_{a \in \mathbb{Z}} \|\hat{a} - a\|_{W_a}^2, \quad (\text{B.1})$$

where

$$\hat{a} = [\hat{a}_1 \hat{a}_2 \dots \hat{a}_n]^T. \quad (\text{B.2})$$

If W_a is a diagonal matrix, the solution of this minimization can simply be computed by rounding the entries of \hat{a} to their nearest integer. However, in case of a full W_a , the nearest integer should be searched considering the mutual correlation among entries of \hat{a} , represented by off-diagonal elements in W_a . In order to do so, the IB estimator uses the concept of sequential conditional rounding and the solution is computed as follows. First, the first entry \hat{a}_1 is rounded to its nearest integer. After that, all other elements of \hat{a} are corrected based on their correlation with the first entry. Then the second corrected entry is rounded to its nearest integer, etc. etc. This sequence of corrections and rounding can be written mathematically as Teunissen (1998):

$$\check{b}_B = \begin{bmatrix} \check{b}_{B,1} \\ \check{b}_{B,2} \\ \vdots \\ \check{b}_{B,n} \end{bmatrix} = \begin{bmatrix} \text{nint}(\hat{a}_1) \\ \text{nint}(\hat{a}_2 - l_{21}(\hat{a}_1 - \check{b}_{B,1})) \\ \vdots \\ \text{nint}(\hat{a}_n - \sum_{i=1}^{n-1} l_{ni}(\hat{a}_i - \check{b}_{B,i})) \end{bmatrix}, \quad (\text{B.3})$$

where $\text{nint}(\cdot)$ is the nearest-integer rounding operator. The notation $\hat{a}_{i|I}$ stands for the i th real-valued entry obtained through a conditioning on the previous $I=1, \dots, i-1$ sequentially rounded entries. The elements l_{ji} are entries of a unit lower triangular matrix L computed from an LDL^T -decomposition of $W_a = LDL^T$.

B.2 Simulation setting

In the synthetic studies, the noise components in interferometric phases were simulated based on given coherence matrices. For construction of the coherence matrices, four decorrelation sources were assumed:

1. *Thermal or system decorrelation*: the influence of thermal noise on system coherence depends on the signal-to-noise (SNR) as Zebker and Villasenor (1992):

$$\gamma_{\text{thermal}} = \frac{1}{1 + \text{SNR}^{-1}}. \quad (\text{B.4})$$

The value for SNR is dependent on system parameters and radar scene's radar cross section (SCR), the latter varying subject to terrain characteristics. In this study, we have assumed the system parameters of the ERS satellite (as reported in Zebker et al. (1994a); Hanssen (2001)) and a SCR of -14 dB, resulting in a SNR of 12 dB and a γ_{thermal} of 0.92.

2. *Coregistration induced decorrelation*: this is mainly a function of the accuracy of image coregistration. Assuming a subpixel coregistration accuracy of $\sigma_{\text{coreg},a}$ and $\sigma_{\text{coreg},r}$ in azimuth and range directions, the decorrelation induced by coregistration γ_{coreg} is computed as Just and Bamler (1994); Hanssen (2001):

$$\gamma_{\text{coreg}} = \text{sinc}(\sigma_{\text{coreg},a})\text{sinc}(\sigma_{\text{coreg},r}). \quad (\text{B.5})$$

For the noise simulation here, we have assumed a coregistration accuracy of 0.1 resolution cell in both azimuth and range directions, resulting in $\gamma_{\text{coreg}}=0.96$.

3. *Geometric decorrelation*: The geometric or baseline decorrelation is a result of different incidence angles between the two radar paths at the earth's surface. For an interferometric pair of two radar images, geometric decorrelation is defined as Hanssen (2001):

$$\gamma_{\text{geom}} = \max\left(1 - \frac{|B_{\perp}|}{B_{\perp\text{max}}}, 0\right). \quad (\text{B.6})$$

where B_{\perp} is the perpendicular baseline between two images, and $B_{\perp\text{max}}$ the critical baseline. In this simulation, the critical baseline is assumed as 1.1 km, which is equal to the ERS critical baseline for flat terrains. Perpendicular baselines are simulated randomly as normally distributed with zero mean and standard deviation of 300 m.

4. *Temporal decorrelation*: As the range of physical mechanisms causing temporal decorrelation is too wide, there is no single analytical model to evaluate coherence loss induced by this effect. In this study, we have assumed two arbitrary scenarios for temporal decorrelation: exponential decay and seasonal decay. In case of exponential decay, the temporal coherences are modeled as Rocca (2007):

$$\gamma_{\text{temp}} = e^{B_{\tau}/\tau}, \quad (\text{B.7})$$

where B_{τ} is the temporal baseline, and τ is the *decorrelation rate*, assumed here to be 200 days. For the seasonal effect scenario, it is assumed that the coherence

is exponentially decreasing but has also some seasonal variation. This is realistic for areas with some degree of coherence during winter but very low coherence during summer or vice versa. Such behavior has been observed by Morishita and Hanssen (2015b) in pasture areas.

After computing all the aforementioned coherences, the total simulated coherence (γ_{sim}) is derived as:

$$\gamma_{\text{sim}} = \gamma_{\text{thermal}}\gamma_{\text{coreg}}\gamma_{\text{geom}}\gamma_{\text{temp}}. \quad (\text{B.8})$$

By computing the γ_{sim} for all the interferometric combinations and for the two temporal decorrelation scenarios, we construct the two coherence matrices C_e and C_s for the exponential decay and seasonal decay scenarios respectively, visualized in fig. 5.1.

Bibliography

- Abramowitz, M. and Stegun, I. A., editors (1965). *Handbook of Mathematical Functions; with Formulas, Graphs, and Mathematical Tables*. Dover Publications, New York, 9th edition.
- Abramowitz, M. and Stegun, I. A. (1970). *Handbook of Mathematical Functions*. Dover books on advanced mathematics. Dover, New York, 9 edition.
- Adam, N., Kampes, B. M., and Eineder, M. (2004). Development of a scientific persistent scatterer system: Modifications for mixed ERS/ENVISAT time series. In *ENVISAT & ERS Symposium, Salzburg, Austria, 6–10 September, 2004*, page 9.
- Adam, N., Kampes, B. M., Eineder, M., Worawattanamateekul, J., and Kircher, M. (2003). The development of a scientific permanent scatterer system. In *ISPRS Workshop High Resolution Mapping from Space, Hannover, Germany, 2003*, page 6 pp.
- Agram, P. S. and Simons, M. (2015). A noise model for InSAR time series. *Journal of Geophysical Research: Solid Earth*, 120(4):2752–2771.
- Alkhatib, H. (2007). *On Monte Carlo Methods with Applications to the current satellite gravity missions*. PhD thesis, University of Bonn, Bonn, Germany.
- Amelung, F., Galloway, D. L., Bell, J. W., Zebker, H. A., and Laczniak, R. J. (1999). Sensing the ups and downs of Las Vegas: InSAR reveals structural control of land subsidence and aquifer-system deformation. *Geology*, 27(6):483–486.
- Amiri-Simkooei, A. (2010). *Variance component estimation in linear models: Theoretical and practical aspects on Global Positioning System*. VDM Verlag Dr. Müller, -. ISBN-10: 3639268512.
- Arikan, M., van Leijen, F., Guang, L., and Hanssen, R. (2008). Improved image alignment under the influence of elevation. In *Fifth International Workshop on ERS/Envisat SAR Interferometry, 'FRINGE07', Frascati, Italy, 26 Nov-30 Nov 2007*, page 4 pp.
- Baarda, W. (1968). *A testing procedure for use in geodetic networks*, volume 5 of *Publications on Geodesy*. Netherlands Geodetic Commission, Delft, 2 edition.
- Bähr, H. (2013). *Orbital Effects in Spaceborne Synthetic Aperture Radar Interferometry*. KIT Scientific Publishing, Karlsruhe. ISBN 978-3-7315-0134-3.
- Bamler, R., Adam, N., Davidson, G. W., and Just, D. (1998). Noise-induced slope distortion in 2-d phase unwrapping by linear estimators with application to SAR interferometry. *IEEE Transactions on Geoscience and Remote Sensing*, 36(3):913–921.
- Bamler, R. and Hartl, P. (1998). Synthetic aperture radar interferometry. *Inverse Prob-*

- lems*, 14:R1–R54.
- Bamler, R. and Just, D. (1993). Phase statistics and decorrelation in SAR interferograms. In *International Geoscience and Remote Sensing Symposium, Tokyo, Japan, 18–21 August 1993*, pages 980–984.
- Bamler, R. and Schättler, B. (1993). SAR data acquisition and image formation. In Schreier, G., editor, *SAR Geocoding: data and systems*, pages 53–102. Wichmann Verlag, Karlsruhe.
- Bara, M., Scheiber, R., Broquetas, A., and Moreira, A. (2000). Interferometric SAR signal analysis in the presence of squint. *Geoscience and Remote Sensing, IEEE Transactions on*, 38(5):2164–2178.
- Barber, B. C. (1993). The phase statistics of a multichannel radar interferometer. *Waves in Random Media*, 3:257–266.
- Basilico, M., Ferretti, A., Novali, F., Prati, C., and Rocca, F. (2004). Advances in permanent scatterer analysis: semi and temporary PS. In *European Conference on Synthetic Aperture Radar, Ulm, Germany, 25–27 May 2004*, pages 349–349.
- Beauducel, F., Briole, P., and Froger, J.-L. (2000). Volcano wide fringes in ERS synthetic aperture radar interferograms of Etna. *Journal of Geophysical Research*, 105(B7):16391–16402.
- Bendat, J. S. and Piersol, A. G. (1986). *Random Data: Analysis and Measurement Procedures*. Wiley-Interscience, New York, 2 edition.
- Berardino, P., Casu, F., Fornaro, G., Lanari, R., Manunta, M., Manzo, M., and Sansosti, E. (2004). A quantitative analysis of the SBAS algorithm performance. *International Geoscience and Remote Sensing Symposium, Anchorage, Alaska, 20–24 September 2004*, pages 3321–3324.
- Berardino, P., Fornaro, G., Lanari, R., and Sansosti, E. (2002). A new algorithm for surface deformation monitoring based on small baseline differential SAR interferograms. *IEEE Transactions on Geoscience and Remote Sensing*, 40(11):2375–2383.
- Bishop, C. (2006). *Pattern Recognition and Machine Learning*. Springer-Verlag, New York, US.
- Born, M., Wolf, E., and Bhatia, A. B. (1959). *Principle of optics; electromagnetic theory of propagation, interference and diffraction of light*. Pergamon Press, New York.
- Brown, L. G. (1992). A survey of image registration techniques. *ACM Computing Surveys*, 24(4):325–376.
- Calais, E., d’Oreye, N., Albaric, J., Deschamps, A., Delvaux, D., Déverchère, J., Ebinger, C., Ferdinand, R. W., Kervyn, F., Macheyeki, A. S., Oyen, A., Perrot, J., Saria, E., Smets, B., Stamps, D. S., and Wauthier, C. (2008). Strain accommodation by slow slip and dyking in a youthful continental rift, East Africa. *Nature*, 456(doi:10.1038/nature07478):783–788.
- Cao, N., Lee, H., and Jung, H. C. (2015). Mathematical framework for phase-triangulation algorithms in distributed-scatterer interferometry. *IEEE Geoscience and Remote Sensing Letters*, 12(9):1838–1842.
- Cao, N., Lee, H., and Jung, H. C. (2016). A phase-decomposition-based PSInSAR processing method. *IEEE Transactions on Geoscience and Remote Sensing*, 54(2):1074–

- 1090.
- Caro-Cuenca, M. (2012). *Improving radar interferometry for monitoring fault-related surface deformation: Applications for the Roer Valley Graben and coal mine induced displacements in the southern Netherlands*. PhD thesis, Delft University of Technology, Delft, the Netherlands.
- Chang, L. (2015). *Monitoring civil infrastructure using satellite radar interferometry*. PhD thesis, Delft University of Technology, Delft, the Netherlands.
- Chang, L. and Hanssen, R. F. (2016). A probabilistic approach to InSAR time-series post-processing. *IEEE Transactions on Geoscience and Remote Sensing*, 54(1):421–430.
- Chen, C. W. (2001). *Statistical-cost network-flow approaches to two-dimensional phase unwrapping for radar interferometry*. PhD thesis, Stanford University.
- Cimini, D., Pierdicca, N., Pichelli, E., Ferretti, R., Mattiolo, V., Bonafoni, S., Montopoli, M., and Perissin, D. (2012). On the accuracy of integrated water vapor observations and the potential for mitigating electromagnetic path delay error in InSAR. *Atmospheric Measurement Techniques Discussion*, 5.
- Coleman, T. and Li, Y. (1996). An interior, trust region approach for nonlinear minimization subject to bounds. *SIAM Journal on Optimization*, 6:418–225.
- Costantini, M. (1998). A novel phase unwrapping method based on network programming. *IEEE Transactions on Geoscience and Remote Sensing*, 36(3):813–821.
- Costantini, M., Falco, S., Malvarosa, F., Minati, F., and Trillo, F. (2009). Method of persistent scatterer pairs (PSP) and high resolution SAR interferometry. In *Geoscience and Remote Sensing Symposium, 2009 IEEE International, IGARSS 2009*, volume 3, pages III–904–III–907.
- Costantini, M., Malvarosa, F., and Minati, F. (2012). A general formulation for redundant integration of finite differences and phase unwrapping on a sparse multidimensional domain. *Geoscience and Remote Sensing, IEEE Transactions on*, 50(3):758–768.
- Crosetto, M., Monserrat, O., Cuevas-González, M., Devanthéry, N., and Crippa, B. (2016). Persistent scatterer interferometry: A review. *ISPRS Journal of Photogrammetry and Remote Sensing*, 115:78–89.
- Cuenca, M. C., Hooper, A. J., and Hanssen, R. F. (2011). A new method for temporal phase unwrapping of persistent scatterers insar time series. *IEEE Transactions on Geoscience and Remote Sensing*, 49(11):4606–4615.
- Cumming, I. and Wong, F. (2005). *Digital Processing Of Synthetic Aperture Radar Data: Algorithms And Implementation*. Artech House Publishers, New York. ISBN 1580530583.
- Dainty, J. C., editor (1975). *Laser Speckle and Related Phenomena*, volume 9 of *Topics in Applied Physics*. Springer-Verlag, Heidelberg.
- Dammert, P. B. G. (1997). Accuracy of INSAR measurements in forested areas. In *'FRINGE 96' workshop on ERS SAR Interferometry, Zürich, Switzerland, 30 Sep–2 October 1996*. ESA SP-406, Vol II.
- Davenport, W. (1970). *Probability and random processes: An introduction for applied scientists and engineers*. Mcgraw-Hill College, New York.

- Davenport, Jr, W. B. and Root, W. L. (1987). *An Introduction to the Theory of Random Signals and Noise*. IEEE Press, New York.
- Davidson, G. W. and Bamler, R. (1999). Multiresolution phase unwrapping for SAR interferometry. *IEEE Transactions on Geoscience and Remote Sensing*, 37(1):163–174.
- De Zan, F., Zonno, M., and Lopez Dekker, P. (2015). Phase inconsistencies and multiple scattering in SAR interferometry. *Geoscience and Remote Sensing, IEEE Transactions on*, 53(12):1441–1452.
- Delacourt, C., Briole, P., and Achache, J. (1998). Tropospheric corrections of SAR interferograms with strong topography. application to Etna. *Geophysical Research Letters*, 25(15):2849–2852.
- Deledalle, C.-A., Denis, L., and Tupin, F. (2011). Nl-insar: Nonlocal interferogram estimation. *Geoscience and Remote Sensing, IEEE Transactions on*, 49(4):1441–1452.
- Dheenathayalan, P., Small, D., Schubert, A., and Hanssen, R. F. (2016). High-precision positioning of radar scatterers. *Journal of Geodesy*, 90(5):403–422.
- Ding, D., Li, Z., Zhu, J., Feng, G., and Long, J. (2008). Atmospheric effects on InSAR measurements and their mitigation. *Sensors*, 8:5426–5448.
- Dixon, T. H., Amelung, F., Ferretti, A., Novali, F., Rocca, F., Dokka, R., Sella, G., Kim, S.-W., Wdowinski, S., and Whitman, D. (2006). Space geodesy: Subsidence and flooding in New Orleans. *Nature*, 441:587–588.
- Dixon, T. H. and Dokka, R. K. (2008). Earth scientists and public policy: Have we failed new orleans? *Eos, Transactions American Geophysical Union*, 89(10):96–96.
- DUT (1998). *Delft Object-oriented Radar Interferometric Software (DORIS), User's manual and technical documentation*. Delft Institute of Earth Observation and Space Systems (DEOS), Delft University of Technology, Delft, The Netherlands.
- Eineder, M. and Holzner, J. (1999). Phase unwrapping of low coherence differential interferograms. In *International Geoscience and Remote Sensing Symposium, Hamburg, Germany, 28 June–2 July 1999*, pages cdrom, 4 pages.
- Elliott, J. R., Walters, R. J., and Wright, T. J. (2016). The role of space-based observation in understanding and responding to active tectonics and earthquakes. *Nature Communications*, 7.
- England, P. and Jackson, J. (2011). Uncharted seismic risk. *Nature Geoscience*, 4(6):348–349.
- Erkens, G., van der Meulen, M. J., and Middelkoop, H. (2016). Double trouble: subsidence and CO₂ respiration due to 1,000 years of dutch coastal peatlands cultivation. *Hydrogeology Journal*, 24(3):551–568.
- Famiglietti, J. S., Lo, M., Ho, S. L., Bethune, J., Anderson, K. J., Syed, T. H., Swenson, S. C., de Linage, C. R., and Rodell, M. (2011). Satellites measure recent rates of groundwater depletion in California's Central Valley. *Geophysical Research Letters*, 38(3).
- Ferretti, A. (1997). *Generazione di mappe altimetriche da osservazioni SAR multiple*. PhD thesis, Politecnico di Milano, Milano, Italy.
- Ferretti, A., Fumagalli, A., Novali, F., De, Z., Rucci, A., and Tebaldini, S. (2011a).

- Process for filtering interferograms obtained from SAR images acquired on the same area. CA Patent App. CA 2,767,144.
- Ferretti, A., Fumagalli, A., Novali, F., Prati, C., Rocca, F., and Rucci, A. (2011b). A new algorithm for processing interferometric data-stacks: SqueeSAR. *IEEE Transactions on Geoscience and Remote Sensing*, 49(9):3460–3470.
- Ferretti, A., Fumagalli, A., Novali, F., Rucci, A., Prati, C., and Rocca, F. (2012). DEM reconstruction with SqueeSAR. In *2012 Tyrrhenian Workshop on Advances in Radar and Remote Sensing (TyWRRS)*, pages 198–201.
- Ferretti, A., Monti-Guarnieri, A., Prati, C., Rocca, F., and Massonnet, D. (2007). *InSAR Principles: Guidelines for SAR Interferometry Processing and Interpretation*. ESA Publications, TM-19. ISBN 92-9092-233-8.
- Ferretti, A., Morali, F., Passera, E., and Rocca, F. (2005). Statistical analysis of atmospheric components in ERS SAR data.
- Ferretti, A., Prati, C., and Rocca, F. (2000). Nonlinear subsidence rate estimation using permanent scatterers in differential SAR interferometry. *IEEE Transactions on Geoscience and Remote Sensing*, 38(5):2202–2212.
- Ferretti, A., Prati, C., and Rocca, F. (2001). Permanent scatterers in SAR interferometry. *IEEE Transactions on Geoscience and Remote Sensing*, 39(1):8–20.
- Fisher, N. (1995). *Statistical Analysis of Circular Data*. Cambridge University Press.
- Fishman, G. (2003). *Monte Carlo: Concepts, Algorithms and Applications*. Springer, New York, 2nd edition.
- Fornaro, G., Reale, D., and Serafino, F. (2009). Four-dimensional sar imaging for height estimation and monitoring of single and double scatterers. *IEEE Transactions on Geoscience and Remote Sensing*, 47(1):224–237.
- Fornaro, G., Verde, S., Reale, D., and Pauciuolo, A. (2015). CAESAR: an approach based on covariance matrix decomposition to improve multibaseline-multitemporal interferometric SAR processing. *Geoscience and Remote Sensing, IEEE Transactions on*, 53(4):2050–2065.
- Foster, J., Brooks, B., Cherubini, T., Shacat, C., Businger, S., and Werner, C. L. (2006). Mitigating atmospheric noise for InSAR using a high resolution weather model. *Geophysical Research Letters*, 33(L16304):doi:10.1029/2006GL026781.
- Foster, M. R. and Guinzy, N. J. (1967). The coefficient of coherence: its estimation and use in geophysical data processing. *Geophysics*, 32(4):602–616.
- Fruneau, B., Achache, J., and Delacourt, C. (1996). Observation and modelling of the Saint-Étienne-de-Tinée landslide using SAR interferometry. *Tectonophysics*, 265(3-4):181 – 190.
- Fuhrmann, T., Caro Cuenca, M., Knopfler, A., van Leijen, F., Mayer, M., Westerhaus, M., Hanssen, R., and Heck, B. (2015). Estimation of small surface displacements in the Upper Rhine Graben area from a combined analysis of PS-InSAR, levelling and GNSS data. *Geophysical Journal International*, 203(1):614.
- Gabriel, A. K., Goldstein, R. M., and Zebker, H. A. (1989). Mapping small elevation changes over large areas: differential radar interferometry. *Journal of Geophysical Research*, 94(B7):9183–9191.

- Gatelli, F., Monti-Guarnieri, A., Parizzi, F., Pasquali, P., Prati, C., and Rocca, F. (1994). The wavenumber shift in SAR interferometry. *IEEE Transactions on Geoscience and Remote Sensing*, 32(4):855–865.
- Gauss, C. F. (1809). *Theoria Motus Corporum Coelestium*. Perthes und Besser, Hamburg.
- Gentle, J. (2003). *Random Number Generation and Monte Carlo Methods*. Wiley, 2nd edition.
- Ghiglia, D. C. and Pritt, M. D. (1998). *Two-dimensional phase unwrapping: theory, algorithms, and software*. John Wiley & Sons, Inc, New York.
- Goel, K. and Adam, N. (2014). A distributed scatterer interferometry approach for precision monitoring of known surface deformation phenomena. *IEEE Transactions on Geoscience and Remote Sensing*, 52(9):5454–5468.
- Goldstein, R. (1995). Atmospheric limitations to repeat-track radar interferometry. *Geophysical Research Letters*, 22(18):2517–2520.
- Goldstein, R. M., Engelhardt, H., Kamp, B., and Frolich, R. M. (1993). Satellite radar interferometry for monitoring ice sheet motion: Application to an antarctic ice stream. *Science*, 262:1525–1530.
- Goldstein, R. M., Zebker, H. A., and Werner, C. L. (1988). Satellite radar interferometry: Two-dimensional phase unwrapping. *Radio Science*, 23(4):713–720.
- Goodman, J. W. (1976). Some fundamental properties of speckle. *Journal of the Optical Society of America A*, 66:1145–1150.
- Goodman, N. R. (1963). Statistical analysis based on a certain multivariate complex Gaussian distribution (an introduction). *Annals of Mathematical Statistics*, 34(1):152–177.
- Gradshteyn, I. S., Ryzhik, I. M., and Jeffrey, A. (1994). *Table of integrals, series, and products*. Academic Press, Boston, 5 edition. Original Title: Tablitsy integralov, summ, ryadov i proizvediniy, 1965.
- Gundlich, B., Koch, K., and Kusche, J. (2003). Gibbs sampler for computing and propagating large covariance matrices. *Journal of Geodesy*, 77(9):514–528.
- Hagberg, J. O., Ulander, L. M. H., and Askne, J. (1995). Repeat-pass SAR interferometry over forested terrain. *IEEE Transactions on Geoscience and Remote Sensing*, 33(2):331–340.
- Hannan, E. J. and Thomson, P. J. (1971). The estimation of coherence and group delay. *Biometrika*, 58(3-481):469.
- Hanssen, R. (2001). *Radar Interferometry: Data Interpretation and Error Analysis*. Kluwer Academic Publishers, Dordrecht.
- Hanssen, R. and Bamler, R. (1999). Evaluation of interpolation kernels for SAR interferometry. *IEEE Transactions on Geoscience and Remote Sensing*, 37(1):318–321.
- Hanssen, R., Zebker, H., Klees, R., and Barlag, S. (1998). On the use of meteorological observations in SAR interferometry. In *International Geoscience and Remote Sensing Symposium, Seattle, Washington, USA, 6–10 July 1998*, pages 1644–1646.
- Hanssen, R. F. and Ferretti, A. (2002). Parameter estimation in PS-InSAR deformation studies using integer least-squares techniques. *EOS Trans. AGU, Fall Meet. Suppl.*,

Abstract G62A-06, 83(47):F37.

- Hanssen, R. F., van Leijen, F. J., van Zwieten, G. J., Bremmer, C., Dortland, S., and Kleuskens, M. (2008). Validation of existing processing chains in terrafirma stage 2; product validation: Validation in the amsterdam and alkmaar area. Technical report, Delft University of Technology, The Netherlands; TNO, The Netherlands. European Space Agency TerraFirma report, ESRIN contract No. 19366/05/I-E.
- Hanssen, R. F., Teunissen, P. J. G., and Joosten, P. (2001). Phase ambiguity resolution for stacked radar interferometric data. In *International Symposium on Kinematic Systems in Geodesy, Geomatics and Navigation, Banff, Canada, 5–8 June 2001*, pages 317–320.
- Hartl, P., Thiel, K. H., Wu, X., Doake, C., and Sievers, J. (1994). Application of SAR interferometry with ERS-1 in the Antarctic. *Earth Observation Quarterly*, 43:1–4.
- Helmert, F. R. (1980). *Die mathematischen und physikalischen Theorien derhöheren Geodäsie*. Teubner, Leipzig. (reprint Minerva GmbH, Frankfurt a.M.1961).
- Hobiger, T., Kinoshita, Y., Shimizu, S., Ichikawa, R., Furuya, M., Kondo, T., and Koyama, Y. (2010). On the importance of accurately ray-traced troposphere corrections for interferometric SAR data. *Journal of Geodesy*, 84(9):537–546.
- Hoen, E. W. and Zebker, H. A. (2000). Penetration depths inferred from interferometric volume decorrelation observed over the Greenland ice sheet. *IEEE Transactions on Geoscience and Remote Sensing*, 38(6):2571–2583.
- Holzner, J. and Bamler, R. (2002). Burst-mode and ScanSAR interferometry. *IEEE Transactions on Geoscience and Remote Sensing*, 40(9):1917–1934.
- Hooper, A. (2006). *Persistent Scatterer Radar Interferometry for Crustal Deformation Studies and Modeling of Volcanic Deformation*. PhD thesis, Stanford University.
- Hooper, A. (2008). A multi-temporal InSAR method incorporating both persistent scatterer and small baseline approaches. *Geophysical Research Letters*, 35:L16302.
- Hooper, A. (2010). Statistical-cost approach to unwrapping the phase of InSAR time series. In *fringe09*.
- Hooper, A., Bekaert, D., Spaans, K., and Arikan, M. (2012). Recent advances in SAR interferometry time series analysis for measuring crustal deformation. *Tectonophysics*, 514:1– 13.
- Hooper, A., Segall, P., and Zebker, H. (2007). Persistent scatterer InSAR for crustal deformation analysis, with application to volcan alcedo, galapagos. *Journal of Geophysical Research*, 112.
- Hooper, A. and Zebker, H. (2007). Phase unwrapping in three dimensions with application to InSAR time series. *Journal of the Optical Society of America A.*, 24(9):2737–2747.
- Hooper, A., Zebker, H., Segall, P., and Kampes, B. (2004). A new method for measuring deformation on volcanoes and other non-urban areas using InSAR persistent scatterers. *Geophysical Research Letters*, 31:L23611, doi:10.1029/2004GL021737.
- Horn, R. A. and Johnson, C. R. (1990). *Matrix Analysis*. Cambridge University Press.
- Horn, R. A. and Johnson, C. R. (1991). The hadamard product. In *Topics in matrix analysis*, pages 298–381. Cambridge University Press. Cambridge Books Online.

- Jammalamadaka, S. R. and SenGupta, A. (2001). *Topics in Circular Statistics*. World Scientific, Series on Multivariate Analysis.
- Jazaeri, S., Amiri-Simkooei, A. R., and Sharifi, M. A. (2011). Fast integer least-squares estimation for gnss high-dimensional ambiguity resolution using lattice theory. *Journal of Geodesy*, 86(2):123–136.
- Jiang, M., Ding, X., Hanssen, R., Malhotra, R., and Chang, L. (2014a). Fast statistically homogeneous pixel selection for covariance matrix estimation for multitemporal InSAR. *IEEE Transactions on Geoscience and Remote Sensing*, (99):1–12.
- Jiang, M., Ding, X., and Li, Z. (2014b). Hybrid approach for unbiased coherence estimation for multitemporal InSAR. *IEEE Transactions on Geoscience and Remote Sensing*, 52(5):2459–2473.
- Jolivet, R., Grandin, R., Lasserre, C., Doin, M.-P., and Peltzer, G. (2011). Systematic InSAR tropospheric phase delay corrections from global meteorological reanalysis data. *Geophysical Research Letters*, 38(17). L17311.
- Joughin, I. R. and Winebrenner, D. P. (1994). Effective number of looks for a multilook interferometric phase distribution. In *International Geoscience and Remote Sensing Symposium, Pasadena, CA, USA, 8–12 August 1994*, pages 2276–2278.
- Just, D. and Bamler, R. (1994). Phase statistics of interferograms with applications to synthetic aperture radar. *Applied Optics*, 33(20):4361–4368.
- Kalos, M. H. and Whitlock, P. A. (2008). *Monte Carlo Methods*. Wiley, New York, 2nd edition.
- Kampes, B. (2005). *Displacement Parameter Estimation using Permanent Scatterer Interferometry*. PhD thesis, Delft University of Technology, Delft, the Netherlands.
- Kampes, B. and Hanssen, R. (2004). Ambiguity resolution for permanent scatterer interferometry. *IEEE Transactions on Geoscience and Remote Sensing*, 42(11):2446–2453.
- Kampes, B. M. and Adam, N. (2004). Deformation parameter inversion using permanent scatterers in interferogram time series. In *European Conference on Synthetic Aperture Radar, Ulm, Germany, 25–27 May 2004*, pages 341–344.
- Kampes, B. M. and Adam, N. (2006). The STUN algorithm for persistent scatterer interferometry. In *Fourth International Workshop on ERS/Envisat SAR Interferometry, 'FRINGE05', Frascati, Italy, 28 Nov-2 Dec 2005*, page 14 pp.
- Ketelaar, G., van Leijen, F., Marinkovic, P., and Hanssen, R. (2005). Initial point selection and validation in PS-InSAR using integrated amplitude calibration. In *International Geoscience and Remote Sensing Symposium, Seoul, Korea, 25–29 July 2005*, pages 5490–5493.
- Ketelaar, V. B. H. (2008). *Monitoring surface deformation induced by hydrocarbon production using satellite radar interferometry*. PhD thesis, Delft University of Technology, Delft, the Netherlands.
- Khan, S. A., Wahr, J., Bevis, M., Velicogna, I., and Kendrick, E. (2010). Spread of ice mass loss into northwest greenland observed by GRACE and GPS. *Geophysical Research Letters*, 37(6).
- Kremer, C., Holt, W. E., and Haines, A. J. (2003). An integrated global model of

- present-day plate motions and plate boundary deformation. *Geophysical Journal International*, 154(1):8–34.
- Krishnan, V. and Chandra, K. (2006). *Probability and Random Processes*. Wiley-Interscience, 1st edition.
- Kvam, P. H. and Vidakovic, B. (2007). *Nonparametric Statistics with Applications to Science and Engineering*. Wiley, Hoboken, NJ.
- Laakso, T. I., Välimäki, V., Karjalainen, M., and Laine, U. K. (1996). Splitting the unit delay. *IEEE Signal processing magazine*, pages 30–60.
- Lanari, R., Mora, O., Manunta, M., Mallorquí, J. J., Berardino, P., and Sansosti, U. (2004). A small-baseline approach for investigating deformations on full-resolution differential SAR interferograms. *IEEE Transactions on Geoscience and Remote Sensing*, 42(7):1377–1386.
- Lauknes, T., Zebker, H., and Larsen, Y. (2011). InSAR deformation time series using an L1-Norm small-baseline approach. *Geoscience and Remote Sensing, IEEE Transactions on*, 49(1):536–546.
- Laur, H., Bally, P., Meadows, P., Sanchez, J., Schaettler, B., Lopinto, E., and Esteban, D. (2002). Derivation of the backscattering coefficient σ^0 in ESA ERS SAR PRI products. Technical Report ES-TN-RS-PM-HL09, ESA. Issue 2, Rev. 5d.
- Lavalle, M., Simard, M., and Hensley, S. (2012). A temporal decorrelation model for polarimetric radar interferometers. *Geoscience and Remote Sensing, IEEE Transactions on*, 50(7):2880–2888.
- Lee, J.-S., Cloude, S., Papathanassiou, K., Grunes, M., and Woodhouse, I. (2003). Speckle filtering and coherence estimation of polarimetric SAR interferometry data for forest applications. *Geoscience and Remote Sensing, IEEE Transactions on*, 41(10):2254–2263.
- Lee, J. S., Hoppel, K. W., Mango, S. A., and Miller, A. R. (1994). Intensity and phase statistics of multilook polarimetric and interferometric SAR imagery. *IEEE Transactions on Geoscience and Remote Sensing*, 30:1017.
- Lee, J.-S., Papathanassiou, K. P., Ainsworth, T. L., and adn Andreas Reigber, M. R. G. (1998). A new technique for noise filtering of SAR interferometric phase images. *IEEE Transactions on Geoscience and Remote Sensing*, 36(5):1456–1465.
- Li, Z., Fielding, E., Cross, P., and Muller, J.-P. (2006a). Interferometric synthetic aperture radar atmospheric correction: GPS topography-dependent turbulence model. *Journal of Geophysical Research*, 111(B02404).
- Li, Z., Muller, J.-P., Cross, P., Albert, P., Fischer, J., and Bennartz, R. (2006b). Assessment of the potential of MERIS near-infrared water vapour products to correct ASAR interferometric measurements. *International Journal of Remote Sensing*, 27:349–365.
- Li, Z., Muller, J.-P., Cross, P., and Fielding, E. J. (2005). Interferometric synthetic aperture radar (InSAR) atmospheric correction: GPS, moderate resolution imaging spectroradiometer (MODIS), and InSAR integration. *Journal of Geophysical Research*, 110(B03410):doi:10.1029/2004JB003446.
- Li, Z. W., Ding, X. L., and Liu, G. (2004). Modeling atmospheric effects on InSAR with meteorological and continuous GPS observations: algorithms and some test results. *Journal of Atmospheric and Solar-Terrestrial Physics*,

- 66(doi:10.1016/j.jastp.2004.02.006):907–917.
- Lidberg, M., Johansson, J. M., Scherneck, H.-G., and Milne, G. A. (2010). Recent results based on continuous GPS observations of the GIA process in fennoscandia from BIFROST. *Journal of Geodynamics*, 50(1):8 – 18.
- Liu, J. (2001). *Monte Carlo strategies in scientific computing*. Springer, Berlin Heidelberg New York.
- Liu, S. (2012). *Satellite Radar Interferometry: estimation of atmosphere delay*. PhD thesis, Delft University of Technology, Delft, the Netherlands.
- Liu, S., Mika, A., Gong, W., Hanssen, R., Meyer, F., Morton, D., and Webley, P. (2011). The role of weather models in mitigation of tropospheric delay for SAR interferometry. In *Geoscience and Remote Sensing Symposium (IGARSS), 2011 IEEE International*, pages 2562–2565.
- Lombardini, F. (2005). Differential tomography: A new framework for SAR interferometry. *IEEE Transactions on Geoscience and Remote Sensing*, 43(1):37–44.
- Lucido, M., Meglio, F., Pascazio, V. P., and Schirinzi, G. (2010). Closed-form evaluation of the second-order statistical distribution of the interferometric phases in dual-baseline SAR systems. *IEEE Transactions on Geoscience and Remote Sensing*, 58(3):1698–1707.
- Lyons, S. and Sandwell, D. (2002). Fault creep along the southern San Andreas from InSAR, permanent scatterers, and stacking. *Journal of Geophysical Research*, 108(B1):24 pp.
- Madsen, S. N. (1986). *Speckle Theory: Modelling, analysis, and applications related to Synthetic Aperture Radar Data*. PhD thesis, Technical University of Denmark.
- Madsen, S. N., Zebker, H. A., and Martin, J. (1993). Topographic mapping using radar interferometry: Processing techniques. *IEEE Transactions on Geoscience and Remote Sensing*, 31(1):246–255.
- Mahapatra, P. (2015). *Geodetic network design for InSAR: Application to ground deformation monitoring*. PhD thesis, Delft University of Technology, Delft, the Netherlands.
- Mahapatra, P., Samiei-Esfahany, S., and Hanssen, R. (2015). Geodetic network design for InSAR. *Geoscience and Remote Sensing, IEEE Transactions on*, (99):1–12.
- Mahapatra, P., Samiei-Esfahany, S., van der Marel, H., and Hanssen, R. (2014). On the use of transponders as coherent radar targets for SAR interferometry. *Geoscience and Remote Sensing, IEEE Transactions on*, 52(3):1869–1878.
- Mandic, D. P. and Goh, V. S. L. (2009). *Complex Valued Nonlinear Adaptive Filters: Noncircularity, Widely Linear and Neural Models*. Wiley, New York, 2nd edition.
- Mardia, K. V. and Jupp, P. E. (2000). *Directional Statistics*. Wiley Series in Probability and Statistics.
- Marinkovic, P. and Hanssen, R. (2007). Dynamic persistent scatterers interferometry. In *International Geoscience and Remote Sensing Symposium, Barcelona, Spain, 23–27 July 2007*, page 4 pp.
- Marinkovic, P., Ketelaar, G., van Leijen, F., and Hanssen, R. (2008). InSAR quality control: Analysis of five years of corner reflector time series. In *Fifth International Workshop on ERS/Envisat SAR Interferometry, 'FRINGE07', Frascati, Italy, 26 Nov-*

- 30 Nov 2007, page 8 pp.
- Markoff, A. A. (1912). *Wahrscheinlichkeitsrechnung*. Teubner, Leipzig.
- Massonnet, D., Briole, P., and Arnaud, A. (1995). Deflation of Mount Etna monitored by spaceborne radar interferometry. *Nature*, 375:567–570.
- Massonnet, D. and Feigl, K. L. (1998). Radar interferometry and its application to changes in the earth's surface. *Reviews of Geophysics*, 36(4):441–500.
- Massonnet, D., Holzer, T., and Vadon, H. (1997). Land subsidence caused by the east mesa geothermal field, California, observed using SAR interferometry. *Geophysical Research Letters*, 24(8):901–904. Correction in GRL v.25,n.16,p.3213,1998.
- Massonnet, D., Rossi, M., Carmona, C., Adagna, F., Peltzer, G., Feigl, K., and Rabaute, T. (1993). The displacement field of the Landers earthquake mapped by radar interferometry. *Nature*, 364(8):138–142.
- Massonnet, D. and Souyris, J.-C. (2008). *Imaging with Synthetic Aperture Radar*. CRC Press. ISBN 9780849382390.
- MATLAB (2014). *version R2014a, statistical toolbox*. The MathWorks Inc., Natick, Massachusetts.
- Meyer, F., Bamler, R., Jakowski, N., and Fritz, T. (2006). The potential of low-frequency SAR systems for mapping ionospheric TEC distributions. *Geoscience and Remote Sensing Letters, IEEE*, 3(4):560–564.
- Michel, R., Avouac, J.-P., and Taboury, J. (1999). Measuring ground displacement from SAR amplitude images: application to the Landers earthquake. *Geophysical Research Letters*, 26(7):875–878.
- Monti-Guarnieri, A. and Prati, C. (1996). ScanSAR focusing and interferometry. *Geoscience and Remote Sensing, IEEE Transactions on*, 34(4):1029–1038.
- Monti-Guarnieri, A. and Prati, C. (1997). SAR interferometry: A “quick and dirty” coherence estimator for data browsing. *IEEE Transactions on Geoscience and Remote Sensing*, 35(3):660–669.
- Monti-Guarnieri, A. and Rocca, F. (1999). Combination of low- and high-resolution SAR images for differential interferometry. *IEEE Transactions on Geoscience and Remote Sensing*, 37(4):2035–2049.
- Monti-Guarnieri, A. and Tebaldini, S. (2007). Hybrid Cramér-Rao bounds for crustal displacement field estimators in SAR interferometry. *Signal Processing Letters, IEEE*, 14(12):1012–1015.
- Monti-Guarnieri, A. and Tebaldini, S. (2008). On the exploitation of target statistics for SAR interferometry applications. *IEEE Transactions on Geoscience and Remote Sensing*, 46(11):3436–3443.
- Mora, O., Mallorqui, J. J., and Broquetas, A. (2003). Linear and nonlinear terrain deformation maps from a reduced set of interferometric SAR images. *IEEE Transactions on Geoscience and Remote Sensing*, 41(10):2243–2253.
- Morishita, Y. and Hanssen, R. F. (2015a). Deformation parameter estimation in low coherence areas using a multisatellite InSAR approach. *IEEE Transactions on Geoscience and Remote Sensing*, 53(8):4275–4283.
- Morishita, Y. and Hanssen, R. F. (2015b). Temporal decorrelation in L-, C-, and X-band

- satellite radar interferometry for pasture on drained peat soils. *IEEE Transactions on Geoscience and Remote Sensing*, 53(02):1096–1104.
- Muntendam Bos, A., Hanssen, R., van Thienen-Visser, K., and Samiei-Esfahany, S. (2009). PS-InSAR analyse van de bodemdaling in Noordwest Friesland. Technical report, TNO Bouw en Ondergrond. Technical report submitted to State supervision of mines, Dutch ministry of economic affairs.
- Neeser, F. and Massey, J. (1993). Proper complex random processes with applications to information theory. *Information Theory, IEEE Transactions on*, 39(4):1293–1302.
- Nerem, R. S., Leuliette, E., and Cazenave, A. (2006). Present-day sea-level change: A review. *Comptes Rendus Geoscience*, 338(14-15):1077–1083.
- Nico, G., Tome, R., Catalao, J., and Miranda, P. (2011). On the use of the WRF model to mitigate tropospheric phase delay effects in SAR interferograms. *Geoscience and Remote Sensing, IEEE Transactions on*, 49(12):4970–4976.
- Nitti, D. O., Hanssen, R. F., Refice, A., Bovenga, F., Milillo, G., and Nutricato, R. (2008). Evaluation of DEM-assisted SAR coregistration. In *SPIE Europe Remote Sensing, Proceedings 15–18 September 2008, Cardiff, United Kingdom*, pages 1–14.
- Nitti, D. O., Hanssen, R. F., Refice, A., Bovenga, F., and Nutricato, R. (2011). Impact of DEM-assisted coregistration on high-resolution SAR interferometry. *IEEE Transactions on Geoscience and Remote Sensing*, 49(3):1127–1143.
- Oberhettinger, F. (1970). Hypergeometric functions. In Abramowitz and Stegun (1970), chapter 15, pages 555–566.
- Onn, F. and Zebker, H. A. (2006). Correction for interferometric synthetic aperture radar atmospheric phase artifacts using time series of zenith wet delay observations from a GPS network. *Journal of Geophysical Research*, 111(B09102):doi:10.1029/2005JB004012.
- Papoulis, A. (1968). *Systems and Transforms with Applications in Optics*. McGraw-Hill series in Systems Science. McGraw-Hill, New York.
- Papoulis, A. (1991). *Probability, Random variables, and stochastic processes*. McGraw-Hill series in Electrical Engineering. McGraw-Hill, New York.
- Parizzi, A. and Brcic, R. (2011). Adaptive InSAR stack multilooking exploiting amplitude statistics: A comparison between different techniques and practical results. *Geoscience and Remote Sensing Letters*, 8(3):441–445.
- Pepe, A., Euillades, L., Manunta, M., and Lanari, R. (2011). New advances of the extended minimum cost flow phase unwrapping algorithm for SBAS-DInSAR analysis at full spatial resolution. *Geoscience and Remote Sensing, IEEE Transactions on*, 49(10):4062–4079.
- Pepe, A. and Lanari, R. (2006). On the extension of minimum cost flow algorithm for phase unwrapping of multitemporal differential SAR interferograms. *IEEE Transactions on Geoscience and Remote Sensing*, 44(9):2374–2383.
- Pepe, A., Yang, Y., Manzo, M., and Lanari, R. (2015). Improved EMCF-SBAS processing chain based on advanced techniques for the noise-filtering and selection of small baseline multi-look DInSAR interferograms. *Geoscience and Remote Sensing, IEEE Transactions on*, 53(8):4394–4417.

- Pettitt, A. (1976). A two-sample Anderson–Darling rank statistic. *Biometrika*, 63(1):pp. 161–168.
- Picinbono, B. and Bondon, P. (1997). Second-order statistics of complex signals. *Signal Processing, IEEE Transactions on*, 45(2):411–420.
- Pinel-Puysegur, B., Michel, R., and Avouac, J. (2012). Multi-Link InSAR time series: Enhancement of a wrapped interferometric database. *IEEE Journal of Selected Topics in Applied Earth Observations and Remote Sensing*, 5(3):784–794.
- Plag, H. and Pearlman, M. (2009). *Global Geodetic Observing System: Meeting the Requirements of a Global Society on a Changing Planet in 2020*. Springer Berlin Heidelberg.
- Poland, M. P., Hamburger, M. W., and Newman, A. V. (2006). The changing shapes of active volcanoes: History, evolution, and future challenges for volcano geodesy. *Journal of Volcanology and Geothermal Research*, 150(1-3):1–13.
- Prati, C. and Rocca, F. (1992). Range resolution enhancement with multiple SAR surveys combination. In *International Geoscience and Remote Sensing Symposium, Houston, Texas, USA, May 26–29 1992*, pages 1576–1578.
- Prats-Iraola, P., Scheiber, R., Marotti, L., Wollstadt, S., and Reigber, A. (2012). TOPS interferometry with TerraSAR-X. *Geoscience and Remote Sensing, IEEE Transactions on*, 50(8):3179–3188.
- Press, W. H., Flannery, B. P., Teukolsky, S. A., and Vetterling, W. T. (1989). *Numerical Recipes, the art of scientific computing (fortran version)*. Cambridge University Press, Cambridge.
- Press, W. H., Teukolsky, S. A., Vetterling, W. T., and Flannery, B. P. (2007). *Numerical Recipes 3rd Edition: The Art of Scientific Computing*. Cambridge University Press, New York, NY, USA, 3 edition.
- Puyssegur, B., Michel, R., and Avouac, J. P. (2007). Tropospheric phase delay in InSAR estimated from meteorological model and multispectral imagery. *Journal of Geophysical Research*, in press.
- Quegan, S., Dutra, L., and Grover, K. (1994). Phase measurements in MAESTRO polarimetric data from the UK test sites. *International Journal of Remote Sensing*, 15(14):2719–2736.
- Reed, I. (1962). On a moment theorem for complex gaussian peocesses. *Information theory, IRE Transactions on*, (8):194–195.
- Reigber, A. and Moreira, A. (2000). First demonstration of airborne SAR tomography using multibaseline L-band data. *IEEE Transactions on Geoscience and Remote Sensing*, 38(5):2142–2152.
- Rice, J. (2001). *Mathematical Statistics and Data Analysis*. Duxbury Press, 3 edition.
- Ripley, B. D. (1987). *Stochastic Simulation*. John Wiley & Sons, Ltd., New York.
- Rocca, F. (2007). Modeling interferogram stacks. *IEEE Transactions on Geoscience and Remote Sensing*, 45(10):3289–3299.
- Rocca, G. F. A. M.-G. F. (2000). Optimal, space-varying spectral filtering of IFSAR data. In *International Geoscience and Remote Sensing Symposium, Honolulu, Hawaii, 24–28 July 2000*.

- Rodriguez, E. and Martin, J. M. (1992). Theory and design of interferometric synthetic aperture radars. *IEE Proceedings-F*, 139(2):147–159.
- Roering, J. J., Stimely, L. L., Mackey, B. H., and Schmidt, D. A. (2009). Using dinsar, airborne lidar, and archival air photos to quantify landsliding and sediment transport. *Geophysical Research Letters*, 36(19).
- Rogers, G. and Dragert, H. (2003). Episodic tremor and slip on the cascadia subduction zone: The chatter of silent slip. *Science*, 300(5627):1942–1943.
- Rommen, B., Gala, L., Hanssen, R., Liu, S., Mätzler, C., Mika, A., Morland, J., Santoro, M., Wegmüller, U., Werner, C., and Zelle, H. (2009). The ESA METAWAVE project—correcting for atmospheric water vapour effects in InSAR products. In *Third European Conference on Antennas and Propagation, Berlin, Germany, 23–27 March 2009*, page in preparation.
- Rosen, P. A., Hensley, S., Zebker, H. A., Webb, F. H., and Fielding, E. J. (1996). Surface deformation and coherence measurements of Kilauea volcano, Hawaii, from SIR-C radar interferometry. *Journal of Geophysical Research*, 101(E10):23109–23125.
- Rott, H., Stuefer, M., Siegel, A., Skvarca, P., and Eckstaller, A. (1998). Mass fluxes and dynamics of Moreno Glacier, Southern Patagonia Icefield. *Geophysical Research Letters*, 25(9):1407–1410.
- Rummel, R. (2014). Geodäsie in zeiten des wandels — versuch einer standortbestimmung. *ZFV Journal for Geodesy, Geoinformation and Land Management*, 139(4):211–216.
- Rummel, R. and Teunissen, P. (1988). Geodetic boundary value problem and linear inference. In *Holota, P. (Ed.): Proceedings of the International Symposium: Figure and Dynamics of the Earth, Moon and Planets, Prag*, pages 227–264.
- Samiei-Esfahany, S., Martins, J. E., van Leijen, F., and Hanssen, R. F. (2016). Phase estimation for distributed scatterers in InSAR stacks using integer least squares estimation. *IEEE Transactions on Geoscience and Remote Sensing*, 54(10):5671–5687.
- Samiei-Esfahany, S., van Leijen, F. J., Marinkovic, P., Ketelaar, G., and Hanssen, R. F. (2008). Lessons learned from PSIC4: Improving PSI results for a constrained test site. In *Fifth International Workshop on ERS/Envisat SAR Interferometry, 'FRINGE07', Frascati, Italy, 26 Nov-30 Nov 2007*, page 7 pp.
- Samson, J. (1996). Coregistration in SAR interferometry. Master's thesis, Faculty of Geodetic Engineering, Delft University of Technology.
- Sandwell, D. T. and Price, E. J. (1998). Phase gradient approach to stacking interferograms. *Journal of Geophysical Research*, 103(B12):30183–30204.
- Sansosti, E., Berardino, P., Manunta, M., Serafino, F., and Fornaro, G. (2006). Geometrical SAR image registration. *IEEE Transactions on Geoscience and Remote Sensing*, 44(10):2861–2870.
- Sarabandi, K. (1992). Derivation of phase statistics from the mueller matrix. *Radio Science*, 27(5):553–560.
- Scheiber, R., Jager, M., Prats-Iraola, P., De Zan, F., and Geudtner, D. (2015). Speckle tracking and interferometric processing of terraSAR-X tops data for mapping nonstationary scenarios. *Selected Topics in Applied Earth Observations and Remote Sensing, IEEE Journal of*, 8(4):1709–1720.

- Scheiber, R. and Moreira, A. (2000). Coregistration of interferometric SAR images using spectral diversity. *IEEE Transactions on Geoscience and Remote Sensing*, 38(5):2179–2191.
- Scheiber-Enslin, S. E., LaFemina, P. C., Sturkell, E., Hooper, A. J., and Webb, S. J. (2011). Geodetic investigation of plate spreading along a propagating ridge: the eastern volcanic zone, iceland. *Geophysical Journal International*, 187(3):1175–1194.
- Schmidt, D. A. and Bürgmann, R. (2003). Time-dependent land uplift and subsidence in the Santa Clara valley, California, from a large interferometric synthetic aperture radar data set. *Journal of Geophysical Research*, 108(B9):doi:10.1029/2002JB002267.
- Scholz, F. and Stephens, M. (1987). K-sample Anderson-Darling tests. *Journal of the American Statistical Association*, 82(399):pp. 918–924.
- Schreier, P. and Scharf, L. (2003). Second-order analysis of improper complex random vectors and processes. *Signal Processing, IEEE Transactions on*, 51(3):714–725.
- Schwäbisch, M. (1995). Die SAR-Interferometrie zur Erzeugung digitaler Geländemodelle. Forschungsbericht 95-25, Deutsche Forschungsanstalt für Luft- und Raumfahrt, Oberpfaffenhofen.
- Sella, G. F., Stein, S., Dixon, T. H., Craymer, M., James, T. S., Mazzotti, S., and Dokka, R. K. (2007). Observation of glacial isostatic adjustment in stable north america with GPS. *Geophysical Research Letters*, 34(2). L02306.
- Seymour, M. S. and Cumming, I. G. (1994). Maximum likelihood estimation for SAR interferometry. In *International Geoscience and Remote Sensing Symposium, Pasadena, CA, USA, 8–12 August 1994*, pages 2272–2275.
- Shanker, A. P. and Zebker, H. (2010). Edgelist phase unwrapping algorithm for time series insar analysis. *Journal of Optical Society of America*, 27(3):605–612.
- Shanker, P. (2006). *Persistent Scatterer Interferometry in Natural Terrains*. PhD thesis, Stanford University.
- Sigmundsson, F., Hooper, A., Hreinsdottir, S., Vogfjord, K. S., Ofeigsson, B. G., Heimisson, E. R., Dumont, S., Parks, M., Spaans, K., Gudmundsson, G. B., Drouin, V., Arnadottir, T., Jonsdottir, K., Gudmundsson, M. T., Hognadottir, T., Fridriksdottir, H. M., Hensch, M., Einarsson, P., Magnusson, E., Samsonov, S., Brandsdottir, B., White, R. S., Agustsdottir, T., Greenfield, T., Green, R. G., Hjartardottir, A. R., Pedersen, R., Bennett, R. A., Geirsson, H., La Femina, P. C., Bjornsson, H., Palsson, F., Sturkell, E., Bean, C. J., Mollhoff, M., Braiden, A. K., and Eibl, E. P. S. (2015). Segmented lateral dyke growth in a rifting event at Bardarbunga volcanic system, Iceland. *Nature*, 517(7533):191–195.
- Sigmundsson, F., Vadon, H., and Massonnet, D. (1997). Readjustment of the Krafla spreading segment to crustal rifting measured by satellite radar interferometry. *Geophysical Research Letters*, 24(15):1843–1846.
- Stephens, M. A. (1970). Use of the Kolmogorov-Smirnov, Cramer-Von mises and related statistics without extensive tables. *Journal of the Royal Statistical Society. Series B (Methodological)*, 32(1):pp. 115–122.
- Strozzi, T., Luckman, A., Murray, T., Wegmuller, U., and Werner, C. (2002). Glacier motion estimation using SAR offset-tracking procedures. *Geoscience and Remote Sensing, IEEE Transactions on*, 40(11):2384–2391.

- te Brake, B., Hanssen, R., van der Ploeg, M., and de Rooij, G. (2013). Satellite-based radar interferometry to estimate large-scale soil water depletion from clay shrinkage: Possibilities and limitations. *Vadose Zone J*, 12.
- Teunissen, P. J. G. (1990). Quality control in integrated navigation systems. *IEEE Aerospace and Electronic Systems Magazine*, 5(7):35–41.
- Teunissen, P. J. G. (1993). Least-squares estimation of the integer GPS ambiguities. In *Invited Lecture, Section IV Theory and Methodology, IAG General Meeting, Beijing, China, august 1993*. Also in: Delft Geodetic Computing Centre, LGR Series, No. 6, 1994.
- Teunissen, P. J. G. (1995). The least-squares ambiguity decorrelation adjustment: a method for fast GPS integer ambiguity estimation. *Journal of Geodesy*, 70(1-2):65–82.
- Teunissen, P. J. G. (1998). Success probability of integer GPS ambiguity rounding and bootstrapping. *Journal of Geodesy*, 72:606–612.
- Teunissen, P. J. G. (1999). An optimality property of the integer least-squares estimator. *Journal of Geodesy*, 73:587–593.
- Teunissen, P. J. G. (2006). On InSAR ambiguity resolution for deformation monitoring. *Artificial Satellites*, 41(1):17–22.
- Teunissen, P. J. G. (2007). Best prediction in linear models with mixed integer/real unknowns: theory and application. *Journal of Geodesy*, 81(12):759–780.
- Teunissen, P. J. G. (2008). On a stronger-than-best property for best prediction. *Journal of Geodesy*, 82(3):167–175.
- Teunissen, P. J. G. and Amiri-Simkooei, A. R. (2008). Least-squares variance component estimation. *Journal of Geodesy*, 82:65–82.
- Teunissen, P. J. G. and Kleusberg, A., editors (1998). *GPS for geodesy*. Springer-Verlag, 2 edition.
- Tienstra, J. M. (1956). *Theory of the adjustment of normally distributed observations*. Argus, Amsterdam.
- Torge, W. and Müller, J. (2012). *Geodesy*. Walter De Gruyter, Berlin/Boston. ISBN 3-11-012408-4.
- Tosi, L., Teatini, P., and Strozzi, T. (2013). Natural versus anthropogenic subsidence of venice. *Scientific Reports*, 3.
- Tough, R. J. A., Blacknell, D., and Quegan, S. (1995). A statistical description of polarimetric and interferometric synthetic aperture radar. *Proceedings of the Royal Society London A*, 449:567–589.
- Touzi, R. and Lopes, A. (1996). Statistics of the Stokes parameters and of the complex coherence parameters in one-look and multilook speckle fields. *IEEE Transactions on Geoscience and Remote Sensing*, 34(2):519–531.
- Touzi, R., Lopes, A., Bruniquel, J., and Vachon, P. (1996a). Unbiased estimation of the coherence from multi-look SAR data. In *International Geoscience and Remote Sensing Symposium, Lincoln, Nebraska, USA, 27–31 May 1996*, volume 1, pages 662–664.
- Touzi, R., Lopes, A., Bruniquel, J., and Vachon, P. W. (1999). Coherence estimation for SAR imagery. *IEEE Transactions on Geoscience and Remote Sensing*, 1(37):135–149.

- Touzi, R., Lopes, A., and Vachon, P. W. (1996b). Estimation of the coherence function for interferometric SAR applications. In *European Conference on Synthetic Aperture Radar, Königswinter, Germany, 26–28 March 1996*, pages 241–244.
- Usai, S. (1997). The use of man-made features for long time scale InSAR. In *International Geoscience and Remote Sensing Symposium, Singapore, 3–8 Aug 1997*, pages 1542–1544.
- Usai, S. (2003). A least squares database approach for SAR interferometric data. *IEEE Transactions on Geoscience and Remote Sensing*, 41(4):753–760.
- Usai, S. and Hanssen, R. (1997). Long time scale InSAR by means of high coherence features. In *Third ERS Symposium—Space at the Service of our Environment, Florence, Italy, 17–21 March 1997*, pages 225–228.
- Usai, S. and Klees, R. (1999). On the interferometric characteristics of anthropogenic features. In *International Geoscience and Remote Sensing Symposium, Hamburg, Germany, 28 June–2 July 1999*.
- van der Hoeven, A., Hanssen, R. F., and Ambrosius, B. (2002). Tropospheric delay estimation and analysis using GPS and SAR interferometry. *Physics and Chemistry of the Earth*, 27:385–390.
- Van der Kooij, M. (2003). Coherent target analysis. In *Third International Workshop on ERS SAR Interferometry, 'FRINGE03', Frascati, Italy, 1-5 Dec 2003*.
- van der Kooij, M. W. A., van Halsema, D., Groenewoud, W., Mets, G. J., Overgaauw, B., and Visser, P. N. A. M. (1995). *SAR Land Subsidence Monitoring*, volume NRSP-2 95-13. Beleidscommissie Remote Sensing, Delft.
- van Leijen, F. (2014). *Persistent Scatterer Interferometry based on geodetic estimation theory*. PhD thesis, Delft University of Technology, Delft, the Netherlands.
- van Leijen, F. and Hanssen, R. (2008). Ground water management and its consequences in Delft, the Netherlands as observed by persistent scatterer interferometry. In *Fifth International Workshop on ERS/Envisat SAR Interferometry, 'FRINGE07', Frascati, Italy, 26 Nov-30 Nov 2007*, page 6 pp.
- van Leijen, F. J. and Hanssen, R. F. (2007). Persistent scatterer density improvement using adaptive deformation models. In *International Geoscience and Remote Sensing Symposium, Barcelona, Spain, 23–27 July 2007*, page 4 pp.
- Vasile, G., Trouvé, E., Ciuc, M., and Buzuloiu, V. (2004). General adaptive neighborhood technique for improving synthetic aperture radar interferometric coherence estimation. *Journal of Optical Society of America*, 21(8):1455–1464.
- Vasile, G., Trouve, E., Lee, J.-S., and Buzuloiu, V. (2006). Intensity-driven adaptive-neighborhood technique for polarimetric and interferometric SAR parameters estimation. *Geoscience and Remote Sensing, IEEE Transactions on*, 44(6):1609–1621.
- Velicogna, I. and Wahr, J. (2006). Measurements of time-variable gravity show mass loss in antarctica. *Science*, 311(5768):1754–1756.
- Wadge, G., Webley, P. W., James, I. N., Bingley, R., Dodson, A., Waugh, S., Veneboer, T., Puglisi, G., Mattia, M., Baker, D., Edwards, S. C., Edwards, S. J., and Clarke, P. J. (2002). Atmospheric models, GPS and InSAR measurements of the tropospheric water vapour field over Mount Etna. *Geophysical Research Letters*, 29(19):11/1–4.

- Wang, Y. and Zhu, X. X. (2016). Robust estimators for multipass SAR interferometry. *IEEE Transactions on Geoscience and Remote Sensing*, 54(2):968–980.
- Wang, Y., Zhu, X. X., and Bamler, R. (2011). Optimal estimation of distributed scatterer phase history parameters from meter-resolution SAR data. In *International Geoscience and Remote Sensing Symposium, Vancouver, Canada, 24–29 July 2011*, pages 3468–3471.
- Wang, Y., Zhu, X. X., and Bamler, R. (2012). Retrieval of phase history parameters from distributed scatterers in urban areas using very high resolution SAR data. *ISPRS Journal of Photogrammetry and Remote Sensing*, 73:89 – 99.
- Wdowinski, S. and Eriksson, S. (2009). Geodesy in the 21st century. *Eos, Transactions American Geophysical Union*, 90(18):153–155.
- Webley, P. W., Bingley, R. M., Dodson, A. H., Wadge, G., Waugh, S. J., and James, I. N. (2002). Atmospheric water vapour correction to InSAR surface motion measurements on mountains: results from a dense GPS network on Mount Etna. *Physics and Chemistry of the Earth, Parts A/B/C*, 29(4-5):363–370.
- Werner, C., Wegmuller, U., Strozzi, T., and Wiesmann, A. (2003). Interferometric point target analysis for deformation mapping. In *International Geoscience and Remote Sensing Symposium, Toulouse, France, 21–25 July 2003*, pages 3 pages, cdrom.
- Williams, S., Bock, Y., and Fang, P. (1998). Integrated satellite interferometry: Tropospheric noise, GPS estimates and implications for interferometric synthetic aperture radar products. *Journal of Geophysical Research*, 103(B11):27,051–27,067.
- Wright, T., Parsons, B., and Fielding, E. (2001). Measurement of interseismic strain accumulation across the North Anatolian Fault by satellite radar interferometry. *Geophysical Research Letters*, 28(10):2117–2120.
- Wright, T. J., Sigmundsson, F., Pagli, C., Belachew, M., Hamling, I. J., Brandsdottir, B., Keir, D., Pedersen, R., Ayele, A., Ebinger, C., Einarsson, P., Lewi, E., and Calais, E. (2012). Geophysical constraints on the dynamics of spreading centres from rifting episodes on land. *Nature Geoscience*, 5(4):242–250.
- Zebker, H. A. and Chen, K. (2005). Accurate estimation of correlation in InSAR observations. *Geoscience and Remote Sensing Letters*, 2(2):1682–1690.
- Zebker, H. A. and Goldstein, R. M. (1986). Topographic mapping from interferometric synthetic aperture radar observations. *Journal of Geophysical Research*, 91(B5):4993–4999.
- Zebker, H. A., Rosen, P. A., Goldstein, R. M., Gabriel, A., and Werner, C. L. (1994a). On the derivation of coseismic displacement fields using differential radar interferometry: The Landers earthquake. *Journal of Geophysical Research*, 99(B10):19617–19634.
- Zebker, H. A., Rosen, P. A., and Hensley, S. (1997). Atmospheric effects in interferometric synthetic aperture radar surface deformation and topographic maps. *Journal of Geophysical Research*, 102(B4):7547–7563.
- Zebker, H. A. and Villasenor, J. (1992). Decorrelation in interferometric radar echoes. *IEEE Transactions on Geoscience and Remote Sensing*, 30(5):950–959.
- Zebker, H. A., Werner, C. L., Rosen, P. A., and Hensley, S. (1994b). Accuracy of topographic maps derived from ERS-1 interferometric data. *IEEE Transactions on Geoscience and Remote Sensing*, 32(4):823–836.

-
- Zhu, C., Byrd, R. H., Lu, P., and Nocedal, J. (1997). Algorithm 778: L-BFGS-B: Fortran subroutines for Large-scale Bound-constrained Optimization. *ACM Trans. Math. Softw.*, 23(4):550–560.
- Zhu, X. and Bamler, R. (2010). Tomographic SAR inversion by L1 norm regularization—The compressive sensing approach. *IEEE Transactions on Geoscience and Remote Sensing*, 48(10):3839–3846.
- Zwieback, S., Liu, X., Antonova, S., Heim, B., Bartsch, A., Boike, J., and Hajnsek, I. (2016). A statistical test of phase closure to detect influences on DInSAR deformation estimates besides displacements and decorrelation noise: Two case studies in high-latitude regions. *IEEE Transactions on Geoscience and Remote Sensing*, PP(99):1–14.



About the Author

Sami Samiei Esfahany (1982) was born in Tehran, Iran. He studied Civil/Surveying Engineering at Amirkabir University of Technology (B.Sc., 2004, Tehran, Iran), and Geomatics Engineering at Delft University of Technology (M.Sc., 2007, Delft, the Netherlands). During his Master studies, he was involved in the technical feasibility study on the potential of satellite radar interferometry for monitoring dikes in the Netherlands. He graduated with an M.Sc. thesis on *improving in the processing algorithms of Persistent Scatterer Interferometry for deformation monitoring*. Following his graduation, he joined the group of Mathematical Geodesy and Positioning (MGP) at TU Delft, as a researcher working for one year on the project *PS-InSAR analysis of subsidence in Northwest Friesland*, in collaboration with TNO. In 2009, he started his Ph.D. research at TU Delft, working on the exploitation of distributed scatterers in InSAR. Since 2013, he is a researcher at the Department of Geoscience and Remote Sensing (GRS), TU Delft. During this period, he was involved in a research and development project for geodetic deformation monitoring, contributing to the long-term study on anomalous time-dependent subsidence in the Wadden Sea region, with close collaboration with NAM/Shell.

During his research work, Sami has also been involved in different educational activities at TU Delft. He has been the co-instructor of the master course *Geo-Measurement Processing (Estimation Theory)*, and the co-developer and instructor of the online EdX course *Observation Theory: Estimating the Unknown*. He was a guest lecturer in courses on Geodesy and Natural Hazards, Radar Remote Sensing and Deformation Analysis, Multivariate Data Analysis, and Geostatistics. He lectured tutorials on InSAR processing during the Advanced Workshop on Evaluating, Monitoring and Communicating Volcanic and Seismic Hazards at International Center for Theoretical Physics (ICTP) (2009 and 2013, Trieste, Italy), and he held a workshop on *InSAR for earthquake modeling* at University of Tehran (2016, Iran).

His current research interests include estimation theory and mathematical geodesy with applications to SAR interferometry and deformation monitoring.

List of Publications

Journal Papers:

Samiei-Esfahany, S., Hanssen, R.F. (*submitted manuscript*). A Periodic Temporal Decorrelation Model in InSAR Stacks for Distributed Scatterers in Pasture and Agricultural Areas. *IEEE Transactions on Geoscience and Remote Sensing*.

Mahapatra, P.S., van der Marel, H., van Leijen, F., **Samiei-Esfahany, S.**, Klees, R, Hanssen, R.F. (*submitted manuscript*). InSAR Datum Connection Using GNSS-Augmented Radar Transponders. *Journal of Geodesy*.

Samiei-Esfahany, S., Martins, J., van Leijen, F., Hanssen, R.F. (2016). Phase Estimation for Distributed Scatterers in InSAR Stacks using Integer Least Squares Estimation. *IEEE Transactions on Geoscience and Remote Sensing*, Volume:54 , Issue:10.

Mahapatra, P.S., **Samiei-Esfahany, S.**, Hanssen, R.F. (2015). Geodetic Network Design for InSAR. *IEEE Transactions on Geoscience and Remote Sensing*, Volume:53 , Issue:7.

Mahapatra, P.S., **Samiei-Esfahany, S.**, van der Marel, H., Hanssen, R.F.(2014). On the Use of Transponders as Coherent Radar Targets for SAR Interferometry. *IEEE Transactions on Geoscience and Remote Sensing*, Volume:52, Issue:3.

Conference Proceedings:

Samiei-Esfahany, S., López-Dekker P., Hanssen, R.F. (*accepted*). On the effect of soil moisture phase inconsistencies on distributed scatterers phase estimators in InSAR stacks. *Fringe 2017 workshop, Advances in the Science and Applications of SAR Interferometry and Sentinel-1 InSAR, Helsinki, Finland, June 2017*.

Mahapatra, P.S., **Samiei-Esfahany, S.**, Hanssen, R.F. (2014). Geodetic network design for InSAR using reflectors and transponders. *International Geoscience and Remote Sensing Symposium, Québec, Canada, July 2014*.

Kiseleva E., Mikhailov V., Smolyaninova E., Dmitriev P., Golubev V., Timoshkina E., Hooper A., **Samiei-Esfahany, S.**, Hanssen R.F. (2014). PS-InSAR monitoring of landslide activity in the Black Sea coast of the Caucasus. *Proceedings of CENTERIS 2014*.

Samiei-Esfahany, S., Hanssen, R.F. (2013). New algorithm for InSAR stack phase triangulation using integer least squares estimation. *International Geoscience and Remote Sensing Symposium, Melbourne, Australia, July 2013*.

Mahapatra, P.S., **Samiei-Esfahany, S.**, Hanssen, R.F., van der Marel, H. (2013). Geodetic quality assessment of a low-cost InSAR transponder. *International Geoscience and Remote Sensing Symposium, Melbourne, Australia, July 2013*.

Mahapatra, P.S., van der Marel, H., Hanssen, R.F., Holly, R., **Samiei-Esfahany, S.**, Komac, M., Fromberg, A. (2012). Radar transponders and their combination with GNSS for deformation monitoring. *International Geoscience and Remote Sensing Symposium, Munich, Germany, July 2012*.

Mahapatra, P.S., Hanssen, R.F., **Samiei-Esfahany, S.** (2011). Compact Active Transponders for SAR Interferometry: Experimental Validation. *Fringe 2011 workshop, Advances in Science and Applications of SAR Interferometry proceedings, Frascati, Italy, September 2011.*

Bähr, H., **Samiei-Esfahany, S.**, Hanssen, R.F. (2011). On the Effect of Reference Frame Motion on InSAR Deformation Estimates. *Fringe 2011 workshop, Advances in Science and Applications of SAR Interferometry proceedings, Frascati, Italy, September 2011.*

Samiei-Esfahany, S., Hanssen, R.F. (2011). Time-Series InSAR: An Integer Least-Squares Approach for Distributed Scatterers. *Fringe 2011 workshop, Advances in Science and Applications of SAR Interferometry proceedings, Frascati, Italy, September 2011.*

Liu, S., Hanssen, R.F., **Samiei-Esfahany, S.**, Hooper, A., van Leijen, F. (2011). Separating Non-Linear Deformation and Atmospheric Phase Screen (APS) for InSAR Time Series Analysis Using Least-Squares Collocation. *Fringe 2011 workshop, Advances in Science and Applications of SAR Interferometry proceedings, Frascati, Italy, September 2011.*

Caro Cuenca, M., **Samiei-Esfahany, S.**, Hanssen, R.F. (2010). A least squares approach for joining persistent scatterer InSAR time series acquired by different satellites. *Proceedings of the ESA Living Planet Symposium, Bergen, Norway, June 2010.*

Samiei-Esfahany, S., Hanssen, R.F., Thienen-Visser, K., Muntendam-Bos, A. (2009). On The Effect of Horizontal Deformation on InSAR Subsidence Estimates. *Fringe 2009 workshop, Advances in Science and Applications of SAR Interferometry, proceedings, Frascati, Italy, December 2009.*

Samiei-Esfahany, S., van Leijen, F., Marinkovic, P., Ketelaar, G., Hanssen, R.F. (2007) Lessons learned from PSIC4: Improving PS-InSAR Results For a Constrained Test Site. *Fringe 2007 workshop proceedings, Fifth International Workshop on ERS/Envisat SAR Interferometry, Frascati, Italy, November 2007.*

Project Reports:

van Leijen, F., **Samiei-Esfahany, S.**, van der Marel, H., Hanssen, R.F. (2016) Uniformization of geodetic data for deformation analysis, for long-term study on anomalous time-dependent subsidence in the Wadden Sea Region, Phase-II. *TU Delft Project Report.*

Samiei-Esfahany, S., Bähr, H. (2015). Research and Development Project for Geodetic Deformation Monitoring, for long-term study on anomalous time-dependent subsidence in the Wadden Sea Region. *NAM/Shell Project Report.*

Muntendam Bos A.G., Hanssen R.F., van Thienen-Visser K., **Samiei-Esfahany, S.** (2009). PS-InSAR-analyse van de bodemdaling in Noordwest-Friesland. *TNO Rapport (in dutch), November, 2009, Client: Dutch ministry of economic affairs..*

Dentz F.; van Halderen L.; Possel B.; **Samiei-Esfahany, S.**; Slobbe C.; Wortel T. (2006). POSEIDON: On the potential of satellite radar interferometry for monitoring dikes of the Netherlands. *Delft Institute of Earth Observation and Space Systems, TU Delft, 2006, Technical Report.*

